AN EXPERIMENTAL AND COMPUTATIONAL FLUID DYNAMICS STUDY OF THE INFLUENCE OF FLUID MIXING AND FLUID STRESS ON DNA PURIFICATION

A thesis submitted for the degree of

Doctor of Philosophy

by

Francis Jeremiah Meacle

Advanced Centre for Biochemical Engineering

Department of Biochemical Engineering

University College London (UCL)

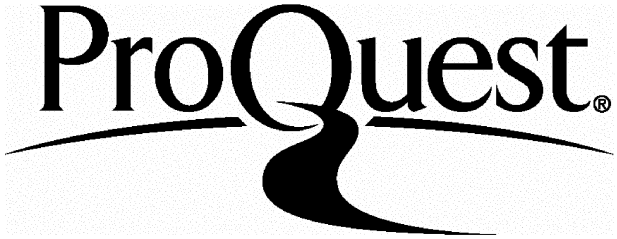

ACKNOWLEDGEMENTS

I would like to offer a very special thanks to Pat, Misti, Tina, and Julia for sharing this experience with me, Clarissa for sharing me with this experience and Nigel for all his experience, without whom this would have been infinitely less fun.

I would also like to acknowledge the much appreciated help and support of Parviz, Ann, Barry and Russ.

And my Parents, and Roisin and Mary....of course.

ABSTRACT

Interest in the field of pure DNA manufacture has been driven in recent years by the explosion of research into gene therapy. Gene therapy technology offers a new paradigm for treating human diseases where defective cells are transformed with gene vectors capable of expressing therapeutic protein. Administration is often via direct injection of naked or lipid-coated plasmid DNA. Plasmid for gene therapy is usually produced in *Escherichia coli*. The challenge in manufacturing plasmid is primarily the removal of impurities like proteins, lipids, lipopolysaccharides, RNA, non-supercoiled plasmid variants, and host chromosomal DNA. Long chain polymers, such as DNA, are uniquely prone to chain scission at moderate to high fluid stresses that commonly occur in biotechnology equipment. Stress-induced degradation of both plasmid DNA and host chromosomal DNA must be minimised to optimise plasmid yield and purity. Such degradation plays a critical role during alkaline lysis, a key step in DNA isolation. The effect of lysis reagent on DNA stability, the required level of fluid mixing, the effect of the resultant fluid stresses on DNA degradation, and the effect of DNA fragmentation on subsequent downstream purification performance are all poorly understood. This thesis sets out to characterise the effect of lysis reagent concentration on DNA so as to determine the required level of fluid mixing during alkaline lysis, to characterise the effect of the resultant fluid stress on DNA degradation and to determine the effects of stress-induced degradation on downstream processing. The following paragraphs outline the key finding of the thesis, which together provide a framework for the design of a robust lysis process.

Two novel HPLC-based procedures were developed, based on polyethylenimine and quaternary amine anion exchange chromatography resins, capable of simultaneously measuring supercoiled plasmid DNA and chromosomal DNA in process samples, in addition the form of the chromosomal DNA.

Experiments using *E. coli* cells containing 6 kb to116 kb plasmids showed that cell lysate should be maintained below 0.13 ± 0.03 M NaOH to prevent irreversible denaturation of supercoiled plasmids and above 0.08 M NaOH to ensure complete conversion of chromosomal DNA to single-stranded form. Conversion of chromosomal DNA to single-stranded form was shown not to significantly affect its removal during alkaline lysis, but was advantageous for subsequent purification. Complete conversion of chromosomal DNA to single-stranded form enabled complete removal by a variety of inexpensive and scaleable purification methods, significantly reducing the cost of plasmid DNA manufacture. Denaturation-renaturation of DNA, either during alkaline lysis or further downstream, was shown to be an effective method of removing non-supercoiled plasmid variants.

The level of mixing required is highly dependent on the sodium hydroxide (NaOH) concentration in the lysis buffer. More highly concentrated lysis buffer reduced the overall lysate volume, but rapid mixing was essential to avoid irreversible supercoiled plasmid degradation. Mixing tanks provided adequate mixing only at low NaOH concentrations. Opposed jets provided excellent mixing characteristics for lysis buffer addition, and concentrated NaOH could be used, significantly reducing the volume increase over alkaline lysis. Opposed jets provided a suitable method for denaturing residual double-stranded chromosomal DNA downstream of alkaline lysis. Hence, inexpensive methods for single-stranded DNA removal could be utilised to remove all residual chromosomal DNA. Computational fluid dynamics (CFD) simulations were used to develop appropriate scaling rules for opposed jets, and the CFD predictions were verified against published experimental data.

Capillary shear degradation studies with pure solutions of 6kb to 116 kb plasmids and chromosomal DNA, determined that DNA degraded at capillary entrances, not internally. Large plasmids degraded at significantly lower fluid flow rates than small plasmids. CFD simulations were used to determine fluid flow properties (turbulent energy dissipation rates, shear stresses, elongational stresses and pressure drops) at the entrance to, and within, capillaries and to correlate breakage of chromosomal and plasmid DNA with fluid flow parameters. Results indicated that elongational fluid stresses caused significantly more DNA degradation than shear stresses. An assay to monitor plasmid degradation in dilute solutions was developed using Picogreen dye, enabling different size plasmids to be used as probes for fluid stress-induced degradation in large-scale industrial equipment.

Results showed that fluid stresses during alkaline lysis led to chromosomal DNA fragmentation. Despite causing chromosomal fragmentation, it was shown that fluid stresses during lysis did not significantly increase chromosomal contamination in cell lysates; chromosomal DNA removal over alkaline lysis/neutralisation not being a strong function of chromosomal DNA size. High levels of fluid stress during the neutralisation step were also shown not to increase chromosomal DNA contamination. The effects of chromosomal DNA fragment size on its removal in different downstream purification steps demonstrated which steps were sensitive to DNA size, enabling better selection of downstream unit operations based on DNA fragmentation upstream.

TABLE OF CONTENTS

List of Figures

LIST OF TABLES

1 Introduction

This chapter describes the rationale for this thesis: a study into the effects of fluid mixing and fluid stresses on DNA purification. The principal aim of this work is the improvement of pure DNA production processes through a better understanding of DNA stress-induced degradation in industrially relevant unit operations. The work presented here primarily focuses on the primary DNA purification step, cell lysis, but also deals with the knock-on effects of cell lysis on downstream purification. This chapter opens with an explanation of the reasons why pure DNA is an important substance; its emerging clinical importance as a therapeutic and prophylactic agent making it a novel and exciting area of research within the biopharmaceutical industry. The current methodologies used for production of DNA at small to moderate scales are described, along with the hurdles that have to be overcome to manufacture DNA in sufficient quantities and at a sufficiently economical price to make it a widely administered medication of the future. This chapter then describes in more detail the primary downstream purification step, cell lysis, and briefly outlines why the physio-chemical properties of DNA make it uniquely sensitive during processing to degradation caused by low levels of fluid mixing or high levels of fluid stress. The specific aims of this thesis are presented, briefly outlining the experimental and computational studies to be performed to achieve these aims. This chapter ends with a description of the structure of this thesis, outlining the purpose of each chapter and the information found therein.

1.1 Gene therapy

Interest in the field of pure DNA manufacture (Ferreira et al., 2000; Prazeres et al., 1999; Levy et al., 2000) has been driven in recent years by the explosion of research into gene therapy. Gene therapy is the delivery of a functional gene for expression in somatic tissues with the intent to selectively correct or modulate disease conditions. Gene therapy can theoretically modify specific genes resulting in a cure following a single administration (Friedman, 1997). Since the discovery of the structure of DNA by Watson and Crick in 1953, treating disease by modifying the genes has become the ultimate dream. Four decades later, and more quickly than anticipated, this dream has become a reality thanks to rapid developments in molecular biology and recombinant DNA techniques, the discovery of the polymerase chain reaction, and the establishment of the Human Genome Project. The advent of gene therapy and the potential of DNA vaccination for the treatment of genetic disorders and acquired diseases has led to an exponential increase in research interests into gene therapy since the first clinical trials began in 1990 (Marquet et al., 1995; Mountain, 2000).

1.1.1 Licensed gene therapies and gene therapy trials

Gene therapy was initially envisioned for the treatment of genetic disorders, but it is currently being studied for a wide range of diseases including cancer, arthritis, neurodegenerative disorders, AIDS and other acquired disorders. Table 1.1 shows some of the applications of gene therapy. Currently, there are more than 400 active clinical gene therapy protocols worldwide (Mhashilkar et al., 2001). The majority of gene therapy protocols focus on treating acquired diseases such as cancer or HIV (Muthumani et al., 2002). Inherited disorders is the second principal focus.

Disorder		Disease
Cancer	Vaccines/immunotherapy	
	Tumour suppressor genes	Ovarian Cancer, Pulmonary carcinoma, Head and neck cancer, Non-small-cell lung cancer, Hematologic malignancies
	Suicide genes	Leptomeningeal carcinomatosis Adenocarcinoma, Glioblastoma GvDH control in allogenic bone marrow transplantation
Cytokines		
Monogenic diseases		X-linked severe combined immunodeficiency, Mucopolysaccharidosis, Familial hypercholesterolemia, Cystic fibrosis, Haemophilia B Chronic granulomatosis
Infectious diseases		AIDS, HIV-1 specific cytotoxic
Other diseases		Coronary heart disease, Angiogenesis, Amyotrophic laterial sclerosis, Rheumatoid arthritis

Table 1.1. Applications of gene therapy. Taken from Mhashilkar et al., 2001.

1.1.2 Gene vectors

The range of gene therapy strategies is quite diverse, and certain key elements are required for their success. The most important and basic of these is that a potential gene of interest must be

identified and cloned in the appropriate expression vector. There are two types of expression vector used: viral vectors and DNA-based vectors (Mountain, 2000). Transfer of new genetic material to cells is by transduction or transfection. Transduction involves the use of viral vectors that are able to infect human cells, but are rendered non-pathogenic and incapable of replication. Among the viral vectors, retrovirus and adenovirus are the two most commonly used vectors that have been tested in phases I/II clinical trials (Mhashilkar et al., 2001). These viruses are made replication-defective by the deletion of one or more viral genes that are essential for replication. The therapeutic gene of interest replaces the essential vial genes that were deleted. Transfection involves the use of non-viral vectors: plasmid DNA. Plasmid DNA based gene vectors can either be pure plasmid DNA or plasmid DNA coated with phospholipids or conjugated with polycations to improve the uptake and expression of the plasmid in the cell (Nabel, 1993). This work of this thesis deals with the production of pure plasmid DNA for DNA-based gene vectors.

1.1.3 DNA vectors

Native DNA is double stranded; the two strands are wound about each other in a double helix with the heterocyclic bases paired between them by hydrogen bonding and hydrophobic interactions. The most common type of helix found in double-stranded DNA is known as the B-form and contains 10.5 bp per turn, and has a 3.4 angstrom axial rise between the planar bases of the right-handed helix (Abeles et al., 1992). DNA is contained within chromosomes and in micro-organisms in extrachromosomal elements such as plasmids. Plasmids consist of a length of double-stranded DNA joined together at either end to form a circle. Plasmids can range in size up to several hundred thousand base pairs, but at present the size of the plasmid DNA being used in clinical trials is at the lower end of the possible range, typically < 10 kb (Levy et al., 2000). Under most conditions of cell growth they are dispensible to their host cell and depend on its metabolic functions for their reproduction. DNA is not structurally rigid and it can undergo conformational and other tertiary structural changes, the dominant form of plasmid tertiary structure of interest being supercoiling, where the piece of circular DNA is wound-up upon itself. In general, bacterial plasmids are primarily isolated as covalently closed-circular DNA molecules in negatively supercoiled forms (Lyubchenko et al., 1997; Langowski et al., 1989). Negatively supercoiled DNA contains fewer helical turns and is therefore under-wound, creating torsional tension in the plasmid (Strick et al., 1998). Figure 1.1 shows a schematic representation of supercoiled, open-circular and linear plasmid DNA.

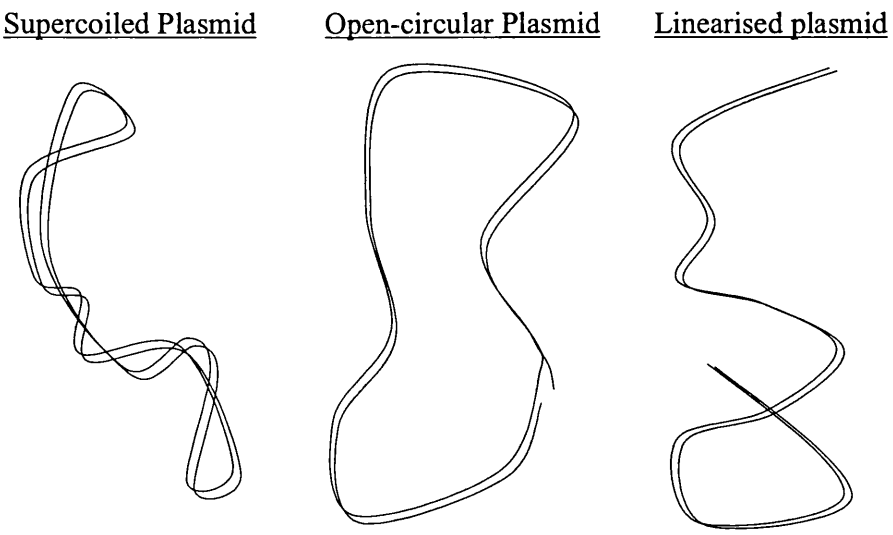

Figure 1.1. Schematic representation of supercoiled, open-circular, and linearised plasmid DNA

1.2 Plasmid DNA manufacture

Large-scale plasmid DNA production processes should be designed to produce a certain amount of plasmid within certain specifications of purity, potency, identity, efficacy and safety that are inherent in the intended therapeutic use (Marquet et al., 1995; Middaugh et al., 1998). Plasmid DNA is typically fermented from a suitable recombinant *Escherichia coli* strain. There is a current understanding that plasmid vectors should be mostly in the supercoiled form which is thought to be more effective at transferring gene expression than non-supercoiled plasmid variants (open-circular, linear, denatured or multimeric plasmids). A combination of plasmid and host-strain selection, with optimisation of media and fermentation, can result in plasmid yields of 0.2 g plasmid /L fermentation broth, or higher (Varley et al. 1999; Prazeres et al., 1999). The fermentation and cell-strain should maximise supercoiled plasmid DNA at the expense of non-supercoiled plasmid variants.

As with recombinant proteins, the majority of problems in the production of plasmid are encountered during the downstream processing operations which are essentially aimed at eliminating cellular components of the host strain (cell debris, protein, RNA, endotoxin, chromosomal DNA and non-supercoiled plasmid variants). Figure 1.2 shows a typical breakdown of macromolecules in *E. coli* by dry cell weight reproduced from the data of Ingrahm et al., 1983. The chromosomal DNA typically accounts for about 3% of the macromolecules present. The amount of plasmid DNA present can vary considerably

depending on the plasmid copy number, which can vary from 1 to several hundred copies per cell. High copy number plasmids make up at least 1 % to 3 % of the macromolecules present (Varley et al. 1999, Levy et al., 2000).

Following cell harvest, the initial recovery step involves cell lysis. The process of choice for cell lysis is most often a variation of the alkaline-lysis procedure originally described by Birnboim (1979). This is certainly a crucial step in the process and the one at which most problems occur (Prazeres et al., 1999). Alkaline lysis will be discussed in detail in the section 1.3. After cell lysis, the lysate is clarified by centrifugation or filtration to remove flocculated impurities, followed by several other purification steps to remove protein, endotoxin, RNA and DNA impurities. In recent years there has been considerable advances in DNA purification. Table 1.2 lists some of the published techniques for the removal of impurities that are reported in the published literature. There are now a range of well-understood, low cost, low shear, and scaleable processes for the removal of cell debris, protein and RNA. Endotoxins can still be difficult to reduce to safe levels because they are negatively charged like DNA and because they have to be reduced to very low levels due to their toxicity. However, a combination of several of the steps listed in Table 1.2 is usually sufficient to reduce endotoxins to acceptable levels.

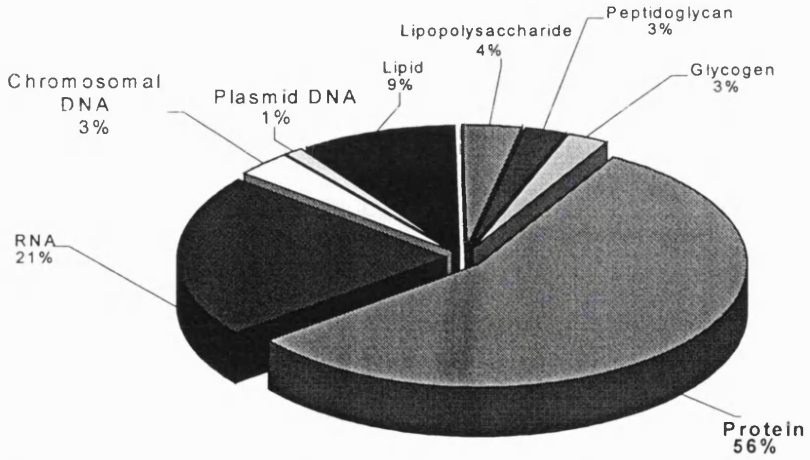

Figure 1.2. Macromolecules in E. coli by % Dry Cell Weight. Adapted from Ingrahm et al., 1983.

Until recently the only method for the removal of chromosomal DNA (chDNA) was chromatography (Ferreira et al., 2000). This usually consisted of an initial purification step (precipitation, filtration or anion exchange chromatography), followed by reversed-phase (RPC), hydrophobic interaction (HIC) or size exclusion (SEC) chromatography which separated the chromosomal and plasmid DNA. Because of the high molecular weight of plasmid and chromosomal DNA, these molecules are excluded from the pores of chromatographic resins such as AE, HIC and RP. This significantly reduces the binding capacity of chromatographic

resins 10- to 100- fold lower than typical values for proteins (Ferreira et al., 1998; Chandra et al., 1992; Prazeres et al., 1998). This significantly increases the cost of chromatographic purification. The large size of DNA molecules makes them difficult to separate on SEC resins, again, due to the lack of available resins with sufficient pore size to accommodate DNA molecules (Moreau et al., 1987; Ferreira et al., 1997). Combined with the high cost of chromatographic resins, the potential high dose of plasmid DNA therapies and the prohibitive cost of chromatographic buffers at manufacturing scale make chromatographic purification a very expensive purification strategy.

Throughout the supercoiled plasmid purification process, the high molecular mass of plasmid and chromosomal DNA make them particularly sensitivity to chain scission by fluid stresses. Long before the large-scale production of DNA was envisaged, studies by Davison et al. (1959), Hershey et al. (1960) and Leventhal et al. (1961) showed that chromosomal DNA could be stretched and fragmented by relatively low levels of fluid stress in syringes, stirred vessels and capillaries, respectively. Since then, several studies have confirmed the susceptibility of chromosomal DNA to fluid stress, and demonstrated that larger DNA molecules break at significantly lower levels of stress than smaller DNA molecules. Fluid stress can easily break the large *E. coli* chromosome down into much smaller chromosomal fragments. More recent studies by Levy et al. (1998) have shown that plasmid DNA is also susceptible to degradation by fluid stresses. If fluid stress causes one of the strands of a supercoiled plasmid to break, supercoiling is lost and an open-circular form is created; therefore, destroying the product of interest while simultaneously creating a difficult to remove impurity. If a break occurs in both strands, at or near the same point, a linear form of the DNA is generated.

Stress degraded plasmid DNA and host chromosomal DNA fragments can be very difficult to remove due to both their similarities in size, and chemistry, to the supercoiled plasmid. There are still few available methods for their removal that are both inexpensive and easily scaleable, as shown in Table 1.2. Because removal of chromosomal DNA and non-plasmid variants add significantly to the purification cost it is essential to minimise the formation of non-plasmid variants and chromosomal DNA fragments. Currently, there are only limited data on the stress-induced degradation of chromosomal and plasmid DNA in typical purification equipment.

Impurity	Unit Operation	Removal Technique	Cost	Shear Level	Performance & Scaleability
Cell Debris	Lysis/flocculation	Depth Filtration	Low	Moderate	Good
Protein	Lysis/flocculation	Depth Filtration	Low	Moderate	Good
	Ultrafiltration		Moderate	High	Fair
	Precipitation	CTAB	Low	Low	Good
	Chromatography	AE	High	High	Fair
RNA	Precipitation	CTAB	Low	Low	Good
		$CaCl_2$	Low	Low	Fair
	Chromatography	AE	High	High	Fair
Endotoxin	Lysis/flocculation	Depth Filtration	Low	Moderate	Good
	Precipitation	CTAB	Low	Low	Good
	Chromatography	AE	High	High	Fair
	Adsorption	LRA	Moderate	Low	Good
chDNA	Lysis/flocculation	Depth Filtration	Low	Moderate	Fair
	Precipitation	$CaCl_2$	Low	Low	Fair
	Adsorption	LRA	Moderate	Low	Good
		Cell. Acetate	Moderate	High	Fair
	Chromatography	RP	High	High	Fair
		HIC	High	High	Fair
		SIC	High	High	Poor
		Affinity	High	High	Fair

Table 1.2. Current purification strategies for DNA

This study focuses on the effects of fluid stress on one particular unit operation: alkaline cell lysis. Alkaline lysis was considered a suitable unit operation to investigate for two reasons. Firstly, being the primary recovery step, DNA degradation during lysis affects the entire downstream process. Secondly, a certain level of fluid stress is virtually unavoidable during alkaline lysis as good mixing of cells and lysis buffer is essential. Because fluid stresses are inevitable, understanding the effects of the resultant fluid stress on DNA is essential.

1.3 Alkaline lysis

Plasmid DNA for gene therapy is typically produced in *E. coli* fermentation (Marquet et al., 1995; Prazeres et al., 1999; Levy et al., 2000). Following cell harvest, the *E. coli* cells are typically resuspended in a Tris-EDTA buffer, pH 8.0 (TE). The Tris maintains a pH of 8.0 where DNA is most stable (Middaugh et al., 1998; Evans et al., 2000). The EDTA serves two functions: firstly to disrupt the *E. coli* cell walls by chelating divalent cations, and secondly the EDTA reduces DNAase activity which relies on divalent cations as cofactors. Sucrose and Triton are sometimes added to the resuspension buffer to promote cell lysis (Sambrook et al., 1989). Following resuspension, the cells are lysed. *E. coli* cells expressing recombinant proteins are lysed in the biotechnology industry by using mechanical disruption. However, Carlson et al. (1995) has shown that mechanical disruption equipment, such as high-pressure homogenisers, microfluidisers and bead-bills, can cause substantial damage to shear sensitive plasmid DNA. Instead, *E. coli* cells expressing plasmid for gene therapy are usually lysed chemically, using either lysozyme and heat (Lee et al., 1996; Sambrook et al., 1989) or a variation of the alkaline-lysis procedure. The alkaline lysis procedure was originally developed by Birnboim et al. (1979) as a laboratory technique for the rapid isolation of supercoiled plasmid DNA, and is generally considered the method of choice for cell lysis (Prazeres et al., 1999).

In the first stage of alkaline lysis, the host cells resuspended in TE buffer are mixed with an alkali solution of sodium dodecyl sulphate (SDS). The anionic detergent SDS disrupts all the non-covalent interactions found in the cell wall (Scopes, 1994). A schematic of the *E. coli* cell wall is shown in
Figure 1.3. Electrostatic interactions between the detergent and the cationic sites of the cell wall proteins occur, causing protein denaturation. Each SDS molecule binds to two amino acids (Igou, 1974) forming SDS-protein complexes. This solubilises the cell membrane causing the release of cellular contents. Ciccolini et al. (1999) reported cell solubilisation times on the order of a few seconds. The high pH further enhances protein denaturation (Creighton, 1993) and causes the irreversible denaturation of chromosomal DNA. It is known that supercoiled plasmid DNA denatures at a slightly higher pH than chromosomal DNA. Birnboim et al. (1979) reported that for the irreversible denaturation of the chromosomal DNA, without denaturation of plasmid DNA, the pH should be maintained between 12.0 - 12.6. More recently, Thatcher et al. (1997) have reported that plasmid DNA molecules useful for gene therapy irreversibly denature at a pH between 12.1 and 12.9, and plasmid goes from a completely intact supercoiled form to a completely denatured form over a narrow range of about 0.2 pH units.

In the second stage of alkaline lysis (neutralisation), the pH of the solution is reduced to a value close to 5.5 by addition of ice-cold, 3M potassium acetate, pH 5.5. The increase in ionic strength causes a salting-out of the SDS, which together with the pH change causes flocculation of SDS, denatured protein, cell wall debris and denatured chromosomal DNA. The supercoiled plasmid DNA remains in solution. Centrifugation or filtration achieves separation of the floc from the liquor containing the plasmid DNA. It has been reported by Levy et al. (1999) and Ciccolini et al. (2002) that the flocculate must be handled under low fluid stress conditions to avoid returning the precipitated chromosomal DNA from the solid to the liquid phase leading to increased chromosomal contamination. Although alkaline lysis is universally used, there has not been any published data on what percentage of the total supercoiled plasmid DNA, or total chromosomal DNA is removed during alkaline lysis and neutralisation.

1.3.1 Problems with alkaline lysis

Thatcher et al. (1997) has reported that there is an optimal pH for alkaline lysis that is dependent on the denaturation pH of the plasmid being purified. Alkaline lysis is typically carried out by the addition of one volume of resuspended cells to one volume of 0.2 M NaOH, 1% SDS to give a cell lysate in 0.1 M NaOH. Although previous work has reported the importance of pH during alkaline lysis, no information on the relationship between NaOH added versus the final pH in the lysate has been published. Measurement of pH during alkali addition is complicated by the highly viscous nature of the cell lysate, which together with the high concentration of proteins in the lysate, quickly leads to fouling of the pH probe making accurate pH measurement impossible. For a particular plasmid, it is necessary to determine by trial and error the optimal level of NaOH to add during cell lysis.

The pH of typical alkaline lysis buffer (0.2 M NaOH, 1% SDS) is pH 13.3. The alkaline lysis reagent should be added and mixed in such a way that local lysis buffer concentration extremes are avoided, because supercoiled plasmids are known to denature between pH 12 and 13. However, to date there has not been a detailed study published on the effect of lysis buffer concentration and lysis buffer mixing on plasmid yield and purity. In addition, physical damage to chromosomal DNA in the early stages of the recovery process may complicate further downstream recovery and purification of the plasmid DNA, particularly if chromosomal DNA fragments produced by breakage were comparable to the size of the plasmid DNA. There have been conflicting reports that fluid stress during cell lysis may or may not cause increased chromosomal contamination. Ciccolini et al. (2000) stated that increased fluid stress led to moderate increases in chromosomal DNA contamination, up to 25% chDNA contamination at a fluid strain rate of 760 s^{-1}. A study by Chamsart et al. (2001) showed that fluid strain rate up to

760 s^{-1} did not lead to chromosomal DNA contamination greater than 2% after further downstream purification. However, they did not report on chromosomal contamination immediately following alkaline lysis and clarification. Information on chromosomal degradation and final fragment size is needed in the selection of the most appropriate recovery and purification steps following the cell lysis operation.

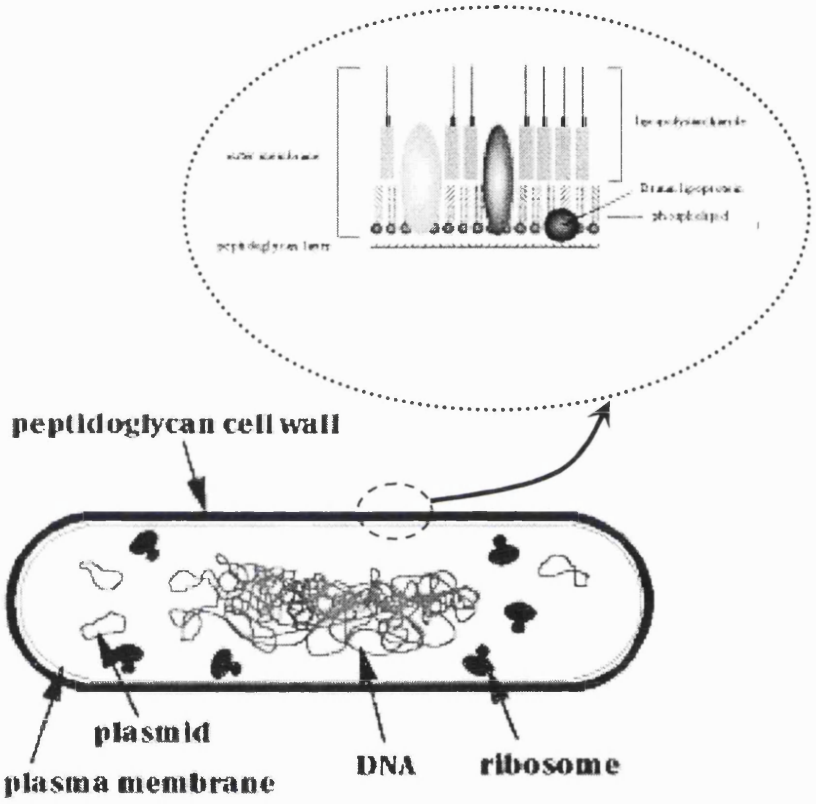

Figure 1.3 Schematic of *E. coli* recombinant cell showing structure of cell wall.

For alkaline lysis, the need to ensure uniformity of composition demands a short mixing time in the lysis reactor. As the cellular contents are released, the rheology of the lysis solution alters from an initially Newtonian state with a viscosity close to water to a non-Newtonian viscoelastic state (Ciccolini et al. 1998). Under steady fluid stress, the apparent viscosity is dominated by the higher molecular weight of chromosomal DNA, with a maximum viscosity value 25 to 30 times that of water. Achieving adequate mixing during alkaline lysis, while avoiding high fluid stresses, is not a trivial problem.

Two principle mixing strategies have been employed for alkaline lysis: stirred tanks and static mixers, both of which are discussed in greater detail in chapter 2. Alkaline lysis in stirred tanks, at scales up to 15 L, has already been demonstrated (Chamsart et al., 2000; Theodossiou et al.

1999; Varley et al., 1999). Chamsart reported that following further purification by Qiagen purification and alcohol precipitation, the purified product contained a satisfactorily low concentration of chromosomal DNA (< 2% contamination), together with a satisfactory supercoiled plasmid yield (1 mg/g wet cell weight). Of the static mixers used for alkaline lysis, two principle types of have been used for alkaline lysis: conventional in-line static mixers (Wan et al., 1998) and an opposed jet mixer (Ciccolini et al., 2000). To date, little has been published on the performance of either of these static mixers for alkaline lysis. Ciccolini reported high clarified lysate purity after using opposed jets for alkaline lysis mixing compared to small scale mixing in a test-tube. Unfortunately, different batches of cell paste were used in the jet and non-jet lysis experiments.

1.4 Organisation and aims of the thesis

1.4.1 Aims of the thesis

The principal objective of this thesis will be to determine the effect of fluid stress on plasmid and chromosomal DNA degradation to better predict and avoid stress-induced degradation during large-scale plasmid DNA production. Both laboratory experimentation and Computational Fluid Dynamics modelling will be performed to achieve this goal. The overall goal of the thesis has been broken down into the following 5 steps that are presented separately in chapters 4 to 8:

1. **Develop analytical methods to study DNA in both model systems and manufacturing-scale equipment (chapter 4).**
   Current analytical techniques are not sufficient to accurately and rapidly measure plasmid and chromosomal DNA denaturation and fragmentation. Novel analytical techniques will have to be developed to analyse the yield and purity of plasmid and chromosomal DNA solutions after fluid mixing, and stress-induced degradation, experiments. Development of new assays to monitor plasmid degradation under highly dilute plasmid concentrations would enable plasmids to be used as probes for fluid stress in large-scale equipment. Probes for fluid stress would be particularly useful where the type and magnitude of fluid stress in a particular piece of equipment is poorly understood.

2. **Assess the effect of different types of fluid stress on plasmid and chromosomal DNA stress-induced degradation (chapter 5).**
   Knowledge of the magnitude of fluid stress is not in itself sufficient to determine levels of DNA degradation; different types of fluid stress occur in flowing fluids, and the effects of

the different types of fluid stress on DNA degradation is currently poorly understood. The principal types of fluid stresses are shear stresses, elongational stresses and fluctuating (turbulent) stresses. Different types and magnitudes of fluid stress are found in different pieces of purification equipment. Experimental and CFD studies using pure plasmid and chromosomal DNA solutions will be performed to better understand which types of fluid stress cause DNA degradation.

3. **Determine the required level of mixing during alkaline lysis and the effects of the resultant fluid stresses on DNA yield and purity (chapter 6).**
   The required level of mixing will determine what level of fluid stress will be generated during alkaline lysis. Previous studies by Levy et al. (1999) and Chamsart et al. (2001) have looked at the effect of fluid stresses on alkaline lysis over a narrow range of stresses, in isolation of what levels of fluid mixing and stress are likely to occur during lysis. Determination of the required level of mixing will require understanding the effects of lysis buffer on both plasmid and chromosomal DNA denaturation. After determining the required fluid mixing, the effect of the resulting fluid stress on plasmid DNA degradation and chromosomal DNA fragmentation in alkaline lysates will be examined. The effect of chromosomal DNA size on its removal during alkaline lysis and clarification will also be studied.

4. **Determine the effect of DNA degradation on downstream purification (chapter 7).**
   After determining the effect of lysis mixing and stress on chromosomal DNA denaturation and size, studies will be performed to assess how the DNA denaturation and fragment size affects subsequent downstream purification operations.

5. **Develop an improved alkaline lysis reactor (chapter 8).**
   After elucidating the mixing requirements and the effects of fluid stress during alkaline lysis, a goal of this work will be to design an improved lysis reactor. The improved reactor is based on mixing using opposed jets. To fully characterise the mixing rates and stress levels likely to occur in opposed jets, extensive computational fluid dynamics (CFD) simulations will be used to model the opposed jet lysis reactor, before testing the device experimentally.

1.4.2 Organisation of the thesis

Chapter 1: The rational for the thesis is presented, along with outline of thesis.

Chapter 2: The theory of fluid mixing and fluid stress is presented, along with a description into the mechanism of DNA degradation in fluid stress fields.

Chapter 3: The theory of computer modelling and analysis of fluid flows to determine mixing time scales and stress levels is described. This is followed by a detailed description of the computer modelling techniques that were used in the thesis to model fluid flows in capillaries and in opposed jets.

Chapters 4 to 8: Experimental results are presented (refer to previous section for chapter descriptions). Each chapter is divided into:

i) A brief summary of results
ii) An introduction to the studies performed in the chapter
iii) Description of the Materials and Methods used
iv) Presentation of results
v) Discussion of results.

Chapter 9: The methodologies used in this thesis are discussed. The results from all the previous chapters are amalgamated and examined with respect to designing DNA purification processes.

Chapter 10: The conclusions of this thesis are presented along with potential future work for which this thesis provides a foundation.

2 Mixing and stress in fluids

This thesis investigates the effects of fluid mixing and fluid stresses on DNA degradation during DNA purification processes. In this chapter, the theory of fluid mixing and fluid shear will be described. In this thesis, three different pieces of equipment, stirred tanks, opposed jets and capillaries, are used in mixing or shear experiments. Fluid mixing and fluid shear theory specific to each of these devices will be also described. Finally, the current knowledge of the effect of fluid stress on DNA macromolecules will be presented.

2.1 Introduction

In many biochemical engineering unit operations fluid mixing is a critical process parameter. An example of a unit operation where mixing is believed to play an important role is the alkaline lysis step in DNA purification, discussed in chapter 1, 6 and 8. However, due to intermolecular forces between fluid molecules all types of fluid flow generate internal fluid forces. These internal fluid forces, acting between planes of moving fluid, are usually reported on a force per unit area basis, which is defined as fluid stress. More rapidly flowing fluids or move viscous fluids generate higher levels of fluid stress within the fluid. These fluid stresses not only act between planes of solvent molecules, but also act on solute molecules. Because the vast majority of organic and inorganic molecules are small relative to the local variation of fluid stress, the fluid stress across most molecules is uniform, causing no net deformation of the molecule. However, DNA is such a large molecule that internal fluid stresses can actually cause molecular stretching, leading in extreme cases to chain scission. Hence, the downstream processing of DNA is complicated considerably because high levels of fluid stress must be avoided. For unit operations such as alkaline lysis, where mixing is important, avoiding DNA fragmentation is difficult. A thorough understanding of the fluid mixing requirements, and the resulting fluid stress effects on DNA breakage, is essential in designing appropriate mixing equipment.

2.2 Fluid mixing

The theory of fluid mixing is described, followed by more detailed descriptions of fluid mixing in stirred tanks and opposed jets which are relevant to alkaline lysis.

2.2.1 Theory of fluid mixing

In all liquid-mixing devices, it is necessary to have two elements. Firstly, there must be overall bulk or convective fluid flow so that no stagnant regions exist within the device. Secondly, there must be an intensive or high-stress mixing region that is capable of providing the reduction in inhomogeneities required. Both these processes require energy to sustain them, the

energy being finally dissipated as heat. In most fluid flow situations, mixing regimes may be characterised as laminar or turbulent. Laminar flow is associated normally with high viscosity liquids. At typical rates of energy input, viscosities greater than about 10 Pa s are required if the flow is to be truly laminar (Harnby et al., 1992). The solution viscosity during DNA purification will be significantly lower than this (0.001 – 0.030 Pa s), so that flow will generally be turbulent.

According to Kolmogoroff's theory of isotropic turbulence, turbulent motion in a fluid can be considered as a superposition of a spectrum of velocity fluctuations and eddy sizes on an overall mean flow (Levich, 1962). The large primary eddies have large velocity fluctuations of low frequency. Interaction of the large eddies with slow-moving streams produces smaller eddies of high frequency which further disintegrate until finally they are dissipated into heat by viscous forces. In turbulent fluids, it is very difficult to model the transport phenomena in full physical detail. Qualitatively, however, the following sequence may be visualised after the feed streams have met (Harnby et al., 1992).

(a) *Distributive mixing.* Relatively large eddies exchange positions and convect material so that macroscopic uniformity of concentration results.
(b) *Dispersive mixing.* The larger eddies decay in size through the effect of turbulent shear and a finer-grained mixture is formed. At molecular scale the mixture remains, however, highly segregated.
(c) *Diffusive mixing.* Diffusion within the finely dispersed structure operates over short distances and proceeds to randomise the mixture at the molecular scale, forming a homogenous mixture.

An indication of whether a fluid flow will be laminar or turbulent is obtained by calculating the appropriate Reynolds number for that type of flow. The Reynolds number is the ratio of the inertial to viscous forces (the ratio of the forces causing chaotic motion to the forces suppressing chaotic motion). Analytical expressions for Reynolds number have been determined for a wide range of flow devices, such as pipes, mixing tanks, and jets. Provided the Reynolds number of the main flow is high enough, Kolmogoroff's theory of local isotropic turbulence can be used to give some insight into a turbulent flow. Kolmogoroff argued that for large Reynolds number the smallest eddies are independent of the bulk fluid motion, are isotropic, and are a function of the local energy dissipation rate (ε) and the kinematic viscosity ($\nu = \mu/\rho$). From dimensional reasoning, the size of the smallest eddies (the Kolmogoroff length, λ_k) is defined as:

$$\lambda_k = [\ \nu^3 / \varepsilon_{max}\ ]^{1/4}$$

Equation 2.1

Micro-mixing which is particularly dependent on turbulent eddy size and their associated forces are likely to be well correlated by energy dissipation rate (Harnby et al., 1992). High turbulent energy dissipation creates small eddies (from Equation 2.1) leading to faster mixing by diffusion. The time taken for diffusion to completely mix a species (t) can be related to the size of the smallest eddies divided by the diffusion rate (D) of that species, and is given by,

$$t_{micro} = 0.5\ \lambda_k^2/4D$$
$$= (\nu^{3/2}/8D)\ .\ \varepsilon_{max}^{-1/2}$$

Equation 2.2

For example, if a dilute solution of NaOH ($D = 1.5x10^{-9}\ m^2/s$) is mixed with water ($\mu = 1$ mPa s, $\rho = 1000\ kg/m^3$) such that the rate of turbulent energy dissipation is 1 W/kg, the Kolmogoroff length will be about 30 microns and the micro-mixing time will be about 80 ms. In summary, rapid mixing is best achieved by ensuring high levels of turbulent energy dissipation.

2.2.2 Mixing in stirred vessels.

Macro-mixing

Mixing time in a stirred tank is a function of many factors including the geometry and scale of the reactor and its operational parameters as well as the physical properties of the fluids. For geometrically similar vessels, the overall mixing time (distributive mixing time) can be correlated with the average energy dissipation in the vessel. For example, in fully turbulent flow in a mechanically agitated vessel (Re>10,000), Voit et al. (1988) recommend that the macro-mixing time, t_{vessel} may be calculated from

$$t_{vessel} = 7.3\ .\ D_{vessel}^{2/3}\ .\ \varepsilon_{average}^{-1/3}$$

Equation 2.3

D_{vessel} is the vessel diameter and $\varepsilon_{average}$ is the average energy dissipation rate in the vessel. This equation predicts that as a vessel increases in size, the average energy dissipation rate must increase to maintain the same macro-mixing time. The average energy dissipation rate in a stirred vessel can not be directly measured, but can be determined from the power input (P) to the vessel, where

$$\varepsilon_{average} = P / \rho\ V_{vessel}.$$

Equation 2.4

For a given geometrically similar vessels and impellers, under turbulent flow conditions (Coulson et al. 1991), the power input to a stirred tank is related to the impeller speed (N) by

$$P / \rho N^3 D_{impeller}^5 = k''$$

Equation 2.5

k" is an experimentally determined constant for a geometrically similar tank-impeller system. Typical values of k" are 1 to 5 for a Rushton turbine in a baffled vessel. Hence, based on a certain overall mixing time requirement, one can calculate the required average energy dissipation and impeller speed. Typical values of energy dissipation in stirred tanks range from about 0.2 W/ kg for blending low viscosity liquids, to 4 W/kg for blending pastes and dough (Harnby et al., 1992). Combining Equation 2.3, Equation 2.4 and Equation 2.5, the macro-mixing time in a stirred tank is inversely proportional to the impeller speed.

$$t_{vessel} \propto N^{-1}$$

Equation 2.6

Therefore to maintain constant macro-mixing time in different size stirred tanks, simply maintain the same impeller speed, noting that the power input will increase rapidly as D_{vessel}^5.

The flow in a stirred tank is usually turbulent at Reynolds numbers greater than about 1000 to 10000. The Reynolds number (Re), for a stirred tank, is defined as

$$Re = \rho N D_{impeller}^2 / \mu$$

Equation 2.7

Micro-mixing

The energy dissipation in a stirred tank is not uniform, but varies from a maximum near the impeller to a minimum in the tank extremities. The energy dissipation close to the impeller is typically 10 to 100 times higher than the average tank energy dissipation,

$$\varepsilon_{max} = k' \varepsilon_{av}$$

Equation 2.8

A value for $\varepsilon_{max} / \varepsilon_{av}$ of 40 is reported for Rushton turbines (Yim et al., 2000) and used in subsequent calculations. If two solutions are being mixed in a stirred tank, and the solution being added is fed directly into the impeller, then a considerable amount of micro-mixing (dispersive and diffusive mixing) will occur while the fluid remains in the region close to the impeller. This can considerably improve the mixing in a stirred tank for the same overall power input. Note that the micro-mixing time is only a function of the energy dissipation rate near the impeller, Equation 2.2. Therefore, the energy dissipation rate in a stirred tank does not have to increase as the tank increases in size to maintain a constant micro-mixing time. Thus, maintaining constant mixing time requires less power, than maintaining a constant macro-mixing time, upon scale-up of a stirred tank; this is demonstrated in Figure 2.1.

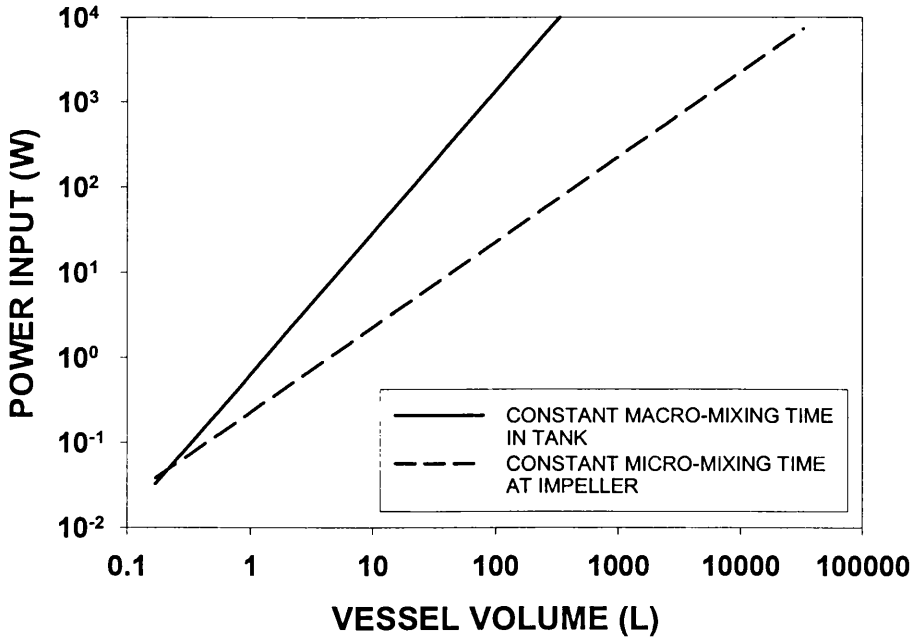

Figure 2.1. Plot showing the increase of power input to a stirred tank of water in order to maintain a constant macro-mixing time of 1s or alternatively to maintain a constant micro-mixing time of 0.3s, as the tank volume increases.

2.2.3 Mixing in opposed jets

Opposed jets are often used to mix two fluids together when extremely short mixing times, on the order of milliseconds, are required (Tosun, 1987; Mahajan et al., 1996). A schematic of an opposed jet mixer for the alkaline lysis operation is shown in Figure 2.2. When two opposed jets impinge, a significant amount of the kinetic energy in the jets is transferred into turbulent energy and dissipated as viscous friction. This high level of turbulent energy dissipation that is localised in the region where the jets impinge generates the excellent fluid mixing in an opposed jet device. The micro-mixing time in this region can be estimated from Kolmogoroff turbulence theory; the greater the rate of turbulent energy dissipation, the better is the fluid mixing. Unfortunately, it is not currently possible to analytically calculate the turbulent energy dissipation rate between opposed jets.

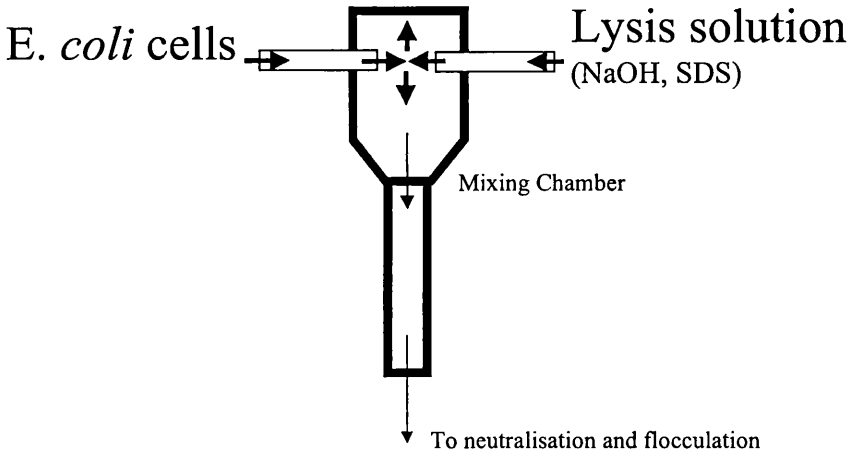

Figure 2.2. Schematic of opposed jet alkaline lysis mixer

In order to approximate the turbulent energy dissipation rate in opposed jets, assume that all of the kinetic energy in the jets is dissipated as turbulent energy in the region directly between the jets. Consider two opposed jets with the same volumetric flowrate, Q, and velocity, u. From the definition of kinetic energy, the kinetic energy per unit mass in the two impinging jets of fluid is equal to $u^2/2$. The mass transported through the two jets per second is $2\rho Q$, which equals $2\rho(\pi d_{jet}^2/4)u$. Hence, the energy transported through the two jets per second (the jet power) is $\rho\pi d_{jet}^2 u^3/4$. Now, a fraction of this energy, κ_1, is dissipated in a volume, V, directly between the jets. Assume this volume is a proportional to the cube of the jet diameter, d_{jet}. Hence, the volume of the high energy dissipation region is $\kappa_2(\pi/6)d_{jet}^3$, where κ_2 is some constant which defines the size of the high energy dissipation region. Combining these equations one gets:

$$\varepsilon_{actual} = (3\kappa_1/2\kappa_2)\, u^3/d_{jet} = \kappa\, u^3/d_{jet}$$

Equation 2.9

Assume that the percentage of the total energy dissipated between opposed jets is always a constant, not a function of jet velocity, jet diameter or fluid properties. Also, assume that the volume in which energy dissipation occurs is always proportional to the jet diameter cubed. If both these assumptions are true, then κ will be a constant. It has been reported in the literature for single jets flowing at high velocity, subsurface, into a large body of liquid (unbounded free jets) that κ is around 0.1 (Yim et al., 2000), which corresponds to about 7% of the total kinetic energy being dissipated in a sphere of diameter, d_{jet}. These equations imply that the turbulent energy dissipation is a strong function of the jet velocity. By increasing jet velocity, the turbulent energy dissipation can be significantly increased, leading to better mixing. It is

important to note that there is very limited data available on the performance of opposed jets, or the applicability of Equation 2.9 to predict jet mixing. Therefore additional investigations are required to understand the performance of opposed jets.

Once the turbulent energy dissipation is known, the micro-mixing time, t_{micro} can be estimated from Kolmogoroff turbulence theory by combining Equation 2.2 and Equation 2.9:

$$t_{micro} \propto u^{-3/2} d_{jet}^{1/2}$$

Equation 2.10

The Reynolds number for opposed jets is defined as,

$$Re_{jet} = \rho u d_{jet} / \mu$$

Equation 2.11

The jet velocity is u and d_{ijet} is the jet nozzle diameter. A jet is fully turbulent at a jet Reynolds number, Re_{jet} of 1000-2000, and laminar below 50-1000 (Unger at al. 1998, Unger et al. 1999).

Applying Equation 2.1, Equation 2.2 and Equation 2.9, 12 mm ID opposed jets of water (μ = 1 mPa s, ρ = 1000 kg/m^3) at 3 m/s jet velocities will have an energy dissipation of 225 W/kg. This energy dissipation rate corresponds to a Kolmogoroff length and a micro-mixing time of 8 microns and 5 ms, respectively, assuming κ= 0.1. One can see that the micro-mixing time for opposed jets has the potential to be very short. Based on these rough analytical calculations, energy dissipation between 10 to 100 W/kg in an opposed jet mixer should provide very fast mixing (< 1 s).

2.3 Fluid stress

Short mixing times are achieved by ensuring high levels of turbulence in the region of fluid mixing. This can be achieved using high impeller speeds in stirred tanks or high jet velocities in opposed jets. The following section describes how turbulent energy dissipation rate, impeller speed, jet velocity and fluid velocity gradients relate to the fluid stresses within fluids being mixed.

2.3.1 Calculation of fluid stresses.

Fluid stresses arise when the fluid is strained (made to flow). The stress (force per unit area) in a flowing fluid is caused by the interactions of fluid molecules moving relative to each other that arise when the fluid is deformed (strained). There are three principal types of fluid stress (τ) which are of interest for this thesis: 1) shear stresses, 2) elongational stresses and 3)

chaotically fluctuating (turbulent) stresses. The shear stress on a fluid element is the force per unit area acting *parallel* to the surface of the fluid element. The elongational stress on a fluid element is the force per unit area acting *perpendicular* to the surface of the fluid element. Turbulent stresses consist of a rapidly changing, *random fluctuations* of both stresses.

If there are stresses present in a flowing liquid, and that liquid contains macromolecules, the macromolecules will experience the stress, causing the macromolecules to deform. This change in macromolecular conformation generates strain at the molecular level that can result in fracture of macromolecules if the molecular strain is sufficiently high. To calculate whether a specific macromolecule, such as a piece of DNA, will break in a flowing liquid, we need to know the magnitude of stress that causes the piece of DNA to break and compare that to the magnitude of the stresses that are present in the liquid. Hence, it is important to be able to calculate the fluid stresses in a flowing fluid.

Stresses occur in fluids when the fluids are strained, and the stress in the fluid can be calculated based on the strain. The relationship between stress and strain in a material is known as the constitutive relation for that material and this relationship can be very different depending on the fluid. For liquids, the simplest constitutive equation is Newton's law of viscosity, which says that the stress at a point in a fluid is directly proportional to the *rate* of straining at that point. The rate of straining at a point is equal to the change of fluid velocity (velocity gradient) at that point. By convention, if a fluid element is being strained perpendicular to the direction of fluid motion, then the fluid element is undergoing shear strain (γ) and is experiencing a shear stress. If the fluid element is being strained in the direction the fluid is moving, then the fluid element is undergoing elongational strain (ε) and experiencing an elongational stress. For many liquids, the shear stress (τ_s) is proportional to the shear strain rate (γ') and the elongational stress (τ_e) is proportional to the elongational strain rate (ε')

$$\tau_s = \mu\gamma' \quad (\gamma' = d\gamma/dt = dV_x/dy).$$
$$\tau_e = 3\mu\varepsilon' \quad (\varepsilon' = d\varepsilon/dt = dV_x/dx).$$

Equation 2.12

The constant of proportionality μ, is called the viscosity of the solution. V_x is the velocity of the fluid in the x-direction, y is the direction perpendicular to the x-direction. Any fluid that obeys this law is known as a Newtonian fluid (Macosko, 1994). In general, the Newtonian constitutive equation accurately describes the rheological behaviour of low molecular weight liquids or dilute aqueous solutions. Knowing the velocity gradient at a point in an aqueous solution, and knowing the solution viscosity, the fluid stress can be easily calculated from Newton's Law.

In addition to the shear and elongational stresses caused by the mean velocity gradient, turbulent stresses arise due to the additional velocity fluctuations, $\sqrt{(u'^2)}$, that are present in the flow when there is turbulence. As explained in section 2.2.1 on turbulent mixing, turbulent fluid flow can be considered as a superposition of a spectrum of velocity fluctuations and eddy sizes on an overall mean flow. The resulting turbulent stresses are partly shear and partly elongational in character. The magnitude of stress that a particle experiences is determined primarily by eddies of a size comparable to that of the particle. In the velocity field of the determining eddies, the particles experience a dynamic stress according to the Reynolds stress:

$$\tau_t = \rho \sqrt{(u'^2)}$$

Equation 2.13

The relevant equations for determining particle stress (τ_p), which is dependant on the size of the particles (d_p) relative to the eddy size (λ_k), are (Henzler, 2000):

$$\tau_p = 0.0676\ \rho(\nu\varepsilon)^{1/2}\ (d_p / \lambda_k)^2 \qquad \lambda_k < d_p < 6\lambda_k \quad \text{dissipation range}$$

$$\tau_p = 0.22\ \rho(\nu\varepsilon)^{1/2}\ (d_p / \lambda_k)^{4/3} \qquad 6\lambda_k < d_p < 25\lambda_k \quad \text{transition range}$$

$$\tau_p = 1.9\ \rho(\nu\varepsilon)^{1/2}\ (d_p / \lambda_k)^{2/3} \qquad d_p > 25\lambda_k \quad \text{inertial range}$$

Equation 2.14

Therefore knowing the particle size and the energy dissipation rate, one can calculate the stress on a particle. In general, the smaller a particle, the smaller turbulent stress it will experience. For particles smaller than the Kolmogoroff length, such that they are contained within the smallest eddies, a rough estimate of the mean turbulent strain rate the particles experience can be made from the turbulent energy dissipation and kinematic viscosity (Cherry, 1990).

$$\tau_t = (\varepsilon / \nu)^{1/2}$$

Equation 2.15

For most polymeric liquids, emulsions and concentrated suspensions, viscosity (μ) is not a constant and is a strong function of the strain rate. Also, many polymeric liquids show time dependence in their elastic response. This time-dependent response is known as viscoelasticity and is typical of all polymeric liquids such as concentrated DNA solutions (Macosko, 1994). This can significantly complicate fluid stress calculations and frequently only rough estimates of fluid stress can be made for viscoelastic fluids.

2.3.2 Overview of fluid flows in purification equipment and their associated stresses

As already described, there are 3 principal types of fluid stress. These shear, elongational and turbulent fluid stresses can have different effects on DNA molecules in solution, as discussed in section 2.4. The magnitude of these stresses will depend on the type of fluid flow.

(a) Shear flows

A shear flow, where the velocity gradient is perpendicular to the flow direction, is the type of fluid flow that occurs within a pipe or between rotating disks under laminar conditions. Individual fluid elements undergo periodic stretching and compression, while simultaneously rotating in this type of flow. The stress in a Newtonian fluid is proportional to the strain rate, $\tau = \mu\gamma'$. Non-Newtonian fluids, such as concentrated DNA solutions can undergo significant shear thinning (decrease on solution viscosity) at high strain rates, due to the molecules re-orienting in the flow field (Macosko, 1994).

(b) Elongational Flow

An elongational flow occurs when the velocity gradient is in the same direction as the flow direction. This type of fluid flow occurs in nozzles, capillary entrances, jets, and pumps and between beads in chromatography columns. Individual fluid elements undergo significant stretching in the flow direction. The stress in a Newtonian fluid is proportional to the elongational strain rate (ε'), but the constant of proportionality is 3 times larger, $\tau = 3\mu\varepsilon'$, than for laminar shear flow (Macosko, 1994). Non-newtonian fluids, such as solutions of polymers, can undergo significant shear thickening at high elongational strain rates, due to the molecules re-orienting and lining up in the flow field. This shear thickening increases the stress pulling macromolecules apart.

(c) Turbulent Flow

Turbulent flows are present in almost all biochemical engineering equipment, while laminar flow exists only in boundary layers which often are of subordinate importance. The stress that a particle experiences will vary considerably depending on the size of the particle. If particles are sufficiently small they will be convected within turbulent eddies and not experience the turbulent stresses between eddies. For smaller DNA molecules like plasmids, high levels of energy dissipation are required to produce eddies sufficiently small to stress the plasmids. Large chromosomal DNA can experience significant levels of fluid stress even at low turbulent energy dissipation rate.

Table 2.1 shows the types of fluid stresses that occur within some commonly used industrial processing equipment, relevant to plasmid purification. Different equipment generates different magnitudes and types of fluid stresses. Frequently, different types of fluid stresses are found at different locations within the same piece of equipment. By careful design and operation of equipment, different fluid stresses can often be maximised or minimised.

Equipment	Elongational Stress	Shear Stress	Turbulent Stress
Stirred tanks	Low levels	At impeller	In bulk fluid
Opposed Jets	Between jets	Low levels	Between jets
Centrifuges	At feed, discharge	Against bowl	Against walls
Crossflow filters	At entrance	Within filter	Within filter
Chromatography columns	Between beads	Between beads	Low levels
Filling Needles	At entrance	Within Needle	Within Needle

Table 2.1. Different fluid stresses that occur with Industrial purification equipment.

2.3.3 Fluid stresses in stirred vessels

The principal form of fluid stress in stirred vessels is turbulent stress due to turbulent fluid mixing. The magnitude of turbulent stress increases with increased energy dissipation rate, Equation 2.14. The energy dissipation is determined by the power input to the reactor, which is a function of the impeller speed and size, Equation 2.4 and Equation 2.5. Even at very high average energy dissipation rates for a stirred tank , $\varepsilon_{average}$ = 10 W/kg, the size of the smallest eddies far from the impeller, λ_k, are always larger than about 20 microns, Equation 2.1. Close to the impeller the energy dissipation rate can be 10 to 100 times higher than the average energy dissipation, but eddies close to the impeller would still be at least 5 microns in size, significantly larger than the size of small plasmids (< 1 μm). As described previously, particles will not experience significant levels of turbulent stress if the particles are smaller than the smallest turbulent eddies. Therefore small plasmid would probably not be affected by turbulent stresses in stirred vessels. Larger macromolecules, such as chromosomal DNA and large plasmids would be affected by turbulent stress.

The other form of fluid stress in stirred tanks is due to stress in the fluid boundary layer of the impeller. For turbulent boundary layers, the formulae for wall shear stress on a rotating impeller blade in a stirred tank is:

$$\tau_{bl} = 0.029\ \rho\ v_{tip}^2\ (\rho\ V_{tip}\ L\ /\ \mu)^{-0.20}$$

Equation 2.16

Here, L is the distance from the leading edge of the impeller, and V_{tip} is the impeller tip speed of the impeller.

2.3.4 Fluid stresses in opposed jets

The fluid stresses in opposed jets are from a combination of turbulent and elongational strain rates. The elongational strain rate, ε', at the stagnation point between opposed jets can be roughly estimated assuming the jets behave like a point-sink flow (Odell, 1994):

$$\varepsilon' = u / z$$

Equation 2.17

u is the jet velocity and z the jet separation. If jet energy dissipation rate, Equation 2.9, is kept constant, then this equation will predict that the elongational strain rate will decrease as the jet size increases, assuming the jet separation is kept proportional to the jet diameter.

As well as the stresses due to elongational deformation of the fluid, there are turbulent stresses due to the turbulent nature of the fluid flow between the jets. The turbulent stresses are calculated from the energy dissipation rate and the particle size, using Equation 2.9 and Equation 2.14.

2.3.5 Fluid stresses in capillaries

All the types of fluid stress (shear, elongational and turbulent) can occur at the entrance to, and within, capillaries. At Reynolds numbers ($Re = \rho v d/\mu$) below about 2000, the stress inside the capillary is due to laminar shear; the maximum shear (τ_{wall}) occurs along the inside walls of the capillary and is given by (Coulson, 1991).

$$\tau_{wall,\ laminar} = \mu\ 8\ u / d$$

Equation 2.18

For Reynolds numbers above 4000, the flow inside the capillary is fully turbulent. The highest stress occurs in the boundary layer next to the capillary wall, which is given by

$$\tau_{wall,\ turbulent} = 0.0396\ \mu\ (\rho u^2)\ Re^{-0.25}$$

Equation 2.19

As well as the shear stress inside the capillary, if the diameter of the capillary is much smaller than the diameter of the flow upstream, there is elongational stress at the entrance to the capillary as the fluid accelerates. There is not an exact analytical solution for the flow at the entrance to a capillary. If the diameter of the capillary is small compared to the upstream flow diameter, the flow can be approximated by a point sink flow (Metzner, 1970), as shown in Figure 2.3. The elongational strain rate in a point sink flow is:

$$\varepsilon' = dV_r / dr = Q / \{ \pi r^3 (1 - \cos\Theta) \}$$

Equation 2.20

where at the capillary entrance, $r = (d/2) \sin \Theta$. The drawback of calculating the elongational strain rate using this formula, is that the entrance angle Θ must be known to calculate the strain rate. Measurements of Θ in pipes to be about 15° to 25° but can vary significantly for different pipe diameters and flow conditions (Moan, 1979; Metzner, 1970).

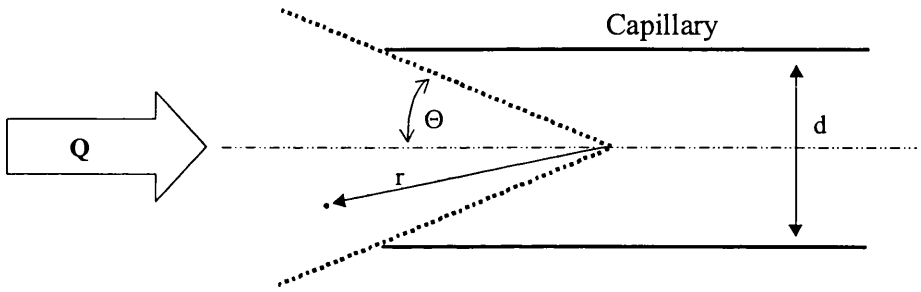

Figure 2.3 Schematic of capillary entrance flow.

As well as elongational stress at the entrance to capillaries, there also can be significant turbulent energy dissipation. No good analytical expressions exist for determining the magnitude of the turbulent stresses at the capillary entrance.

The pressure drops within, and at the entrance to, capillaries can be calculated from:

$$\Delta p_{internal} = 2 f L \rho u^2 / d$$

$$\Delta p_{entrance} = 1/(C_D^2) \, . \, (\tfrac{1}{2} \rho v^2)$$

$$f = 16/Re \text{ (laminar flow)}$$

$$f = 0.0792 \, Re^{-1/4} \text{ (turbulent flow)}$$

Equation 2.21

The turbulent energy dissipiation rate (ε) within the capillary can be estimated from the turbulent pressure drop over the capillary:

$$\varepsilon = (\Delta p_{internal} / \rho) (u/L)$$

Equation 2.22

C_D is the coefficient of discharge which varies depending on the Reynolds number (Coulson, 1991). For non-viscous flows, where no energy is dissipated, C_D is 1.0. Typically C_D varies between 0.5 and 0.9 depending on entrance geometry and Reynolds number. The capillary entrance length is the distance downstream from the entrance of the capillary before the fluid

velocity distribution is no longer is affected by the capillary entrance, and is given by (Coulson, 1991):

$$\Delta L_{entrance} = 0.06\ d\ Re \text{ (laminar flow)}$$
$$= 4.4\ d\ Re^{1/6} \text{ (turbulent flow)}$$

Equation 2.23

Applying Equation 2.1 and Equation 2.20 to Equation 2.22 to a flow of water through a 0.25 mm ID capillary at 80 ml/min, then the Reynolds number is 6700, the predicted turbulent wall stress is 3000 Pa and the average energy dissipation rate within the capillary is $1.3x10^6$ W/kg. This level of turbulent energy dissipation corresponds to a Kolmogoroff length of 0.9 microns. At the capillary entrance the elongational strain rate is $1x10^5$ s^{-1}. Hence, capillaries are capable of generating very high stresses and energy dissipation rates.

2.4 DNA degradation by fluid stress

In the previous section, fluid mixing requirements in industrially relevant mixing equipment were described, as well as the fluid stresses and strains that were likely to be generated. In this section, the structure of DNA molecules in solution is described, followed by likely effects of the different types of fluid stresses (elongational, shear and turbulent) on the DNA polymer.

2.4.1 DNA conformation in stagnant solution

A polymer chain, such as a fragment of DNA, adopts a random-coil conformation in stagnant solution, a prolate ellipsoid in shape (Solc et al., 1971). The radius of gyration of this coil can be several orders of magnitude smaller than the contour length (stretched-out length) of the molecule (Nguyen et al., 1992; Macosko, 1994). Table 2.2 gives some properties of 3 DNA molecules of different sizes: a linear *E. coli* chromosome, a 50 kb chromosomal fragment, and plasmid pSVβ. The equations and constants used to calculate these values shown are shown in Table 2.2 and Table 2.3. All three molecules would typically be present during pSVβ purification from *E. coli* host.

The sizes of the molecules, in terms of contour length or radius of gyration, are substantially different. The relaxation time, which is a measure of how quickly the molecule returns to its equilibrium conformation after being deformed, is significantly longer for the larger molecules (Rouse, 1953). Hence, larger molecules will more easily deform and stretch under the influence of stress. The coil-overlap concentration is, as the name implies, the concentration of DNA at which the total volume enclosed by all of the DNA random-coils is greater than the volume of the solution, therefore the coils overlap, and entangle. Due to their large size, chromosomal DNA coils will overlap and entangle with each other, even at low concentrations, while plasmid

DNA molecules will typically not overlap with each other in solution. The coil-overlap concentration for a 50kb fragment of double-stranded chromosomal DNA was estimated to be about 70 μg/ml. Entanglement can significantly alter the effect of fluid stress on DNA (Nguyen et al., 1992).

Table 2.2 also gives some estimates of the elongational strain rates required to break the DNA molecules, based on Equation 2.24. The susceptibility of DNA to fluid stress increases as the molecule increases in size. For host chromosomal DNA, the strain rates required for chain breakage are so low that it is almost impossible not to cause some chromosomal fragmentation during processing.

Parameter	***E. coli* Chromosome[2]**	**Chromosomal fragment**	**pSVβ plasmid**
Kilo-Base Pairs	4800	50	6
Mw (Daltons)	3.0×10^9	3.1×10^7	3.7×10^6
Contour length (μm)	1632	17	2.0
Maximum Extension (μm)	1632	17	0.7
Radius of gyration (μm)	7.3	0.7	0.2
Relaxation Time[1], Rouse (s)	300	0.4	2×10^{-3}
Coil-Overlap Conc.[3] (μg/ml)	6	70	> 250
Breakage Strain Rate[3] (1/s)	1.5	1.6×10^4	$> 1 \times 10^6$

Table 2.2. Physical characteristics of DNA molecules. [1] The relaxation times are calculated at the chain overlap concentration. [2] The *E. coli* chromosome is taken to be linear. [3]All calculations are based on linearised DNA.

Parameter	Value or Equation	Ref.
Solvent temperature, T	298 K	
Solvent viscosity, μ_s	0.001 Pa s	
Boltzmann constant, k	1.38×10^{-23} J/K	
Avogadro's Number, N_{AV}	6.02E+23 molecules mol^{-1}	
Fox-Flory constant, Θ	2.25E+23 mol^{-1}	1
Number of DNA base pairs, N_{BP}	4,000,000 or 50,000 or 6,000	
Molecular weight base pair, M_{WBP}	623 Daltons	2
Axial rise between base pairs, H_{BP}	0.34 nm	2
Persistence Length of DNA, L_p	50 nm	3, 4
Expansion factor for solvent effects	30%	
Force required to break ds-DNA chain, F_{break}	450 pN	5
6 kb Plasmid diffusion coefficient, D	4.11E-08 $cm^2\ s^{-1}$	6
Molecular weight molecule, M_W	$N_{BP} * M_{WBP}$	
Contour Length, $L_{contour}$	$N_{BP} * H_{BP}$	
Maximum extension of intrawound superhelix	$2^{-3/2} * L_{contour}$	7
Length of Kuhn Statistical Rod, L_{rod}	$2 L_p$	1
Number of Kuhn Statistical Rods, N_{rod}	$L_{contour} / L_{rod}$	1
End-to-end distance, R_{EE}	$(1+E_f)* N_{rod}^{0.5} * L_{rod}$	1
Radius of Gyration, R_G	$6^{-1/2} * R_{EE}$	1
Volume of DNA coil, V_{DNA}	$(\Theta / 2.5*N_{AV}) * R_{EE}^3$	1
Coil overlap concentration, c	$M_W / V_{DNA}*N_{AV}$	1
Elongational strain rate to break chain, E_{break}	$12 * F_{break} / (\mu_s L_{contour}^2)$	8
Intrinsic viscosity, $[\mu]$	$=\Theta R_{EE}^3 / M_W$	1
Chain Relaxation time (Zimm model), t_{Zimm}	$= 0.95[\mu]\mu_s M_W/RT$	1
Chain Relaxation time (Rouse model), t_{Rouse}	$= 0.61[\mu]\mu_s M_W/RT$	1
Closed chain relaxation time (Rouse), t_{closed}	$= \pi^2 D / 2 R^2_G$	6

Table 2.3. List of equations and constants used to calculate values in Table 2.2.

Ref. Number	Reference
1	Nguyen et al., 1992
2	Abeles et al., 1992
3	Smith et al., 1996
4	Strick et al., 1998
5	Noy et al., 1997
6	Fishman et al., 1996
7	Langowski et al., 1989
8	Odell et al., 1994

Table 2.4. References to equations used in Table 2.3.

2.4.2 DNA degradation by elongational fluid stress

In dilute solutions, mechano-chemical reactions are restricted to polymers due to the unique propensity of polymers to store free-energy upon deformation and to sustain a high level of stress for a time sufficiently long for chemical reactions to occur. It was shown theoretically by De Gennes (1974) that elongational flow with a velocity gradient parallel to the direction of flow, is capable of achieving a large degree of molecular coil extension. A polymer in elongational flow begins to deform when the force due to hydrodynamic friction across the molecule exceeds the entropic elasticity that tends to coil it. If the extensional flow is of sufficient duration, called quasi-steady flows (QSS), the DNA chains will have time to unravel and will eventually break in a highly stretched state. An example of such a flow would be the flow between opposed jets, or in a bead mill. For a fully extended macromolecule aligned with the flow, simple calculations by Frenkel (1944) using Stoke's Law for a stretched out chain of beads of total length L, in a steady extensional flow (ε'), gave a parabolic distribution of force along the chain, the maximum at the centre where scission occurs preferentially. The force on the molecule, at the midpoint of the chain is given by:

$$F_{max} = K_1 \mu \varepsilon' L^2$$

Equation 2.24

K_1 is 0.085 to 0.100 for DNA (Odell et al., 1994; Bird et al., 1977). Thus, the strain rate at which the molecule breaks decreases significantly as its molecular weight increases, refer to Table 2.2. Because the molecule is fully stretched-out, the following relationship between strain rate at fracture (ε'_f) and molecular weight was predicted by Frenkel:

$$\varepsilon'_f \propto 1/M_w^2$$

Equation 2.25

Atkins et al. (1992), using a QSS flow in opposed jets, observed that DNA molecules break almost exactly in half which was predicted by Frenkel. They observed breakage of λ-DNA at strain rates at and above 6,000 s^{-1}. Using Equation 2.24, the stretching force on 50 kb λ- DNA in a constant flow field of 6,000 s^{-1} is about 420 to 490 pN, using an extensional viscosity for water of 3 mPa s. In comparison, when individual DNA molecules were stretched using either microscopy (Noy et al., 1997) or surface tension (Bensimon et al., 1995), the force necessary to break double-stranded DNA was estimated to be between 500 to 900 pN. Based on the strength of the covalent bonds in the backbone of DNA, the strength of a DNA molecule should be about 5000 pN.

Most elongational flows, however, are short in duration and are called fast transient (FT) flows. Examples of FT flows are the entrance flows in syringes and orifices, the flows between beads in chromatography columns, between the pores in filters, between the lobes of rotary lobe pumps and in the entrance regions to cross-flow filters. Davison et al. (1959) performed the first experiments on stress-induced scission of DNA by forcing DNA solutions through narrow syringes. In FT flow it is unlikely that the DNA coil has time to fully unravel before breaking. Hunkler, Nguyen and Kausch (1996) used tapered orifices to examine the breakage of polymers in FT flows. They observed that the strain rate for chromosomal DNA breakage was roughly proportional to the inverse of the molecular weight, and that DNA breakage was still mid-point chain scission.

$$\varepsilon_f' \propto 1/M_w^{0.9\text{-}1.1}$$

Equation 2.26

The different exponent in FT flow was rationalised in terms of the yo-yo breakage model for DNA (Ryskin, 1987) where the DNA molecule only has time to elongate in the middle of the chain, either end remaining coiled. Much higher strain rates are achievable in FT flows compared to QSS flows, and most of the fluid flow will experience the region of high strain rate in FT flows, compared to QSS where only a small fraction of the fluid experiences high strain rate region. Therefore, FT flows can cause significantly more DNA degradation than QSS flows. The actual force on the molecule, at the midpoint of an unraveling chain, in an entrance flow, is given by

$$F_{max} = k'' \mu E L^2 \quad 0.4 < k'' < 0.7$$

Equation 2.27

Comparing this equation and the previous equation for steady extensional flows, the force experienced by the molecule is 5- to 10-times greater in FT flows for the same strain rate. For entrance effect FTF flows, degradation of T7 DNA (38 kb) has been observed by Reese et al. (1989). Degradation of T7 DNA was observed at strain rates above $10^4 s^{-1}$, corresponding to forces on a stretched out molecule of 3000 pN. However, based on the very short residence time of the DNA molecules in the area of high elongational stress, it is highly unlikely that the DNA molecules had time to stretch-out before breaking.

2.4.3 DNA shear degradation in shear flow

Most of the early studies of DNA shear degradation were done under conditions of idealised laminar flow. For example, early studies in capillary shear flows (Levinthal et al., 1961) observed scission of T2 DNA while studying the effects of hydrodynamic shear. A simple shear flow, where the velocity gradient is perpendicular to the flow direction, is the type of fluid flow that occurs within a pipe or between rotating disks under laminar conditions. A polymer chain in a simple shear flow is predicted to adopt an elliptical shape (Solc et al. 1971). This molecule will rotate with the fluid element at an angular velocity proportional to the fluid strain rate, γ', and is subjected twice per turn to a linear dilation rate, $\gamma'/2$, and compression rate, $\gamma'/2$, in the diagonals. Only limited expansion of the molecular coil should be expected (Smith et al. 1999). Although many early studies observed DNA degradation in laminar shear (Bowman et al., 1972; North et al., 1974; Adam et al., 1977), there is evidence that simple shear flows may only be capable of inducing scission in the presence of intermolecular entanglements or turbulence (Odell et al., 1992). Although laminar shear flows may be present in the boundary layers of impellers at low speeds, DNA degradation in laminar boundary layers is probably limited, under dilute conditions.

2.4.4 DNA degradation in turbulent flow

Fluid stress-induced degradation of DNA molecules is seen in turbulent flows (Hershey et al, 1960, Burgi et al., 1962) during impeller mixing in stirred vessels. Turbulent flows have a high elongational component and have stagnation points between vortices. Therefore the forces on DNA molecules larger than the sizes of the smallest eddies can be substantial. Detailed studies into the effects of turbulence on DNA stress-induced degradation are limited in the scientific literature.

2.4.5 Other solution properties effecting DNA degradation

Cavitation

DNA degradation is commonly observed in ultrasonic cavitation (Fuciarelli, 1995). Mechanical degradation in flow occurs in the order of microseconds, and on this time scale no detailed description of turbulent behaviour is available at present. Cavitating flows usually do not occur in most downstream purification equipment involving biological materials, but they can occur, so the engineer must be aware of its extremely detrimental effects on DNA and other biological molecules.

Chemical Degradation

One mechanism of DNA chain scission in fluid flows has been shown to be a base-catalysed hydrolysis of the phosphate-ester linkage, where it is apparent that the reaction rate is enhanced by hydroxyl ions at higher pH (Adam et al., 1977). Hydroxyl radicals react readily with both DNA bases and the deoxyribose sugar to generate nearly 100 different products (Evans et al., 2000). Therefore the rates of DNA degradation due to fluid stresses should increase at higher pH. This is particularly relevant to the flow induced degradation of DNA during alkaline lysis.

Although little information is available on the mechanisms of DNA damage that occur during storage of highly purified plasmid DNA, it is clear that trace metal ions are able to catalyse many oxidative processes, including the production of hydroxyl radicals by the reduction of hydrogen peroxide (Luo et al. 1994). The available data suggests that free radical oxidation of DNA may occur in vitro through the generation of superoxide, hydrogen peroxide and hydroxyl radicles.

One of the major degradative pathways for DNA in vivo is the two-step process of depurination and β-elimination leading to cleavage of the phosphodiester backbone (Lindahl et al., 1997). Since depurination and β-elimination of DNA are processes that will occur in almost any conceivable aqueous solution near neutral pH, this pathway of degradation will also be a major factor limiting the aqueous stability of plasmid DNA in vitro. The depurination reaction is acid catalysed. Therefore, when the alkaline lysate is being neutralised, it is important not to over acidify the lysate and damage the DNA.

Solution Effects

The ionic strength of the solution critically influences the degree of condensation of the polymer and its overall conformation. In a high ionic strength buffer, the DNA coil will shrink considerably (Lyubchenko et al., 1997). This decrease in size at high ionic strength is due in

part to the reduction in the electrostatic repulsion of the charged phosphate groups, and in part to a decrease in DNA chain stiffness (Smith et al., 1992; Smith et al., 1996). Supercoiled plasmids at high ionic strength were shown by Levy et al (1998) to be less susceptible to shear forces.

Solution concentration has been observed to have a significant effect, where a 'self-protection' effect has been observed at higher DNA concentrations (Hershey et al., 1960). This may be due to suppression of turbulent eddies at higher concentrations of polymer, or a decreased ratio of OH^- ions to DNA base pairs. Alternatively, intermolecular interactions between the polymer chains can affect the degree of stress-induced degradation. For polymer solutions, there are three relevant concentration, c, regimes:

$$\text{Dilute, } c < c^*$$

$$\text{Coil overlapping, } c^* < c < c^+$$

$$\text{Entangled, } c^+ < c$$

The coil overlap concentration, c^*, can be estimated from $c^* \sim c[\eta]$, and the entanglement concentration, c^+, can be estimated from $c^+ \sim 10\, c[\eta]$, where $[\eta]$ is the intrinsic viscosity. Most theoretical investigations of DNA stress-induced degradation have been using dilute polymer solutions.

Increasing the solution temperature has the effects of lowering the activation energy for bond cleavage which increases the degradation rate, while decreasing the solution viscosity and hence the stress on the molecule which decreases the degradation rates (Nguyen et al. 1992). These competing effects often cancel each other out over moderate ranges of temperature.

The presence of air-liquid interfaces has been shown to significantly increase the rate of DNA degradation in high shear systems (Levy et al 1998). The presence of air-liquid interfaces could increase the dissolved air in the DNA solution, leading to increased cavitation effects and increased OH^- catalysed reaction rates.

2.5 Conclusion

Large macromolecules are known to degrade under conditions of high fluid stress. Frequently, the fluid stresses are a result of fluid mixing; the mixing being required to either promote the blending of fluids, such as in mixing tanks, or to promote mass transfer for component separation, such as in chromatography columns or ultrafiltration systems. Reduction of fluid stress in these unit operations involves understanding the mixing requirements for that operation as well as the evolution of fluid stress. The theory and formulae presented in this chapter

provide a starting point for the estimation of the shear-, elongational- and turbulent- stresses within those devices that have high levels of fluid stress. As described in this chapter, the type of fluid stress, as well as the magnitude of stress, has been shown to significantly affect DNA degradation rates. To date, the vast majority of studies into the degradation of DNA have been focussed on the degradation on linear DNA. In chapter 5, studies with pure plasmid DNA and chromosomal DNA will investigate which of the fluid stresses (shear, elongational and turbulent) are more likely to cause both plasmid DNA and chromosomal DNA chain scission. The results of degradation experiments will be compared to analysed based on the theory of DNA stress-induced degradation presented in this chapter. In subsequent chapters, the effect of fluid stress on DNA chain scission in actual DNA purification unit operations will be investigated and overall process performance evaluated and optimised with respect to maximising supercoiled plasmid yield and minimising DNA impurities.

3 Computational fluid dynamics:

3.1 Introduction

The objective of this thesis is to gain a better insight into the effects that fluid mixing and fluid stresses have on DNA during its purification. The previous chapter outlined some of the basic theory of fluid mixing and fluid stress and discussed the effects of those stresses on DNA. In chapter 5, stress-induced degradation of pure plasmid and chromosomal DNA solutions will be studied in capillaries as a model flow system. In addition, the effects of mixing and fluid stresses during alkaline lysis will be investigated in chapters 6 and 8, using stirred tanks, opposed jets and capillaries. In order to understand the effects of fluid stresses on DNA, it was essential to characterise the mixing times and fluid stresses in these devices. As explained in the previous chapter, the fluid stresses are functions of the shear and elongational strain rates as well as the turbulent energy dissipation. Although formulae exist that can be used to roughly estimate strain rates and turbulent energy dissipation rates (refer to previous chapter), exact analytical solutions to the fluid flow equations are not yet available. Therefore, to more accurately determine these fluid flow parameters, computer modelling of the fluid flow in opposed jets and capillaries was performed.

This chapter describes the theory behind the computer modelling of fluid flow, and describes the methodologies that were used in this thesis. The opposed jet and capillary computer models were based on laboratory scale equipment used in mixing and shear experiments. All computer simulation was performed using the Computational Fluid Dynamics (CFD) software CFX from AEA Technology.

The results of the CFD simulations of capillary shear devices and opposed jet mixers are presented in chapter 5 and chapter 8 respectively.

3.2 Computational fluid dynamics theory and methods

As described in chapter 2, fluid mixing requirements and the resulting fluid stress on DNA are determined by specific fluid flow parameters, such as turbulent energy dissipation and fluid strain rates. To design and optimise DNA purification equipment, knowledge of these fluid flow parameters throughout the flow domain is essential. However, it is often difficult, if not impossible, to determine experimentally all the relevant fluid flow parameters within manufacturing-scale process equipment. When analytical expressions exist to calculate flow

parameters such as pressure drops, mixing times and fluid stresses, these equations are usually only valid for very simple flow geometries, providing only rough estimates in more complicated flow geometries. For most fluid flows through industrially relevant equipment, analytical expressions are usually not applicable. Hence, detailed knowledge of actual flow behaviour in biochemical engineering equipment is frequently poor.

An alternative approach to experimentally determining fluid flow behaviour within a piece of equipment is to use Computational Fluid Dynamics (CFD). CFD programs use numerical methods to solve the basic equations describing the conservation of mass, momentum, and heat in fluids across a flow domain. With the aid of fluid physical property information and the appropriate boundary conditions (inlet flowrates, outlet pressures, wall stresses) the fluid flow equations are solved yielding typically three components of the velocity, pressure, and temperature for each point in the flow domain. Ideally, one would like to calculate the flow field in an entire piece of engineering equipment. However, for the foreseeable future, this task is well beyond even the most powerful computers available (Versteeg, 1995). In practice, engineering knowledge of the system is used to identify the critical regions ('hot-spots') where fluid flow most critically affects equipment performance, for example, the discharge region of a centrifuge, the mixing region of opposed jets or the impeller region of a stirred tank.

CFD has many advantages over more traditional, experimentally based, design methods. CFD is a more fundamental approach, providing the designer with information about the physics of the problem to be solved and providing a complete picture of the flow. Experimentally, it is typically neither feasible, nor cost effective, to determine all the fluid flow parameters to the same detail provided by CFD. In addition, once a CFD model is up and running it is easy to make small changes in geometry, flowrates or pressures. Alternative designs can be investigated rapidly. This ability to carry out 'what if' calculations and investigate alternative scenarios makes CFD a powerful and flexible design tool.

3.2.1 Flow geometry and computational grid size.

Solving a particular problem involves generating a computer model of the physical geometry where the fluid flow of interest occurs (such as the entrance region of a filling needle or the exit region of a centrifuge). Once the geometry is created in the computer, it is discretised into a 3-dimensional (or 2-dimensional) grid comprising many individual blocks. At each block in the grid, between 3 and 20 variables are associated: the pressure, the three velocity components, density, temperature, etc. Furthermore, capturing physically important phenomena such as turbulence requires extremely fine meshes in parts of the physical domain. Currently grids with

20,000 to 2,000,000 blocks are common, leading to systems with up to 40,000,000 unknowns (Versteeg, 1995). This discretization (gridding) is straightforward for very simple geometries such as rectangles or circles, but is a difficult problem for more complicated objects. The generation of the grid is perhaps the most important stage of setting up a CFD simulation taking typically 80% of the total effort. This is because the number and distribution of blocks can effect whether a solution is obtained, the speed at which it is obtained, and the accuracy of the simulation. If too few cells are used in the grid, the fine details of the flow may not be seen by the calculation and the conservation of mass, momentum and energy may not be maintained. In general, the more blocks used in a grid, the more accurate will be the solution, but the more expensive (running time, computing cost) will be the simulation. In general it is necessary to solve the flow problem using finer and finer grids to check that the solution is converging, i.e. that the solution is grid size independent (Versteeg, 1995).

3.2.2 Navier Stokes equations

The basic set of equations solved by the CFD program for laminar flows comprise equations for conservation of mass and momentum; these equations are the continuity equation and momentum equation, respectively:

$$\partial\rho / \partial t + \nabla \bullet (\rho\, U) = 0$$

Equation 3.1

$$\partial (\rho U) / \partial t + \nabla \bullet (\rho\, U \otimes U) = B + \nabla \bullet \sigma$$

Equation 3.2

Here ρ is the fluid density, U is the fluid velocity vector, p is the pressure, t is the time and σ is the stress tensor. The relationship between the strains and stresses in a particular substance are given by a constitutive equation for that substance. For a Newtonian fluid the viscous stresses are directly proportional to the rates of strain, and the 3-dimensional stress tensor is given by:

$$\sigma = -p\delta + (\lambda - 2/3\mu)\, \nabla \bullet U\delta + \mu(\nabla U + (\nabla U)^T)$$

Equation 3.3

This is the 3-dimensional equivalent of Equation 2.12 presented in chapter 2. Taken together Equation 3.1, Equation 3.2 and Equation 3.3 are known as the Navier-Stokes equations. On the discretised flow domain, the Navier-Stokes equations take the form of a large system of non-linear equations. Except for special cases, no closed-form solutions exist to the Navier-Stokes equations. The system of non-linear equations is typically solved by an iterative, Newton-like method, which in turn requires solving a large, sparse system of equations on each iterative step. That is, the values of all the variables (velocity, pressure, energy dissipation, etc.) are initially

guessed. These values are then updated by feeding them back into the equations that one is trying to solve. If the updated values are the same as previous values (to a desired tolerance) the solution is said to have 'converged'. Otherwise, the iterative process is repeated, until convergence is achieved.

3.2.3 Turbulence models

All flows encountered in engineering practice become unstable above a certain Reynolds number. A chaotic and random state of motion develops in which the velocity and pressure change continuously with time within substantial regions of flow. The Navier-Stokes equations, described in the previous section for laminar flows, are in fact valid for turbulent flows as well. Turbulent flows are just very complex unsteady laminar flows. However, we are currently limited in our ability to solve these equations accurately for high Reynolds numbers, and we have to resort to turbulence modelling which solve transport equations for the Reynolds-averaged quantities (Versteeg, 1995), which are defined as:

$$\underline{\Phi}(t) = 1 / (2dt) \int_{t-\delta t}^{t+\delta t} \underline{\Phi}(t)\, d\tau$$

Equation 3.4

Here δt is a time-scale large relative to the time scale of turbulent fluctuations, and small relative to the time scale to which we wish to resolve. Applying Reynolds averaging to the continuity equation and the momentum equation, we obtain

$$\partial \rho / \partial t + \nabla \bullet (\rho U) = 0$$

Equation 3.5

$$\partial (\rho U) / \partial t + \nabla \bullet (\rho U \otimes U) = B + \nabla \bullet (\sigma - \rho \underline{u \otimes u})$$

Equation 3.6

The Reynolds-averaged continuity equation is the same as the equation that has not been averaged. However, the momentum equation contains an additional turbulent flux term, the Reynolds stress $\underline{u \otimes u}$. This term reflects the fact that convective transport due to turbulent velocity fluctuations will act to enhance mixing, over and above that caused by thermal fluctuations at the molecular level. Different turbulent models provide different models for the computation of the Reynolds stress. The most frequently used models are eddy viscosity models. Eddy viscosity models calculate the Reynolds stresses in terms of known mean quantities; in the eddy viscosity hypothesis the Reynolds stresses can be linearly related to the mean velocity gradients in a manner analogous to the relationship between the stress and strain tensors in laminar Newtonian flow:

$$-\rho \underline{u \otimes u} = = -(2/3)pk\delta - (2/3)\mu_T \nabla \bullet U\delta + \mu_T(\nabla U + (\nabla U)^T)$$

Equation 3.7

Here, k is the turbulent kinetic energy $\frac{1}{2} \underline{u}^2$, and μ_T is an additional viscosity, called the turbulent viscosity. Eddy viscosity models are distinguished by the manner in which they prescribe the eddy viscosity, μ_T.

The k-ε eddy viscosity model is the most widely used and validated turbulence model (Versteeg, 1995). In the k-ε model, it is assumed that the eddy-viscosity, μ_T, is equal to $C_\mu \rho k^2 / \varepsilon$. The model contains five adjustable constants. The standard κ–ε model employs values for the constants that are arrived at by comprehensive data fitting for a wide range of turbulent flows. $C_\mu = 0.09$, $\sigma_\kappa = 1.00$, $\sigma_\varepsilon = 1.30$, $C_{1\varepsilon} = 1.44$, $C_{2\varepsilon} = 1.92$. The model performs particularly well in confined flows, however it shows only moderate agreement in unconfined flows.

An alternative model, the low Reynolds number k-ε model, is a modification of the standard k-ε model to allow calculation of turbulent flows at low Reynolds number, typically in the range 5,000 – 30,000. The model involves a damping of the eddy viscosity when the local turbulent Reynolds number is low, a modified definition of ε so that it goes to zero at walls and modifications of the source terms in the ε equation. The model used natural boundary conditions at walls rather than wall functions (discussed in next section), so the equations are integrated through the laminar sublayer (Versteeg, 1995). The model can be used for flows at any Reynolds number provided the grid is fine enough for this integration through the sublayer to be accurate.

3.2.4 Boundary conditions

Flow boundaries

At flow boundaries in the model, the fluid enters and leaves the flow domain. At inlets, the velocity, turbulent energy and turbulent energy dissipation are specified, and the pressure is extrapolated from downstream. Generally, the inlet velocity is known but the turbulent energy and energy dissipation are not known at the inlets. Approximations for the inlet distributions for κ and ε in internal flows can be obtained by means of the following simple assumed forms:

$$k = 3/2\ (UT_i)^2\ ;\ \varepsilon = C^{3/4}k^{3/2}/l\ ;\ l = 0.07R$$

Equation 3.8

Pressure boundaries

The constant pressure condition is used in situations where exact details of the flow distribution are unknown but the boundary values of pressure are known. At a pressure boundary, the fluid pressure is specified, and the velocity and turbulent scalars are extrapolated from upstream.

Wall Boundaries

The wall is the most common boundary encountered in confined fluid flow problems. The no-slip condition (velocities perpendicular and normal to the wall are zero) is the appropriate condition for the velocity components at solid walls.

For turbulent flows, immediately adjacent to the wall we have an extremely thin viscous sub-layer followed by a buffer layer and a turbulent core. The number of mesh points required to resolve all the details in the turbulent layers would be prohibitively large and normally we employ wall functions to represent the effect of the wall boundaries. At high Reynolds number the standard κ–ε model avoids the need to integrate the model equations right through to the wall. This model makes use of the universal behaviour of near wall flows, where the mean velocity from the wall is related to the distance from the wall through the log-law (Versteeg et al. 1995). Using the log-law assumption and that the rate of turbulence production equals the rate of dissipation, it is possible to develop wall functions to describe the mean velocity, turbulence production and turbulence dissipation at walls.

At low Reynolds numbers the log-law is not valid so the above-mentioned wall functions cannot be used. Wall damping needs to be applied to ensure that viscous stresses take over from more turbulent Reynolds stresses at low Reynolds numbers and in the viscous sub-layer adjacent to solid walls. In the low Reynolds number version of the κ–ε model, the equations are integrated to the wall through the laminar sublayer (Versteeg, 1995), where the shear stress is proportional to the strain rate. The standard no-slip conditions with zero values for κ and ε at the wall boundary are therefore used.

3.3 Modelling hardware and software

A Hewlett Packard, Vectra VL, with 192 Mbytes RAM, running Windows NT 4.00, was used for all computations. The CFD modelling software package CFX version 4.2 was used for all simulations which comprised CFX Build version 4.2, CFX Solver version 4.2 and CFX View version 4.2.

3.4 CFD modeling of opposed jets lysis reactor.

3.4.1 Model geometry.

The opposed jets mixing device was modelled as 2 opposing pipes inside an infinitely large chamber, as shown in Figure 3.1. Both equal diameter and non-equal diameter opposed jets were modelled. Only the fluid flow in the pipes and in a rectangular region directly around where the jets impinged was modelled, as shown in Figure 3.1. Both the model geometry and the fluid flow are symmetric in the θ direction; thus, the three-dimensional geometry could be converted to a two-dimensional problem by re-writing the geometry in cylindrical co-ordinates, r, θ, and z. This significantly reduced the size of the problem and the computational time. Because this system possessed an axis of symmetry along the centreline of the jets only the top half of the geometry needed to be modelled. If equal diameter and equal flowrate jets were modelled, then the flow system also possessed an axis of symmetry along the vertical axis between the jets. In this case, only one quadrant of the system needed to be modelled, as shown by the darker shaded region in Figure 3.1.

Figure 3.2 shows in more detail the model geometry that was used for equal jets (top) and non-equal jets (bottom), along with the appropriate boundary conditions. The equal-jets model consisted of one flow inlet, two pressure outlets, two symmetry boundaries, and three wall boundaries. Note, that while one wall boundary could have been used to model the wall of the pipes, using three walls took into account the thickness of the pipe. Initial simulations using only one wall tended to generate regions of excessive turbulence at the infinitely sharp pipe outlet. The jets modelled were 0.5, 4 and 12mm internal diameter, and the jet separation was typically set at twice the jet diameter, unless otherwise noted.

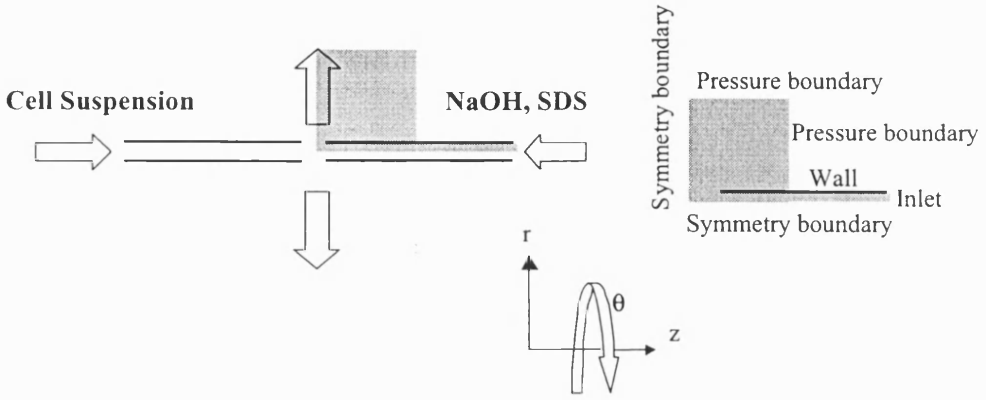

Figure 3.1 **Left: Schematic of opposed jet mixer; for equal jets the region modelled is shaded. Right: Schematic showing the showing boundary conditions.**

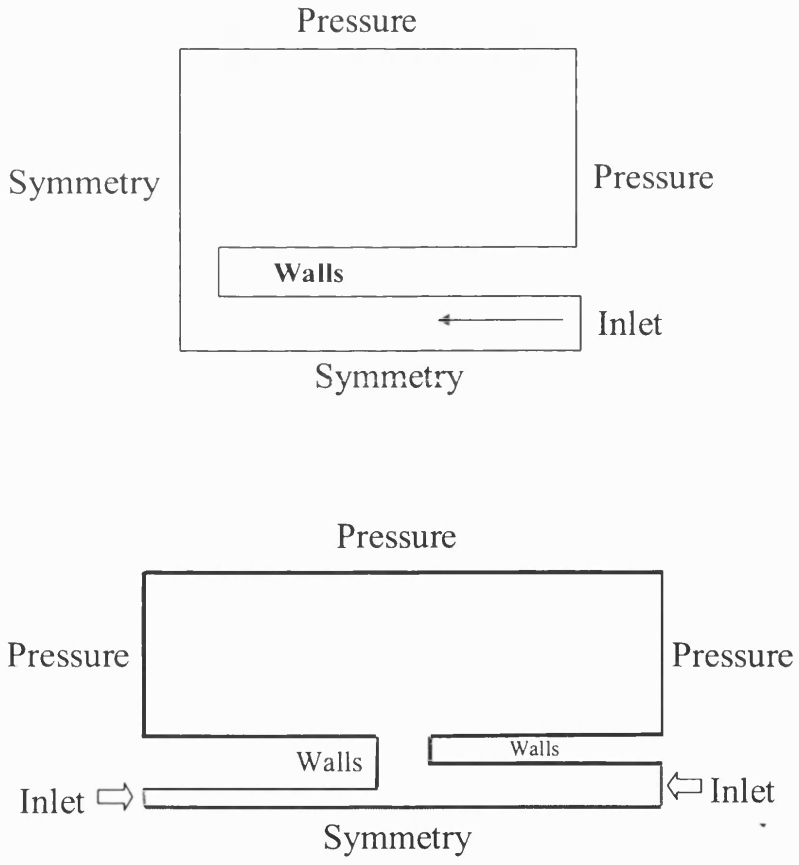

Figure 3.2 **Top: Schematic showing model geometry used for equal velocity and diameter jets (upper right quadrant). Bottom: Schematic showing model geometry used for non-equal jets (upper left and right quadrants).**

3.4.2 CFD model equations

The Navier-Stokes equations with an eddy-diffusion turbulence model, and with appropriate initial and boundary conditions, were solved across the entire flow domain. Refer to section 3.2.3 for a description of the relevant fluid flow equations. Both the κ-ε and low Re κ-ε turbulence models were used to model the fluid flow. These turbulence models can be easily specified in the CFX software.

3.4.3 Number of fluid phases

In practice mixing in an opposed jet device, for alkaline lysis, would involve three distinct fluid phases: the aqueous phase containing the cell resuspension, the lysis buffer, and air in which the two liquids impact and mix. Alternatively, if the mixing chamber within which the jets impinge was small, the mixing chamber could quickly become flooded with cell lysate, in which case the jets would impinge subsurface and the system would be a two-phase system, as air would be excluded. If the cell resuspension and lysis buffers are assumed to have the same physical properties, then the problem can be reduced to one-phase if the mixing chamber is assumed to be flooded. Opposed jet simulations were run where one, two or three separate phases were specified:

i) One-phase simulations. These consisted of two equal jets of the same liquid impacting subsurface in a flooded impingement chamber.

ii) Two-phase simulations. These consisted of two jets of the same liquid impacting in a chamber filled with air; there were two fluid phases present, liquid and air.

iii) Three-phase simulations. These consisted of two jets of different liquids impacting in a chamber filled with air; there were three phases present, two liquid phases and one air phase.

3.4.4 Initial conditions and boundard condtions

For one-phase simulations, the entire model geometry was initially set full of stagnant liquid. For two- and three-phase simulations, the entire model geometry was initially set full of stagnant air. At inlet boundaries, the fluid velocities of the entering liquid phases were specified. The pressure was set to atmospheric pressure at the fluid outlets (pressure boundary). The wall boundary conditions used depended on the turbulence model used, refer to section 3.2.4. The turbulent energy (κ) and turbulent energy dissipation (ε) at the inlets were specified based on the recommended values given in the CFX user-manual:

$$\kappa = 0.002\ U_{inlet}^{2}$$

$$\varepsilon = \kappa^{1.5} / 0.2385$$

Equation 3.9

3.4.5 Fluid physical parameters

In an opposed jet lysis reactor, the phases present before mixing are all Newtonian fluids and are a) cells resuspended in TE, b) 0.2 M NaOH and c) air in the mixing chamber. Following mixing of the cells and lysis solution, the fluid becomes visco-elastic. Because the residence time of the fluid in the jet is on the order of milliseconds and the time taken for the mixture to become visco-elastic is on the order of seconds (Ciccolini et al. 1998) the fluid should remain Newtonian until well after it has left the jet mixer. Therefore, all fluids were modelled as Newtonian fluids, vastly simplifying the calculations. Table 3.1 lists the physical properties of the phases modelled.

	Phase 1 Water	**Phase 2 Air**	**Phase 3 NaOH-Water**
Density (kg/m^3)	997	1.181	1200
Viscosity (mPa)	1.0	0.018	1.2

Table 3.1. Physical parameters of the fluid phases modelled.

3.4.6 Heat transfer

Initial simulations were run with and without heat transfer included in the model. From the simulation results it was determined that including heat transfer in the model had a negligible effect on the final solution (the fluid velocities, pressures, strain rates and turbulent energies were not significantly affected by heat transfer). Hence, all further simulations were run without heat transfer in order to save computational time.

3.4.7 Surface sharpening algorithim

Numerical truncation can lead to a blurring of the surfaces between distinct phases in multi-phase simulations. In order to rectify this, the CFX program has an algorithm to sharpen the surfaces between phases. Simulations were run comparing the results with, and without, surface sharpening. It was found the use of the surface sharpening algorithm had no effect on the overall solution, while using surface sharpening significantly increased the computational time. Thus, all future calculations were done without surface sharpening.

3.4.8 Solution convergence and grid-size indepenence.

The model geometry was gridded using CFX-Build. Variable rectangular grids were used to grid the geometry. The grids were designed to be smallest near the jet impingement region,

gradually became larger further from this region. The finer grid in the jet impingement region was designed to better capture the more rapidly changing fluid flow parameters in that region. The geometric increase in the variable mesh, from one grid to its neighbour, was set throughout at 1.1 ± 0.02. Figure 3.3 shows a typical variable mesh and model geometry. Initial jet simulations used a small number of large grids (coarse mesh). After grid generation, the CFX solver program was run to solve the relevant flow equations. The solver program was stopped when there was no further significant change in the flow variables (velocity, pressure, turbulent energy and turbulent energy dissipation). The number of iterations required to solve a particular problem varied considerably depending on the number of grids and the number of phases present and was typically from 1,000 – 100,000 iterations. After obtaining a solution for a particular grid size, the number of grids was increased (finer mesh) to determine if the final flow solution was grid size independent. In theory, for a suitably fine mesh, the final fluid flow solution should not be a function of the number of grids; obviously, a real physical fluid flow is not a function of a computer generated mesh size. Only CFD simulations that were found to be grid size independent were analysed.

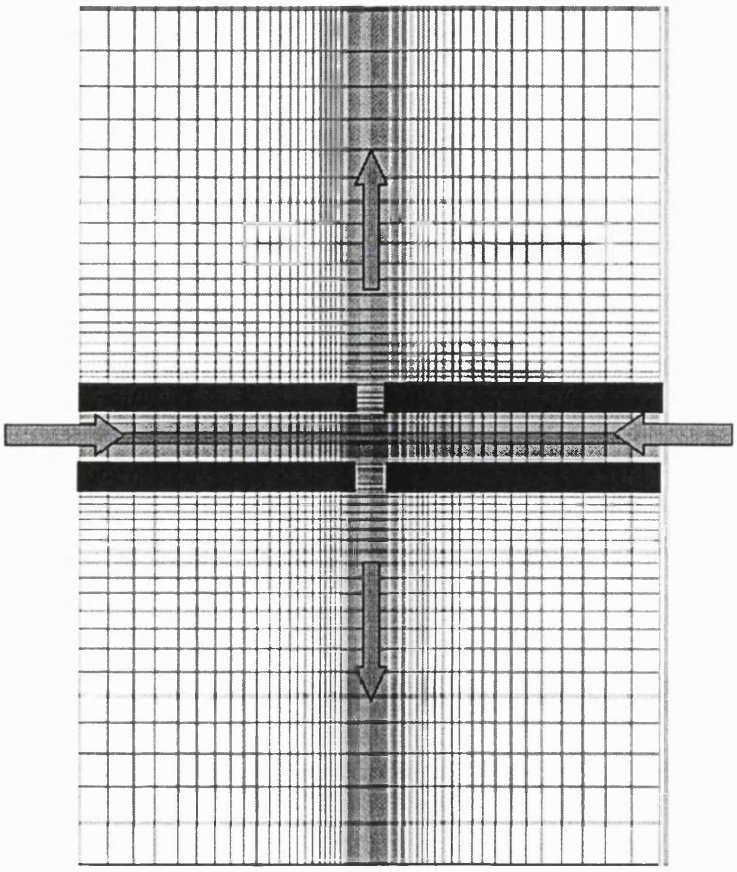

Figure 3.3. Grid distribution for equal opposed jet simulations. Due to symmetry, only the upper rightmost quadrant was modelled for equal opposed jets. The grid used was coarse at the extremities of the model, becoming significantly more fine in the region where the jets impinge.

3.4.9 Model convergence

The following set of simulations, Table 3.2, were carried out to check if the one-, two, and three-phase models were grid size independent. Each simulation was run using different size grids to check for grid size independence. The results are given in chapter 8. Only grids that gave grid size independent results were used in subsequent simulations.

Model	Djet1 mm	Djet2 mm	Ujet1 m/s	Ujet2 m/s	Phase 1	Phase 2	Phase 3
One-phase	4	4	5	5	Water	N/A	N/A
Two-phase	4	4	1	1	Water	Air	N/A
Three-phase	0.5	1.6	25.4	8	Water	NaOH-water	Air

Table 3.2. Simulations run to check for model grid-size independence.

3.4.10 Submerged versus non-submerged simulations

Two simulations, presented in Table 3.3, were run to examine the effect on the energy dissipation of the jets impinging subsurface in a flooded chamber, versus impinging in air. Simulations were run using the Low Re κ–ε model.

Model	Djet mm	Ujet m/s	Phase 1	Phase 2
One-phase	4	5	Water	N/A
Two-phase	4	5	Water	Air

Table 3.3. Simulations run to examine the effect of jets being submerged.

3.4.11 Effect of turbulence model.

There are several different turbulence models that are commonly used to model fluid flows. Of these, by far the most frequently used and validated are the eddy-diffusion models. The two most common eddy-diffusion turbulence models are the κ–ε and Low Re κ–ε turbulence models. The κ–ε model is most applicable at high Reynolds numbers, above 10,000. As the name implies, the Low Re κ–ε model is applicable at lower Reynolds numbers. Provided the grid size is suitably fine, the Low Re κ–ε model should be applicable over all Reynolds numbers (Versteeg, 1995). Simulations were run to compare the results using the two different turbulence models. The following two simulations, Table 3.4, were run to compare the effects of the κ–ε and Low Re κ–ε turbulence models on the simulation results. The results are presented in chapter 8.

Model	Djet mm	Ujet m/s	Phase 1	Phase 2	Turbulence Model
Two-phase	4	1	Water	Air	K–ε
Two-phase	4	1	Water	Air	Low Re K–ε

Table 3.4. Simulations run to examine the effect of turbulence model.

3.4.12 Effect of jet velocity, jet diameter, fluid viscosity and fluid density

In order to determine the effects of jet operating conditions, fluid properties and jet scale-up on jet performance, 19 simulations of equal opposed jets impinging in air were run, as shown in

Table 3.5. Each simulation was run until convergence was reached. A detailed analysis of the results of this series of simulations is presented in chapter 8.

Model	Djet	Ujet	Jet separation	Phase 1 Viscosity	Phase 1 Density
	mm	m/s	mm	mPa s	kg/m^3
Two-phase	0.508	1	0.508	1	1000
Two-phase	0.508	2.5	0.508	1	1000
Two-phase	0.508	5	0.508	1	1000
Two-phase	4	0.5	4	1	1000
Two-phase	4	1	4	1	1000
Two-phase	4	2.5	4	1	1000
Two-phase	4	5	4	1	1000
Two-phase	4	10	4	1	1000
Two-phase	4	2.5	4	5	1000
Two-phase	4	10	4	5	1000
Two-phase	4	1	4	1	2000
Two-phase	4	1	10	1	1000
Two-phase	4	2.5	10	1	1000
Two-phase	4	5	10	1	1000
Two-phase	12	1	12	1	1000
Two-phase	12	2.5	12	1	1000
Two-phase	12	5	12	1	1000

Table 3.5. Simulations of equal opposed jets impinging in air.

3.4.13 Non-equal opposed jets

Opposed jets will not be equal if different fluids are used in each jet, or if each jet is given a different fluid velocity. In addition, the diameters of the jets can be varied to increase the velocity and momentum of one of the jets. For non-equal opposed jets, another variable, the ratio of jet diameters, can affect the performance of the jets. In order to examine the effect of jet diameter ratio on the performance of non-equal opposed jets, the following set of simulations was performed, shown in Table 3.6.

NaOH Conc. (M)	Q_{cells} / Q_{lysis}	V_{cells} (m/s)	d_{cells} (inch)	d_{cells} (mm)	d_{lysis} (inch)	d_{lysis} / d_{cells}
0.4	0.33	0.5, 2.5, 8	0.02	0.508	0.005	0.250
0.4	0.33	0.5, 2.5, 8	0.02	0.508	0.007	0.350
0.4	0.33	0.5, 2.5, 8	0.02	0.508	0.010	0.500
0.4	0.33	0.5, 2.5, 8	0.02	0.508	0.020	1.000
0.4	0.33	0.5, 2.5, 8	0.062	1.5748	0.010	0.161
0.4	0.33	0.5, 2.5, 8	0.062	1.5748	0.020	0.323
0.4	0.33	0.5, 2.5, 8	0.062	1.5748	0.040	0.645
0.4	0.33	0.5, 2.5, 8	0.062	1.5748	0.062	1.000
0.4	0.33	0.5, 2.5, 8	0.472	12.00	0.076	0.161
0.4	0.33	0.5, 2.5, 8	0.472	12.00	0.152	0.323
0.4	0.33	0.5, 2.5, 8	0.472	12.00	0.305	0.645
0.4	0.33	0.5, 2.5, 8	0.472	12.00	0.472	1.000

Table 3.6. Simulations of non-equal opposed jets.

3.5 CFD modelling of capillary shear device

3.5.1 Model geometry

Figure 3.4 shows the model geometry used for the capillary shear device. The model was based on the actual geometry of the capillary shear device used in laboratory shear experiments. The device consisted of a piece of large bore capillary tubing connected to a piece of small bore capillary tubing, making a sudden and sharp flow constriction. The internal diameter of the wide tubing was 0.062 inches (1.57 mm) and the size of the small tubing was 0.007 inches (0.178 mm). Similar to the case for opposed jets, described previously, the system has an axis of symmetry down the centreline of the capillaries, and can be converted to a two-dimensional problem using cylindrical co-ordinates.

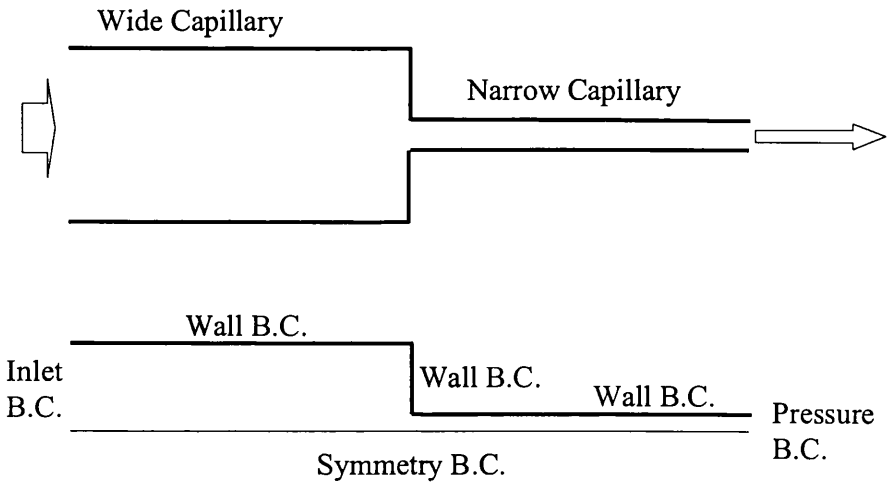

Figure 3.4 Schematic showing the capillary shear device (top diagram). Using flow and geometry symmetry arguments, only the top half of the geometry needed to be modelled (bottom diagram).

3.5.2 Model equations

The model equations were the same as those used for opposed jets.

3.5.3 Number of fluid phases

All capillary simulations were run using one liquid phase. The liquid phase was taken to have the properties of liquid water, with the properties shown in Table 3.1.

3.5.4 Initial conditions and boundard condtions

The entire model geometry was initially set full of stagnant liquid. At the inlet boundary, the fluid velocity of the entering liquid was specified. The pressure was set to atmospheric pressure at the pressure boundary. The turbulent eddy viscosities and diffusivities at the inlets were calculated, as described previously, based on Equation 3.9. The wall boundary conditions used were those appropriate to the Low Re k-e turbulent model, refer to section 3.2.4.

3.5.5 Heat transfer

Initial simulations were run with, and without, heat transfer being included in the model. As with opposed jet simulations, it was determined that including heat transfer in the model had only a negligible effect on the final solution (the fluid velocities, pressures, strain rates and

turbulent energies were not significantly affected by heat transfer). Hence, all further simulations were run without heat transfer in order to save computational time.

3.5.6 Grid size convergence and solution convergence

The model geometry was gridded in CFX-Build. Similarly to the opposed jet simulations, a variable rectangular mesh was used to grid the geometry. The grid was finest in the region between the wide and narrow bore capillaries, and in the region close to the capillary walls. The geometric increase in the variable mesh from one grid to its neighbour was set throughout at 1.5 ± 0.1. Figure 3.5 shows a typical variable mesh and model geometry. Grid size analysis was performed as described in section 3.4.8 . The number of grids was increased until a grid-size independent solution was obtained. The number of iterations required to solve a particular problem varied considerably depending on the number of grids and, similar to opposed jet simulations, was typically from 1,000 – 100,000 iterations. The results of the grid size convergence study is given in chapter 5 on capillary shear.

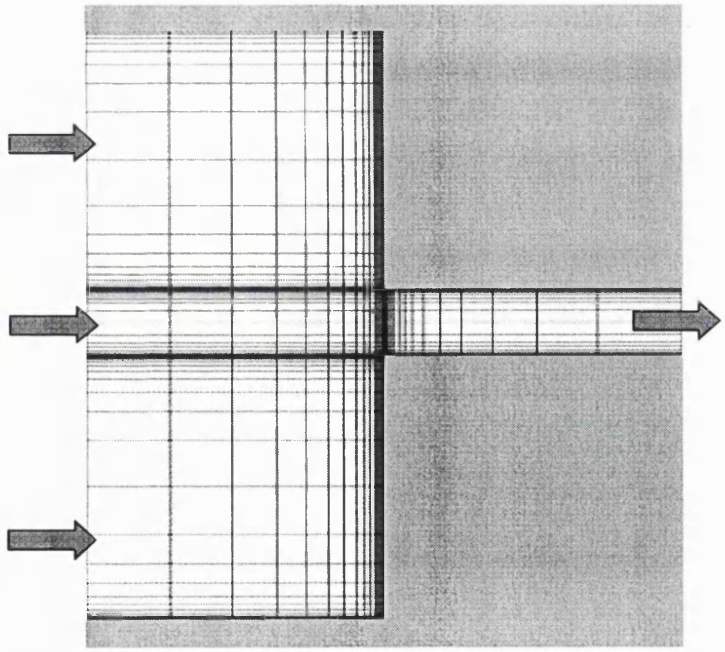

Figure 3.5. Schematic of capillary model geometry showing the grid distribution.

3.5.7 Effect of capillary diameter and fluid velocity

The following set of simulations, shown in Table 3.7, was run to determine the effect of fluid flow velocity on pressure drop, elongational strain rate, and turbulent energy dissipation in capillaries. The Low Re κ–ε models was used throughout. A detailed analysis of the results of this set of simulations is presented in chapter 5on capillary shear

Downstream capillary ID inches	Flowrate ml/min	Upstream capillary ID inches	Downstream capillary Re
0.010	16	0.062	955
0.010	50	0.04	2904
0.007	1	0.062	119
0.007	4	0.062	477
0.007	8	0.062	955
0.007	12	0.062	1432
0.007	16	0.062	1900
0.007	20	0.062	2307
0.007	25	0.04	2904
0.007	30	0.08	3501
0.007	50	0.08	5808
0.005	0.5	0.062	119
0.005	2	0.062	477
0.005	4	0.062	955
0.005	6	0.062	1432
0.005	8	0.062	1900
0.005	10	0.062	2307
0.005	12	0.04	2904
0.005	15	0.08	3501

Table 3.7. CFD simulation conditions examining the effect of capillary internal diameter and fluid velocity on fluid stresses and energy dissipation rates.

3.6 Post-simulation calculations: jets and capillaries

3.6.1 Shear rate calculations

After a particular fluid flow problem had been solved to the required tolerance by the program CFX-solver, all of the final flow variables for each grid point in the model geometry (velocity, speed, energy dissipation, turbulence energy) were output to a results file. The CFD program, CFX-view, generated contour plots of all the principal fluid parameters within the model geometry based on the information in the results file. Unfortunately, the version of CFX-view available, version 4.2, did not calculate the fluid strain rate throughout the flow domain. In order to calculate fluid strain rates for the opposed jet and capillary systems, a program was

written in FORTRAN that read in the velocity data from the simulation results file and calculated the local shear rates from the velocity data.

The local shear rate at a point was calculated from the deformation rate tensor, D that in turn is calculated from the velocity gradient tensor. For cylindrical co-ordinates, r, θ,z, the velocity gradient tensor, GRAD(V), is calculated from the velocity flow field as follows:

$$GRAD(V) = \begin{matrix} dVr/dr & (1/r)(dVr/d\theta) - (V_\theta/r) & dVr/dZ \\ dV_\theta/dr & (1/r)(dV_\theta/d\theta) - (Vr/r) & dV_\theta/dZ \\ dVz/dr & (1/r)(dVz/d\theta) & dVz/dZ \end{matrix}$$

For these symmetric systems, $d/d\theta = 0$, $V_\theta = 0$.

$$\text{HENCE, } GRAD(V) = \begin{matrix} dVr/dr & 0 & dVr/dZ \\ 0 & -(Vr/r) & 0 \\ dVz/dr & 0 & dVz/dZ \end{matrix}$$

Equation 3.10

The deformation rate tensor $D = grad(V) + grad(V^T)$,

$$D = \begin{matrix} 2dVr/dr & 0 & \{dVr/dZ + dVz/dr\} \\ 0 & -2(Vr/r) & 0 \\ \{dVr/dZ + dVz/dr\} & 0 & 2dVz/Dz \end{matrix} = \begin{matrix} D_{11} & D_{12} & D_{13} \\ D_{21} & D_{22} & D_{23} \\ D_{31} & D_{32} & D_{33} \end{matrix}$$

Equation 3.11

The strain rate, ε' , $= 2^{ND}$ INVARIANT(D) = D11*D22 + D11*D33 + D22*D33 - D13*D31

Equation 3.12

A program was written in Matlab to create contour plots of the local strain rate throughout the flow domain for the opposed jet and capillary systems.

3.6.2 Streamline calculations

A program was written in Matlab to calculate and plot the fluid flow streamlines for the opposed jet and capillary systems. Matlab has an in-build routine for calculating fluid flow streamlines based on the velocity field data, which was read in from the CFD results file.

3.7 Conclusion

CFD models were built and simulated for capillaries and opposed jets. Creation of CFD model geometries was relatively straightforward using CFX-Build. The majority of the effort involved in creating the CFD models was determining the grid size independence of the different CFD models, which is discussed in chapters 5 and 8.

The principal assumption of the CFD simulations was that the Low Re κ-ε turbulence model and κ-ε turbulence model accurately described the flow behaviour in the capillary and opposed jet systems. These two models are the most widely used and validated turbulence models, and it has been shown that these models typically provide accurate predictions for confined fluid flows; although for unconfined flows their predictions sometimes deviate from experimental observations (Versteeg, 1995). Therefore it would be expected that the CFD models should provide accurate predictions for the capillary simulations. The results of the capillary CFD simulations are presented in chapter 5. The opposed jet flow is only semi-confined; therefore the CFD predictions for the opposed jets may not be as accurate. Experimental validation of the CFD predictions of opposed jet flow behaviour is warranted. The results of opposed jet simulations are presented in chapter 8, and CFD predictions are compared to experimental observations.

4 Analytical development

4.1 Brief summary of results

Novel analytical techniques were developed to quantify supercoiled plasmid DNA and DNA impurities in pure and in-process samples.

A modified gel electrophoresis procedure was developed to improve the accuracy of supercoiled plasmid quantification. This procedure involved the addition of low melting point agarose to DNA samples prior to electrophoresis to reduce sample diffusion from the sample wells prior to electrophoresis.

Several anion exchange resins and hydrophobic interaction resins were screened for their ability to quantify supercoiled plasmid DNA. Two novel HPLC-based assays were developed which were capable of separately quantifying supercoiled plasmid DNA, open-circular plasmid DNA, double-stranded chromosomal DNA, single-stranded DNA and RNA in process samples. The assays were based on Poros PI and Q-Sepharose anion exchange resins. The assays were automated, fast (< 60 min), robust and accurate (4% to 6 % relative standard deviations for the different species).

A fluorescent-dye-based assay was developed for monitoring supercoiled plasmid DNA degradation. This assay was used to monitor supercoiled plasmid degradation under very dilute conditions, allowing plasmids to be potentially used as shear probes in large-scale equipment. A modified agarose gel procedure was developed to improve agarose gel accuracy. These assays were used in subsequent experiments on DNA stress-induced degradation, alkaline lysis and downstream purification.

4.2 Introduction

Analysis of experimental samples involved determining the quantity, size and form of plasmid DNA and chromosomal DNA molecules. This task was complicated enormously because native plasmid DNA and chromosomal DNA are chemically identical, differing only in physical size and topology. This makes plasmid and chromosomal DNA particularly difficult to distinguish and separate from each other. As a further complication, both plasmid and chromosomal DNA can be found in several forms in solution. Supercoiled plasmid DNA can be degraded to open-circular and linear forms by DNAases or fluid stress, or it can be converted

to a compact, denatured form by high pH. Chromosomal DNA can be found as either a single- or double-stranded helix, depending on whether it has or has not been denatured by high temperature or high pH. In addition, both plasmid and chromosomal DNA can be broken into linear fragments of varying sizes. For example, it is frequently necessary to determine the concentration of native supercoiled plasmid DNA from a mixture of double- and single-stranded chromosomal DNA fragments and supercoiled-, open-circular-, linear-, and denatured-plasmid forms. Table 4.1 shows the principal forms of plasmid and chromosomal DNA present in *E. coli* cell lysates.

Plasmid DNA			
Native forms	Supercoiled, ds-DNA	Open-circular, ds-DNA	Linear, ds-DNA
Denatured forms	Compact, ss-form	Linear, ss-DNA	Linear, ss-DNA

Chromosomal DNA	
Native forms	Linear, ds-DNA
Denatured forms	Linear, ss-DNA

Table 4.1. Showing principal forms of plasmid and chromosomal DNA.

Total DNA (chromosomal DNA + all plasmid forms) can be quantified colorimetrically (Sambrook et al. 1989), fluorometrically (Singer et al., 1997; Levy et al., 2000) or by HPLC (Ferreira et al., 1999). However, these assays do not distinguish between the different DNA forms. Instead, several assays are required to quantify the different DNA forms. Plasmid DNA (supercoiled, open-circular and linear forms) can be quantified using agarose gel electrophoresis (Barton et al., 1995; Sambrook et al., 1989; Wang et al., 1995), but electrophoresis does not accurately measure chromosomal DNA. Moreover, gel electrophoresis is not very accurate at quantifying plasmid (a 20% standard deviation between replicate samples is typical) and is time consuming to run. Chromosomal DNA can be quantified using Quantitative Polymerase Chain Reaction (qPCR) (Lahijani et al., 1998); however, impurities can interfere with qPCR so upstream process samples require additional purification before they can be assayed. These additional purification steps, such as chromatography or filtration, can remove the chromosomal DNA that one is trying to assay. Another drawback of qPCR is that it cumbersome, has a slow turn-around time and is highly susceptible to contamination. Alternatively, southern blot can be

used to estimate chromosomal DNA; however, it is not accurate. Another novel technique for plasmid analysis is capillary gel electrophoresis (Raucci et al., 2000). This has the advantage of being able to distinguish different plasmid forms, however, it requires specialised equipment to run, and it is unknown how it will perform using crude upstream process samples.

This chapter describes the development of novel electrophoretic-, chromatographic- and fluorescent-based assays for quantification of plasmid and chromosomal DNA. These new assays were essential tools in properly analysing the effects of fluid mixing and fluid stress on DNA molecules.

4.3 Materials and methods

The following section details the experimental methods used in developing new analytical techniques for quantifying DNA and RNA.

4.3.1 Materials

RNAse A, λ-ladder, λ-digest, λ DNA, rRNA, RNAse A and agarose for routine use were obtained from Sigma (St. Louis, MMO, USA). Poros PI 20 μm resin was obtained from PerSeptive Biosystems, Inc. (Framingham, MA, USA). 1 mL Q-Sepharose HP HiTrap columns were obtained from Amersham Pharmacia Biotech AB (Uppsala, Sweden). Sodium chloride, sodium hydroxide, Tris-base, boric acid, EDTA, isopropanol and ethanol were obtained from Merck (Dorset, U.K). Ready-lyse lysozyme was obtained from Epicenter Technologies (Madison, WI, U.S.A).

.

4.3.2 Laboratory equipment

Analytical chromatography was performed with a Dionex (Sunnyvale, CA) HPLC system consisting of a GP40 gradient pump, AS3500 autosampler and AD20 absorbance detector. Agarose gels were run using a horizontal mini-gel electrophoresis unit from Merck (Dorset, U.K.). Pulsed-field agarose gels were run using a CHEF II mapper from BioRad (Hercules, California, USA). A purpose-build capillary device was used to degrade chromosomal DNA up to strain rates of 10^6 s^{-1}. The device consisted of a syringe pump (Hamilton, Nevada, USA), Beckton Dickenson plastic syringes and precision PEEK capillary tubing (Upchurch Scientific, WA, U.S.A) of different length and diameter. A Beckman DU70 UV/visible spectrophotometer was used for absorbance readings, and a 96 well plate fluorometer, model Fluorocount (Perkin-Elmer, Boston, USA) was used for fluorescence readings.

4.3.3 Standard buffer preparation

500 mM Tris, pH 8.0 was prepared by dissolving Tris-base or Tris-Cl powder in ultra-pure water and pH adjusting with NaOH or HCl as appropriate. 500 mM EDTA, pH 8.0 was prepared by dissolving EDTA powder in ultra-pure water and pH adjusting as appropriate. TE buffer (10 mM Tris, 1 mM EDTA, pH 8.0 unless otherwise stated) was made-up by diluting 500 mM Tris and 500 mM EDTA to the required concentration. TE with RNAse consisted of TE with 0.1 mg/m RNAse A. RNAse A stock solution at 10 mg/mL in TE was prepared in 1 mM sodium acetate according to Manniatas (Cold Spring Harbor Laboratory Press, Cold Spring Harbor, NY, 1989). The RNAse A stock solution was heat-treated at 55°C for 30 minutes to destroy DNAases. Pure RNA stock solutions were prepared by dissolving pure RNA lyophilised powder in TE buffer at 1 mg/mL. To remove RNA nucleotides, the RNA was precipitated by adding sodium acetate to 0.3 M concentration, followed by one volume of IPA. The material was chilled at –20°C overnight, centrifuged in a Beckman benchtop centrifuge at 13 krpm and resuspended in TE buffer. RNA stocks were kept at –80°C for no longer than 2 weeks.

4.3.4 Fermentation of plasmids and chromosomal DNA.

Two *E. coli* cells strains were selected for analytical development and alkaline lysis studies. *E. coli* DH5α and *E. coli* DH10 are recombination-deficient suppressing strains used for plating and growth of plasmids and cosmids. The bacterial cells were used as wild-type (non-plasmid DNA containing) and in a recombinant form. In total four different plasmids were fermented for use in analytical development and alkaline lysis studies: DH5α pSVβ (6 kb), DH5α pQR186 (13 kb), DH5α pQR150 (20 kb) and DH10 p5176 (113 kb). All fermentations were done at shake-flask scale except for plasmid pSVβ that was produced by 5L fermentation courtesy of A. Kay, UCL PhD candidate. Table 4.2 lists the size of the plasmids used, their copy number and the antibiotic resistance they convey.

Plasmid	Size (kb)	Copy Number	Antibiotic Resistance	Antibiotic concentration (μg/ml)	Cell Strain	Culture Broth
No plasmid	NA	NA	None	NA	DH5α	LB
pSVβ	6	200 - 500	ampicillin	100	DH5α	LB
pQR186	13	200	kanamycin	25	DH5α	LB
pQR150	20	200	kanamycin	25	DH5α	LB
p5176	116	1	chloramphenicol	5[1]	DH10	Super

Table 4.2. Plasmids used in lysis and shear experiments. [1] 12.5 μg/ml chloramphenicol was used for plates, 5 μg/ml for shake-flasks.

Shake flask fermentation

Nutrient agar plates were prepared by pouring sterile nutrient agar (5 g/L yeast extract, 10 g/L NaCl, 10 g/L tryptone, 15 g/L agar technical) containing the required amount of antibiotic, refer to Table 4.2. For *E. coli* DH10 cell strain Super Broth agar was used (20 g/L yeast extract, 5 g/L NaCl, 32 g/L tryptone, 15 g/L agar technical, pH 7.4). Bacterial colonies, from master stocks in 20% glycerol, were streaked on the new plates using aseptic technique. The plates were incubated for 24 h at 37°C for growth of the colonies. Fresh master plates were routinely prepared from working glycerol stocks.

Bacteria strains were cultured using either LB (5 g/L yeast extract, 10 g/L NaCl, 10 g/L tryptone) or Super broth (20 g/L yeast extract, 5 g/L NaCl,. 32 g/L tryptone). The required antibiotic (sterile filtered) was aseptically added to the required concentration, refer to Table 4.2. The inoculum was prepared by transferring aseptically a single colony of *E. coli* cells from a master plate to a glass universal bottle containing 5 mL of sterile culture broth. The inocula were placed in an incubator at 37°C, 200 rpm, for 12 h. 2 L shake flasks were prepared each containing 500 L of appropriate sterile culture broth, containing the appropriate antibiotic. A 5 mL inocula was added to each flask. Each flask was incubated for 16 to 28 h at 37°C, 200 rpm agitation.

5 L fermentation

Plasmid pSVβ was produced in larger amount for extensive alkaline lysis and shear studies using 5 L fed-batch fermentation carried-out by A. Kay, UCL PhD candidate. *E. coli* DH5α pSVβ was grown on SDcas medium containing ampicillin at 100 mg/L, in a 7 L fermenter with a 5.5 L working volume, at 37°C. pH was maintained at 6.3 by the addition of 4 M NaOH and

H_3PO_4 and DO was maintained at 30 % saturation by adjustment of stirrer speed. The fermentation was run in batch mode for 15.5 h before switching to fed batch mode for a further 19.5 h. During the fed-batch mode an exponential glucose feed (40% W/V) was employed to maintain the growth rate at 0.1/h. A linear amino acids feed was used from 20.5 to 35 h.

Cell harvest

All cells were harvested by centrifugation in a Beckman J-10 centrifuge at 10,000 rpm for 40 minutes. Cell paste was frozen at –70°C.

4.3.5 Standard lysis protocol

Alkaline lysis

Prior to lysis, frozen cell paste was resuspended in 0.5 mL TE buffer to 125 g wcw / L, in a 2 mL centrifuge tube. Resuspended cells were lysed using a modification of the alkaline lysis method of Birnboim et al. (1979). One volume of resuspended cells was mixed with one volume of lysis buffer (0.2 M NaOH, 1% SDS). The sample was mixed gently by inversion for 3 minutes. One volume of chilled neutralisation buffer (3 M potassium acetate, pH 5.5, 4°C) was added and mixed gently by inversion. The alkaline lysate was chilled in an ice-bath for 10 minutes.

Proteinase-K digestion

Frozen cell paste was resuspended in 0.5 mL STET buffer (5% sucrose, 25 mM Tris, 10 mM EDTA, 5% Triton, pH 8.0) to 125 g/L in a 2 mL centrifuge tube. Proteinase-K was added to a concentration of 0.1 mg/ml and the lysate incubated for 2 h at 55°C, followed by chilling in an ice-bath for 10 minutes.

Lysozyme plus heat lysis

Harvested cells were resuspended in 0.5 mL STET buffer at 125 g wcw / L. Ready-lyse lysozyme was added to 10 EU/mL and the samples were incubated at 37°C for 1 h with gentle mixing. The samples were placed in a water bath for 5 minutes at 20°, 70°, 75°, 80°C and 85°C, followed by quenching on ice for 10 minutes.

4.3.6 Standard clarification protocol

All lysates were centrifuged at 13,000 rpm for 30 min in a Beckman bench-top centrifuge and the pellets discarded. For alkaline lysates, the supernatant was precipitated with 1 volume of isopropanol (IPA). For non-alkaline lysates, 5 M NaCl was added to the supernatant to a

concentration of 0.3 M, followed by one volume of IPA. All IPA precipitates were centrifuged at 13,000 rpm for 30 minutes and the supernatants discarded. The pellets were washed with 70 % ethanol and resuspended in TE with 0.1 mg/ml RNAse to make clarified lysates. The pellet was always resuspended in a volume of TE that was equal to the original clarified lysate volume.

4.3.7 Preparation of pure plasmid and chromosomal DNA standards

Plasmid DNA purification

To prepare pure supercoiled plasmid DNA in TE, clarified alkaline lysates were further purified using Qiagen giga-prep kit according to Qiagen giga-prep handbook (1999). Pure plasmid DNA was further purified by Q-Sepharose chromatography (Prazeres et al., 1998). After elution of the chromatography column, the supercoiled plasmid fraction was collected, ethanol precipitated, 70% ethanol washed and resuspended in TE. Agarose gel electrophoresis was run to confirm that the material was essentially pure supercoiled DNA. Clarified alkaline lysates containing plasmid p5176 were not purified by Qiagen method, but instead were CTAB precipitated (Lander et al., 2000), washed with TE and resuspended in 1.2 M NaCl. After resuspension, two volumes of ethanol were added to precipitate the plasmid, followed by a 70% ethanol wash and resuspension in TE with 0.1 mg/ml RNAse A.

Chromosomal DNA purification

Wild-type *E. coli* cells (non-plasmid containing) were resuspended in STET (5% sucrose, 25 mM Tris, 10 mM EDTA, 5% Triton, 0.1 mg/ml RNAse A, pH 8.0) to 125 g/L. Proteinase-K was added to a concentration of 0.1 mg/ml and the lysate incubated for 2 hours at 55°C. 5 M NaCl was added to a concentration of 0.3 M. One volume of IPA was added while stirring continuously with a glass rod. The precipitated chromosomal DNA wound around the glass rod and was removed. The precipitate was washed with 70% ethanol and resuspended in TE with 0.1 mg/ml RNAse A to make pure chromosomal DNA. Chromosomal DNA was further purified by adsorption to diatomaceous earth (DE) using a modification of the method of Carter *et al.* (1991). DNA was adsorbed to DE at 4M NaCl, washed twice with 2 volumes 2 M NaCl, once with 1 volume of 100% ethanol, once with 1 volume of 70% ethanol, and resuspended with one volume of TE to make ultra-pure chromosomal DNA. Single-stranded DNA was prepared from double-stranded DNA by denaturation at 0.1 M NaOH, followed by adjustment back to pH 8 with 500 mM Tris, pH 7.5.

Size reduction of DNA

Prior to HPLC, all samples containing chromosomal DNA were size reduced by shearing the samples though a narrow capillary. The samples were placed in a 1 ml syringe and pushed by hand through a 2 cm length of PEEK tubing (0.007" ID) at approximately 3 to 6 ml/min. Samples were then sucked back into the syringe through the same piece of PEEK tubing. This was repeated 10 times for each sample. Size reduction was always performed before denaturation-renaturation.

Generation of open-circular plasmid DNA

Pure supercoiled plasmid DNA in TE was degraded at 60 °C over 60 h. Agarose gel electrophoresis showed that 90% of the original supercoiled plasmid DNA had been degraded to open-circular and linear plasmid forms.

Standard DNA denaturation-renaturation procedure

One volume of clarified alkaline lysate, or pure supercoiled plasmid DNA in TE, was rapidly mixed with 1/3rd volume of 0.2 M NaOH. After 2 to 3 minutes at room temperature, one volume of 500 mM Tris pH 7.5 was added to each sample.

4.3.8 Standard analytical techniques

Pure DNA and pure RNA standard concentration by UV absorbance

Concentrations of ultra-pure plasmid DNA, ultra-pure chromosomal DNA, and RNA solutions in TE were determined by measuring their absorbance at 260 nm in a 1 cm path length quartz cuvette. Their optical density was measured against TE buffer. Samples were diluted to fall with the range 0.1 - 0.5 OD at 260nm. An OD of 1.0 was taken to be 50 μg/ml double-stranded DNA, 40 μg/ml single-stranded DNA and 30 μg/ml RNA. The absorbance at 280 nm was also measured for DNA samples. Only samples with an OD_{260nm}/OD_{280nm} of 1.85 ± 0.05 were considered pure (Sambrook et al., 1989).

DNA concentration by Picogreen fluorescence

The total DNA concentrations of pure and ultra-pure plasmid DNA and chromosomal DNA, and clarified lysates were determined by Picogreen fluorescence. The flourescence of samples was measured using a flourescence plate-reader from BioProbes. The flourescene-plate reader from BioProbes comes with a selection of removeable excitation and emission wavelength filters. The optimum combination of filters for a particular assay is determined by the excitation and emission spectra of the flourescent dye used. Of the filters that were available, there were four excitation wavelength filters (360, 460, 485 and 530 nm) and four emission wavelength

filters (530, 570, 580 and 590 nm) that could be selected in the flourescence reader. The excitation and emission filters for Picogreen were set at 485 nm and 530 nm, throughout, as recommended by Molecular Probes. For ethidium bromide, the 16 possible combinations of filters were tested to determine the optimum combination.

Samples were diluted to approximately 0.3 ng/ml using ultra-pure water (UPW). Picogreen stock reagent was diluted 1:200 in UPW. 100 mL of dilute Picogreen solution was added to 100 mL of each sample in a 96-well plate. Ultra-pure plasmid DNA samples, diluted in the range 0.020 ng/mL to 1 ng/mL were run on each plate as standards. TE buffer was run as a blank. A linear standard curve was fitted to the fluorescence versus concentration of the ultra-pure plasmid standards. The concentration of samples was determined by comparison to the standard curve.

Determination of supercoiled and open-circular plasmid concentration using agarose gel

Clarified lysates and pure DNA samples were run on 0.8% agarose gels in 3X TAE buffer at 30 V for 2 h using 50 mL volume mini-gels. All samples were RNAse digested for 1 h at 37°C in 0.1 mg/ml RNAse A prior to loading. Samples were loaded at 20 to 200 ng DNA/well, 20 µl per well. Ultra-pure supercoiled plasmid DNA at 20, 50, 100 and 200 ng/well and λ-DNA digest were run as standard. Agarose gels were stained for 4 hours in 0.5 µg/ml ethidium bromide solution on a rocker-plate. Gels were illuminated with UV light (300 nm excitation) and scanned using a digital camera. Gels were analysed using Scion image gel analysis software. A standard curve was generated from the band areas of the pure supercoiled plasmid standards. Because open-circular plasmid binds more ethidium bromide than the equivalent supercoiled plasmid, the band areas for open-circular plasmid were divided by 2.5, an approximate correction factor (Ciccolini et al., 2002) in order to determine open-circular concentrations.

Determination of chromosomal and large plasmid size by pulsed-field gel electrophoresis

Clarified lysates and pure DNA samples were run on 1.0 % agarose gels, 100 ml, in 0.5 X TBE buffer at 6 V/cm at 14°C. Switch times used were from 2 s to 16 s and from 1 s to 200 s for plasmid p5176 and chromosomal DNA, respectively. Run times were 16 h and 24 h for plasmid p5176 and chromosomal DNA, respectively. Samples were loaded at approximately 500 ng DNA/well, 20 to 30 µl per well. Agarose gels were stained, scanned and analysed as already described. A λ–digest mid-range ladder and λ–ladder were run as standards on all gels.

4.3.9 HPLC assay development

All HPLC was done using the Dionex HPLC system described in section 4.3.1. The buffer flowrate used was 0.3 ml/min for all experiments. All HPLC was done at room temperature. 100 µl on sample was injected onto the HPLC column for all experiments. Different analytical columns were switched in and out of the HPLC system as needed.

4.3.10 Fluorescence assay development

Using ethidium bromide to monitor supercoiled plasmid degradation

Supercoiled plasmid, and stress-degraded, plasmid samples were prepared at concentrations of 0.5 to 3 µg DNA/ml in TE by serial dilution of pure plasmid pSVβ DNA, and fluid stress-degraded pSVβ plasmid stocks. Based on a binding capacity of ethidium bromide to DNA of one EtBr molecule to 4 DNA base pairs, about 0.15 volumes of ethidium bromide at 3 µg/ml is required to saturate one volume of linear, double-stranded DNA at 3 µg/ml. To add an excess of ethidium bromide, either 0.2 volumes or 1.0 volumes of ethidium bromide at 3 µg/ml, was mixed with one volume (100 µL) of supercoiled or shear-degraded plasmid sample in a 96-well plate. There were four excitation wavelength filters (360, 460, 485 and 530 nm) and four emission wavelength filters (530, 570, 580 and 590 nm) that could be selected in the flourescence reader. The 16 possible combinations of filters were tested to determine the optimum combination for ethidium bromide fluorescence.

4.4 Gel electrophoresis development

Agarose gel electrophoresis is probably the most common method for measuring plasmid DNA concentration. Plasmid containing samples are typically electrophoresed at 5 V/cm in 0.8 – 1.2 % agarose gels and stained with ethidium bromide. The fluorescence of the different plasmid bands is recorded by digital camera. The fluorescence of a plasmid band of interest is compared to known standards, run on the same gel, to determine the plasmid concentration. The principal disadvantage of agarose gel electrophoresis is the significant standard deviation of the assay (typically about 20% relative standard deviation between replicate samples). Other disadvantages are the low number of samples can be assayed per gel, the low fluorescence of single-stranded DNA, and the varying fluorescence intensity of different plasmid forms.

A maximum of 40 wells was available per agarose gel (2 lanes x 20 wells per lane). Typically, a 4 point standard curve and 4 to 6 samples were loaded in quadruplicate per gel. Due to diffusion of the ethidium bromide during sample loading and during electrophoresis (ethidium bromide is charged and migrates in an electric field), it was found that staining the agarose gel

with ethidium bromide after running the gel gave significantly more consistent results. Despite running samples in quadruplicate, the standard deviations between replicate samples was high.

A significant source of error was sample diffusion from the wells of the gel during sample loading. In order to reduce sample diffusion during gel loading, low melting point agarose was added to all samples and standards, prior to sample loading. A gel loading solution, containing 4X loading dye and 1% low melting point agarose, was heated to 100°C for 3 minutes to melt the solution. The loading solution was equilibrated at 40°C and then one volume of loading solution was mixed rapidly with one volume of each sample. Each sample was immediately loaded into a well of the agarose gel. It was found that chilling the gel for 20 minutes at 4°C prior to loading, and blotting the gel with a kim-wipe to remove residual buffer in the sample wells, further reduced sample diffusion and improved assay accuracy. Loaded samples would solidify quickly in less than one minute. The gel was immersed in running buffer and run as normal. Using this technique, accurate standard curves and low standard deviations between replicate samples could be achieved. Figure 4.1 shows a typical agarose gel standard curve for supercoiled plasmid DNA using the improved technique.

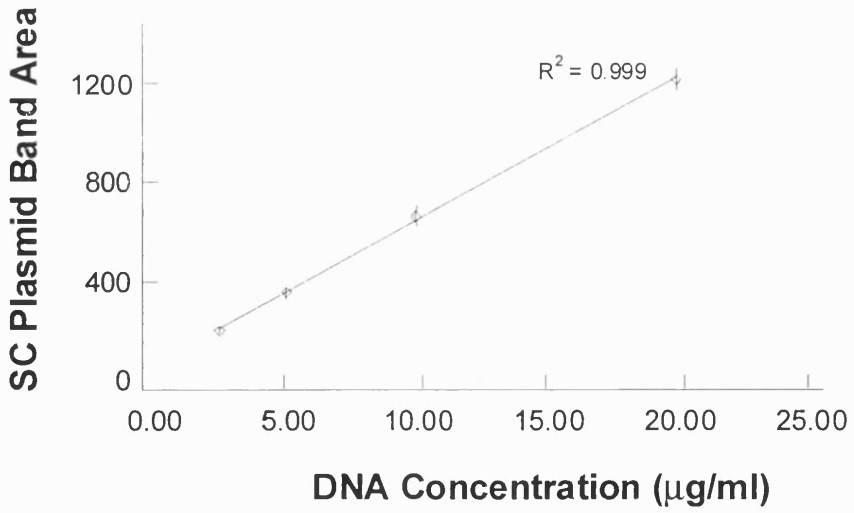

Figure 4.1 Agarose gel standard curve using improved method with low melting point agarose in samples. The error bars indicate 95% confidence intervals.

As well as measuring plasmid DNA forms, agarose gels have been frequently used to assess chromosomal DNA contamination in plasmid samples. Ciccolini et al (2002), and Nino et al (2001), both used agarose gel electrophoresis to assess chromosomal DNA contamination in alkaline lysates. The majority of chromosomal DNA in alkaline lysates is typically in single-stranded form due to the high pH during lysis. However, ethidium bromide bound to single-

stranded DNA fluoresces only weakly compared to double-stranded DNA; hence, measurement of single-stranded DNA impurities relative to double-stranded supercoiled plasmid may underestimate the amount of single-stranded impurities.

In order to assess agarose gel electrophoresis as an analytical technique for measuring chromosomal DNA, samples of double-stranded chromosomal DNA of known concentration were pH adjusted to pH 8, pH 12, pH 12.5 and pH 13, followed by renaturation to pH 8.0. The samples were then electrophoresed, stained and scanned. Figure 4.2 shows this agarose gel. There was a significant reduction in the fluorescence of the chromosomal DNA samples between pH 12.0 and 12.5, showing that chromosomal DNA denatures to single-stranded form in the pH range 12.0 to 12.5. The low fluorescence of single-stranded DNA relative to double-stranded DNA indicates that agarose gel electrophoresis is not a suitable technique for measuring chromosomal DNA contamination in alkaline lysates, where the pH of the lysate typically exceeds pH 12.0. It was concluded that using agarose gel electrophoresis and ethidium bromide staining, the amount of contaminating single-stranded chromosomal DNA could be significantly under-estimated.

Another potential source of error using agarose gels to quantify chromosomal DNA contamination was the effect of DNA size on the assay. It was observed that that shearing clarified alkaline lysates immediate prior to loading significantly increased the amount of chromosomal DNA that entered the gel. The DNA within the gel usually fluoresced significantly higher than the equivalent DNA trapped in the well. Thus, there often appeared to be increased chromosomal contamination in the sheared clarified lysates, while in fact the increased DNA in the gel was solely due to the smaller DNA fragments being able to penetrate the agarose matrix. This made gel electrophoresis particularly unsuitable for quantifying samples subjected to varying levels of fluid shear.

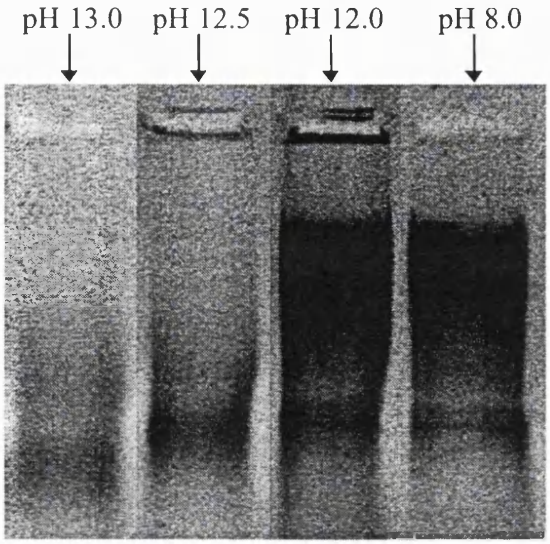

Figure 4.2 Agarose gel comparing the fluorescence of double-stranded versus single-stranded DNA by Ethidium Bromide.

4.5 Anion exchange HPLC development

Using the improved agarose gel electrophoresis technique, section 4.4, supercoiled, open-circular and linear plasmid DNA forms could be quantified. However, chromosomal DNA could not be quantified using agarose gel electrophoresis. In addition, quantification of plasmid forms using gels was labour intensive, slow, and required many replicate samples to reduce assay error. An accurate, robust and fast analytical technique capable of simultaneously measuring supercoiled plasmid DNA, non-supercoiled plasmid forms, and chromosomal DNA was required.

Anion exchange HPLC development was performed in collaboration with Pat McHugh, UCL PhD candidate. Four different anion exchange HPLC resins were screened: Poros PI and Poros HQ resins from Poros, Q-Sepharose HP from Pharmacia and NucleoPac from Dionex. All 4 resins were found to be suitable for determining total DNA concentration, but only Poros PI and Q-Sepharose were able to quantify supercoiled plasmid separately from the other DNA impurities, after sample pre-treatment.

4.5.1 Poros 20 PI HPLC

Ferreira *et al.* (1999) have recently reported the use of Poros PI (polyethylenimine) anionic exchange resin for the quantification of plasmid DNA; however, they reported that their assay did not distinguish between plasmid DNA and chromosomal DNA impurities. It was

demonstrated, in this thesis, that shallow elution gradients allowed separation of single-stranded and double-stranded DNA on the Poros PI resin. A protocol, incorporating a denaturation-renaturation step, was then developed that converted all chromosomal DNA and plasmid impurities to single-stranded form leaving supercoiled plasmid DNA double-stranded. This allowed separation, and hence quantification, of both supercoiled plasmid and DNA impurities using Poros PI resin. All HPLC was performed using a Dionex HPLC system with a 4 cm long, 1 ml volume, analytical HPLC column.

Separation of single-stranded DNA and double-stranded DNA

Ultra-pure chromosomal DNA was injected onto the Poros PI HPLC column. Figure 4.3, chromatogram 1, shows the elution peak of double-stranded chromosomal DNA during a shallow gradient elution from 0.8 M to 1.4 M NaCl over 25 minutes. The double-stranded DNA eluted as a narrow, single peak despite the size range of DNA in the sample. Pure single-stranded chromosomal DNA was injected onto the HPLC column. The single-stranded DNA eluted later than the double-stranded DNA and as a broader peak, Figure 4.3, chromatogram 2. This indicated that under the conditions used, Poros PI could separate double-stranded from single-stranded DNA species.

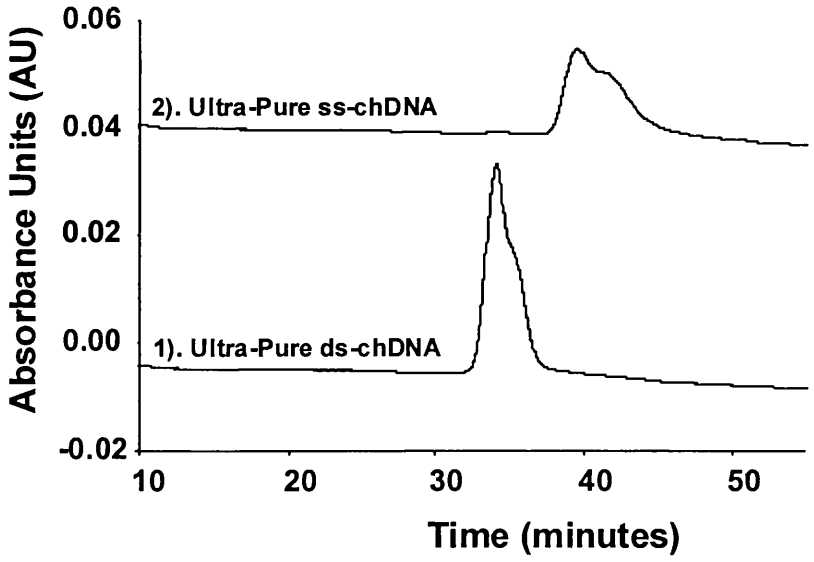

Figure 4.3 Poros PI HPLC chromatogram of ultra-pure chromosomal DNA samples. 1) Chromosomal DNA, double-stranded; 2) Denatured chromosomal DNA

Denaturation-renaturation of chromosomal and supercoiled plasmid DNA

It was demonstrated by Thatcher et al. (1997) that there was typically a pH window, between pH 12 and pH 13, where linear DNA could be denatured to single-stranded form leaving supercoiled DNA double-stranded. NaOH is used during alkaline lysis to create a high pH environment and denature DNA. Experiments were performed to determine if it was possible to irreversibly denature 100% of the chromosomal DNA to single-stranded form without any loss in supercoiled plasmid, using a specific concentration of NaOH. One volume of 0 to 0.4 M NaOH was added to one volume of supercoiled plasmid, one volume of heat-degraded plasmid or one volume of pure chromosomal DNA. After neutralisation the samples were analysed by agarose gel electrophoresis and HPLC.

Figure 4.4 shows the agarose gel after electrophoresis of heat-degraded plasmid samples denatured and renatured at different NaOH concentrations. This sample contained about 90% open-circular plasmid and about 10% supercoiled plasmid. After denaturation at a concentration of 0.04 M NaOH or above, and subsequent renaturation, all of the open-circular DNA was converted to denatured form, as shown in the agarose gel. Note the significant reduction in intensity of the denatured open-circular band, compared to the native open-circular band. This is due to the poor binding of ethidium bromide to single-stranded DNA. In contrast, below a denaturation concentration of 0.1 M NaOH, supercoiled plasmid DNA remained in its supercoiled form after the denaturation-renaturation step. It was not until higher NaOH concentrations, between 0.1 and 0.16 M NaOH, that the supercoiled plasmid DNA became irreversibly denatured and appeared as a separate band on the agarose gel. Above 0.16 M NaOH, all of the plasmid was denatured irreversibly.

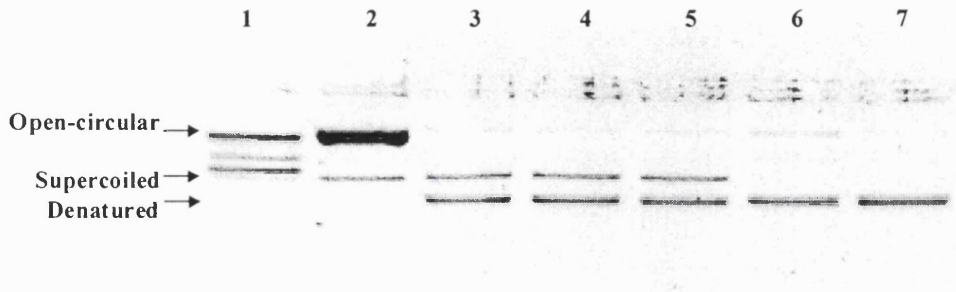

Figure 4.4 Agarose gel electrophoresis on heat degraded plasmid DNA samples, containing open-circular and supercoiled plasmid DNA. 1) λ–digest, 2) 0.0 M NaOH, 3) 0.04 M NaOH, 4) 0.08 M NaOH, 5) 0.12 M NaOH, 6) 0.16 M NaOH, 7) 0.20 M NaOH denaturation concentration.

The denatured-renatured plasmid and chromosomal DNA samples were assayed by HPLC to determine whether denatured-renatured DNA eluted in the double- or single-stranded peaks. Figure 4.5 shows the double-stranded peak area, as a function of NaOH concentration during denaturation, for three samples: i) pure supercoiled plasmid, ii) pure plasmid, 90% open-circular form, 10% supercoiled form and iii) pure chromosomal DNA. The data is plotted as the peak area relative to the peak area at 0 M NaOH denaturation concentration (C/C_0). The figure shows that below 0.1 M NaOH the supercoiled plasmid DNA eluted in the double-stranded peak on the HPLC. Chromosomal DNA and non-supercoiled plasmid variants became irreversibly denatured at lower NaOH concentrations; above 0.03 M NaOH they eluted in the single-stranded peak on the HPLC.

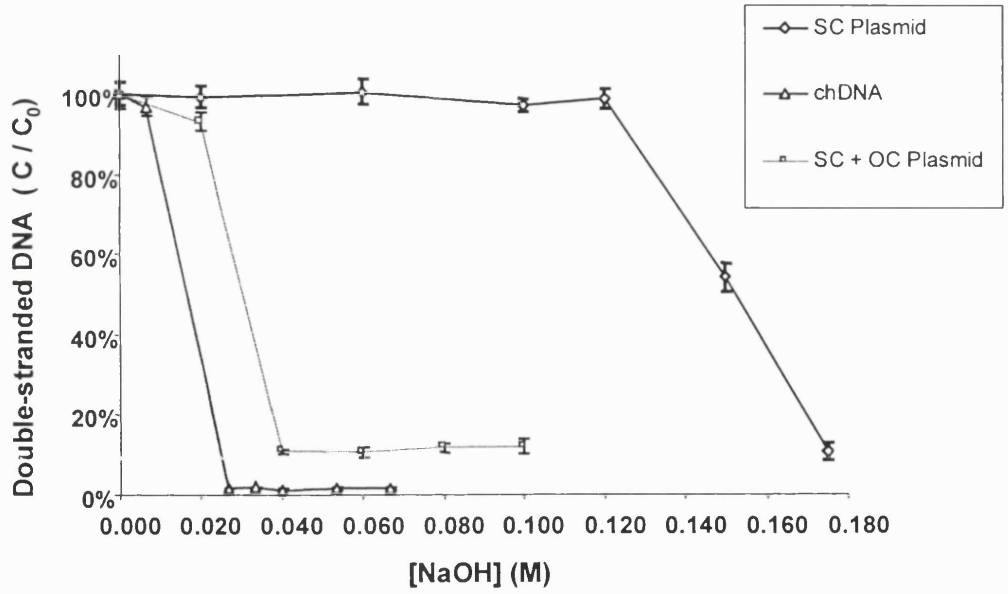

Figure 4.5 Effect of NaOH denaturation concentration on the double-stranded DNA HPLC peak.

Quantification of supercoiled plasmid DNA and DNA impurities

By denaturing plasmid DNA with NaOH between 0.03 and 0.1 M NaOH, the supercoiled plasmid can be quantified separately from the other DNA impurities (chromosomal and non-supercoiled plasmid DNA variants). Figure 4.6 shows the HPLC elution profiles of supercoiled plasmid DNA, chromosomal DNA, a mixture of supercoiled plasmid and chromosomal DNA, and the mixture after denaturation-renaturation (d/r). After injection, the column was washed for one column volume, and the DNA eluted over a 25 minute gradient. Double-stranded chromosomal DNA and supercoiled plasmid eluted at the same time, chromatograms 1, 3 and 4. After denaturation-renaturation, chromosomal DNA became single-stranded and eluted separately from the supercoiled plasmid DNA, chromatogram 2. Linear standard curves, using

ultra-pure double-stranded DNA and ultra-pure single-stranded DNA, were obtained in the range 10 μg to 0.5 μg DNA loaded onto the column, Figure 4.7.

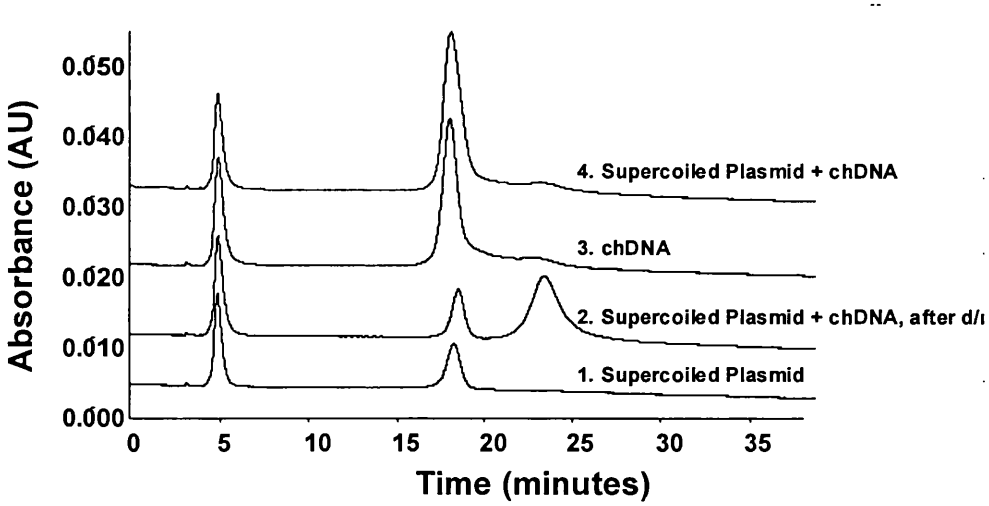

Figure 4.6. Chromatograms of supercoiled plasmid DNA, chromosomal DNA, a mixture of plasmid and chromosomal, and the mixture after denaturation to convert the chromosomal DNA to single-stranded form.

To demonstrate the utility of the assay for process samples, a clarified alkaline lysate and a clarified heat lysate (lysozyme digested followed by heat lysed at 85°C) were assayed by Poros PI HPLC. Figure 4.8 shows the HPLC chromatograms for both samples, both before and after the standard denaturation step described in Materials and Methods section. The double-stranded peak area for the alkaline-lysed sample did not change significantly following denaturation-renaturation indicating the bulk of the DNA impurities were already single-stranded. In contrast, the heat-lysed sample contained a significant amount of double-stranded DNA impurities that were converted to single-stranded DNA after denaturation-renaturation. The assay showed that the yield of supercoiled plasmid was 30% higher using heat lysis compared to alkaline lysis, in this study. Comparison of the double-stranded and single-stranded peak areas showed that the alkaline-lysed sample contained 62% DNA impurities and the heat-lysed sample contained 77% DNA impurities.

In order to verify that a window existed, between 0.03 M NaOH and 0.1 M NaOH, at which the denaturation-renaturation step could be performed, the clarified heat-lysate and clarified alkaline-lysate samples were denatured-renatured over a range of NaOH concentrations from 0 to 0.07 M NaOH, and assayed by HPLC. Figure 4.9 shows the HPLC double-stranded peak area only, as a function of NaOH concentration, for both samples. Above 0.03 M NaOH, the

double-stranded peak areas for both samples remained constant; only supercoiled DNA remained in the double-stranded peak. This demonstrated that there was a relatively wide window in NaOH concentration at which the denaturation-renaturation step could be performed.

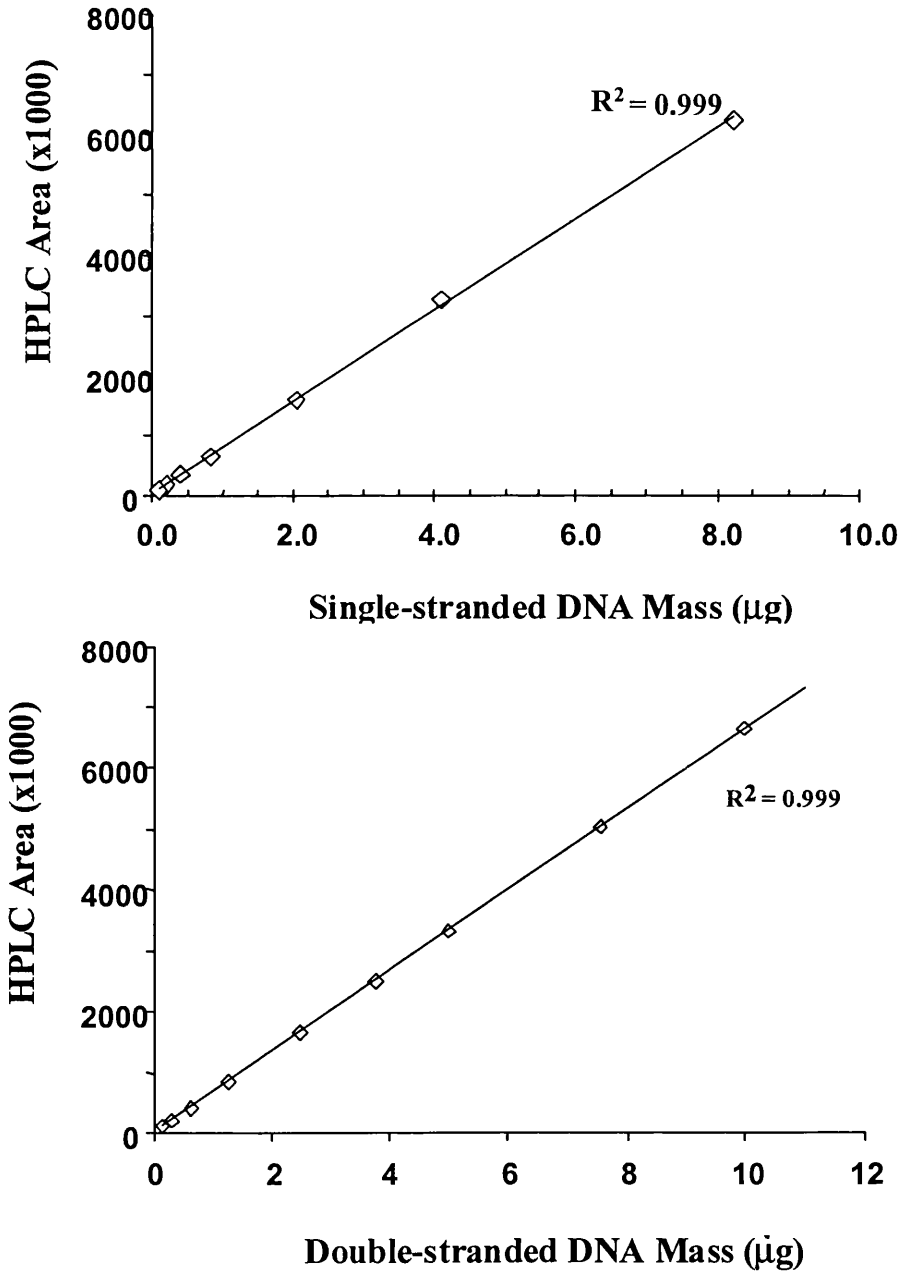

Figure 4.7 Plot showing HPLC standard curves generated using ultra-pure supercoiled plasmid DNA and ultra-pure single-stranded chromosomal DNA.

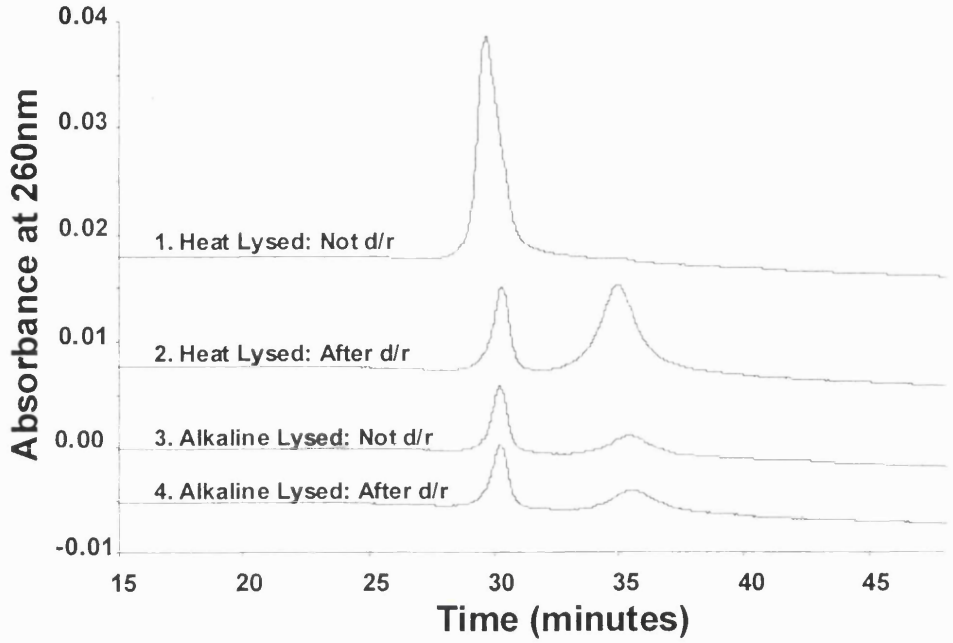

Figure 4.8. HPLC chromatograms of 4 clarified lysate samples: 1) Heat-lysed, 2) denatured-renatured heat-lysed, 3) alkaline lysed, 4) denatured-renatured alkaline lysed.

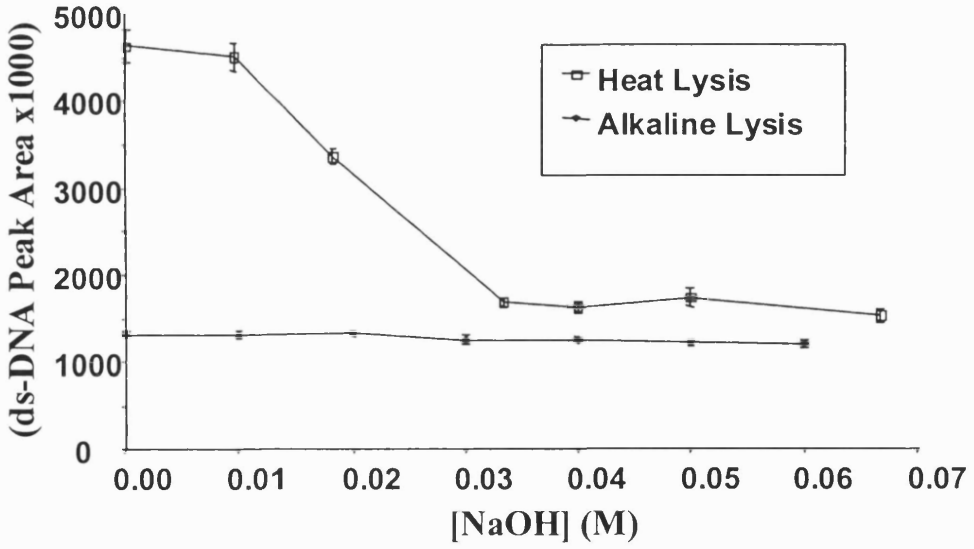

Figure 4.9 Plot showing double-stranded DNA in 2 clarified lysates, by HPLC assay, as a function of NaOH denaturation concentration: i) lysozyme and heat lysis, ii) alkaline lysis.

Supercoiled plasmid yield on HPLC

Studies were performed to determine what fraction of supercoiled plasmid injected onto the column was being recovered after salt elution. Pure plasmid pSVβ (Qiagen purified) was injected on the HPLC system without the HPLC column in place, while running with 1.6 M NaCl, 10 mM TE (elution buffer conditions). The area of the DNA peak was recorded as it passed through the absorbance detector. Pure plasmid was injected onto the HPLC column, eluted with salt, and its elution peak area recorded. The peak areas with and without the HPLC column in place were compared to determine the supercoiled plasmid yield over absorption and elution from the Poros PI column. It was determined that yield of supercoiled plasmid was only 70 to 90 % depending on batch of Qiagen purified plasmid. This lower than expected yield could have been to due to impurities still present in the Qiagen-purified plasmid solutions, giving an artificially high peak area when the column was not in place. Ultra-pure plasmid DNA (refer to section 4.3.7) was injected onto the HPLC system with and without the Poros PI column in-line. Supercoiled plasmid yields were now 99% ± 3%.

Effect of chromosomal DNA size on HPLC.

When in-process samples containing large chromosomal DNA molecules were applied to the HPLC column, a significant fraction of the chromosomal DNA did not elute from the column during the salt gradient elution. This DNA was only removed during a 0.2 M NaOH wash of the column. In contrast the yield of plasmid was almost 100%. Experiments were performed to determine if the low yield of chromosomal DNA was related to the size of the chromosomal DNA molecules. Clarified alkaline lysate samples, from wild-type cells, were subjected to fluid stress by placing each sample in a syringe and manually pushing them through a 5 cm long, 0.01" ID capillary at 3 to 6 mL/min.

Figure 4.10 shows the recovery of single-stranded DNA from the Poros PI HPLC, as a function of the number of capillary passes prior to HPLC sample injection. For this typical clarified alkaline lysate sample, the amount of DNA eluted from the HPLC column significantly increased after the samples were forced through the capillary, reaching a constant after 4 to 8 capillary passes. The 100% yield in Figure 4.10 was based on the HPLC peak area after fragmenting the chromosomal DNA by pushing the clarified lysate through a 0.007" ID PEEK capillary, 20-times, at 15 mL/min using the Hamilton syringe pump. The decreased chromosomal DNA size after shearing evidently prevents the DNA from becoming trapped in the chromatography resin or irreversibly binding to the chromatography resin.

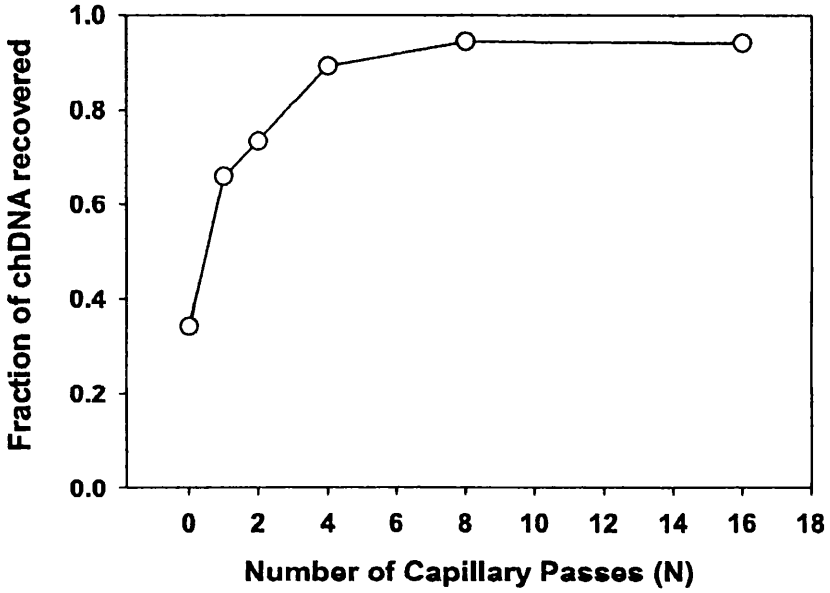

Figure 4.10. Plot of ss-DNA HPLC peak area versus number of passes through 0.007" ID PEEK capillary shear device, for a clarified alkaline lysate sample.

To accurately determine the amount of chromosomal DNA in samples using Poros PI HPLC, it is necessary to fragment the chromosomal DNA to smaller size. While fracturing chromosomal DNA, it is important not to fracture supercoiled plasmid to open-circular or linear plasmid forms. Otherwise, the amount of supercoiled plasmid could be underestimated by the HPLC assay. Figure 4.11 shows an agarose gel of clarified lysate samples containing supercoiled plasmid after manually pushing the samples through a 0.007" PEEK capillary at 3 to 6 mL/min. There was a significant reduction in the amount of large chromosomal DNA trapped in the wells of the gel after shearing the sample. After densitometric analysis of the supercoiled and open-circular plasmid bands, it was determined that plasmid pSVβ was not degraded in the 0.007" ID PEEK-syringe device at this range of flowrates. This concurs with the results of chapter 5, where it was shown that plasmid pSVb does not degrade in 0.007" ID PEEK capillaries until much higher flowrates.

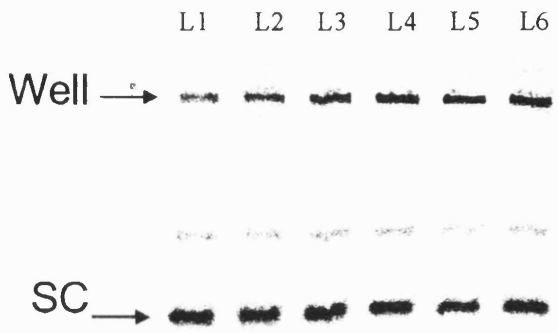

Figure 4.11. Agarose gel showing the effect of pushing a clarified alkaline lysate sample through a 0.007" PEEK capillary on supercoiled and open-circular plasmid concentration (pSVβ). From left to right: 15, 10, 6, 3, 0 syringe passes.

Quantification of RNA

RNA is the principal nucleic acid contaminant by mass in *E. coli* alkaline cell lysates. Efficient clearance of RNA is an essential requirement for any plasmid purification process. RNA can be assayed colorimetrically by orcinol assay [Sambrook et al.]; however, because the orcinol assay also measures DNA it requires subtraction of the DNA contribution to the absorbance reading. Another disadvantage with this assay is that it is prone to interference from the common lysis buffer components, sucrose. It would be advantageous to be able to quantify RNA while simultaneously measuring DNA using HPLC. A series of experiments were performed to evaluate if the Poros PI HPLC resin could be used to quantify RNA in process samples.

Clarified alkaline lysates that were RNAse-treated, and those that were not RNAse-treated, were injected onto the HPLC column at 20% buffer B (0.8 M NaCl). TE buffer was also injected onto the column. Figure 4.12 shows the chromatograms following injection and elution with an increasing salt gradient. Chromatograms 1 and 2 show that the flowthrough peak for the non-RNAse treated sample was the same as for TE buffer; all of the RNA and DNA bound to the column, along with other impurities (that absorb at 260nm). For the sample that was RNAse treated, there was a large flowthrough peak. This flowthrough peak must have been entirely due to the digested RNA, chromatogram 3. Following loading and washing, the bound DNA eluted during the salt gradient. Other impurities were removed from the column using a 0.2 M NaOH wash. Thus, by RNAse-treating all samples prior to HPLC, only RNA will elute in the flowthrough at 0.8 M NaCl load, and the amount of RNA in process samples can be determined.

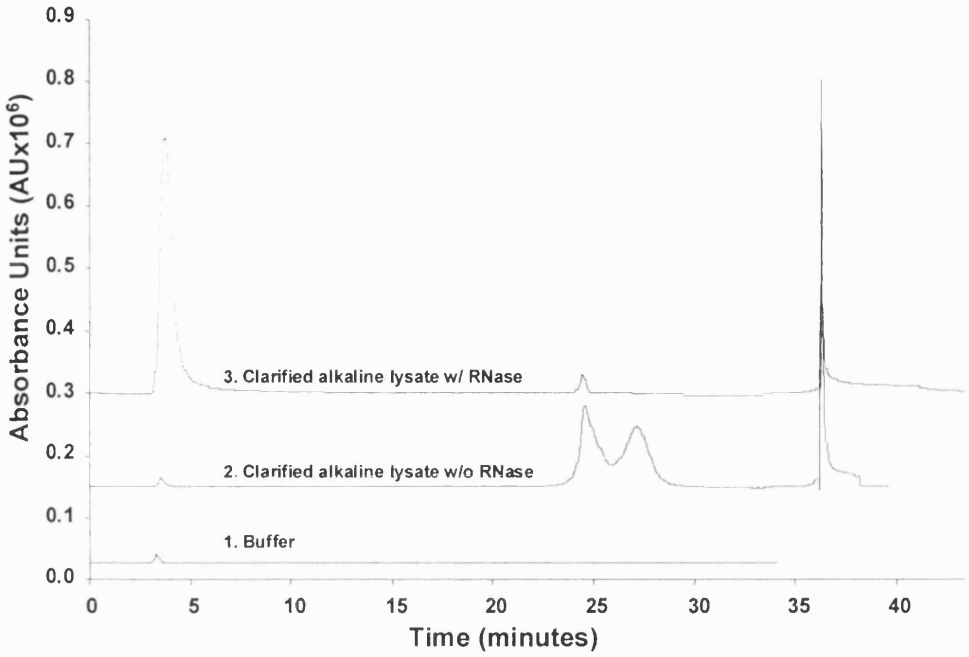

Figure 4.12 HPLC chromatograms of RNAse-treated clarified lysate (top), untreated clarified lysate (middle) and Tris-EDTA (bottom) are shown. RNAse treatment causes the digested RNA to elute as a separate peak.

A pure sample of ribosomal RNA and a clarified alkaline lysate were assayed by HPLC for RNA. The samples were assayed at a range of dilutions which confirmed assay linearity over a 20-fold dilution range, $R^2 = 0.999$ for both samples, as shown in Figure 4.13 and Figure 4.14. 100 µl of diluted sample was injected onto the column each time. The small contribution of EDTA to the flowthrough peak was determined by running a pure TE sample. The EDTA area was subtracted from the total flowthrough peak area.

An RNA spiking experiment was run to investigate RNA recovery. A clarified lysate sample was spiked with an equal volume of RNA stock solution at 0, 50 and 200 µg/ml RNA. Refer to Materials and Methods section for preparation of RNA stock solution. The samples were then isopropanol precipitated and assayed for RNA by HPLC. Each sample was repeated in triplicate. From the standard curve in Figure 4.14, the concentration of RNA in the clarified lysate was determined from the HPLC assay to be 180 µg/ml. Spike recoveries were 97% ± 9% and 107% ± 12% for the 200 µg/ml and 50 µg/ml RNA spikes respectively.

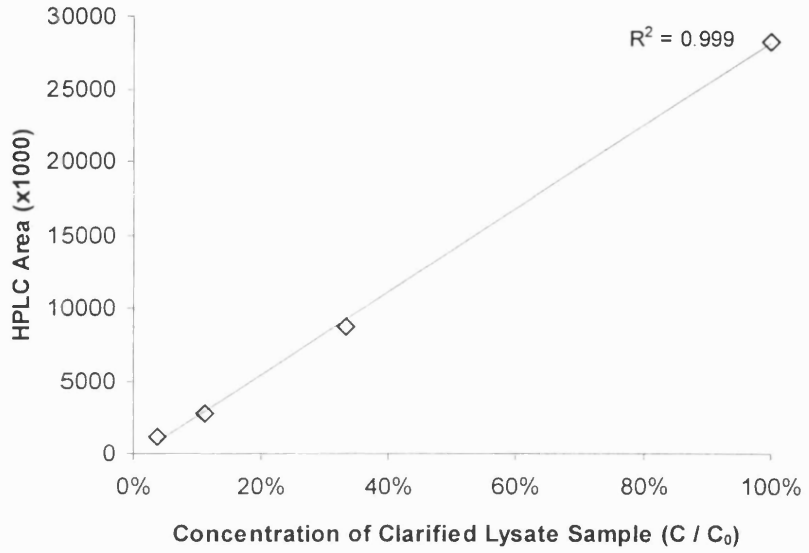

Figure 4.13 HPLC area versus sample dilution for a clarified lysate sample.

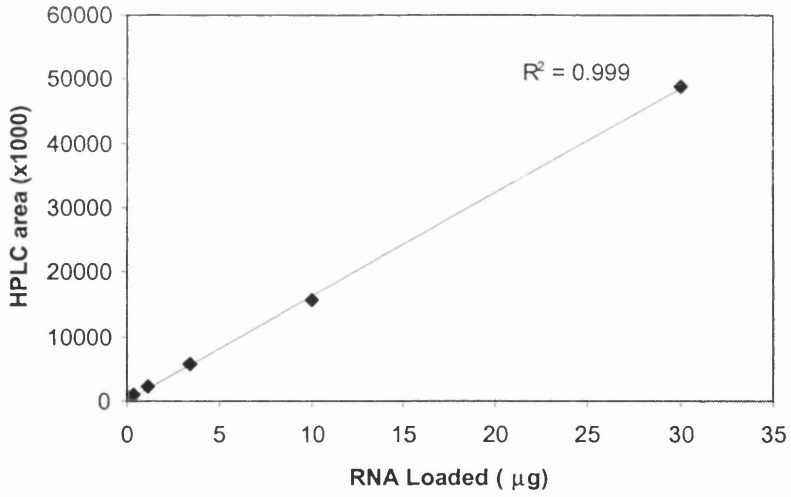

Figure 4.14 HPLC standard curve using pure ribosomal RNA. Pure rRNA at 1.8 mg/ml was digested with 0.1 mg/ml RNAse at 37 °C for 1 hr. The RNA was then diluted to varying concentrations and injected onto the column.

Assay Accuracy

In order to determine the accuracy of the Poros PI20 HPLC assay, 4 different clarified lysate samples, prepared from different frozen cell pastes and lysed at different concentrations were assayed in triplicate for RNA, ds-DNA and ss-DNA. Table 4.3 shows the HPLC areas and

relative standard deviations for the samples assayed. The relative standard deviations for RNA and DNA were 4% and 5%, respectively.

Sample	RNA	ds-DNA	ss-DNA	
1	6592	340	1058	
	7055	362	1103	
	6918	341	1135	
	3%	4%	4%	RSD
2	13661	530	1009	
	13826	515	953	
	12445	548	909	
	6%	3%	5%	RSD
3	12258	470	1088	
	12857	504	1131	
	11998	471	1082	
	4%	4%	2%	RSD
4	19473	723	1511	
	17465	789	1430	
	18641	758	1529	
	5%	4%	4%	RSD
	5%	**4%**	**4%**	**Mean RSD**

Table 4.3 Table showing the RNA, ds-DNA and ss-DNA HPLC peak areas for 4 samples in triplicate and the relative standard deviations.

Monitoring fluid stress-induced degradation of supercoiled plasmid DNA using HPLC

It has already been demonstrated that use of a suitable denaturation-renaturation step converts open-circular plasmid DNA to single-stranded form, leaving supercoiled plasmid DNA intact (refer to Figure 4.5). Hence the shear degradation of supercoiled plasmid DNA, to open-circular and linear forms, can be monitored accurately using the Poros PI HPLC assay by incorporating a denaturation-renaturation step.

4.5.2 Q-Sepharose HPLC

Ferreira et al. (1999) and Chandra (1992) have shown that Q-Sepharose resin (quartenary-amine) can be used to bind plasmid DNA and remove RNA and proteins during plasmid processing. Some clearance of chromosomal DNA was reported due to chromosomal DNA remaining on the column after the salt gradient. This resin was investigated to determine if it

could be used to separate, and quantify, plasmid and chromosomal DNA. 1 mL HiTrap columns were used for all experiments.

Preliminary experiments were done using pure supercoiled plasmid pSVβ (Qiagen-purified) and ultra-pure chromosomal DNA (DE-purified) to determine the binding conditions for DNA to Q-Sepharose resin. Figure 4.15 shows a chromatogram after injection of pure plasmid pSVβ onto a Q-Sepharose chromatography column. The column was equilibrated at 0.6 M NaCl, and the DNA was eluted with a shallow salt gradient from 0.60 to 0.85 M NaCl over 30 minutes. The fractions coming off the column were collected, IPA precipitated and run on 1% agarose gels to determine the forms of the DNA present. From injections of pure supercoiled plasmid, pure single-stranded chromosomal DNA and pure double-stranded chromosomal DNA, it was determined that double-stranded chromosomal DNA and supercoiled plasmid DNA both elute together, at about 0.8 M NaCl. When shallow elution gradients were used, open-circular DNA eluted just before supercoiled plasmid, and single-stranded chromosomal DNA eluted just before open-circular DNA. Hence, use of shallow elution gradients gave three distinct peaks: a) single-stranded DNA, b) open-circular plasmid and c) double-stranded chromosomal DNA and supercoiled plasmid. Figure 4.16 shows a standard curve generated by injecting pure supercoiled plasmid onto the Q-Sepharose column.

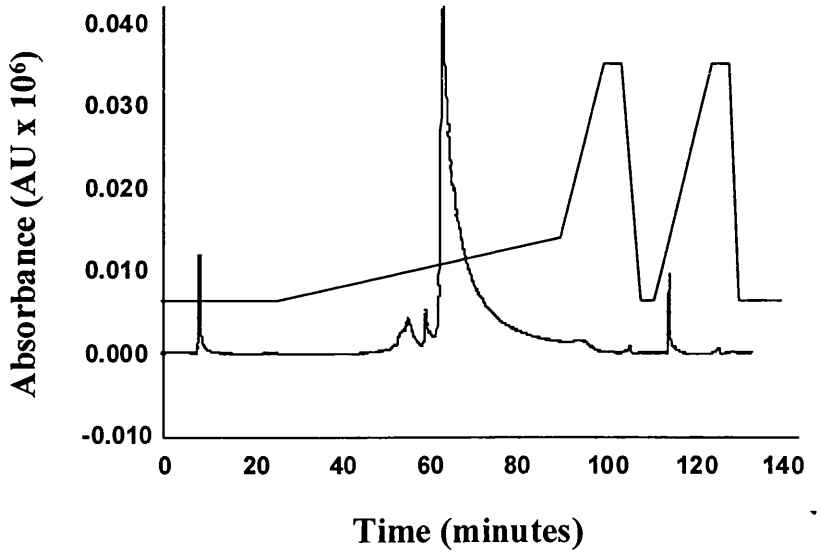

Figure 4.15 Chromatogram showing pure plasmid pSVβ injection onto Q-Sepharose HiTrap column. The large peak at 65 minutes is supercoiled plasmid and chromosomal DNA. The small peaks at 55 and 60 minutes are single-stranded DNA and open-circular plasmid, respectively.

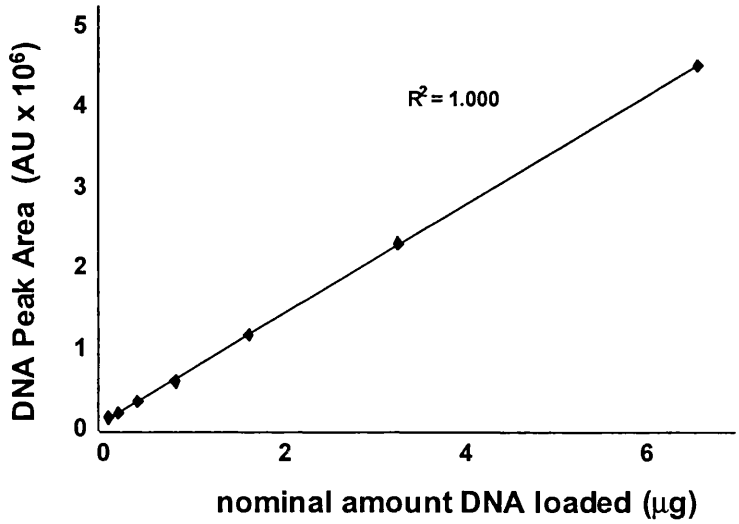

Figure 4.16. Standard curve for pure supercoiled plasmid on Q-Sepharose HPLC resin.

After determining that Q-Sepharose resin separates single-stranded DNA from supercoiled plasmid, an assay procedure was developed using a denaturation-renaturation step to convert all chromosomal DNA to single-stranded form, leaving supercoiled plasmid double-stranded. An appropriate denaturation procedure using high temperature (instead of high pH as described in section 4.5.1) was developed by P. McHugh. Further characterisation of the Q-Sepharose HPLC assay is described by P. McHugh et al., 'An HPLC Assay for Different Nucleic Acid Forms' (in progress), and, P. McHugh et al., 'Purification of DNA using Calcium Chloride', PhD Thesis (in progress).

Supercoiled plasmid and chromosomal DNA yield

Ultra-pure and pure supercoiled plasmid pSVβ was injected onto the HPLC system with and without the Q-Sepharose column in-line. Similarly to the case for Poros PI resin, the supercoiled plasmid yield, over binding and elution on the Q-Sepharose column, was determined to be virtually 100% using ultra-pure supercoiled plasmid.

Pure chromosomal DNA aliquots were placed in a syringe and manually pushed through a 0.007" ID PEEK capillary at a flowrate of 3 to 6 mL/min. Fragmented pure chromosomal DNA samples were injected onto the Q-Sepharose column, and eluted, to determine if there was an effect of DNA size on yield. Figure 4.17 shows the chromosomal DNA peak area versus number of passes though the PEEK capillary. Subjecting the DNA to high levels of fluid stress significantly increased the chromosomal DNA yield on the HPLC column. After several passes through the capillary, the yield of chromosomal DNA from the HPLC reached a constant value.

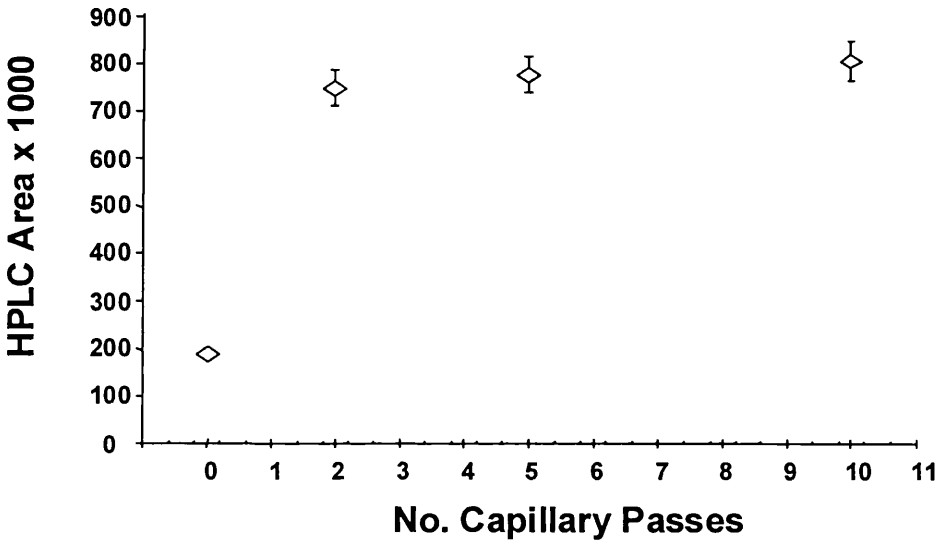

Figure 4.17. Plot of single-stranded HPLC area versus number of passes of pure chromosomal DNA through a 0.007" ID PEEK capillary for a Q-Sepharose column.

Both the Q-Sepharose and Poros PI assay procedures can accurately determine supercoiled plasmid and chromosomal DNA in process samples. The Q-Sepharose assay had the advantage that it can quantify the open-circular form of plasmid pSVβ separately from the supercoiled form. Preliminary work using a different plasmid, pQR150 (20 kb), indicated that Q-Sepharose did not separate the open-circular and supercoiled forms of this larger plasmid. Because open-circular and supercoiled plasmid forms are both double-stranded, and similar in size, any differences in binding to Q-Sepharose must be quite subtle, so it is not surprising that open-circular and supercoiled separation is size dependant. The Poros PI resin had the advantage that it could accurately quantify RNA, in contrast to the Q-Sepharose resin. Generally, the Poros PI resin was used to quantify supercoiled plasmid and DNA impurities in this thesis. This was because the resin was capable to withstanding high pressures (making it more robust to use on a day-to-day basis), because the HPLC assay time was shorter, and because open-circular plasmid levels were generally low after the alkaline lysis step. However, for cases where the amount of open-circular plasmid present was of interest, Q-Sepharose chromatography was used.

4.5.3 Poros 50 HQ and NucleoPac anion exchange resins.

Two additional anion exchange resins were investigated to determine if they could separate supercoiled plasmid and chromosomal DNA. These resins were Poros 50 HQ (quaternary amine) from Pharmacia and NucleoPac (quartenary-ammonium) from Dionex. Figure 4.18 shows a chromatogram after injection and elution of pure plasmid DNA onto a Poros HQ HPLC column. The column was equilibrated at 0.8M NaCl and the DNA eluted at 1.2 M NaCl. A linear standard curve for total DNA was obtained in the range 0.5– 10 µg/ml DNA, 100 µl injection. However, experiments with pure supercoiled plasmid and pure chromosomal DNA showed that this resin did not separate double-stranded and single-stranded DNA, or supercoiled plasmid and chromosomal DNA, effectively. Similarly experiments, using pure chromosomal and pure supercoiled plasmid solutions, showed that although NucleoPac resin could be used to quantify total DNA it did not separate single- and double-stranded DNA, or supercoiled plasmid and chromosomal DNA. Hence, no further studies were done with either Poros 50 HQ or NucleoPac resins.

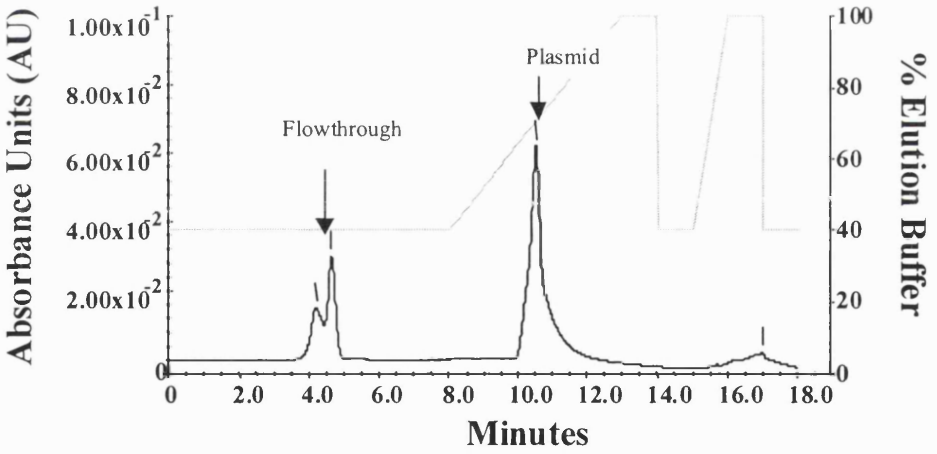

Figure 4.18 Chromatogram. Injection of 100 µl of Qiagen purified plasmid DNA (pSVβ) at 3 minutes at 40% buffer B. The plasmid is eluted in an increasing NaCl gradient at about 45 % buffer B.

4.6 Hydrophobic interaction chromatography development

Hydrophobic interaction chromatography (HIC) is potentially a highly selective form of chromatography. While assay development was proceeding with anion exchange chromatography resins, two HIC-based HPLC resins were screened as potential candidates for quantification of different DNA forms. The resins investigated were i) ToyoPearl Butyl 650 M (from TosoHaas) and ii) 5 µm silica, Lichrosorb® (Alltech, Deerfield, Il, USA).

4.6.1 Butyl resins.

TosoHaas butyl resins have previously been reported as being able to separate chromosomal DNA and plasmid DNA (Ram et al., 1999); however, details on chromatography solvents were not described, and information as to whether the chromosomal DNA was double-stranded or single-stranded was not supplied. Pure samples of plasmid or chromosomal DNA were loaded onto the Butyl column at varying salt concentrations (up to 5 M NaCl, up to 6 M LiCl or up to 5 M ammonium sulphate). For all conditions tested, the DNA did not bind to the resin. No further work was done using this resin.

4.6.2 Silica

It has previously been reported by Carter et al. (1995), Milton et al. (1998), and Melzak et al. (1996) that DNA binds to silica in the presence of concentrated chaotropic salts such as guanidine hydrochloride, sodium perchlorate or sodium iodide. Silica resin was investigated to determine if single- or double-stranded chromosomal DNA, or supercoiled plasmid DNA, had different binding characteristics to silica. The resin used was a 5 micron silica for HPLC, Lichrosorb®. Sodium chloride was investigated as the running buffer to determine if high concentrations of sodium chloride could be used to bind DNA to silica. Preliminary experiments were performed with pure plasmid DNA and pure chromosomal DNA solutions. It was determined that single-stranded DNA bound to silica at 0.8 M NaCl, pH 7.0, while double-stranded DNA bound at 1.8 M NaCl and above. It was determined that RNAse-digested RNA did not bind to silica at or below 2M NaCl. Between pH 6 and pH 8, the binding capacity increased marginally as the pH was reduced. Chromatography was run at pH 7.0.

Figure 4.19 shows a chromatogram after injection of an RNAse-treated clarified lysate onto the silica column, equilibrated at 2 M NaCl, pH 7.0. The sample was denatured-renatured using the standard protocol before injection onto the HPLC column. Running a shallow salt gradient from 2 M NaCl to 0 M NaCl, the double-stranded DNA eluted first, followed by single-stranded DNA. By incorporating a denaturation-renaturation step, supercoiled plasmid DNA could be separated from chromosomal DNA and quantified.

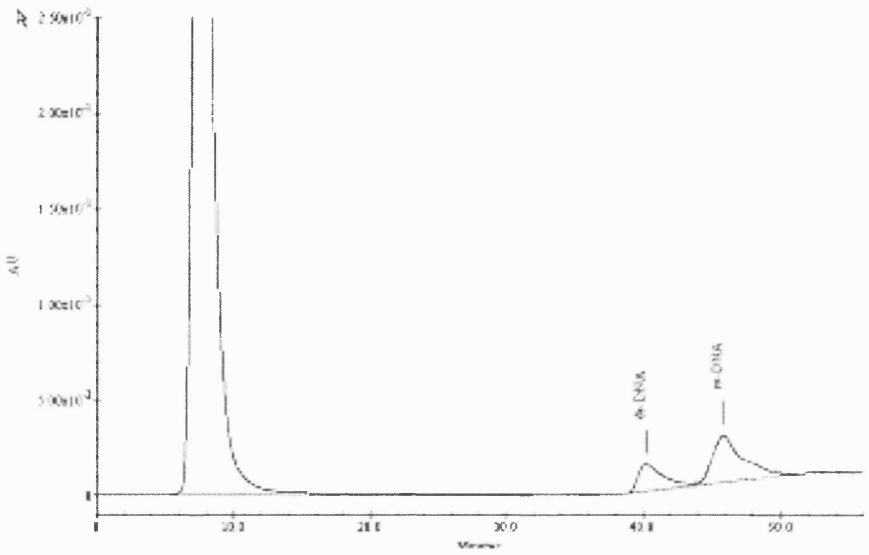

Figure 4.19. Chromatogram showing the injection of a clarified alkaline lysate onto a Lichrosorb silica column at 2 M NaCl. The column was washed for 35 minutes to elute RNA, and the DNA was eluted with a decreasing salt gradient from 2 M to 0 M NaCl.

A study was run to confirm the identity of the separate peaks eluting from the silica column, and to show that silica can be used to separate supercoiled plasmid from open-circular plasmid and other DNA impurities. The clarified lysate from the previous example and the eluate fractions from the previous HPLC run (Figure 4.19) were assayed by agarose gel electrophoresis. Figure 4.20 shows the agarose gel of the starting clarified lysate (before denaturation-renaturation) and the ds-DNA and ss-DNA eluate fractions from the silica column. The ds-DNA elute peak from the HPLC is pure supercoiled plasmid, lanes 4 and 5 on the gel. Lanes 1 and 2 on the gel are from the single-stranded DNA peak. Although HPLC shows there is at least as much single-stranded DNA as supercoiled plasmid in the sample, the fluorescence of the single-stranded DNA in the gel is very weak. This again shows that utilisation of agarose gel electrophoresis to measure chromosomal DNA can lead to significant underestimates of chromosomal contamination due to the poor binding of ethidium bromide to single-stranded DNA.

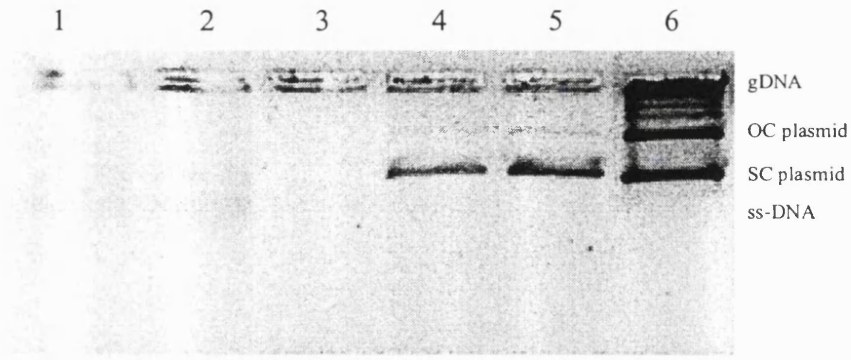

Figure 4.20. Agarose gel of clarified alkaline lysate load onto HPLC column and ds-DNA fractions (lanes 4 and 5) and ss-DNA fractions (lanes 1 and 2).

In general, because the change in salt concentration during the silica assay (from 2 M to 0 M NaCl) was larger than for the Poros PI resin (from 1 M to 2 M NaCl), the baseline was considerably flatter using the Poros PI resin. Clearance of RNA from the silica resin was slower after sample injection than compared to the Poros PI resin. For these two reasons, the Poros PI resin was used routinely rather than the silica resin.

4.7 Fluorescence assay development

It has been demonstrated that Poros PI HPLC or Q-Sepharose HPLC can be used to accurately monitor supercoiled plasmid DNA degradation. The level of quantification of the HPLC assays is about 2 μg/ml. Therefore, to monitor a 10-fold decrease in plasmid concentration during a plasmid shear degradation experiment, the initial supercoiled concentration must be 20 μg/ml. Shear experiments of plasmids in capillaries using the Rainin HPLC pumps (refer to chapter 5) required about 50 mL of solution per experiment; hence, 1 mg of supercoiled plasmid would be required per experiment, which was a considerable amount. An accurate, fast assay, capable of monitoring supercoiled plasmid DNA degradation at much lower concentrations would be highly advantageous. The fluorescence of two dyes, ethidium bromide and Picogreen, were investigated as a means of monitoring supercoiled plasmid DNA degradation in dilute solutions. An accurate, fast, fluorescence-based assay using Picogreen reagent was developed which could monitor supercoiled plasmid DNA shear degradation.

4.7.1 Quantification of sheared plasmid DNA using ethidium bromide

Ethidium bromide is probably the most commonly used flourescent marker for DNA detection and quantitation. Ethidium bromide intercalcates into the helix of double-stranded DNA, and

when bound to DNA fluoreses at 605 nm when excited by radiation in the UV range, or by visible radiation at 518 nm (Sambrook et al., 1989). When ethidium bromide intercalcates into the DNA helix, it disrupts the helix. Due to this disruption, only one molecule of ethidium bromide can bind about every 4 to 5 DNA base pairs in linear DNA. The double-helix of supercoiled plasmid DNA is already more distorted than linear DNA, and less ethidium bromide can bind. Hence, the flourescence of a solution of open-circular or linear DNA will typically be 2- to 3-fold higher than for supercoiled plasmid.

Figure 4.21 shows the flourescence of pure supercoiled plasmid pSVβ samples and stress-degraded plasmid pSVβ samples when combined with ethidium bromide. For this experiment 530 nm excitation and 580 nm emission wavelength filters were used. It was determined that this combination of filters gave the best results, in terms of assay linearity and sensitivity, of the 16 combinations tested. This combination was used for all subsequent EtBr-DNA flourescence experiments. The larger volume of EtBr gave significantly better results than the lower concentration. For the higher EtBr concentration, the assay was approximately linear over the range from 0.3 to 3.0 μg/ml unsheared supercoiled plasmid. At the higher EtBr concentration, there was some increase in flourescence intensity for the sheared plasmid samples compared to the unsheared samples; therefore there was a potential to use EtBr as a means of measuring degraded plasmid.

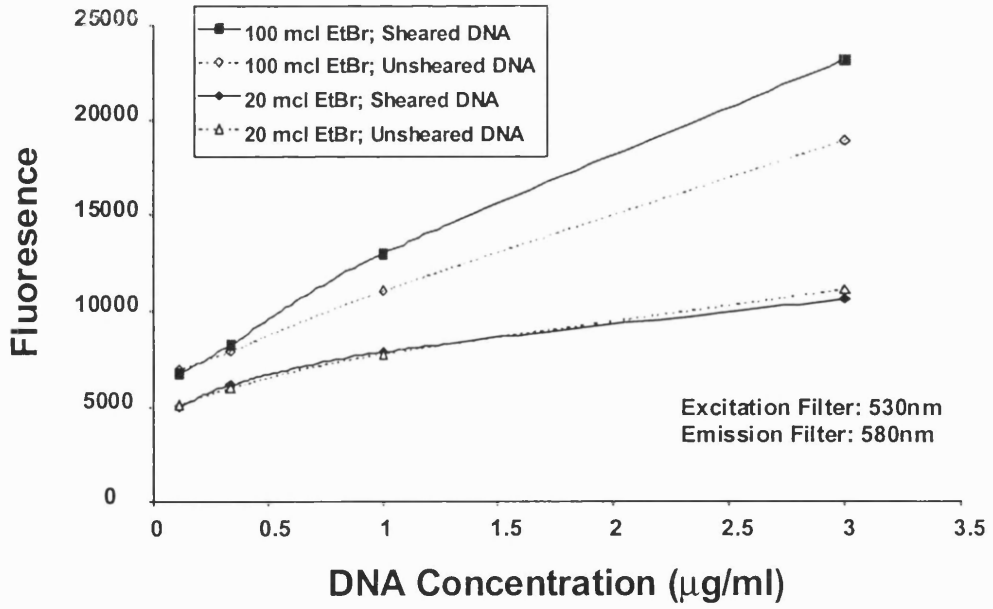

Figure 4.21. Plot showing variation in ethidium bromide fluorescence as a function of plasmid concentration.

Shear degraded plasmid samples, taken from a capillary shear degradation experiment, were assayed by EtBr assay to determine if the assay could be used to monitor supercoiled plasmid degradation. Figure 4.22 shows the flourescence, after EtBr addition, of samples taken during a capillary shear experiment. There was a moderate increase in sample flourescence with increasing degradation time, indicating increased binding of ethidium bromide to open-circular and linear plasmid forms. However, the last sample showed a decreased flourescence which was inconsistent with supercoiled degradation. Moreover, agarose gel electrophoresis showed a significant decrease in supercoiled plasmid over the course of the shear degradation experiment, while the EtBr assay predicted a moderate level of supercoiled plasmid degradation. It was concluded that the EtBr based assay was not suitable for monitoring supercoiled plasmid degradation.

4.7.2 Quantification of sheared plasmid DNA using Picogreen

Picogreen dye from Molecular Probes is a relatively new flourescent marker for DNA. It has a very high flourescence increase upon binding to double-stranded DNA, and it flouresces only weakly in the presence of single-stranded DNA. Picogreen absorption and emission maxima when bound to DNA are 502 nm and 523 nm, respectively. Picogreen has been shown to accurately quantitate DNA at extremely low concentrations, down to 50 pg/ml (Singer et al. 1997). The binding of both flourescent probes to plasmid was investigated as a means of monitoring supercoiled plasmid DNA degradation.

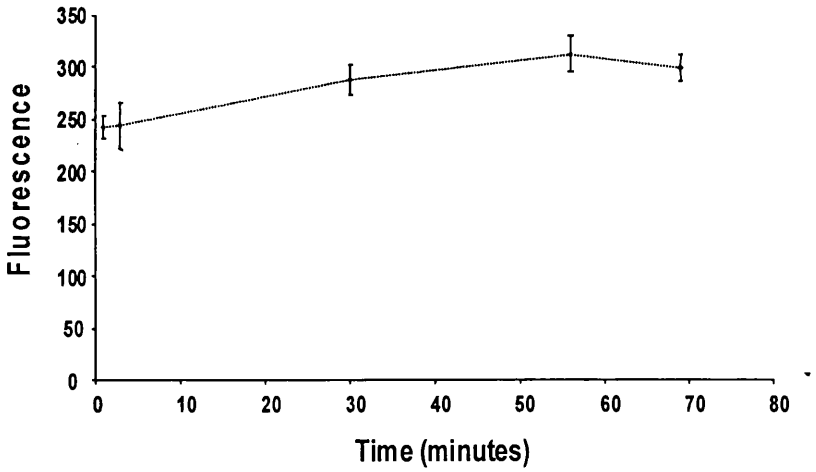

Figure 4.22. Effect of plasmid stress-induced degradation time in a capillary shear device on sample fluorescence using ethidium bromide. Samples were diluted to 1.6 μg/ml for assay. 100 μl sample + 100 μl EtBr at 2.5 μg/ml. Each sample was run in quadruplicate.

Picogreen stock reagent from Molecular Probes was diluted 1:200, and one volume of diluted stock was mixed with one volume of pure supercoiled plasmid over a range of plasmid concentrations. Figure 4.23 shows the flourescence versus supercoiled plasmid concentration. The assay is linear over the range 10 ng/ml to 500 mg/ml, as expected. Also shown is the flourescence of the samples, after denaturation-renaturation using the standard protocol described in the Materials and Methods section. There was a small decrease in flourescence indicating conversion of double-stranded DNA impurities to single-stranded form, leaving the supercoiled plasmid double-stranded.

To determine whether Picogreen dye binds and flouresces differently when bound to supercoiled plasmid versus open-circular plasmid, fluid-stress degraded plasmid samples from a capillary stress-degradation experiment were mixed with Picogreen and the flourescence measured. Figure 4.24 (top curve) shows the sample flourescence versus time during the capillary shear experiment. Although agarose gel electrophoresis predicted a moderate level of supercoiled plasmid shear degradation to open-circular and linear forms, there was no sigificant change in Picogreen flourescence between the samples (top curve). Hence, it was determined that direct measurement of the fluorescence of Picogreen in open-circular and supercoiled plasmid solutions, was not a suitable means of measuring supercoiled plasmid degradation. It appeared that there was only a small difference in Picogreen fluorescence intensity when bound to supercoiled versus open-circular plasmid forms.

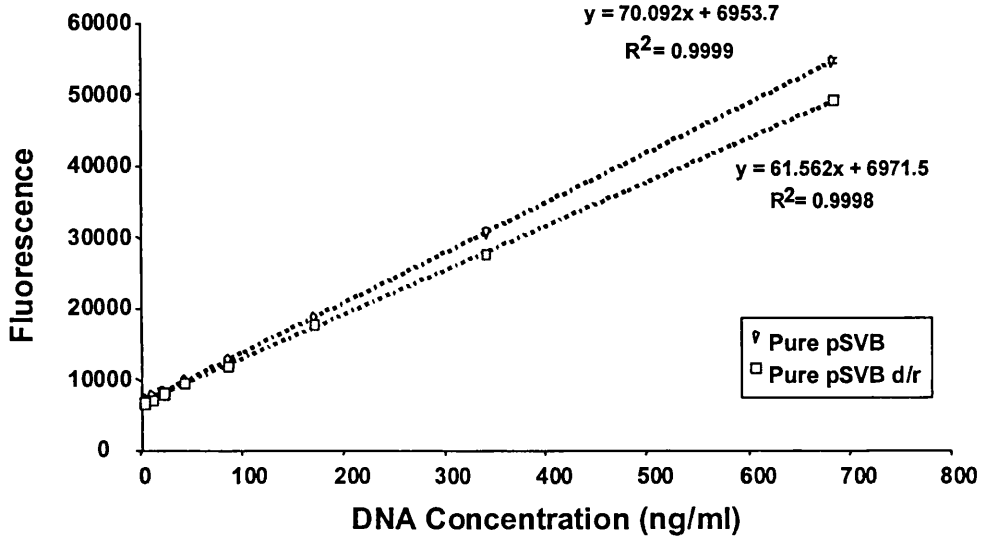

Figure 4.23. Plot showing the fluorescence of plasmid-Picogreen solutions versus shear time in a PEEK capillary.

Figure 4.24 (bottom curve) also shows the flourescence of the shear degraded samples after the samples were denatured-renatured using the standard denaturation protocol described in the Materials and Methods. It has already been demonstrated that the standard denaturation-renaturation protocol converts degraded plasmid to single-stranded forms, leaving only supercoiled plasmid double-stranded. Because the flourescence of single-stranded DNA is significantly lower than double-stranded DNA, the measured flourescence after denaturation-renaturation is predominantly the flourescence of intact, supercoiled plasmid only (with some background flourescence from the single-stranded plasmid degradates). After denaturation-renaturation, samples that had been sheared in the capillary showed a moderately reduced Picogreen flourescence, as shown in Figure 4.24, indicating moderate levels of supercoiled plasmid shear degradation, as predicted by agarose gel electrophoresis. Hence, Picogreen flourescence, in combination with the standard denaturation-renaturation step, had the potential for monitoring supercoiled plasmid shear degradation.

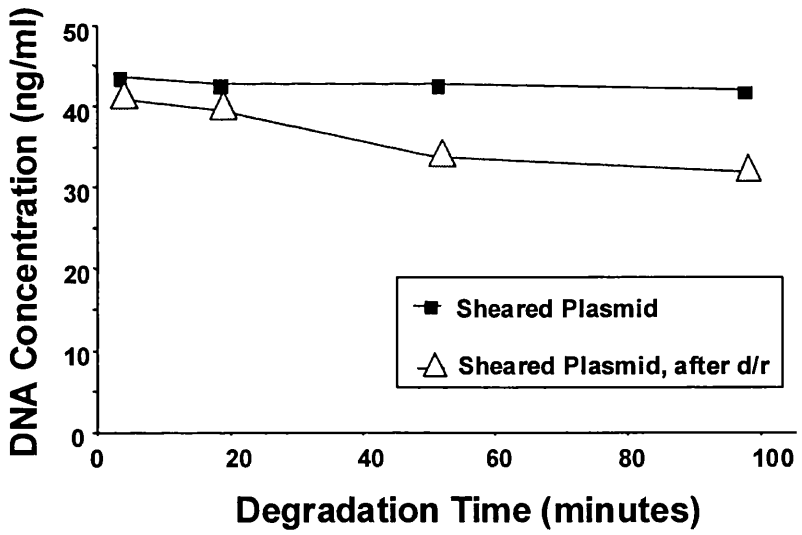

Figure 4.24. Plot showing the fluorescence of plasmid-Picogreen solutions versus shear time in a PEEK capillary.

If Picogreen is used to monitor intact supercoiled plasmid DNA, more accurate results should be obtained if the background fluorescence of single-stranded DNA is taken into account. In order to do this, it is necessary to know the ratio of the single-stranded to double-stranded DNA fluorescence, R_{DNA}. The percentage of the initial supercoiled plasmid DNA in a sample (% SC) can then be calculated from the sample fluorescence (F_{sample}) and the initial sample fluorescence ($F_{initial}$) using the following equation:

$$\% SC = \{F_{sample} - (F_{initial} * R_{DNA.})\} / (1 - R_{DNA.})$$

Equation 4.1

The fluorescence of single-stranded DNA is typically 1% to 30% of the fluorescence of double-stranded DNA, depending on the DNA concentration. The exact value can be determined from tables supplied from the manufacturer (Molecular Probes, 1998), and is plotted in Figure 4.25. Under typical DNA conditions used in these experiments, the background fluorescent of single-stranded DNA did not affect the shear degradation results significantly. The correction using Equation 4.1, did need to be applied when the supercoiled plasmid samples contained a lot of single-stranded impure DNA to begin with, or if most of the supercoiled plasmid was shear degraded during the shear-degradation experiment. In order to determine the appropriate value of R_{DNA}, all of the supercoiled plasmid was shear degraded at very high flowrate for 15 minutes at the end of each shear degradation experiment. The fluorescence of the initial undegraded samples and final fully degraded samples were compared, after denaturation-renaturation, to determine R_{DNA}. The experimentally determined values of R_{DNA} were always close to the predicted values from Figure 4.25.

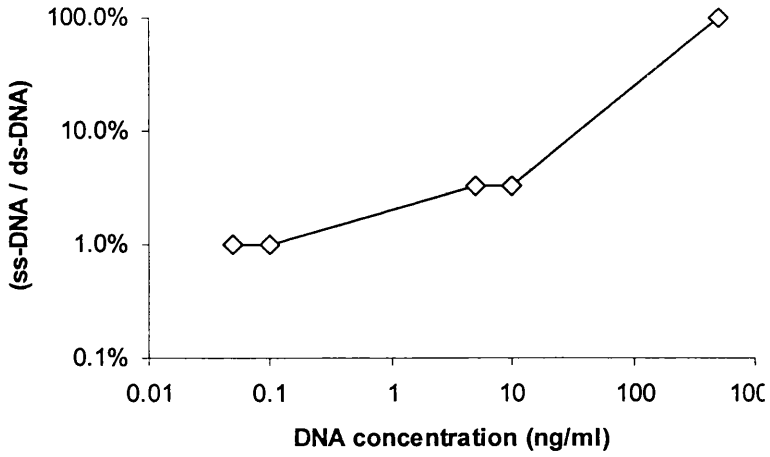

Figure 4.25. Plot showing the fluorescence of single-stranded linear DNA relative to double-stranded linear DNA as a function of DNA concentration. Data from Molecular Probes, Picogreen Assay Procedure.

In order confirm that Picogreen fluorescence, in conjunction with a denaturation-renaturation step, could accurately measure supercoiled plasmid degradation, a capillary fluid stress-degradation experiment was performed, where significant plasmid degradation was expected. Plasmid pSVβ was pumped through a 0.007" ID PEEK capillary at 50 ml/min. Samples were

collected throughout the shear experiment, and assayed by gel electrophoresis and the new fluorescence assay. Figure 4.26 shows the concentration of supercoiled plasmid DNA (as a percentage of the initial supercoiled plasmid concentration) measured by both assays. The shear experiment was run at 20 μg/ml to enable accurate quantification on an agarose gel. For gel electrophoresis, all samples were run in quadruplicate with low melting point agarose added to the samples (refer to section 4.4). For Picogreen analysis, all fluid stress-degraded samples were diluted 1000-fold, denatured-renatured, Picogreen added, and the fluorescence measured. There was excellent agreement between the results of agarose gel and Picogreen assays. This Picogreen-based assay was used to monitor most shear degradation experiments, refer to chapter 5.

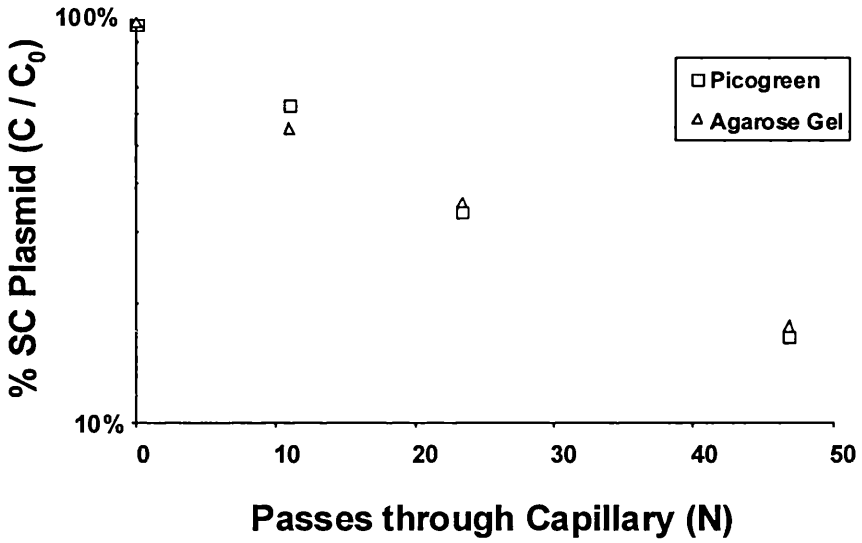

Figure 4.26 Plot showing supercoiled plasmid DNA amount versus time during capillary shear measured by both Picogreen and agarose gel.

The Picogreen assay can accurately measure supercoiled plasmid DNA at concentrations as low as 50 pg/ml. To monitor the degradation of 90% supercoiled plasmid using Picogreen, the starting concentration of supercoiled plasmid required would be 500 pg/ml. At this concentration, 100 L of solution would contain only 50 μg of plasmid DNA. Frequently, due to the high cost and lack of availability of biological products, it is not feasible to test large-scale manufacturing equipment until the equipment is actually being used to purify batches of biological product. Because this new assay can measure plasmid degradation in very dilute solutions, it is now feasible (in terms of amount of plasmid required) to monitor plasmid DNA degradation in large-scale manufacturing equipment prior to running engineering and

consistency lots. This would significantly reduce the chance of unforeseen plasmid degradation upon scale-up.

4.8 Conclusion

Novel assays were developed that enabled the analysis of experiments carried in the following four chapters on DNA stress-induced degradation, alkaline lysis, downstream processing and jet mixing.

An improved agarose gel technique was developed to improve the accuracy of agarose gels.

Two novel assays based on anion exchange HPLC were developed which were capable of separately quantifying supercoiled plasmid DNA, open-circular plasmid DNA, double-stranded chromosomal DNA, single-stranded DNA and RNA in process samples. The HPLC assays required only 0.5 μg/ml of sample per assay. The standard deviation of the Poros PI HPLC assays was 4% and 5% for DNA and RNA, respectively.

A novel assay for monitoring supercoiled plasmid shear degradation in very dilute solutions was developed based on Picogreen fluorescence and pH denaturation of plasmid degradates. This assay enabled accurate quantification of plasmid degradation rates in capillary flows. This assay has the potential to be used in conjunction with different size plasmids as a shear probe in large-scale manufacturing equipment, for cases where fluid stress fields in large-scale equipment are not well defined.

These assays were used to monitor fluid stress-induced degradation of supercoiled plasmid in chapter 5 and were indispensable in quantifying plasmid yield and purity during alkaline lysis and downstream purification in chapters 6, 7 and 8.

5 Degradation of DNA by fluid stress

One of the objectives of this thesis is to understand the influence of fluid stress on DNA molecules during the downstream purification of DNA for gene therapy. Different types of flow fields occur in different types of engineering equipment or in different regions of the same equipment. The principal types of fluid flows are shear flows, elongational flows and turbulent flows, giving rise to shear stresses, elongational stresses and fluctuating stresses, respectively. In order to predict the stress-induced degradation of DNA, it is essential to understand how different types of fluid stress affect DNA, as well as the magnitude of stress required for DNA chain scission to occur.

While a considerable amount of work has been done to understand the stretching and breaking of linear DNA under the influence of fluid stress, DNA flow induced-degradation is still not fully understood (Hunkler et al., 1996, Nguyen et al., 1992). Moreover, most of the work into linear DNA chain scission has been performed under dilute conditions where the DNA chains are not entangled. In contrast, the scission of chromosomal DNA during DNA purification occurs under concentrated conditions in upstream DNA purification processes. A limited number of studies have examined the stress-induced degradation of plasmid DNA (Levy et al., 1999; Levy et al., 2000). Substantially more work must be performed to understand plasmid stress-induced degradation.

This chapter presents the results of studies into the degradation of plasmid and chromosomal DNA under conditions of controlled fluid stress. The goal of these studies was to determine which type of fluid stress was most important in stress-induced degradation of plasmid DNA and chromosomal DNA. This chapter starts with a brief summary of results, followed by an introduction explaining the motivation for the work presented in this chapter. The materials and methods are then described in detail. This is followed by a presentation of the results of Computational Fluid Dynamics simulations of the fluid shear device, after which the experimental results using the fluid shear device are presented. This chapter concludes with a discussion of the results obtained.

5.1 Brief summary of results

To better understand the effects of fluid stress on DNA fragmentation, pure solutions of three supercoiled plasmids (6 kb, 20 kb and 116 kb) and chromosomal DNA were degraded by pumping through different diameter PEEK capillaries at varying flowrates. The effective PEEK

capillary diameters were determined from the best fit to pressure drop data in the laminar flow regime using Equation 2.21. CFD simulations were run to calculate entrance shear rates and entrance turbulent energy dissipation rates for each capillary size.

Supercoiled plasmid degradation was shown to occur at the capillary entrances and the degradation rates observed correlated well against entrance strain rate or entrance pressure drop. Plasmid degradation in the capillary was shown to be a first order reaction and the plasmid degradation rate was shown to fit the TABS model for DNA chain scission (Odell et al, 1988). Larger plasmids were significantly more susceptible to fluid-stress induced chain scission, in agreement with the results of Levy et al. (1999).

Pure chromosomal DNA, at a concentration of 150 μg/ml, was degraded by pushing it through PEEK capillaries at varying flowrates. Chromosomal DNA fragment size decreased with increasing elongational strain rate at the capillary entrance. The relationship between fragment size and strain rate, under more concentrated DNA conditions used here, was similar to that observed by Thorstenson et al. (1998), but was different to that observed by Nguyen et al. (1988). These results indicated that partial extension of the chromosomal DNA was taking place prior to chain scission. Comparing the degradation of chromosomal DNA in the chain-overlapping concentration range, used here, against the dilute concentration range used by Thorstenson et al. (1998), it appears overlapping of the polymer chains in solution did not significantly affect DNA degradation.

5.2 Introduction

To maximise plasmid yield and purity it is important to avoid both plasmid DNA and chromosomal DNA degradation throughout the downstream purification process (Prazeres et al., 1999; Marquet et al., 1995). This can be difficult to avoid, as high levels of fluid stress can occur in industrial purification equipment such as stirred tanks, chromatography columns, crossflow filters, centrifuges and pumps. High elongational stresses occur between the beads of chromatography columns, while high turbulent stresses occur in disc-stack centrifuges. Frequently, different types of fluid stress can be generated within the same piece of equipment. For example, high levels of shear stress can be generated in the boundary layers of impeller blades in stirred tanks, while turbulent stress is generated in the bulk fluid in the tank. Elongational stress occurs at the entrance to crossflow filters, while high levels of shear or turbulent stress occur within the filter. In order to avoid plasmid and chromosomal DNA degradation in large-scale process equipment, it is important to understand not only the magnitude of the fluid stresses present, but also how different types of fluid stress (shear stress,

elongational stress, turbulent stress) cause DNA degradation. Unfortunately the effects of the different fluid stresses on chromosomal is still not fully understood (Nguyen et al, 1992). Moreover the effects of fluid stresses on supercoiled plasmid DNA is even less understood, due to the limited number of studies into stress-induced plasmid degradation.

Levy et al. (1999) investigated the degradation of supercoiled plasmid in capillary device and a rotating disk device. Increasing fluid stress led to increased supercoiled plasmid degradation and larger plasmids were observed to be significantly more susceptible to stress-induced degradation. The fluid strain rates in the capillaries were calculated based on average internal strain rate for laminar flow. For plasmid pQR150 in clarified lysate, the onset of supercoiled degradation was observed at a shear strain rate of about 10^5 s^{-1}. The fluid strain rate in the rotating disk was calculated based on the average shear strain rate in the laminar boundary layer of the rotating disk. For plasmid pQR150 in clarified lysate, the onset of supercoiled degradation was observed at a shear strain rate of about 10^6 s^{-1}. Therefore, there was a very significant discrepancy between the shear strain rates at which plasmid was observed to degrade in capillaries versus in rotating disks. The residence time of the plasmid in the capillary for one pass was 0.1 s, which was similar to the residence time of the plasmid in the boundary layer of the rotating disk, after spinning the disk for 5s. Thus, the fluid stress-induced degradation of supercoiled plasmid is currently not well understood.

The vast majority of studies into chromosomal DNA chain scission have been either under laminar shear stress conditions, or under dilute polymer conditions. Most studies involving DNA degradation using laminar shear stress have been discounted due to the current understanding that shear stress alone cannot cause DNA degradation. Unfortunately the other studies, done under dilute polymer conditions, are not very applicable to DNA purification conditions. Chromosomal DNA will typically be either at higher concentrated conditions (entangled) or semi-dilute (coil overlapping), refer to section 2.4.5. Concentration can significantly affect the behaviour of polymers such as DNA (Macosko, 1994).

In order to examine the effects of the different types of fluid stresses on DNA degradation, flow degradation of DNA in capillaries was studied using plasmid pSVβ (6 kb), plasmid pQR150 (20 kb), plasmid p5176 (116 kb) and pure chromosomal DNA. Capillaries were chosen as a model flow device, because capillaries are capable of generating shear, elongational and turbulent stresses. When fluids flow through capillaries, elongational stresses occur principally at the capillary entrance, shear stresses occur within the capillary at low Reynolds numbers, and turbulent stresses within the capillary at high Reynolds numbers. It was planned that by

carefully adjusting capillary flowrates, diameters and lengths, the effects of the different types of fluid stress on DNA degradation could be differentiated.

The fluid stresses within capillaries can be calculated analytically, however exact analytical expressions for the fluid stress at capillary entrances are not available. To accurately define the fluid stresses throughout the capillary shear device, computational fluid dynamics (CFD) simulations were preformed. This chapter first describes the results CFD simulations run to characterise the fluid flows both entering and within the capillary device. Secondly this chapter describes the results of the DNA shear experiments using the capillary device.

5.3 Materials and methods for CFD simulations

All of the CFD materials and methods have been presented previously in chapter 3.

5.4 Materials and methods for capillary flow experiments

5.4.1 Equipment

A Rainin HPLC pump (Surrey, UK) with 200 ml/min pump heads, capably of running at operating pressures of 6000 psi was used for capillary shear experiments. A Hamilton syringe pump with PHD 2000 infuse/withdraw controller (Harvard Apparatus, Holliston, MA, USA) was used for capillary shear experiments. Sonication was performed using a Soniprep 150 (MSE, UK) with a Sanyo controller.

5.4.2 Capillary flow device

Capillary flow experiments were performed using 0.0025" ID to 0.02" nominal ID PEEK capillary tubing (refer to Table 5.1 for the capillaries diameters dimensions in millimeters). Solutions of plasmid or chromosomal DNA were forced through the capillaries at controlled flowrates using either a Rainin HPLC pump or using a Hamilton syringe pump. The HPLC pump was used for experiments using plasmids pSVb and pQR150, where high fluid stress levels were required to break the plasmids. High levels of fluid stress could not be generated without creating high pressure drops (> 100 psi) across the capillaries. Note, 1 bar pressure equals 14.5 psi. The HPLC pump was capable of operating at high pressure, while the Hamilton syringe pump could not operate at high pressures. The Hamilton syringe pump was used for experiments using chromosomal DNA and large plasmid p5176.

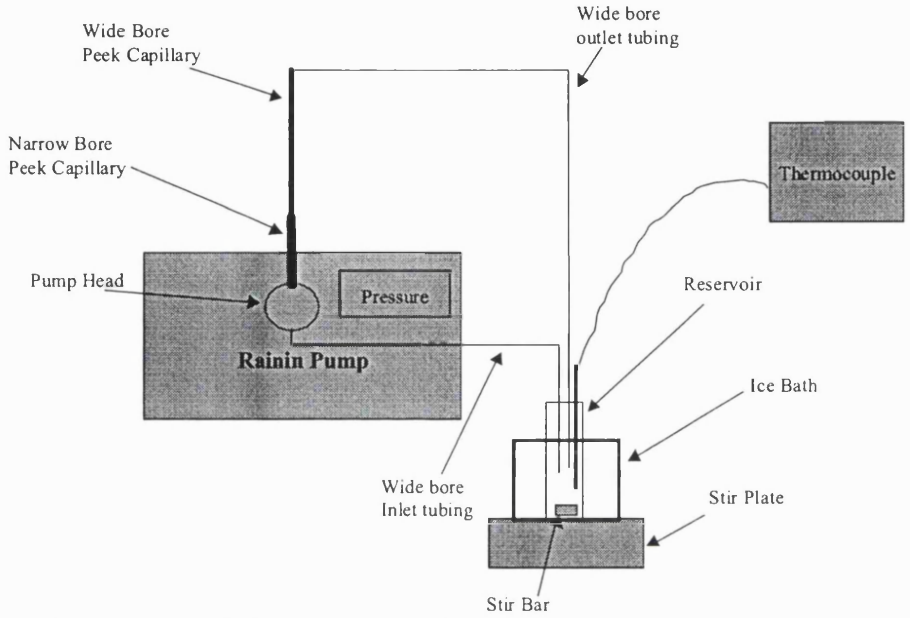

Figure 5.1. Schematic of Capillary shear device.

Nominal ID (Inches)	Nominal ID (mm)
0.0025	0.0635
0.005	0.127
0.007	0.178
0.010	0.254
0.020	0.508
0.030	0.762
0.040	1.016

Table 5.1. Nominal ID of PEEK capillaries, in inches and millimetres

Figure 5.1 shows a schematic of the capillary shear system using the Rainin HPLC pump. The DNA solution was placed in a 50 mL plastic reservoir (retentate reservoir) containing a magnetic stir-bar and thermocouple. The reservoir was placed in a water-bath which was positioned on top of a magnetic stir plate. The inlet line to the Rainin pump was wide-bore plastic tubing (0.2" ID). This tubing was placed subsurface in the retentate reservoir. A short section (2 to 12 cm length) of narrow bore PEEK capillary (0.005" to 0.010" ID) was connected directly to the outlet of the Rainin pump. Plasmid degradation took place in this short section of narrow bore capillary A longer section (20 to 150 cm length) of wider bore PEEK capillary (0.01" to 0.04" ID) was connected to the outlet of the narrow bore PEEK capillary. The purpose of this longer piece of capillary was to add backpressure to the system, reducing

cavitation effects. Finally, a piece of silicone tubing, 0.04" ID, was connected to the outlet of the wide bore PEEK tubing. The outlet of the silicone tubing was placed subsurface into the retentate reservoir. The liquid hold-up in the pump, capillaries, and tubing was 10 mls.

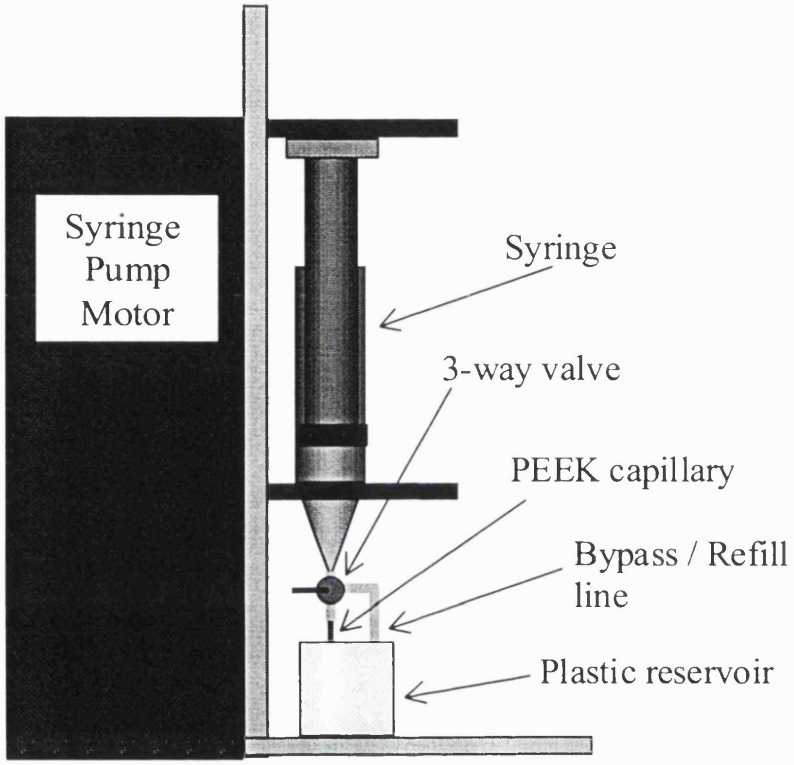

Figure 5.2. Schematic showing the capillary shear device incorporating the Hamilton syringe pump.

The apparatus using the Hamilton syringe pump was somewhat simpler, as shown in Figure 5.2. A Beckton-Dickenson plastic syringe (5 mL) containing DNA solution was placed vertically in the syringe pump. The syringe outlet was connected directly to a short section (2 cm to 12 cm) of narrow bore PEEK capillary (0.005" to 0.02" nominal ID). A short piece of silicone tubing (0.04" ID) was connected to the outlet of the PEEK capillary. The outlet of the silicone tubing was placed at the bottom of a plastic container, which collected the DNA solution after it was forced from the syringe through the capillary. The syringe pump was put in reverse at low flowrate to suck the DNA solution back into the syringe.

5.4.3 Determination of PEEK capillary internal diameter

Before running a series of fluid stress experiments with a particular nominal ID PEEK capillary, water was pumped through the capillaries at varying flowrates. The flowrate versus pressure drop across each capillary was determined from low to high flowrate using at least 3 different lengths of capillary (long, medium and short). By comparing the total pressure drop across

capillaries of different length, the internal capillary pressure drop as a function of flowrate was calculated, as well as the entrance-exit pressure drop. This is known as the Bagley method (Macosko, 1994). The actual capillary internal diameter was then determined by choosing a capillary internal diameter which gave the best fit of Equation 2.21 (internal pressure drop in a pipe), to the experimentally determined internal pressure drop data taken under laminar flow conditions (Re < 1000).

5.4.4 Standard stress-degradation procedure for Rainin capillary shear device

Set-up

The Rainin capillary shear device was set-up as shown in Figure 5.1. A narrow bore PEEK capillary (0.005", 0.007" or 0.010" nominal ID) was placed at the outlet of the Rainin pump. A long section of wider bore PEEK capillary was connected to the outlet of the narrow bore capillary. Depending on the diameter of the narrow bore capillary, a different diameter wide bore capillary was used. The nominal internal diameter of the wide bore tubing used was 0.010", 0.020" or 0.040" ID depending on whether a 0.005", 0.007" or 0.010" nominal ID narrow bore capillary was used, respectively.

Before each experiment, the system was thoroughly cleaned by placing 100 mL of 0.1 M NaOH in the retentate reservoir and recirculating the NaOH solution through the system for 10 minutes. Then the system was flushed through with 2 L of ultra-pure water, followed by 2 L of TE. All TE buffer used for capillary shear experiments was sparged for 40 minutes with helium to reduce dissolved gas in the buffer, and then filtered through a 0.2 μm filter to remove particulates. 30 mL of TE was placed in the retentate reservoir. At this point, the total volume of TE in the system was 40 mL, 30 mL in the reservoir and 10 mL hold-up in the pump and tubing. A 0.2 μm sterile filter was connected in-line to the silicone tubing downstream of the wide-bore capillary, and the TE buffer was recirculated at 5 to 10 mL/min for 40 minutes to further reduce particulates in the system. The temperature of the TE in the reservoir was monitored using the temperature probe and adjusted to 20°C ± 0.5°C throughout, by adding ice to the water bath as needed. Pure plasmid stock (pSVb or pQR150) was added to the system by filtering the required volume (typically 200 μl) through a 0.2 μm filter into the retentate reservoir, followed by a 2 mL flush of the 0.2 μm filter. The plasmid solution was recirculated at a low flowrate (1 mL/min to 4 mL/min) for 30 minutes. After this, the 0.2 μm in-line filter was removed, and the system was ready to start a plasmid stress-degradation experiment.

Operation

Preliminary stress-degradation experiments were typically performed by recirculating the plasmid solution at a fixed low flowrate for 30 minutes, and then increasing the flowrate in 30 minute increments, until a high flowrate was reached. Most stress-degradation experiments lasted 2 h to 5 h. The temperature was maintained at 20°C ± 0.5°C throughout. The pressure drop across the capillary was recorded throughout. 0.5 mL samples were taken every 2 to 30 minutes. At the end of an experiment, the plasmid was recirculated at a very high flowrate for 30 minutes in order to degrade all of the remaining supercoiled plasmid. All samples were assayed by agarose gel and/or Picogreen assay incorporating the denaturation-renaturation step.

After determining the flowrate through a capillary at which 1% to 5% degradation of supercoiled plasmid was occurring per capillary pass, a second capillary degradation experiment was performed at that constant flowrate for 2 h. Time course samples were taken throughout. At the end of an experiment, the plasmid was recirculated at a very high flowrate for 30 minutes in order to shear degrade all of the remaining supercoiled plasmid. All samples were assayed by Picogreen assay incorporating the denaturation-renaturation step.

5.4.5 Effect of capillary length on plasmid degradation rate

The effect of capillary length on supercoiled plasmid degradation rate was investigated by pumping plasmid pSVβ or pQR150 through PEEK capillaries of varying length. Plasmid pSVβ was pumped at 50 ml/min through 0.007" PEEK capillaries of 3.3 and 11.0 cm length. Plasmid pQR150 was pumped at 37 ml/min through 0.010" PEEK capillaries of 3.5 and 11.0 cm length. Samples were taken throughout and analysed for supercoiled concentration by agarose gel electrophoresis and/or Picogreen fluorescence. For each plasmid, the first set of experiments was run using the longer capillaries. Then the capillaries were cut to about 3 cm. The capillaries were cut in-place; they were not removed from the system. This ensured that the entrance section of each capillary was not varied in any way between the long and short capillary experiments.

5.4.6 Control 1: Testing for cavitation

Monitoring the change of KI absorbance in the capillary shear device

Cavitating systems produce free radicals, and free radicals are known to rapidly degrade DNA (Fuciarelli et al., 1995). Monitoring the absorbance of a recirculating potassium iodide solution is a standard test for cavitation (Lander et al., 1999). Free radicals formed by cavitation react with the iodide ions in potassium iodide to form molecular iodine, which absorbs at 500 nm. A solution of 3M potassium iodide (KI) was prepared by dissolving the required amount of

potassium iodide powder in ultra-pure water. A 30 mL solution of 3 M KI was placed in the retentate reservoir of the capillary shear device and using the Rainin HPLC pump was recirculated through the system for 2 h. At first, the solution was recirculated at a low flowrate and then approximately every 20 minutes the flowrate was increased until a high flowrate was reached. Samples of KI solution were taken every 5 minutes and their absorbance at 500 nm measured. This procedure was performed 3 times for 0.005, 0.007 and 0.010" nominal ID PEEK capillaries. The high and low flowrates used were chosen to extend above and below the range of flowrates used during plasmid degradation experiments.

Sonication of supercoiled plasmid

Sonication of a solution is a standard method of producing cavitation (Fuciarelli et al, 1995). To examine the effect of cavitation on supercoiled plasmid, solutions of pure plasmid pSVβ, at 10 μg/mL in TE buffer, were sonicated at 20 kHz by placing a sonic probe into a 10 mL plasmid solution in a plastic tube. The plasmid was sonicated for different lengths of time, and at different amplitudes. After sonication, the plasmid solutions were assayed by Picogreen fluorescence and agarose gel for supercoiled plasmid degradation.

Sonication of Potassium Iodide

As control experiments, solutions of 3 M KI were sonicated at 20 kHz by placing a sonic probe into 10 mL of KI solution and sonicating for different lengths of time, and at different amplitudes. After sonication, the absorbance of the samples at 350 nm was measured. As additional controls, solutions of ultra-pure water were also sonicated and its absorbance at 350 nm measured.

Effect of backpressure on plasmid degradation in Rainin capillary device

Increasing the overall liquid pressure throughout the flow system can usually eliminate cavitation, such that the pressure of the liquid always remains well above its vapour pressure. In order to check that a small level of cavitation was not playing a significant role in plasmid degradation, a wide bore (0.01", 0.02" or 0.04" ID) capillary was placed immediately downstream of the narrow bore capillary. By using different lengths of this 'backpressure' capillary, the backpressure could be increased by 10 psi to 140 psi. This increased the pressure upstream, which should have reduced cavitation if any cavitation was occurring, as a backpressure of 1 atmosphere (14.6 psi) is usually sufficient to stop cavitation. Plasmid degradation rates within the Rainin capillary device were determined for different levels of backpressure to determine if cavitation was causing plasmid degradation.

5.4.7 Control 2: Testing for plasmid degradation outside of capillary

The rate of plasmid degradation in the Rainin capillary system was determined with the narrow bore capillaries removed. The rest of the capillary system was left in place, including the wide-bore backpressure capillary, 0.02" nominal ID. This experiment was performed to check that supercoiled plasmid was only being degraded in the narrow bore capillary and not elsewhere in the system. Plasmid pQR150 was recirculated through the system at varying flowrates for several hours. The highest flowrates tested were well above the flowrates used in typical plasmid degradation experiments. Samples were taken throughout and tested for supercoiled plasmid degradation.

5.4.8 Standard stress-degradation procedure for Hamilton capillary shear device

Set-up

The syringe pump capillary-shear device was set-up as shown in Figure 5.2. A 5 mL Beckton-Dickenson plastic syringe was placed in the syringe pump and connected to the inlet of a 3-way valve. The valve had 2 outlets, one outlet was connected to a short piece of narrow bore capillary (0.005", 0.07", or 0.010" nominal ID). Before each run the syringe, capillary and silicone tubing was flushed with 50 mL of 0.1 M NaOH, 0.5 L ultra-pure water and 0.3 L TE buffer.

Operation

The system was emptied of liquid and the DNA solution to be stress-degraded was placed in the reservoir. Typically 2 ml of DNA solution was degraded per experiment. Chromosomal DNA was used at a concentration of 150 μg/ml; large plasmid p5176 was used at a concentration of 5 μg/ml. Because the Hamilton syringe pump was used to degrade either chromosomal DNA or plasmid p5176, the starting DNA was not sterile filtered, as the large DNA would not have passed freely through a 0.2 μm filter. The DNA solution was sucked into the syringe via the bypass line. Then the 3-way valve was switched to the capillary outlet, and the syringe pump forced the DNA solution through the capillary at a specified fixed flowrate into the retentate reservoir. This was repeated 10- times at a fixed flowrate, after which the flowrate was increased, and the procedure repeated. 100 μL samples were taken after each capillary pass. The temperature of the retentate was room temperature, which was 22°C ± 2 °C.

5.5 CFD simulation results

The capillary geometry that was modelled was chosen to be identical to the geometry of the laboratory shear device. All capillary systems consisted of a wide bore capillary coming directly from the pump making a sharp connection with a much narrower bore capillary where DNA degradation took place. Details of the capillary geometry and fluid flow models are described in chapter 3.

5.5.1 Grid size convergence

A grid size convergence study was performed for the capillary model consisting of a 0.062' capillary constricting to a 0.007" capillary, refer to Figure 3.4. The Low Re κ–ε turbulence models was used for all simulations. The flowrate was set at 50 ml/min. Initial simulations were run using coarse grids, followed by simulations with progressively finer grids. Because the simulations were being run to determine the entrance elongational shear rates and the entrance pressure drops, the convergence of these two fluid properties was monitored as the grid size was reduced. Figure 5.3, Figure 5.4 and Figure 5.5 show the effect of grid size on the entrance pressure drop; the entrance turbulent energy dissipation rate, and the entrance elongational strain rate. The three flow properties converged to constant values using 30 micron grids or smaller. The 30 micron grids were used for all subsequent simulations.

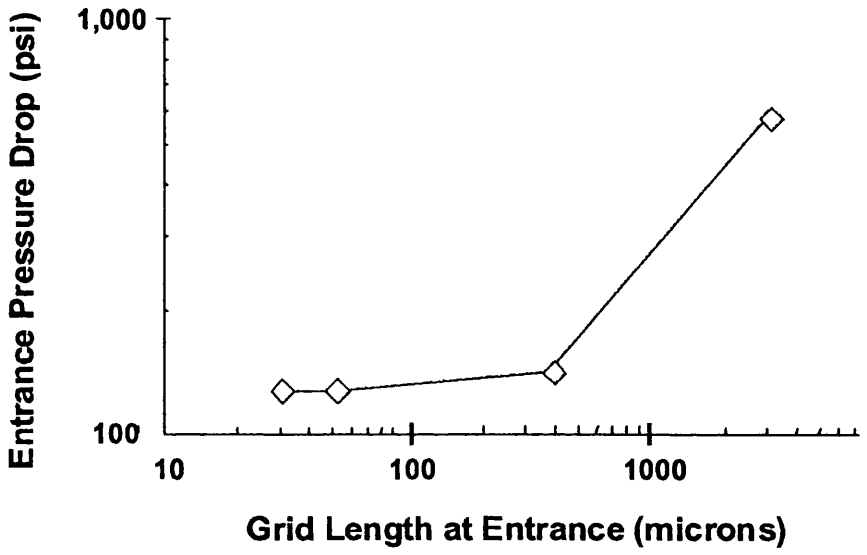

Figure 5.3. Plot from CFD simulation showing the effect of grid size on CFD calculated entrance pressure drop for flow from a 0.062" ID capillary into a 0.007" ID capillary at 50 ml/min, using the Low Re K–ε model.

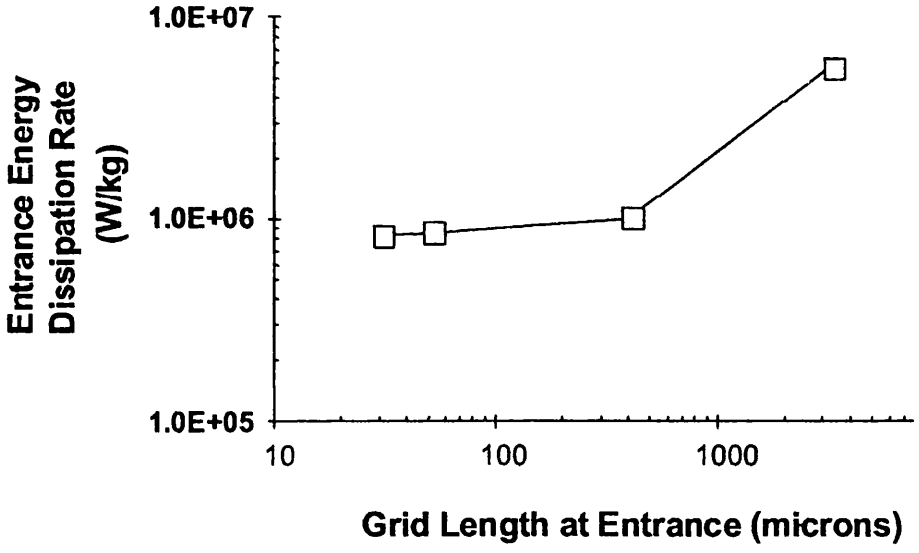

Figure 5.4. Plot from CFD simulation showing the effect of grid size on CFD calculated entrance energy dissipation for flow from a 0.062" ID capillary into a 0.007" ID capillary, at 50 ml/min, using the Low Re κ–ε model.

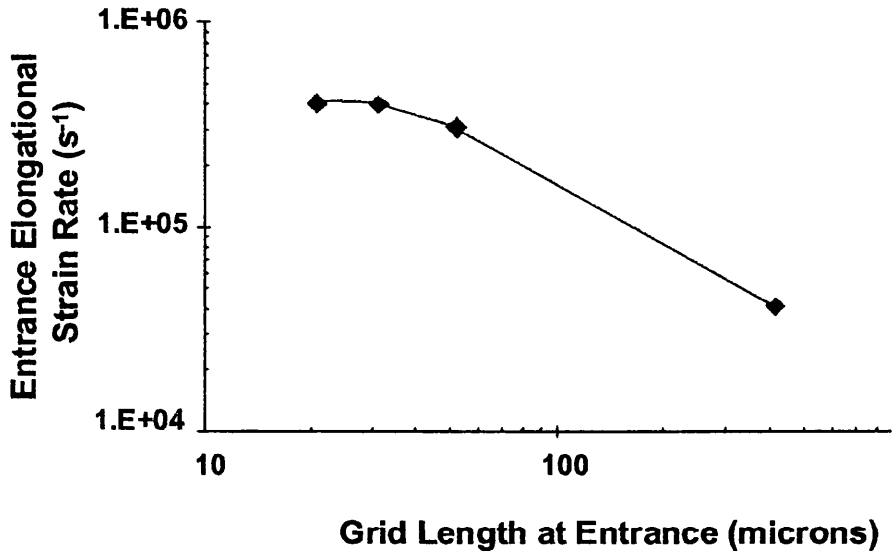

Figure 5.5. Plot from CFD simulation showing the effect of grid size on CFD calculated entrance elongational strain for flow from a 0.062" ID capillary into a 0.007" ID capillary, at 50 ml/min, using the Low Re κ–ϵ model.

5.5.2 Comparison of CFD results with analytical predictions.

In order to check the CFD simulation was giving meaningful results, the CFD predictions for the model consisting of a 0.062" capillary contracting into a 0.007" capillary were compared to analytical predictions. Analytical expressions were available for the pressure drops and strain rates within the system. The approximate strain rate at the entrance to the capillary and within the capillary is given by Equation 2.19 and Equation 2.20. The approximate pressure drop within, and at the entrance to, the capillary is given by Equation 2.21 and Equation 2.22. These predictions were compared to the CFD predictions, as shown in Table 5.2. The simulated results closely matched the analytical results, showing that the CFD simulations were converging to realistic results.

Flow Parameter	Unit	CFD Simulation	Analytical Calculation
Flowrate	ml/min	50	50
Reynolds no.	N/A	6000	6000
Entrance ΔP	psi	128	[2]128
Internal ΔP	psi	2016	1790
Entrance ϵ'	s^{-1}	3.0×10^5	[1]3.5×10^5
Internal γ'	s^{-1}	6×10^5	5×10^5

Table 5.2. Comparison of CFD results with analytically determined results. [1] Assuming an entrance angle of 73 degrees, as predicted by the CFD simulation. [2] Using a discharge coefficient of 0.80 for a converging flow into a short tube.

CFD calculated pressure drop

The CFD pressure drop was determined from the CFD results file. Figure 5.6 shows the fluid pressure along the centreline of the capillaries from the CFD results file. Within the wide bore capillary (0.062" ID), from 0 to 10 cm, the pressure remains high. There is a sudden decrease in pressure as the flow constricts and enters the small capillary at 10 cm; this sudden drop in pressure was taken to be the entrance pressure drop. There was a steady decease in fluid pressure along the length of the narrow capillary from 10 to 20 cm.

The CFD simulated entrance pressure drop as a function of flowrate is plotted in Figure 5.7 for the 0.062" to 0.007" capillary system. Results from simulations using both the laminar and Low Re κ–ε models are shown. The CFD simulated pressure drop using the Low Re κ–ε model gives a lower entrance pressure drop than the laminar flow model. This is not surprising, as the experimentally measured coefficients of discharge typically decreases as turbulence increases (Coulson et al., 1991), so the model which accounts for turbulence should give a lower entrance pressure drop.

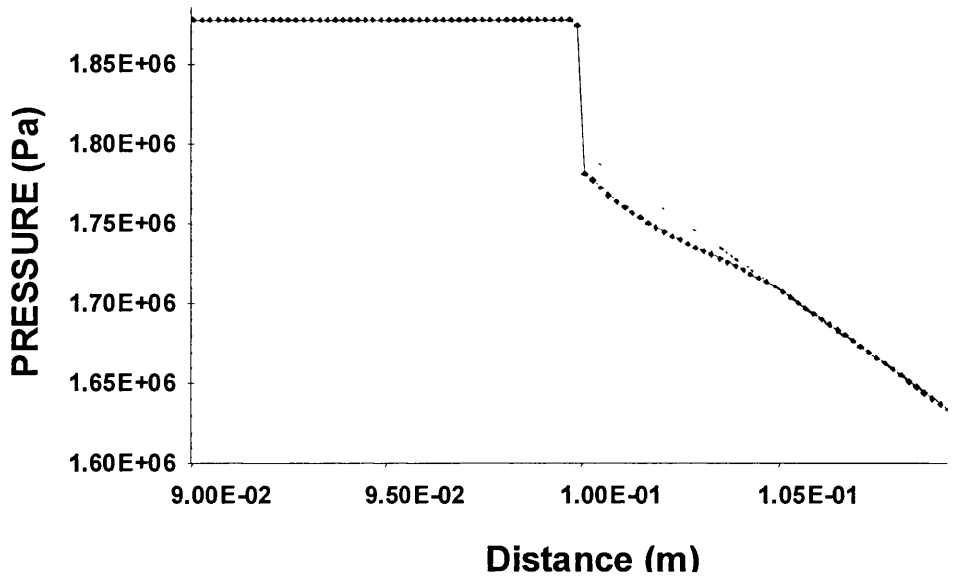

Figure 5.6. Typical CFD simulated centreline pressure for the 0.062" ID, 10 cm capillary going to a 0.007" ID, 10 cm capillary.

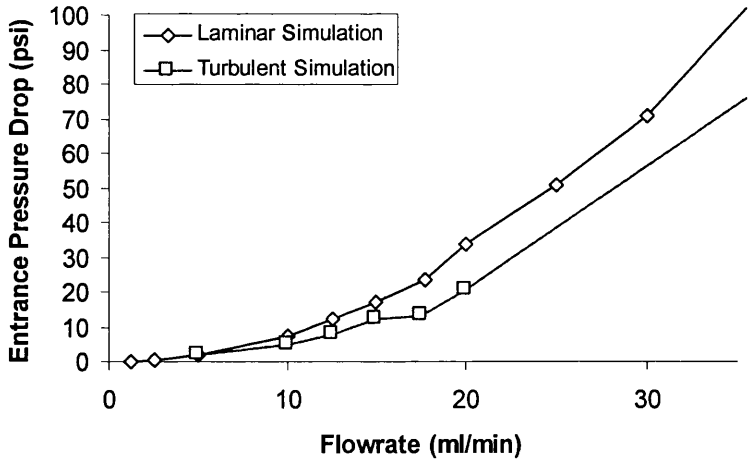

Figure 5.7. CFD simulated entrance pressure drop for 0.007" PEEK capillary

CFD calculated streamlines

The flow streamlines from the large to the small capillary was determined by CFD simulation at several different flowrates. Figure 5.8 shows the CFD simulated streamlines for flow into the capillary, at 50 ml/min, using the Low Re κ–ε turbulence model. From the fluid streamlines,

90% of the fluid enters the capillary within an angle of 73° to the capillary centreline for this flow condition.

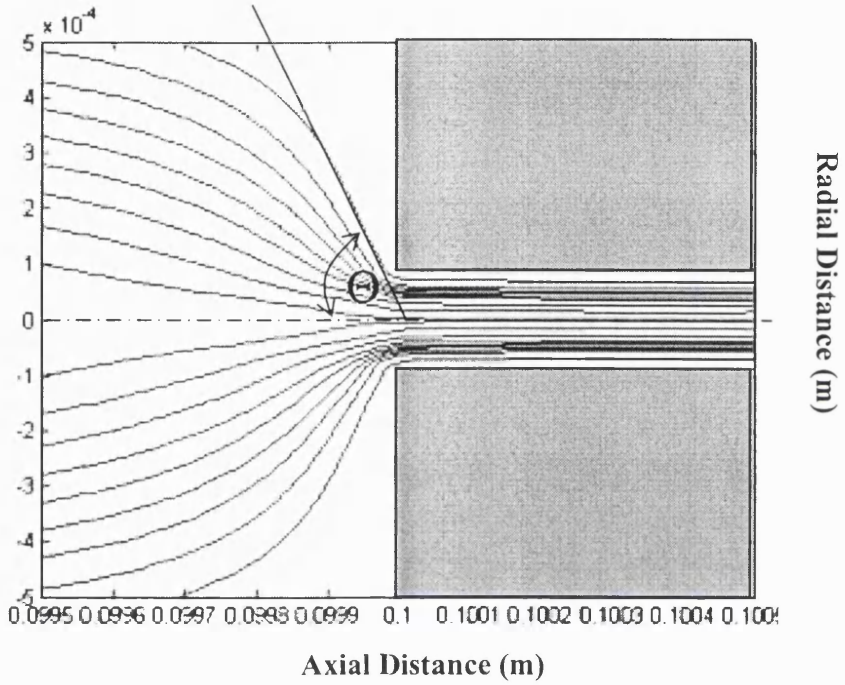

Figure 5.8. CFD simulated streamlines for 0.007" capillary at 10 mL/min flowrate, using the laminar flow model. Θ is the half-cone angle at which 90% of the fluid flows into the capillary entrance.

CFD calculated strain rates

The fluid strain rate at the entrance to, and within each capillary, was calculated from the fluid velocity vectors at the end of the CFD simulation. The total fluid strain rate was comprised of the elongational strain rate and the shear strain rate. The total, elongational and shear strain rates can all be calculated separately from the velocity vectors. Hence, the type and magnitude of fluid strain rate can be determined at any point in the flow domain. For details of the strain rate calculations refer to section 3.6.1. Figure 5.9 shows a contour plot of the strain rate within the 0.062" to 0.007" capillary system at a flowrate of 10 mL/min. As shown in the figure, there is a region of high strain at the entrance to the capillary, $6x10^4$ s^{-1}, and a higher strain rate of 7e5 s^{-1} within the capillary. Breaking down the total strain rate into the elongational and shear components, it can be shown that the entrance strain rate of $6x10^4$ 1/s is almost entirely elongational, while the strain rate against the internal capillary walls is almost entirely shear.

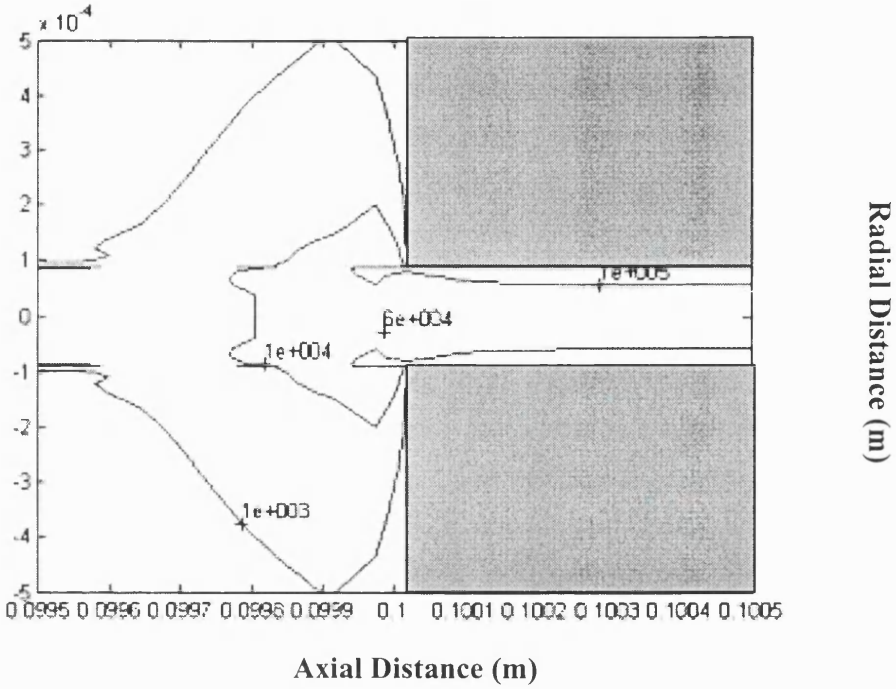

Figure 5.9 shows a contour plot of the strain rate within the 0.062" to 0.007" capillary system, at a flowrate of 10 ml/min, using the laminar flow model.

CFD calculated turbulent energy dissipation

The turbulent energy dissipation, determined by CFD simulation, is shown as a contour plot in Figure 5.10. The highest levels of turbulent energy dissipation occur along the capillary walls, however, there is also a high region of turbulent energy dissipation at the capillary entrance.

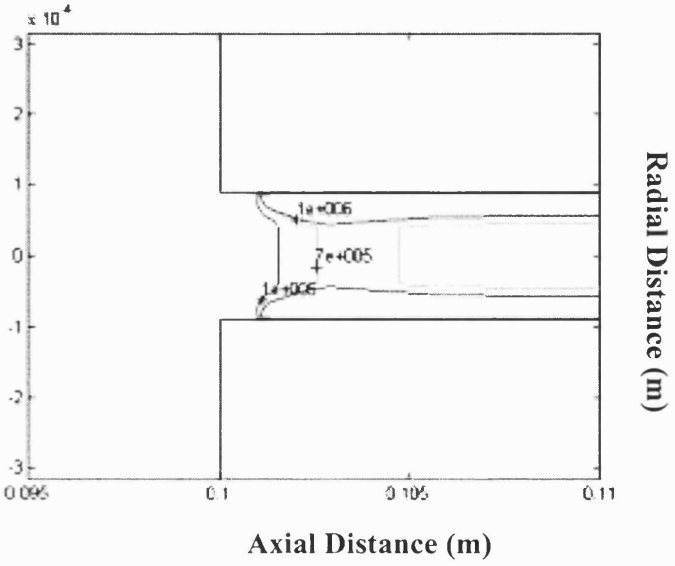

Figure 5.10. Contours of energy dissipation in 0.007" capillary system 50 ml/min

5.5.3 Effect of capillary diameter on fluid stress and entrance pressure drop

A set of simulations were performed using the Low Re κ–ε turbulent model, for three capillary diameters and a range of fluid velocities, to determine elongational strain rates and pressure drops as a function of capillary diameter.

Entrance elongational strain rate

Figure 5.11 shows the maximum elongational strain rate at the capillary entrance as a function of flowrate for the 3 capillary systems: 1) 0.062" to 0.010", 2) 0.062" to 0.007" and 3) 0.062" to 0.005". The CFD simulations predicted linear increase in elongational strain rate with increasing flowrate. Figure 5.12 shows the same elongational strain rate data re-plotted in dimensionless form against Reynolds number. By scaling the dimensionless strain rate (ε'r/u) by the square root of the ratio of the capillary diameters, $\sqrt{(d_i/d_o)}$ and re-plotting versus Reynolds number, all the data falls on a single curve.

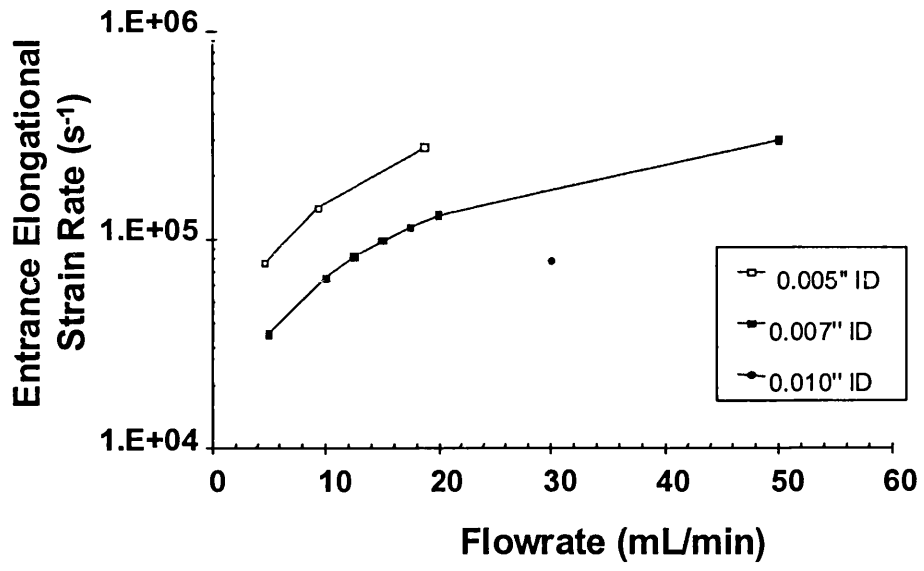

Figure 5.11. Plot showing the elongational strain rate at the entrance to the capillary versus the Reynolds number

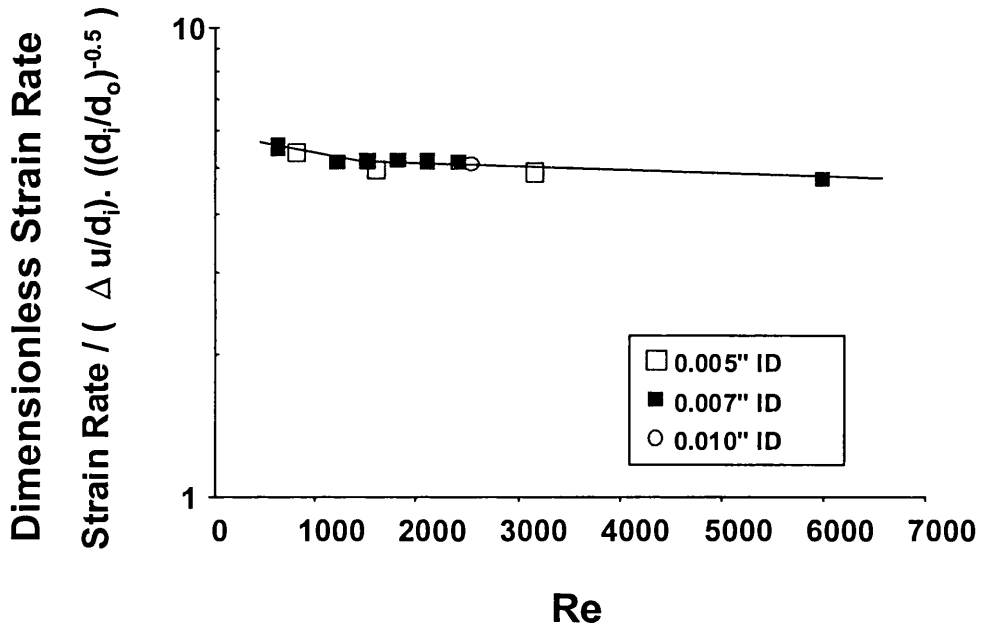

Figure 5.12 shows the dimensionless elongational strain rate (ε'r/u) at the entrance to the capillary versus the Reynolds number.

Entrance pressure drop

Figure 5.13 shows the capillary entrance pressure drop as a function of flowrate for the 3 capillary systems: 1) 0.062" to 0.010", 2) 0.062" to 0.007" and 3) 0.062" to 0.005". The entrance pressure drop increased as the square of the flowrate. Figure 5.14 shows the same entrance pressure drop data re-plotted in dimensionless form against Reynolds number. By scaling the dimensionless pressure drop ($\Delta P/\rho u^2$) by the ratio of the capillary diameters to the power of 0.85 and re-plotting versus Reynolds number, all the data can be made to fall on a single curve.

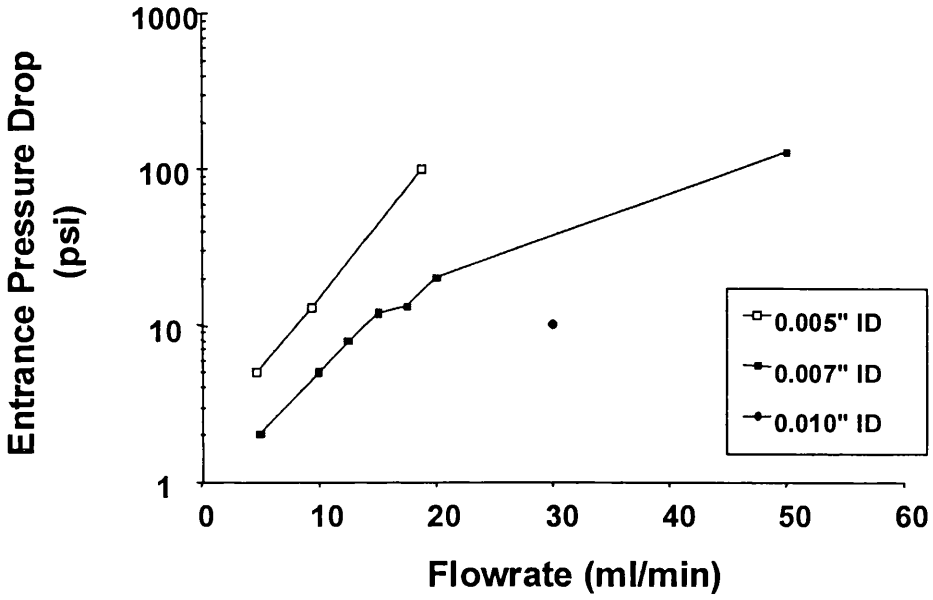

Figure 5.13. Plot of entrance pressure drop versus flowrate for the 3 capillary systems.

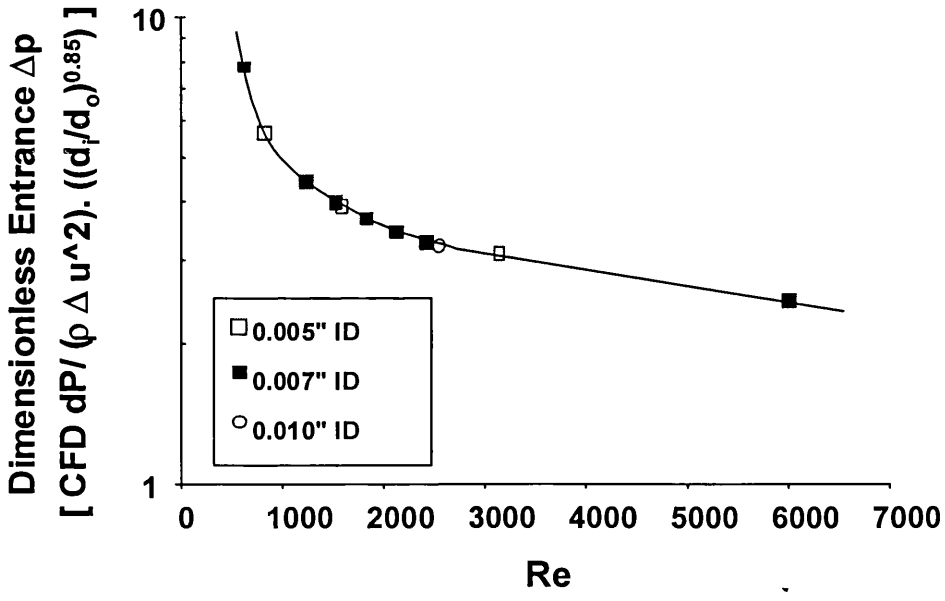

Figure 5.14. Plot of dimensionless entrance pressure drop, scaled by diameter ratio to the power of 0.85, versus Reynolds number for the 3 capillary systems.

5.5.4 Cavitation

Cavitation can cause significant degradation of DNA (Fuciarelli et al., 1995). Cavitation can occur in the capillary system if the pressure anywhere drops below the vapor pressure of the fluid passing through the capillary. This can particularly occur in the capillary entrance region, where pressure energy is transferred to kinetic energy. The pressure profile at the capillary entrance was examined to determine if localised region of low pressure at the capillary entrance dropped below one atmosphere absolute pressure. In all of the simulations investigated, the pressure remained significantly greater than atmospheric pressure, suggesting that cavitation should not be a significant factor in capillary shear studies at the flowrates investigated. Figure 5.15 shows a typical pressure profile at a capillary entrance.

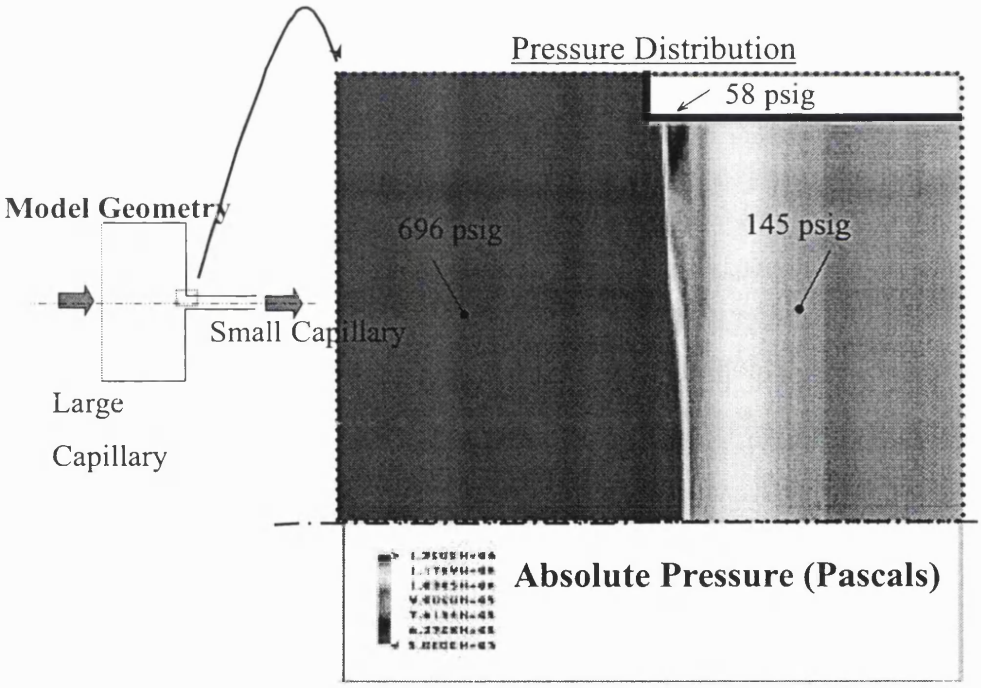

Figure 5.15 Filled-contour plot showing absolute pressure at capillary entrance.

CFD simulation allowed all the important fluid flow properties to be determined in the capillary flow system. Following CFD analysis of the capillary system, laboratory experiments were run to determine plasmid degradation rates, as described in the next section. The plasmid degradation data was then correlated against the fluid flow properties calculated using CFD to determine the underlying causes of DNA degradation.

5.6 Results: stress-induced degradation of plasmids

Plasmid flow degradation experiments consisted of pumping plasmid solutions through narrow bore PEEK capillaries of varying internal diameters and varying lengths. This section first describes pressure-flow measurements to determine the effective capillary internal diameters, secondly describes control experiments to ensure plasmid degradation was due to fluid stress in the capillaries, and thirdly describes the results of the flow degradation experiments.

5.6.1 Determination of effective capillary internal diameters

Before running a series of stress-degradation experiments with a particular lot of PEEK capillary, the flowrate versus pressure profile through different lengths of capillary was measured. Figure 5.16, Figure 5.17 and Figure 5.18 show the pressure drop as a function of capillary flowrate for a 0.01", 0.007" and 0.005" nominal ID PEEK tubing. Also shown on the three plots are the analytically calculated internal pressure drops based on Equation 2.21, using an effective diameter that best fitted the experimental data. Comparison of pressure versus flowrate data against analytical calculations gave a convenient means of determining the actual capillary internal diameters for the various lots of PEEK tubing used. The effective diameters for the 0.010", 0.007" and 0.005" ID capillaries were 0.0107", 0.0075" and 0.0058" ID, respectively. For all subsequent calculations, the effective internal diameters were used, instead of the nominal PEEK diameters.

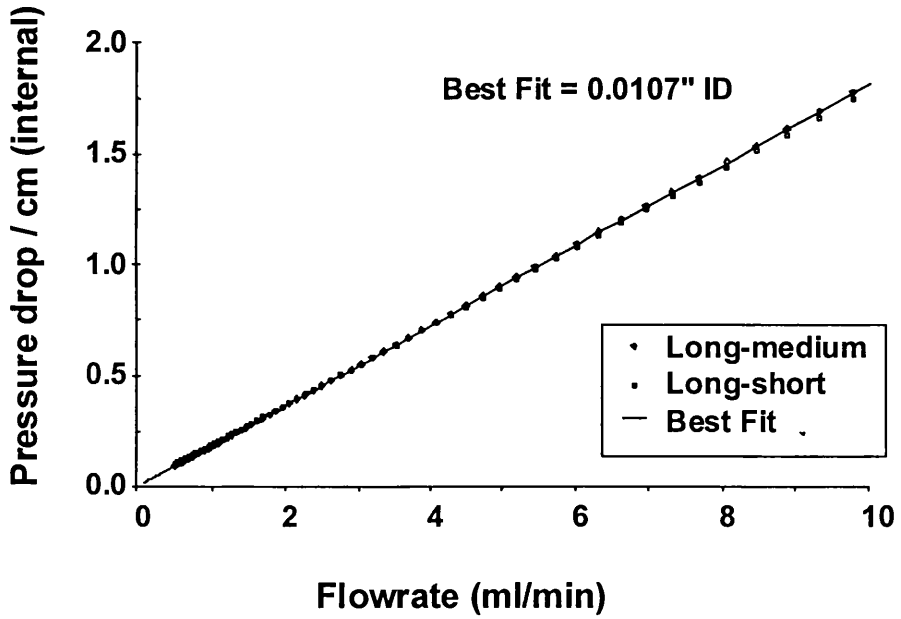

Figure 5.16. Internal Δp per unit length in 0.010" PEEK capillary versus flowrate

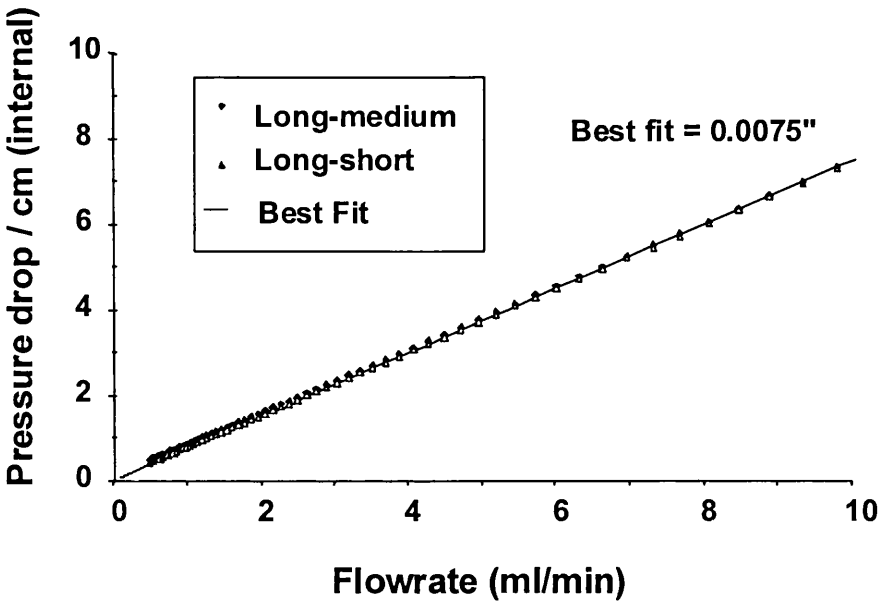

Figure 5.17. Internal pressure drop per unit length in 0.007" PEEK capillary versus flowrate. The internal pressure drop was calculated based on the total pressure drop across long, medium and short capillary tubing.

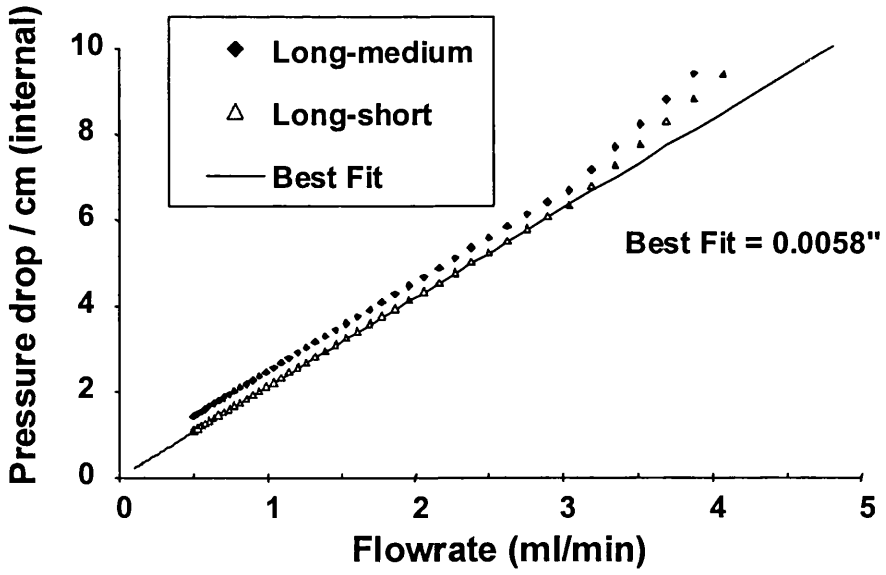

Figure 5.18. Internal pressure drop per unit length in 0.005" PEEK capillary versus flowrate. The internal pressure drop was calculated based on the total pressure drop across long, medium and short capillary tubing

Entrance Pressure Drop

Entrance pressure drops were determined by measuring the total pressure drop across different lengths of the same PEEK tubing, the Bagley method (Macosko, 1995), as shown in Figure 5.19.

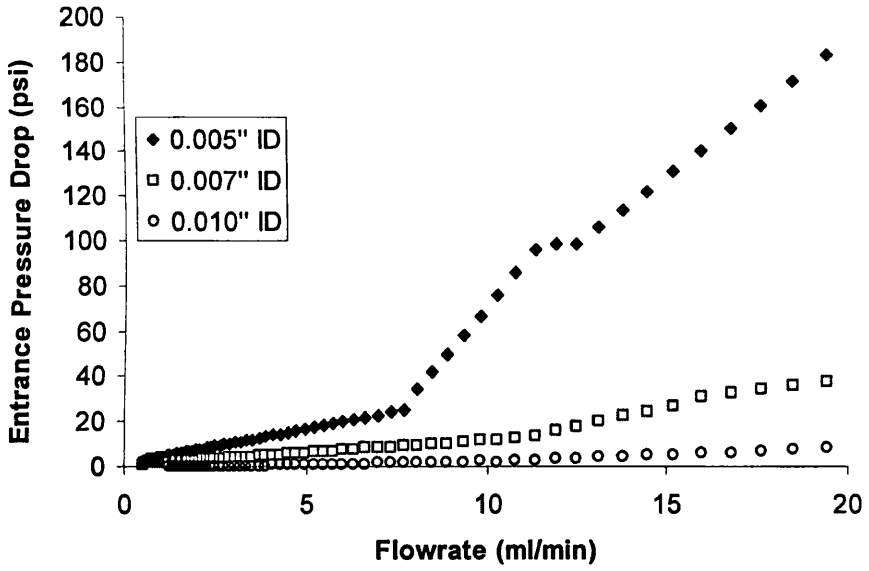

Figure 5.19. Measured entrance pressure drops as a function of flowrate for the three different ID PEEK capillaries.

From the previous section 5.4.8, CFD simulations predicted that all the entrance pressure drop data should fall on one curve when the entrance pressure drop re-plotted in dimensionless form, $\Delta P/\rho u^2$, and scaled by the ratio of the upstream and downstream diameters, $(d_i/d_o)^{0.85}$. After re-plotting the experimental data, it was determined that (d_i/d_o) to the power of 0.75, rather than 0.85, gave a better correlation of the data. The 0.007 and 0.005" nominal ID PEEK capillary entrance pressure drop data did fall on one curve, however the 0.010" nominal ID PEEK data did not. The discrepancy could be errors in measure the pressure drops across the capillaries; accurate measurement of the entrance pressure drop for the 0.010" ID capillary was the most difficult as the pressure drops were considerably smaller. Alternatively, small variations in internal diameter at the capillary entrance would have been difficult to detect. Figure 5.21 shows the same dimensionless entrance pressure drop data re-plotted, but using a value of 0.0117" effective ID, instead of 0.0107" effective ID for the nominal 0.010" ID PEEK capillary; the entrance pressure drop data now falls on one curve. At very low Reynolds number there is still some scatter in the data; at low Reynolds numbers the pressure drops were too low to measure accurately with the pressure gauge available. Interestingly, there is a sudden

change in entrance pressure drop for all capillaries just below a Reynolds number of 2000, indicating a change from laminar/transitional to turbulent flow at the capillary entrance.

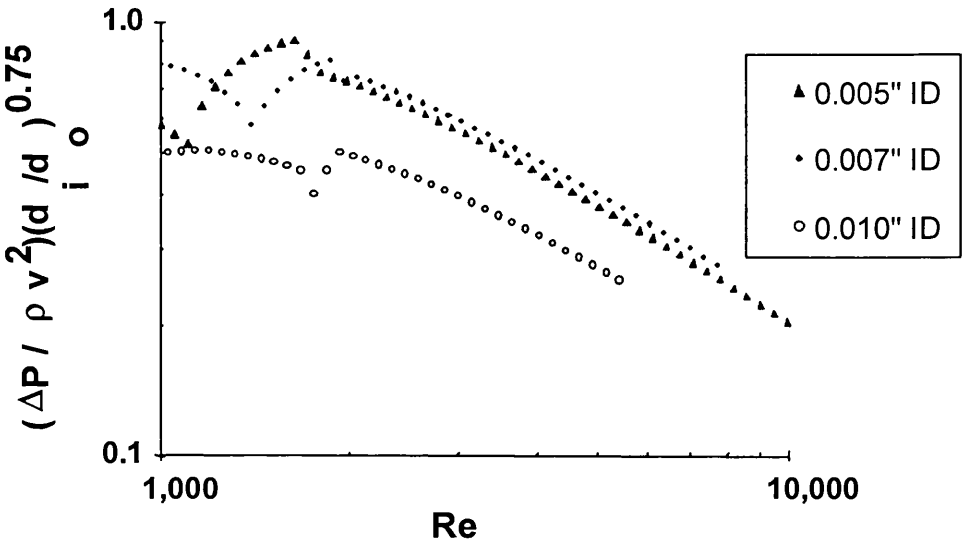

Figure 5.20. Dimensionless entrance pressure drop as a function of Reynolds number. The effective capillary internal diameters 0.0107", 0.0075" and 0.0058" (as measured in section 5.6.1) were used to calculate the dimensionless entrance pressure drop for nominal capillary diameters 0.01", 0.007" and 0.005", respectively.

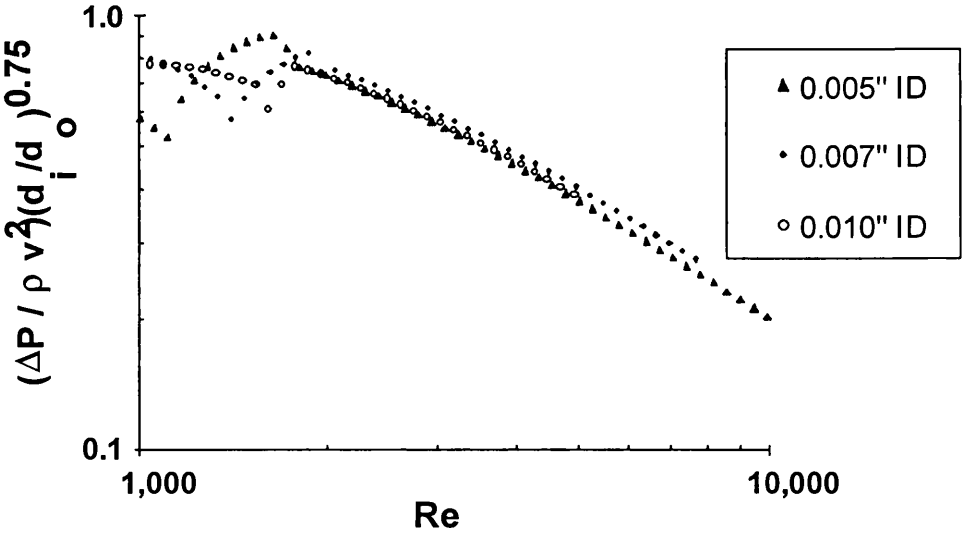

Figure 5.21. Dimensionless entrance pressure drop as a function of Reynolds number. Effective capillary internal diameters of 0.0117", 0.0075" and 0.0058" were used to calculate the dimensionless entrance pressure drop.

5.6.2 Effect of cavitation

The purpose of the capillary degradation experiments was to determine the effects of fluid shear on DNA degradation. However, it was important to check that other effects were not causing DNA degradation. One phenomenon that could have been present in the capillary system, leading to plasmid degradation, was cavitation. It is known that cavitation frequently occurs in high velocity flows, particularly at flow constrictions, and that cavitation can cause severe chromosomal DNA and plasmid DNA degradation. Cavitation is a process that involves the formation of bubbles of gas in flowing liquids followed by subsequent bubble collapse. Very high, localised fluid stresses are created at the point where a bubble collapses.

In general, the pressure drops across the capillaries were on the order of 100 to 1600 psi. These pressures were sufficiently high enough that cavitation effects should be minimal on the upstream side of the capillaries. CFD simulations of the fluid flow entering the narrow bore capillary entrance, refer to section 5.4.8, also indicated that the fluid pressure should be too high for significant cavitation to occur. To further reduce cavitation, all TE buffer was sparged to remove dissolved gases. However, it was still possible that a small amount of cavitation could be present at the capillary outlet, where a fast moving jet of liquid flows into a slower body of liquid (Lander et al., 2000). Because cavitation had been shown to rapidly degrade DNA, several studies were performed to determine if any cavitation was occurring and causing DNA degradation.

Cavitation using a sonication

Figure 5.22 shows the supercoiled plasmid DNA fluorescence as a function of time in the supercoiled plasmid solution at two different sonication amplitudes, using a sonic probe. The samples were denatured-renatured prior to Picogreen assay as per the standard protocol. At 1 micron sonication amplitude, there was no change in supercoiled plasmid fluorescence, but there was an immediate reduction in supercoiled plasmid fluorescence at 5 micron amplitude. Agarose gel electrophoresis showed that 10 minutes sonication at 5 μm amplitude was sufficient to degrade all of the supercoiled plasmid DNA. Therefore, sufficiently intense cavitation quickly degraded supercoiled plasmid pSVβ.

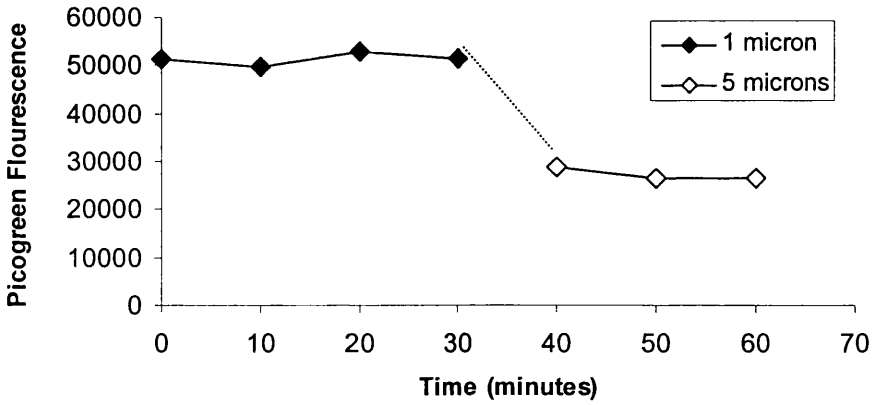

Figure 5.22. Effect of Sonication on supercoiled plasmid DNA.

The change in absorbance of potassium iodide solution as a function of sonication time at 1 and 5 microns was monitored, and is shown in Figure 5.23. There was a significant change in absorbance versus sonication time at 5 microns sonication amplitude; however, there was no significant change in KI absorbance at 1 micron sonication amplitude. Therefore, it was concluded that levels of cavitation capable of causing extensive supercoiled plasmid degradation could be detected by monitoring the change in KI absorbance. Low levels of cavitation, such as produced by 1 micron sonication amplitude, would not be detected by monitoring KI absorbance; however, supercoiled plasmid degradation should be minimal under these conditions (Figure 5.22).

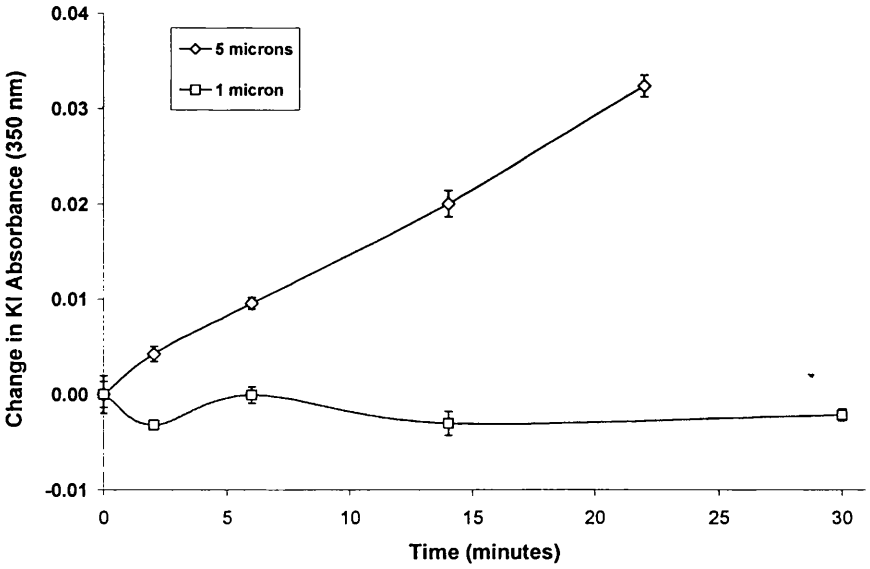

Figure 5.23. Plot showing the change in absorbance of KI versus sonication time at 5 microns and 1 microns sonication amplitude.

Cavitation in Capillary System: Monitoring KI absorbance

Recirculating potassium iodide solution through the flow system was performed as a standard test for cavitation. Figure 5.24 shows the solution absorbance at 350 nm as a function of recirculation flowrate through the capillary device for a 0.01" capillary system. The KI solution was recirculated for 30 minutes at each flowrate. There was no significant change in absorbance, indicating that cavitation was not occurring or was occurring only to a very small extent below the level of detection of the assay.

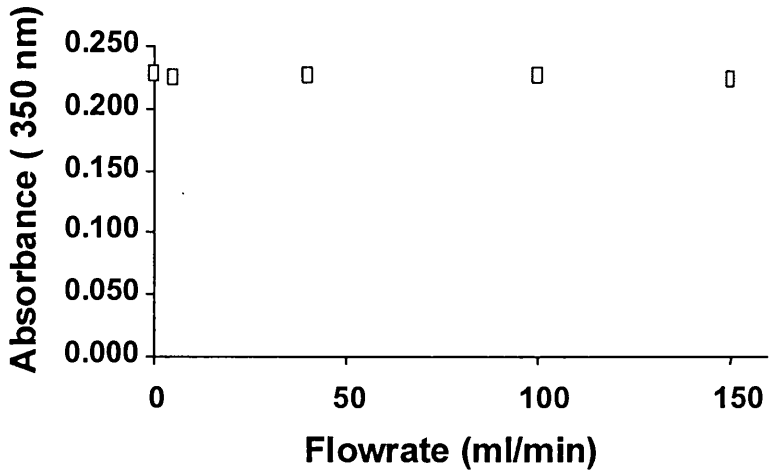

Figure 5.24. Plot showing change in KI absorbance at 350 nm versus flowrate in PEEK capillary.

Cavitation in Capillary System: Effect of backpressure

Based on the change in absorbance while recirculating KI solution through the PEEK capillary system, it was expected that cavitation should be not occurring to a significant extent within the system. As a further test, plasmid degradation experiments were performed with different amounts of backpressure on the capillary flow device. Backpressure increases the overall pressure throughout the flow system and hence reduces cavitation. Figure 5.25 shows the results of three experiments where supercoiled plasmid pQR150 was pumped through a narrow bore 0.007" ID capillary: a) without a backpressure capillary, b) with a short backpressure capillary, c) with a long backpressure capillary. The shear degradation rate with the short backpressure capillary in place (10 psi backpressure) was moderately less than the degradation rate with no backpressure. Hence, cavitation effects were probably causing a small amount of plasmid DNA degradation. This small amount of cavitation was probably at too low a level to be detectable by the KI assay. After significantly increasing the backpressure from 10 psi to 140 psi, by using the longer backpressure capillary, there was no further decrease in plasmid

degradation rate. This showed that a small backpressure of 10 psi was sufficient to eliminate all cavitation effects.

All subsequent shear experiments were done with a 60 to 140 psi backpressure capillary present immediately downstream of the narrow bore capillary to ensure that cavitation was prevented.

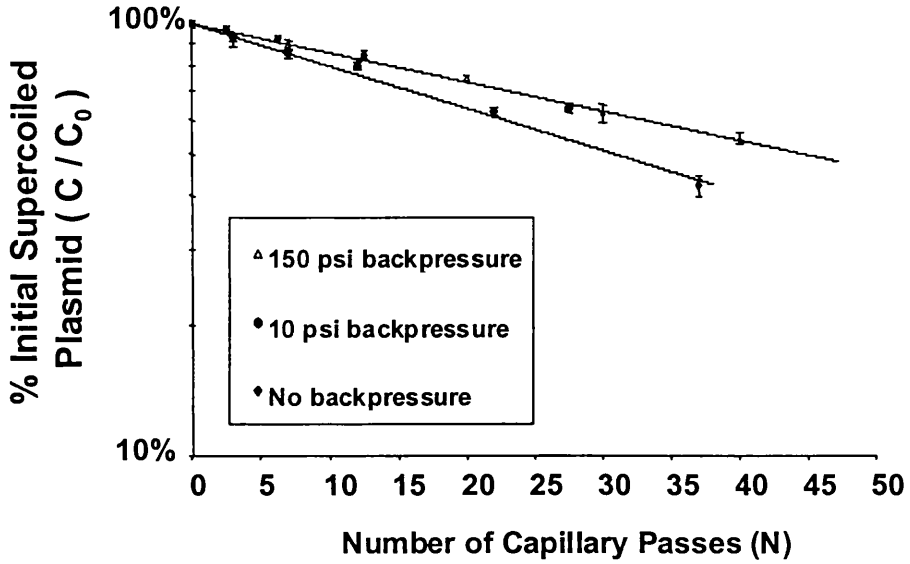

Figure 5.25. Plot showing the decrease in supercoiled plasmid pQR150 versus number of passes through a 0.007" PEEK capillary at 20 ml/min, at 3 different backpressures.

5.6.3 Plasmid degradation without the narrow bore capillary present

Before the rate of shear degradation of DNA was assessed in different diameter capillaries, the rate of plasmid degradation in the system was determined with the narrow bore capillary removed. The wide-bore backpressure capillary (0.02" nominal ID) was left in place. This experiment was performed to check that supercoiled plasmid was only being degraded in the narrow bore capillary and not elsewhere in the system. Figure 5.26 shows the concentration of supercoiled plasmid pQR150 (20 kb), as measured by Picogreen fluorescence, in samples taken every 10 minutes in a capillary shear system without the narrow capillary present. At flowrates up to 50 ml/min, there was no change in the supercoiled plasmid DNA concentration as measured by Picogreen fluorescence. Therefore, the HPLC pump, associated tubing and 0.02' backpressure capillary did not cause any shear damage to plasmid pQR150, at flowrates up to 50 ml/min, when the narrow capillary was not present. A similar study was performed for plasmid pSVβ up to flowrates of 100 ml/min, and showed no plasmid degradation.

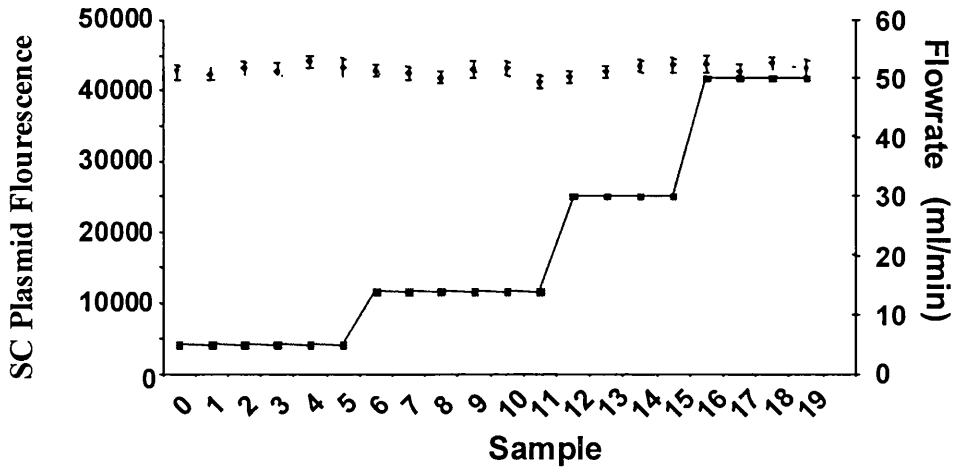

Figure 5.26 Plot showing the fluorescence of supercoiled plasmid DNA during plasmid recirculation through the capillary shear device without the narrow bore capillary in place. Samples were taken every 10 minutes.

5.6.4 Effect of capillary length on plasmid degradation

Figure 5.27 shows the concentration of supercoiled plasmid pSVβ versus time as the solution was pumped through 0.007" nominal ID capillaries at 50 ml/min. The results of experiments using two capillaries of different lengths (3.3 cm or 11.0 cm length) are shown. The degradation rates of supercoiled plasmid pSVβ in the two capillaries were the same as measured by agarose gel electrophoresis. Because the capillary length did not affect the degradation, this strongly suggests that plasmid degradation is occurring at either the entrance or the exit of the capillary system, and not internally. The turbulent energy and elongational strain rates should be many orders of magnitude greater at the capillary entrance, than at the capillary exit; therefore, plasmid degradation was probably occurring at the capillary entrance and not the exit. As shown in Figure 5.27, the plot of the concentration of supercoiled plasmid versus time is linear on a semi-log plot. This indicates that plasmid degradation is a first order reaction, i.e. $C = C_0 e^{-t/\tau}$, where C is the plasmid concentration, C_0 is the initial supercoiled plasmid concentration and τ is the degradation time constant in the capillary shear device. It was expected that the degradation of supercoiled plasmid was first-order, as the fraction of supercoiled plasmid that degrades per unit time should not be affected by the supercoiled plasmid concentration, and indicated that the shear experiment was performing as expected.

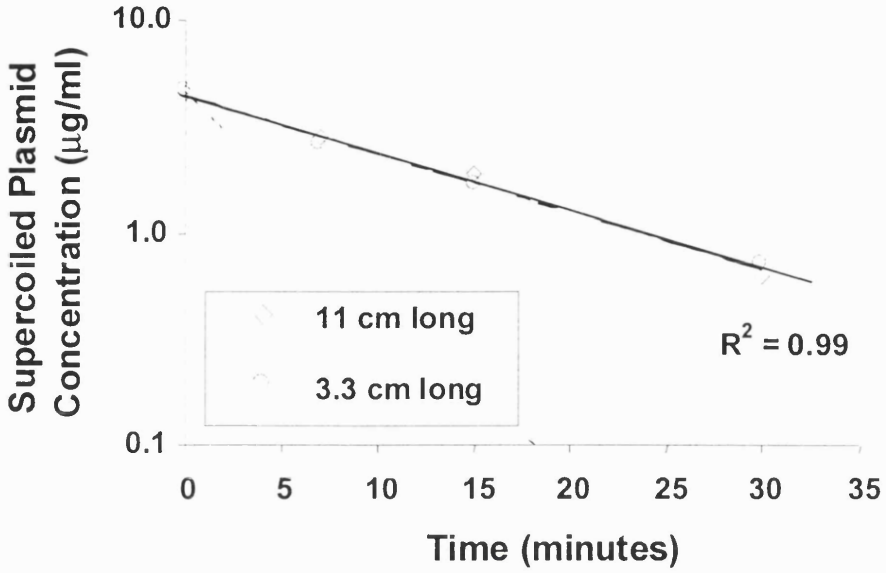

Figure 5.27 Plot showing the decrease in supercoiled plasmid pSVβ concentration over time during two capillary shear experiments. Both experiments were run under the same conditions except for capillary length. Data points shown are the average to 2 separate experiments.

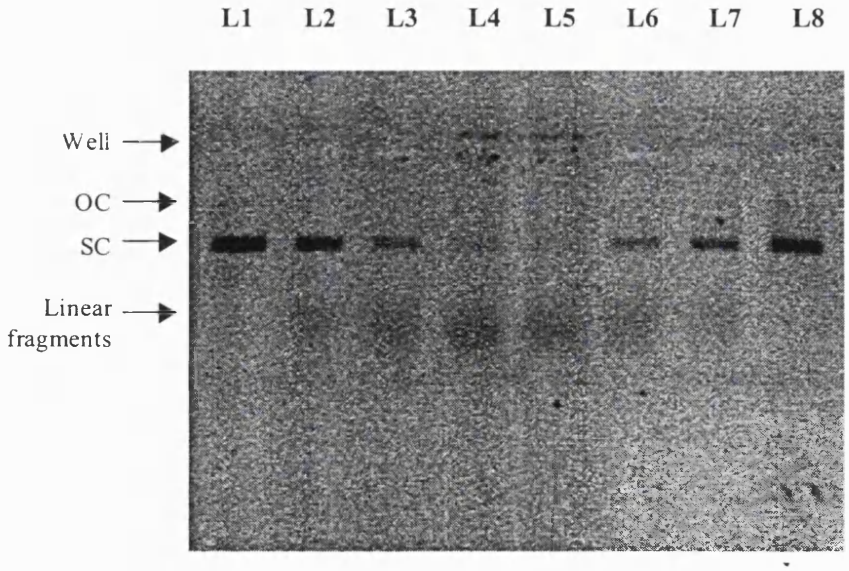

Figure 5.28. An agarose gel of capillary degraded pure supercoiled plasmid pSVβ: Lanes 1 and 8 are 0 passes, lanes 2 and 7 are 11 passes, lanes 3 and 6 are 23 passes, and lanes 4 and 5 are 47 passes through the capillary. The gel was 0.8% agarose, 50 mL volume 2X TBE, and run for 2 h at 3 V/cm.

Figure 5.28 shows an agarose gel after electrophoresis of the capillary degraded pSVβ plasmid samples, from the previous experiment. As the number of capillary passes increases, the

supercoiled plasmid band decreases on the agarose gel. Concurrent with supercoiled plasmid degradation there was an increase in linear plasmid fragments as shown on the gel. However there was not an increase of either open-circular plasmid or full-length linear plasmid, which would be observed above the supercoiled plasmid band on the agarose gel. Therefore, supercoiled plasmid either degraded directly to plasmid fragments, or any open-circular plasmid formed was sufficiently more sensitive to fluid stress that it quickly degraded to linear plasmid fragments and did not accumulate.

The effect of capillary length on the degradation rate of plasmid pQR150 was also investigated by pumping the plasmid through two capillaries of different lengths. Figure 5.29 shows the amount of supercoiled plasmid pQR150, as a percentage of the initial supercoiled plasmid, versus time during the capillary shear experiment. The supercoiled plasmid concentration was measured by Picogreen assay. Similar to the shear degradation experiment using plasmid pSVβ, the shear degradation rates of supercoiled plasmid pQR150 were the same in both the long (11 cm length) and short (3.5 cm length) capillaries. If plasmid degradation was occurring inside the capillaries, then the longer capillary should have a degradation rate 3-times higher than the short capillary. The dotted-lines in Figure 5.29 represent 3-fold higher and 3-fold lower degradation rates. It is clear from the figure that the degradation rates in the long and short capillaries were not 3-fold different. Therefore, it is unlikely that plasmid degradation is occurring to a significant extent within the capillaries.

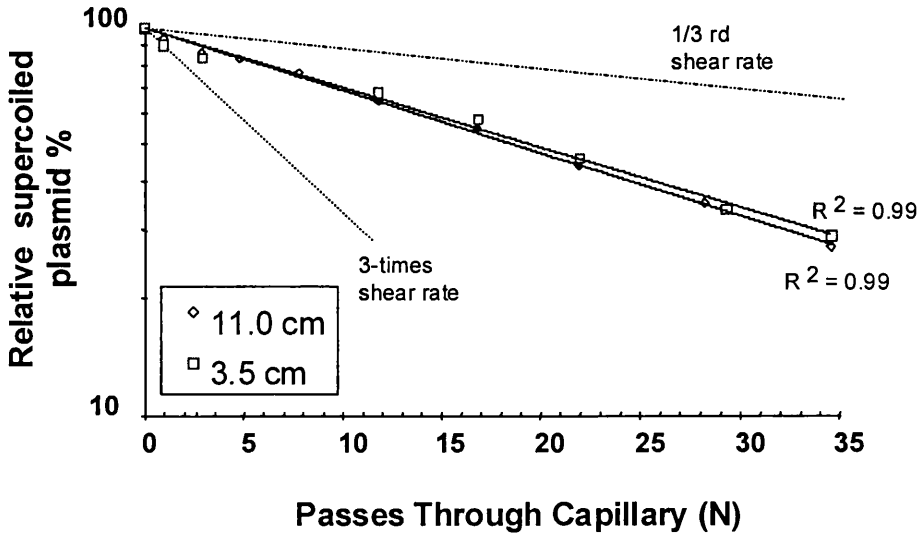

Figure 5.29 Plot showing the decrease in supercoiled plasmid DNA, as a percentage of initial supercoiled plasmid, over time during two capillary shear experiments. Data points represent the averages of two experiments.

5.6.5 Correlation of plasmid degradation with fluid flow properties

A series of capillary shear experiments were run with plasmid pQR150 and three different narrow-bore capillary diameters: 0.010", 0.007" and 0.005" nominal ID. The plasmid was recirculated at varying flow rates through the different capillaries, and samples taken. Supercoiled plasmid degradation rates were measured by Picogreen assay.

The supercoiled plasmid degradation rates per capillary pass were correlated against flowrate (Q), velocity (v), strain rate (v/d), entrance pressure drop (ΔP), CFD calculated elongational strain rate, and CFD calculated energy dissipation rate. In all calculations the effective internal capillary diameters were used, as calculated previously, as opposed to the nominal diameters. It was determined that the supercoiled plasmid degradation rate was best correlated against either strain rate or entrance pressure drop.

Figure 5.30 shows a plot of the supercoiled plasmid degradation rate, per pass through the capillary, as a function of strain rate. Two different definitions of strain rate were used to correlate the degradation data. One strain rate was taken to be v/d, the fluid velocity within the narrow bore capillary divided by the effective capillary diameter. This has the appropriate dimensions of seconds^{-1}. The second strain was the maximum elongational strain rate at the capillary entrance as calculated by CFD. The CFD simulations showed that elongation strain rate, ε', was equal to $5.2.(\Delta u/d_i).(d_i/d_o)^{-0.5}$, refer to Figure 5.12. The supercoiled plasmid degradation data correlated well with either definition of strain rate, but particularly against v/d.

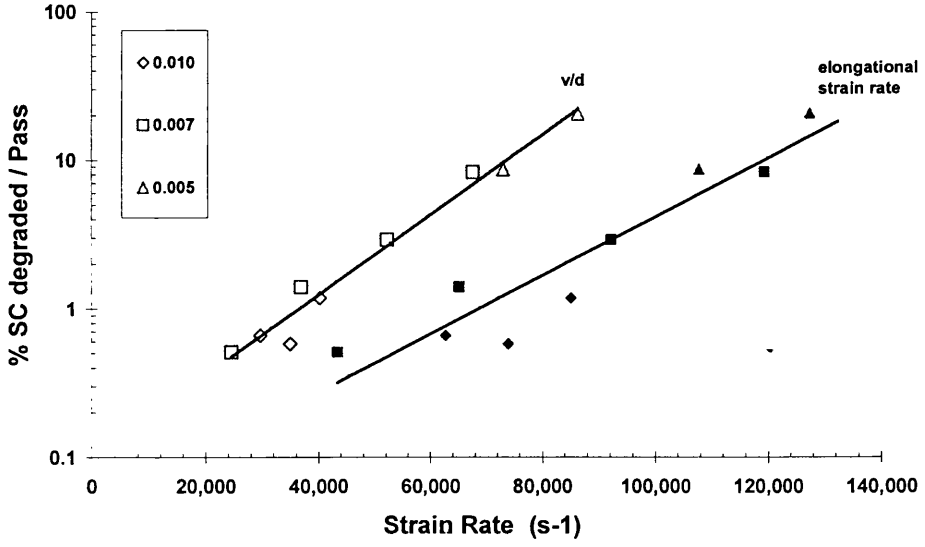

Figure 5.30. Correlation of supercoiled plasmid pQR150 degradation rate against strain rate. Hollow symbols are v/d strain rate, solid symbols are CFD strain rate.

Shown in Figure 5.31 is the supercoiled plasmid degradation rate as a function of entrance pressure drop. The entrance pressure drop were not measured directly for each capillary experiment, but knowing the flowrate for each experiment the entrance pressure drop was obtained from the previously determined entrance pressure drop versus flow rate data, shown previously in Figure 5.19. The supercoiled degradation rate also correlated well against the entrance pressure drop. It was not expected that the supercoiled plasmid degradation rate correlate with both the entrance pressure drop and the entrance strain rate. However, as shown in Figure 5.32, there is a moderate correlation between the entrance strain rate and the entrance pressure drop over the range of strain rates where plasmid pQR150 is degraded.

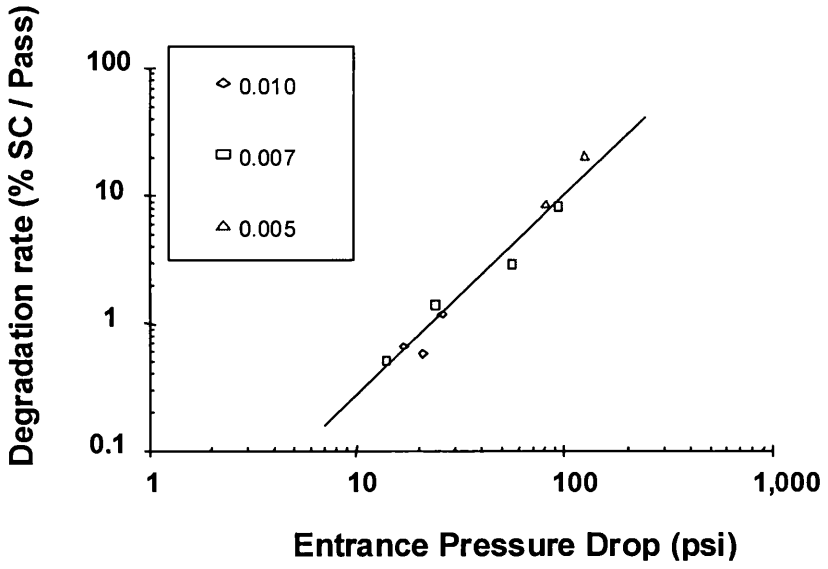

Figure 5.31. Effect of entrance pressure drop on supercoiled plasmid degradation rate.

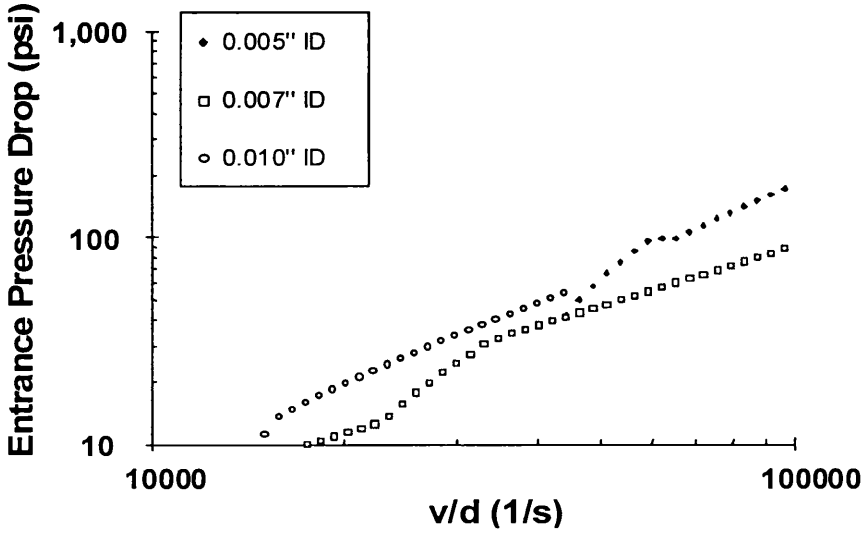

Figure 5.32. Relationship between measured entrance pressure drops and strain rate for the three different diameter PEEK capillaries used.

5.6.6 Effect of plasmid size

The degradation rate of plasmid pSVβ, pQR150 or p5176 in PEEK capillaries was evaluated over a range of flowrates. The Rainin HPLC system with a 0.007" nominal ID capillary was used for pSVβ and pQR150; the syringe pump with 0.010" ID nominal ID capillary was used for plasmid p5176. Figure 5.33 shows the entrance elongational strain rate at which 4% supercoiled plasmid was degraded per pass through the capillary. There was a significant decrease in the strain rate at which the supercoiled plasmid degrades as the size of the plasmid increases. This is in agreement with the results of Levy et al. (1999) where supercoiled plasmids of size 13, 20 and 29 kb, were degraded in capillaries and rotating disks in highly turbulent fluid flows.

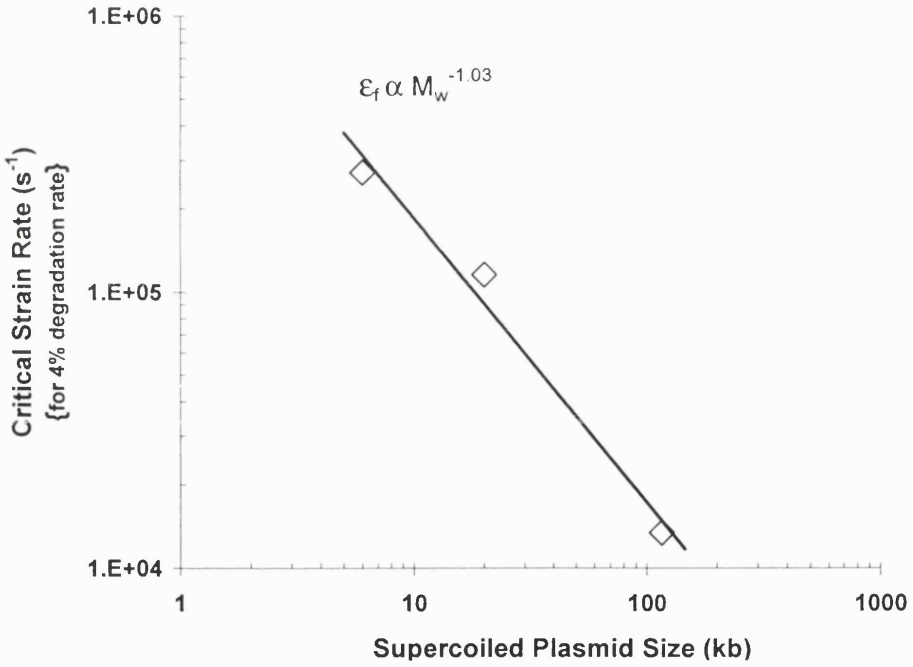

Figure 5.33. Plot showing the effect of plasmid size on the strain rate at which 4% of the supercoiled plasmid is degraded per pass through a PEEK capillary.

5.7 Results: stress-induced degradation of chromosomal DNA

It is important to understand the relationship between fluid stress and chromosomal DNA fragmentation both in order to reduce chromosomal fragmentation and to know what size chromosomal DNA fragments are likely to be generated. In chapter 6 the effect of fluid stress on chromosomal DNA fragment size will be examined in a cell lysate environment, where the relationship between DNA fragment size and shear rate will be determined. In this section, the effect of fluid stress on pure chromosomal DNA in TE buffer is investigated. This is the

solution environment that chromosomal DNA generally experiences during downstream purification, after the lysis and clarification steps.

5.7.1 Effect of strain rate on chromosomal DNA fragment size

Pure solutions of chromosomal DNA, at 150 µg/ml in TE buffer, were pumped at varying flowrates through 0.010", 0.007" and 0.005" nominal ID PEEK capillaries. Each solution was pumped through the capillary exactly 10-times, after which each solution was diluted 10-fold with TE buffer and assayed for DNA size by pulsed-field gel electrophoresis. Linear DNA markers from 25 to 500 kb were run on the same pulsed-field gels to determine the size of the chromosomal DNA fragments. Figure 5.34 shows the relationship between chromosomal DNA size and elongational strain rate for all three different capillary internal diameters. Each data point is the average of two experiments. The elongational strain rates were determined from the effective internal capillary diameters and the CFD simulation as described in the previous section. The elongational strain rate roughly correlates with DNA fragment size, however the correlation is not quite as good as seen in the previous section between plasmid degradation and elongational strain rate.

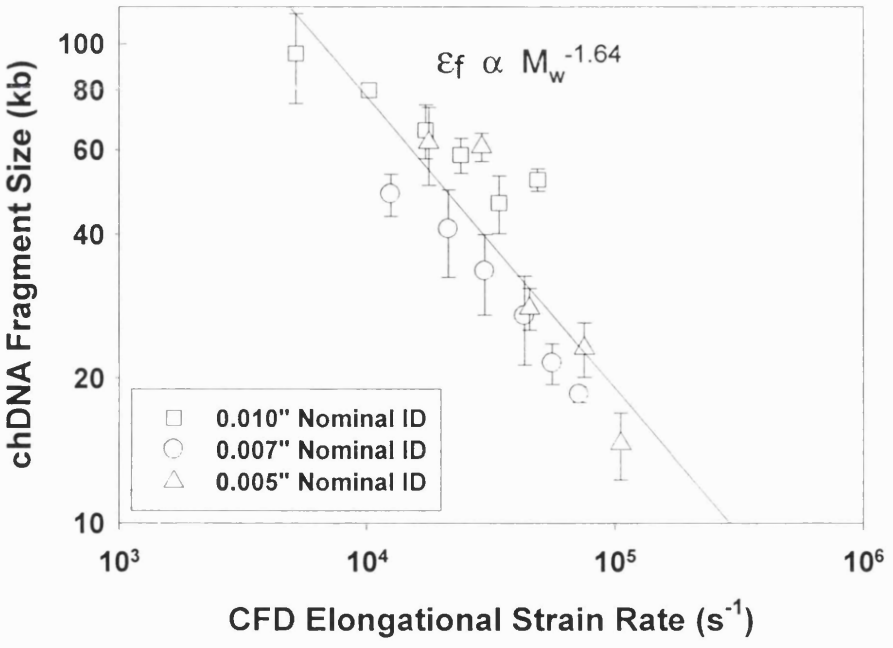

Figure 5.34. Plot showing the relationship between chromosomal DNA fragment size and the CFD calculated elongational strain rate at the capillary entrance.

5.8 Discussion

5.8.1 Comparison of internal and external capillary strain rates

Based on fluid flow experiments with different length capillaries, it was demonstrated that supercoiled plasmid degradation occurred at the entrance to PEEK capillaries and not within the capillaries. At the entrance to a capillary, the fluid stresses are primarily elongational fluid stresses (caused by elongational strain) compared to shear stresses within the capillary (caused by the shear strain). Over the flowrates used in the plasmid degradation experiments, the CFD predicted elongational strain rate at the capillary entrance was 4- to 5-fold lower than the predicted laminar strain rate against the internal capillary wall. Therefore, if plasmid degradation was due to elongational forces at the capillary entrance, elongational strain must be significantly more effective at causing plasmid degradation than shear strain. This is not that surprising as elongational strain causes sustained plasmid stretching, while shear strain causes periodic stretching and compression together with rotation (Odell et al, 1992; Smith et al., 1999).

As well as elongational and shear stresses caused by bulk fluid motion, additional fluid stresses may occur due to fluid turbulence. Fluid flow is generally laminar within capillaries, and at capillary entrances, below Reynolds numbers of 1000 and turbulent above Reynolds numbers of 4000 (Moan et al., 1979; Coulson et al., 1991). Figure 5.35 shows the Reynolds number within the PEEK capillaries as a function of the elongational strain rate at the capillary entrances, for experiments using plasmid pQR150. Also shown in the plot are the ranges of Reynolds number and strain rate over which pQR150 plasmid degradation was observed. It is apparent from the plot that the Reynolds number for the capillary flows was in the transition range ($1000 < Re < 4000$) during supercoiled plasmid degradation. Therefore, it is difficult to determine if turbulent stresses at the capillary entrance, or within the capillary, were present during plasmid degradation experiments, and causing plasmid degradation.

The CFD simulations predicted that the turbulent energy dissipation is the highest close to the internal capillary walls, as shown in Figure 5.10. Because the magnitude of turbulent stress increases with increasing local energy dissipation rate (refer to Equation 2.1, Equation 2.15 and Equation 2.14), turbulent stresses should be the highest within the capillary, and not at the capillary entrance. Average turbulent energy dissipation rates within the capillaries during plasmid pQR150 degradation experiments were calculated to be $1x10^5$ to $2x10^5$ W/kg. This corresponds to Kolmogoroff length scales of 3.5 to 4 microns. The pQR150 supercoiled plasmid radius of gyration is less than 1 micron, and its maximum extension is about 2 microns; hence, the supercoiled plasmid is probably too small to experience significant stress due to

turbulent eddy fluctuations. Using Equation 2.15 to calculate the turbulent stress inside an eddy, or Equation 2.14 to calculate the turbulent stress on a particle inside the viscous dissipation range, the turbulent stress on a 2 micron particle at 2x105 W/kg energy dissipation should be less than 20 Pa. Compare this to an elongational stress of 100 Pa due to elongational strain rate at the capillary entrance predicted by CFD simulation. Therefore it is unlikely that turbulent stress is causing significant plasmid degradation. Moreover, if turbulent stresses were causing significant plasmid degradation, the highest turbulent energy dissipation rates should be at the capillary entrance where plasmid degradation was observed, which is contrary to CFD predictions.

The stress-induced degradation of plasmid p5176 (116 kb) occurred at significantly lower strain rates and Reynolds number than plasmid pQR150, as shown in Figure 5.33. For plasmid p5176, degradation occurred at a Reynolds number of about 500. At this Reynolds number, the flow should be laminar and turbulent stresses should be very low. This supports the conclusion, using plasmids pSVβ and pQR150, that turbulence is not a requirement for supercoiled plasmid degradation.

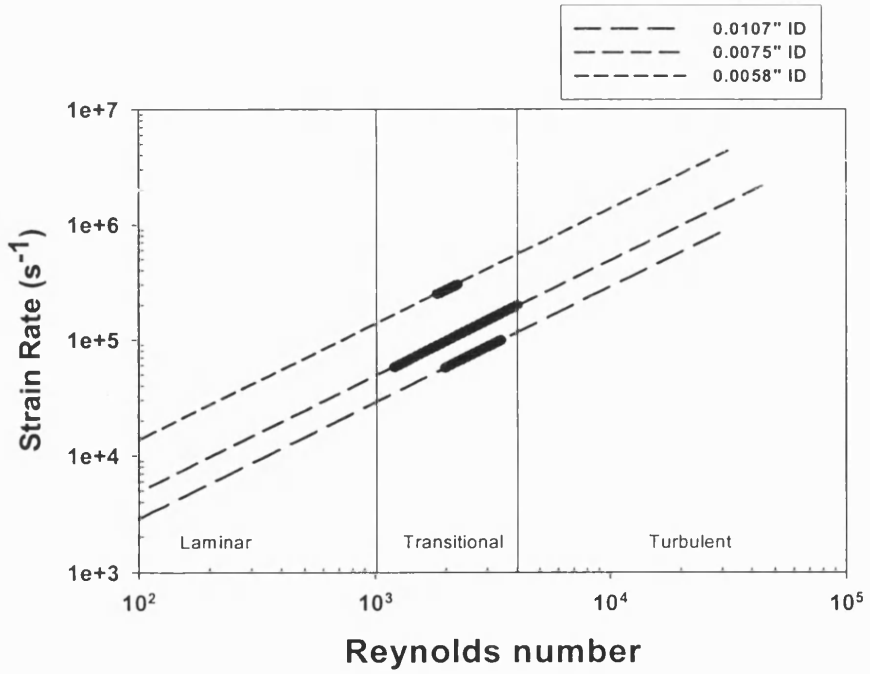

Figure 5.35. Plot showing the relationship between entrance elongational strain rate and internal capillary Reynolds number, for the 3 different diameter PEEK capillaries used in plasmid degradation experiments. The wide lines indicate the strain rate where plasmid degradation rates were measured.

5.8.2 Comparison of degradation rates with literature

Comparison of plasmid degradation in capillaries versus rotating disks

Supercoiled plasmid degradation experiments were performed by Levy et al. (1999) using capillaries and rotating disks. However, the plasmid degradation rates in the two devices were inconsistent based on the calculated fluid stresses in each device. The capillary diameters used by Levy et al. were similar to those used in this thesis, and the plasmid degradation rates in capillaries reported by Levy were similar to the degradation rates observed in this work. However, experiments of Levy et al. did not distinguish whether the plasmid was degrading at the entrance or inside the capillary. In this thesis, experiments showed that supercoiled plasmid degraded exclusively at the capillary entrance. This was consistent with calculations that showed the maximum elongational stresses occurred at the capillary entrance and not inside the capillary.

The analysis of plasmid degradation, in this thesis, showed that plasmid pQR150 is not degraded by turbulent stress at energy dissipation rates of $2x10^5$ W/kg, as discussed in the previous section. This is consistent with the theory that particles are primarily degraded by fluid stress when the Kolmogoroff length scale is smaller than the size of the particles (Henzler, 2000). Levy et al. observed plasmid pQR150 degradation in a rotating disk device at energy dissipation rates above 2 to 4 x 10^6 W/kg. This corresponds to a Kolmogoroff length scale of 1.5 to 2 μm. Considering the maximum extension of plasmid pQR150 is 2 microns, the plasmid could now be considered as being comparable or larger in size than the smallest turbulent eddies in the viscous dissipation region. The calculated turbulent stress on the plasmid in the viscous dissipation region, at 4 x 10^6 W/kg, is over 100 Pa. Interestingly, this is the about the same magnitude of stress at which plasmid pQR150 was shown to degrade at the entrance to capillaries, in this thesis. Therefore, capillaries and rotating disks now give consistent levels of DNA degradation at similar levels of fluid stress.

For double-stranded linear DNA in a QSS extensional flow, the force required for chain scission was estimated using Equation 2.24 and the data of Atkins et al. (1992) and determined to be about 500 pN. In the DNA degradation experiments of Atkins, the DNA molecules were shown to be in a fully extended conformation at chain breakage. The data of Reese et al. (1989) was used to estimate the force required for 38 kb DNA chain scission in a FT extensional flow, using Equation 2.27, and the force was determined to be about 3000 pN. The calculated value of 3000 pN is based on the stretched out length of the 38 kb DNA fragment. In the FT extensional flow it is likely that the DNA is not fully stretched, however, so the force of 3000 pN for chain breakage is probably an over estimate. Supercoiled plasmid DNA pQR150 was

observed to break at $50x10^3$ to $100x10^3$ s^{-1} elongational strain rate at capillary entrances. Using Equation 2.27 to estimate the force on supercoiled plasmid DNA at 1x105 s^{-1} strain rate, and using a fully stretched-out covalently-closed length of 2.4 microns and an extensional viscosity of 3 mPa s, the critical force for chain breakage is 1000 pN. Therefore, the critical force for plasmid DNA chain breakage in extensional flow is in a similar force range as observed in studies using linear double-stranded DNA.

TABS Theory

According to the Thermally Activated Bond Scission (TABS) model for polymer degradation due to fluid stress (Odell et al., 1988) the breakage of bonds in the DNA molecule will be a thermally activated process where the rate is determined by an Arrhenius-type equation. The activation energy for pulling apart a C-C or C-O bond is a function of the force applied to the individual bond being pulled apart. The relation between the rate of scission K_0, and the temperature T, according to this model, is given by

$$K_0 = A \exp[-(U_0 - f) / (KT)]$$

Equation 5.1

U_0 is the bond dissociation energy, K is the Boltzmann constant, and f is the reduction in dissociation energy due to the energy supplied by fluid stress. According to the TABS theory, f is proportional to the strain rate. It is apparent from this equation that if DNA stress-induced degradation is a thermally activated process, then plotting log K_0 versus strain rate should yield a straight line. Figure 5.30 shows that for pQR150 plasmid degradation, there is indeed a linear relationship between log K_0 and strain rate. This demonstrates that the TABS theory does accurately describe supercoiled plasmid DNA degradation in capillaries.

Correlation of plasmid degradation with elongational strain rate

It was determined in this thesis that the degradation rate of plasmid pQR150 in the capillary device was well correlated by the entrance elongational strain rate. In contrast, Nguyen et al. (1988) showed that the degradation rate of synthetic polymers in Fast Transient flows was not well correlated against the entrance elongational strain rate; the entrance elongational strain rate being given by v/d, as for a point-sink flow. Nguyen et al. reported that the degradation rate of polymer molecules in their orifice flow device was better correlated against the average velocity of fluid through the orifice, v, for the 4 different diameter orifices that were used. It should be noted that Metzner et al. (1970) reported that the elongational strain rate in narrow orifices was generally proportional to v and not v/d as expected. This is due to the change in angle at which the flow enters an orifice as the orifice diameter changes. If the strain rate measured by

Metzner et al. for orifices is correct, then the degradation of DNA observed by Nguyen et al. would be well correlated by entrance elongational strain rate. In this thesis, the entrance flow was into a capillary and not an orifice. CFD simulations predicted that the elongational strain rate was proportional to $v/\sqrt{d}$. Therefore, the CFD predicted elongational strain rate ($v/\sqrt{d}$) was intermediate between the ideal strain rate (v/d) and the orifice strain rate (v).

Aggregation

Hershey et al., (1961) and Reese et al. (1990) had reported a delay in the onset of DNA degradation in recirculating flows. Aggregation had been suggested as a reason for the apparent delay in DNA degradation, where it takes time for aggregates to break-up. Alternatively, it had been suggested that the delay time was due to single-stranded nicks accumulating on the DNA chain. Once enough single-stranded nicks had occurred, then full chain scission proceeded. In this work, it was observed that the rate of supercoiled plasmid degradation was highly variably at the start of experiments. Sometimes there was a significant delay in the onset of degradation, and sometimes there was even an increase in supercoiled concentration at the start of an experiment. However, after filtering all plasmid samples through a 0.2 μm filter prior to degradation experiments, these variable degradation rates at the start of experiments completely disappeared. Therefore, it was concluded that these problems were due to plasmid aggregation. Plasmid was always filtered immediately prior to degradation experiments as a general rule. It was still surprising that there was any plasmid aggregation, as all samples were diluted in filtered buffers to relatively low concentrations for degradation experiments. One of the advantages of working with supercoiled plasmid, instead of linear double-stranded DNA, is that supercoiled plasmid must be entirely intact; a single nick will reduce it to open-circular plasmid. In contrast, it is difficult to determine the number of single-stranded nicks in a linear piece of DNA.

5.8.3 DNA stretching and scission

Polymer Stretching

A polymer like DNA will start to stretch in any flow where the product of its relaxation time, τ, and the elongational strain rate, ε, are greater than about 0.5 (Smith et al. 1999). In this case the molecule will rapidly stretch to about 80% of its fully stretched out contour length. Alternatively, a polymer will start to stretch if the product of its relaxation time and the shear strain rate, γ', are greater than about 1. In this case the molecule will stretch gradually as the product $\tau.\gamma$ increases. At $\tau.\gamma = 20$, the molecule will have stretched to about 40% of its contour length (Smith et al., 1999).

$\tau.\varepsilon' \geq 0.5$ or $\tau.\gamma' \geq 1.0$ criteria for molecular stretching to occur

Equation 5.2

The product of relaxation time and strain rate is known as the Deborah number, De, and will vary depending on the flow conditions and the polymer size. The relaxation time, τ, for a polymer is a function of its molecular weight raised to a power. Typically, $\tau \alpha M_w^{1.5-2.0}$ (Rouse, 1953; Zimm, 1956). For example, the relaxation time of λ-DNA (48 kb) is about 0.4 s, and the relaxation time of plasmid pQR150 (20 kb) is about 0.009 s. Hence, λ-DNA (48 kb) will be significantly stretched at elongational strain rates of about 2 s^{-1}, or shear strain rates of about 20 s^{-1}. In contrast, shear strain rates on the order of 200 s^{-1}, 1000 s^{-1} and 4000s^{-1} were required to stretch plasmids p5176, pQR150 and pSVβ, respectively.

When performing DNA degradation experiments, careful consideration must be made to the Deborah number through the flow device. For example, the average shear strain rate in the 0.062" ID tubing (upstream of the narrow capillary tubing where plasmid was degraded) was always less than 500 s^{-1}. Therefore plasmids pSVβ and pQR150 should not be significantly stretched before entering the high stress zone in front of the narrow bore capillary. In contrast, if λ-DNA had been used in flow degradation experiments, it would be in an extended conformation before even reaching the narrow bore capillary, which would presumably have affected its susceptibility to degradation.

Supercoiled DNA Scission

For polymer degradation in extensional flows, if the molecule spends a long time in the extensional part of the flow field and has time to stretch-out (QSS flow), the critical scission strain rate will be inversely proportional to the polymer molecular weight squared ($\varepsilon_f \alpha M_w^{-2}$). This was predicted by Ryskin et al. (1987) and experimentally verified by Odell et al. (1994). Conversely, if the molecule rapidly enters a FT extensional flow and fractures before stretching, the critical strain rate will be inversely proportional to molecular weight ($\varepsilon_f \alpha M_w^{-1}$) (Nguyen et al., 1988). Polymer molecules will typically stretch-out in a time equivalent to their relaxation time. Therefore, in order to predict QSS or FT breakage the relaxation time of molecules has to be compared to the time the molecules spend in the elongational region of the flow.

Analysis of the CFD predictions of elongational strain rate at the capillary entrances showed that the region of high elongational strain extended only 1 mm out from the entrance of the capillary, and reached a maximum strain rate at the capillary entrance. Based on flowrates into capillaries during flow degradation experiments, the average residence time for a plasmid in the high stress zone was on the order 0.1 ms. This was considerably shorter than the relaxation

times for all plasmids used in this work, and for the chromosomal fragments observed. . Thus, in the capillary flow device, all experiments were performed under FT conditions and the plasmids should have broken in a non-stretched out configuration. Hence, a log-log plot of critical scission strain rate versus plasmid size should yield a straight line with a slope of –1. Figure 5.33 shows that the critical strain rate for supercoiled plasmid degradation is indeed inversely proportional to molecular weight, with a slope of -1.

Chromosomal DNA Scission

Chromosomal DNA was fragmented by forcing it through PEEK capillaries at varying flowrates using a syringe and automated syringe pump. Figure 5.34 shows that the strain rate is proportional to the molecular weight of the chromosomal DNA fragments to the power of -1.64. As already described, an exponent of -2 indicates DNA degradation in a stretched-out state, while an exponent of -1 indicates DNA degradation in a non-deformed conformation. The exponent of -1.64 indicates that the DNA is in a partially extended conformation. Based on the short residence time of the DNA molecules in the high stress zone at the capillary entrance, it would be expected that the DNA would be in a non-deformed conformation at chain scission.

The DNA fragments generated during capillary degradation experiments were from 100 to 20 kb. The relaxation time for these fragments will range from about 1 s to 0.1 s. Therefore elongational strain rates of only 1 to 10 s^{-1} are required to stretch these molecules out. Based on the geometry of the syringe, which contained a conical nozzle leading to the peak capillary, the elongational strain rates upstream of the capillary were likely between 10 and 100 s^{-1}. The chDNA fragments would have experienced these low strain rates for several seconds prior to entering the high stress zone in front of the capillary. Therefore it is likely that the DNA molecules were in at least a partly extended state which may explain the exponent of -1.64. Degradation of chromosomal DNA in a non-deformed state is difficult due to the ease at which it deforms when subjected to low strain rates.

Linear ds-DNA has been degraded in QSS flows by Odell et al. (1994) where the molecule was shown to degrade in an extended state, with a critical strain rate proportional to the molecular weight to the power of -2. Conversely, linear ds-DNA has been degraded at the entrance to PEEK capillaries and orifices by Oefner et al. (1996) and Thorstenson et al. (1998) at concentrations up to 40 μg/mL. Nguyen et al. (1998) observed synthetic polymer degradation in orifices, and observed a molecular weight exponent of -1. Using DNA, Oefner observed a molecular weight exponent of –0.9 in 200 m NaCl and an exponent of –1.1 in 5 mM NaCl. Therefore, it appeared that the molecule was breaking in a predominantly non-deformed configuration. In contrast, Thorstenson observed a molecular weight exponent of -1.7, similar

to the value observed in this work. This suggested that the DNA was breaking in a partially extended state. The DNA fragment sizes were similar in both studies, however, the studies of Thorstenson et al. were done using DNA in 0 mM NaCl buffer (0 mM NaCl buffer was used in this thesis), compared to 5 mM and 200 mM buffer used by Oefner et al. A significant increase in DNA chain stiffness has been observed when buffer ionic strength was decreased from 5 mM to 0.5 mM NaCl (Smith et al., 1992; Marko et al., 1996). This increase in chain stiffness would lead to a significantly more extended coil conformation at very low ionic strength making the DNA significantly more susceptible to stretching. In addition, the experiments of Thorstenson et al. used a long piece of medium bore capillary upstream of their degradation capillary, which would have generated shear stresses on the order of 5,000 s^{-1}. This strain rate would certainly have deformed the DNA fragments prior to entering the high shear zone in front of the capillary, explaining why the DNA degradation results suggest chain scission in a partially extended state. The experiments of Nguyen et al. (1988) were performed using an orifice where the upstream strain rates were very low, preventing any chain stretching prior to entering the orifice, explaining their observed molecular weight exponent of –1.

Thorstenson et al. and Oefner et al. both used orifices to degrade linear DNA, as well as short narrow-bore capillaries. The observed marginally lower rates of DNA degradation in orifices compared to the same internal diameter capillaries. They suggested that the elongational flow extended somewhat into the capillary, giving the capillary flow a slightly higher strain rate. Thorstenson observed a small reduction in DNA degradation when 3 mm length capillaries were used instead of 6 mm length capillaries. This is different to the results observed in this thesis, where there was no change in degradation rate going from 3 cm to 11.5 cm long capillaries. The results of Thorstenson can most likely be explained by considering the flow entrance lengths. The entrance length for a particular flow is the distance from the entrance of the capillary to the point at which the flow has become fully developed. Crucially, the entrance length in the experiments by Thorstenson was from 2 to 4 mm, which is similar in size to the capillary lengths used (refer to Equation 2.23). Therefore, switching from 3 mm to 6 mm ID tubing would change the flow profile at the capillary entrance, and hence the elongation stresses at the entrance. In the experiments used in this thesis, care was taken to use capillaries significantly longer than the predicted entrance length, in order not to change the entrance flow characteristics.

DNA concentration

Most of the theory for polymer stretching and scission is based on isolated molecules. The theory of polymer degradation in solutions of overlapping or entangled molecules is extremely limited at present. For entangled solutions a dependence of critical strain rate on molecular

weight to the power of 3 has been predicted (Macosko, 1994). However, most of the degradation studies using DNA have been performed under dilute conditions, $c < c^*$ (refer to section 2.4.5). The studies performed in this thesis, using pure chromosomal DNA, were at a concentration of 150 μg/ml. This concentration was chosen, as it was close to the concentration at which chromosomal DNA is present in solution during alkaline lysis. At this concentration, it was predicted that the chromosomal DNA molecules would have been overlapping, but not entangled, $c^* < c < c^+$.

Reese et al. (1989) observed breakage of T7 DNA, 38 kb, at an extensional strain rate above 10^4 s^{-1}, at dilute conditions. In this thesis, E. coli chromosomal DNA fragments were measured to be about 75 kb after forcing the DNA through capillaries at a strain rate of 10^4 s^{-1} (as shown in Figure 5.34). Therefore, the DNA was less susceptible to fluid stress in this work compared to the experiments of Reese. Similarly, extrapolating the size of the chromosomal fragment sizes observed by Thorstenson et al. (1998) to lower strain rates, the DNA fragments lengths generated were approximately 50% smaller than observed in this thesis. Both the experiments of Reese and Thorstenson had been performed in the dilute DNA concentration range. However, it has been observed by Hershey et al. (1960) that there is a significant "self-protection" effect at higher DNA concentrations; at higher concentrations DNA is less susceptible to chain scission. This may explain the higher levels of fluid stress required to break chromosomal DNA under non-dilute conditions observed in this work.

It was observed in this work that the critical strain rate for DNA breakage was related to the molecular weight to the power of 1.6, which was similar to the results of Thorstenson et al. (1998). Therefore, there did not appear to be a significant effect of coil overlapping on the mechanism of DNA stretching.

5.8.4 Comparison of linear DNA and supercoiled plasmid DNA

From Figure 5.34, an elongational strain rate of 10^5 s^{-1} corresponds to an average linear DNA fragment size of 13 kb after 10 capillary passes. Hence, most linear DNA fragments above about 17 kb would be degraded at this level of strain rate. At this same strain rate, the degradation of supercoiled plasmid pQR150 would only be about 30% after 10 capillary passes, from Figure 5.30. This suggests that a 20 kb piece of DNA, it is somewhat less susceptible to stress degradation if it is supercoiled than if it is linear. Similarly, when supercoiled plasmids are degraded in capillaries and analysed by agarose gel electrophoresis, the degradation of supercoiled plasmid does not correspond to an increase in open-circular plasmid or a single band linear plasmid (refer to Figure 5.28). It appears that open-circular plasmid and linear

plasmids degrade to small fragments at a faster rate than the supercoiled plasmid. This is not surprising, as supercoiled DNA is more compact than linear DNA in solution, and hence should be less susceptible to fluid shear.

5.9 Conclusions

CFD was used to predict elongational strain rates and turbulent energy dissipation rates within a capillary shear device. The CFD simulations were shown to converge to realistic solutions using a sufficient number of simulation grids. The CFD simulations were shown to agree well with analytical expressions for pressure drop and shear rate where analytical expressions were available. The CFD predictions were used to analyse DNA breakage experiments and correlate breakage against entrance elongational strain rate and pressure drop.

Plasmid DNA was shown to degrade in regions of high fluid elongational strain rate at the entrance to narrow capillaries. High levels of shear strain within capillaries did not lead to plasmid DNA chain scission showing that elongational strain is significantly more effective at causing polymer scission than shear strain. High levels of turbulent strain were shown not to be effective at causing plasmid degradation when the plasmids were smaller than the Kolmogoroff length scale of the turbulent flow. The force required to break a plasmid DNA chain was calculated to be roughly similar to the force required to break a linear DNA chain. The degradation kinetics of plasmid DNA was shown to agree with Thermally Activated Bond Scission (TABS) theory, and the strain rate required for plasmid degradation was shown to be inversely proportional to molecular weight. Downstream processing of large plasmids will require careful consideration of fluid stress levels within processing equipment.

The conformation of chromosomal DNA affected its susceptibility to degradation in regions of high fluid stress, which in turn was affected by the DNA size and solution properties such as ionic strength. Chromosomal DNA was shown to break in an extended conformation in capillary stress experiments, with a $M_w^{-1.6}$ dependence. Chromosomal DNA was observed to be less susceptible to extensional fluid stress compared to the results of Reese et al. (1989). This may be due to a "self-protection" effect at the higher chromosomal DNA concentrations used in this work. Fluid strain rates of 10^4 s^{-1} and 10^5 s^{-1} were observed to fragment chromosomal DNA down to the size of large (100 kb) and small (20 kb) plasmids, respectively. Fluid strain rates of 10^4 to 10^5 s^{-1} are common in downstream purification equipment, and hence care must be taken to avoid creating difficult to remove chromosomal DNA fragments similar in size to plasmid DNA products.

Having gained an increased understanding of the effects of fluid stress on DNA stress-induced degradation, the effects of fluid stress during the primary downstream purification step, alkaline lysis, will be examined in the next chapter.

6 Alkaline lysis

The previous chapter investigated the effects of fluid stress in a model flow system on DNA degradation in pure solution. This chapter presents the results of fluid mixing and fluid stress studies on a specific DNA-purification unit operation: alkaline cell lysis. The purpose of this unit operation is the extraction of the plasmid DNA product from the cell, as well as the removal of the majority of the cellular impurities. Alkaline cell lysis is the cellular lysis method most commonly used in DNA purification processes. It was decided to investigate this unit operation because the effects of fluid mixing and fluid stress were thought to be critical process parameters during this step. Moreover, this is one of the most important unit operations in typical DNA purification processes; as the primary isolation step its performance directly, or indirectly, affects the feed material into all of the subsequent purification steps.

This chapter is organised as follows: Firstly, a brief summary of results is presented. This is followed by an introduction into the motivation for the alkaline lysis studies. A detailed description of the materials and methods used to study the alkaline lysis is then presented. The results of the studies are presented as separate sections:

i) Control experiments
ii) Standard lysis protocols
iii) Detergent concentration in lysis buffer
iv) NaOH concentration in lysis buffer: denaturation of plasmid and chDNA
v) Denaturation time
iii) Fluid mixing during lysis
vi) Effect of fluid stress on the lysis of plasmid-deficient cells
vii) Effect of fluid stress on the lysis of plasmid-containing cells
viii) Effect of fluid stress during neutralisation

Finally this chapter concludes with a discussion into the relevance of the results obtained.

6.1 Brief summary of results

Based on the denaturation conditions for plasmid and chromosomal DNA, the optimal NaOH concentration at lysis is plasmid dependent, but is typically around 0.1 M. Different supercoiled plasmids, covering a wide size range from 6 to 116 kb, were all demonstrated to remain in their native supercoiled form up to specific threshold concentrations of NaOH in the lysis buffer, typically between 0.12 and 0.18 M NaOH. Above its specific threshold NaOH concentration, each plasmid completely and irreversibly denatured during alkaline lysis. In contrast, chromosomal DNA and plasmid variants were demonstrated to denature at significantly lower concentrations of NaOH in the lysis buffer. Although, high NaOH concentration, close to 0.1 M, did not decrease chromosomal contamination in the clarified alkaline lysate, it did maximise the denaturation of chromosomal DNA to single-stranded-form. Achieving the required NaOH concentration in the lysate can be achieved by adding 1 volume of 0.2 M NaOH to 1 volume of cells; however, it was shown that supercoiled plasmid irreversibly denatured when exposed to neat lysis buffer (0.2 M NaOH) for only a few seconds. Efficient mixing of equal volumes of cells and lysis buffer, to quickly achieve a homogeneous NaOH concentration close to 0.1 M NaOH, was essential in preventing plasmid degradation.

Experiments with scale-down stirred tanks showed that the mixing time was sufficiently short at moderate impeller speeds to prevent supercoiled plasmid denaturation at typical alkaline lysis buffer concentrations (0.2 M NaOH). High impeller speeds, in stirred tanks, were required when more concentrated lysis buffer (0.4 M NaOH) was used, generating high levels of fluid shear. Significantly shorter mixing times were obtained using opposed jets, at lower levels of fluid shear. Opposed jets results are presented in chapter 8.

Fluid stress during alkaline lysis was shown to fragment chromosomal DNA to progressively shorter pieces as the stress was increased. Exposing chromosomal DNA to fluid stress in cone-and-plate viscometers and in narrow capillaries, at fluid strain rates ranging from 10 s^{-1} to 10^5 s^{-1}, only moderately increased the amount of chromosomal DNA contamination. It appeared that chromosomal DNA flocculation and removal over lysis and neutralization was only weakly dependent on DNA size. Typically about 80% to 90% of the chromosomal DNA was removed over lysis, neutralization and clarification. However, the amount of chromosomal contamination in the clarified lysate was strongly dependent on the starting batch of cell paste. Plasmid pSVβ (6kb) was not damaged by fluid shear during alkaline lysis, at shear rates up to 10^5 s^{-1} in capillaries. Contrary to previous reports, fluid strain rates up to 10^5 s^{-1} neutralization did not affect chromosomal DNA contamination.

6.2 Introduction

The goal of alkaline lysis is to maximise supercoiled plasmid yield and minimise the amount of impurities. In this thesis only the DNA impurities were considered; the quantity of other cell constituents such as cell wall debris, proteins, RNA, and endotoxins were generally not examined. The reason for not examining non-DNA impurities was essentially because this thesis set out to examine the effects of fluid dynamics on DNA integrity, not other compounds. Moreover, reduction of DNA impurities is significantly more important than reduction of other impurities. DNA impurities are both difficult and expensive to separate from the supercoiled plasmid product, as described in chapter 1. In contrast, a variety of scaleable and inexpensive methods exist for removal of non-DNA impurities.

A detailed description of alkaline lysis is given in chapter 1. In general, alkaline lysis involves the addition of NaOH and detergent to lyse cells, release plasmid product and denature DNA impurities. This is followed by neutralization and clarification to remove flocculated impurities. It has been reported that fluid mixing is a critical parameter during alkaline lysis, however, details of why mixing is critical have not been reported. Because fluid mixing is the source of fluid stress during alkaline lysis, it is essential to understand the mixing requirements during alkaline lysis to properly optimize alkaline lysis with respect to fluid stress. The effects of NaOH concentration on cell lysis and product quality was examined in detail in order to ascertain the mixing requirements during alkaline lysis. Studies were then performed to determine the effects of mixing conditions and resultant fluid stress based on the supercoiled plasmid yield, supercoiled plasmid purity (supercoiled plasmid / total DNA), and the chromosomal DNA contamination in clarified alkaline lysates. The novel HPLC assays developed in the chapter 4 were used throughout to measure the concentrations of the different DNA forms, in addition to using agarose gel electrophoresis and Picogreen fluorescence.

6.3 Materials and methods

6.3.1 Standard analytical techniques

Anion exchange HPLC.

Poros PI and Q-Sepharose HPLC (see section 4.5) were used to quantify the various DNA forms before and after alkaline lysis. Refer to chapter 4 for details of the HPLC equipment. HPLC allowed accurate quantification of both the supercoiled plasmid yield and the total DNA purities. It was of interest to determine not only the amount of DNA impurities present in lysate samples, but also whether these DNA impurities came from chromosomal DNA or from degraded plasmid DNA. The DNA impurities consist of four main DNA forms a) open-circular

plasmid, b) native chromosomal DNA, c) single-stranded plasmid and d) single-stranded chromosomal DNA. The HPLC assays could quantify a) open-circular plasmid, b) native chromosomal DNA and c+d) the total single-stranded DNA. The single-stranded plasmid and single-stranded chromosomal DNA could not be quantitated separately. Hence, it was not possible to determine exactly what fraction of the single-stranded DNA impurities were single-stranded plasmid and what fraction was single-stranded chromosomal. Irrespective of origin, all single-stranded DNA is chemically and physically similar. Determining what fraction of the single-stranded DNA is chromosomal can only be definitively achieved by sequence analysis using qPCR. Development of a qPCR-based assay was a non-trivial task. In order to quantify the effects of lysis conditions on chromosomal contamination, without having to resort to qPCR, the effects of lysis on both plasmid-containing cells and plasmid-deficient cells (non-plasmid containing cells) was investigated. The use of plasmid-deficient cells eliminated any potential errors associated with trying to separately quantify single-stranded chromosomal fragments and single-stranded plasmid fragments.

Clarified lysate samples, and pure DNA samples, were assayed by anion exchange HPLC using Poros PI20 resin and/or Q-Sepharose HP resin. All samples were RNAse digested for 1 hour at 37°C in 0.1 mg/ml RNAse A prior to loading, if they had not already been RNAse-treated. All samples containing chromosomal DNA were manually sheared 10-times with a 0.007" PEEK capillary prior to HPLC loading at approximately 3 to 6 mL/min. Clarified lysate samples were usually run once without sample pre-treatment and once after denaturation-renaturation using the standard protocol. The standard denaturation-renaturation protocol involved quickly mixing 1 volume of sample in TE with 1/3rd volume of 0.2 M NaOH, to convert all DNA impurities (all DNA forms except supercoiled plasmid) to single-stranded form. After 2 minutes, 1 volume of 500 mM Tris, pH 8.0 was added. Samples were loaded onto the column at 2 to 100 µg/ml, 100 µl per injection. The Poros and Q-Sepharose columns were equilibrated for 10 minutes prior to sample injection at 0.8 M NaCl, 10 mM Tris, pH 8.0 or 0.64 M NaCl, 10 mM Tris, pH 8, respectively. The flowrate was 0.3 ml/min throughout. After injection, the column was washed for 10 - 20 minutes with equilibration buffer. RNA was quantitated from the flow-through peak of the Poros PI column. A salt gradient from 0.8 - 2.0 M NaCl (Poros) or 0.64 to 1.7 M NaCl (Q-Sepharose) was then applied to the column over 25 minutes (Poros column) or 40 minutes (Q-Sepharose column). Columns were cleaned with 0.1 M NaOH for 5 minutes at the end of each sample.

Picogreen fluorescence

Pure supercoiled plasmid DNA and clarified lysate samples were assayed for supercoiled concentration using Picogreen fluorescence. Picogreen stock reagent from Bioprobes (CA, USA) was diluted 1:200 with water and 100 µl was added to 100 µl of sample in a 96 well plate. Samples were excited at 540 nm and fluorescence measured at 600 nm. A pure plasmid DNA standard curve was generated by running pure plasmid DNA standards from 50 pg to 500 ng. Samples containing open-circular and linear plasmid, or chromosomal DNA, were denatured prior to Picogreen analysis using the standard denaturation protocol described in the previous section.

6.3.2 Control experiments

Effect of freeze-thawing cell paste on clarified lysate purity

After fermentation, the *E. coli* cells are typically harvested by batch centrifugation. After harvest, the cells are typically frozen at -80°C until further use. An experiment was run to verify that this freeze-thaw step was not leading to increased or decreased chromosomal DNA contamination. DH5α wild-type cell paste from a 500 mL shake flask fermentation was harvested by batch centrifugation. Some of the cell paste was alkaline lysed directly after cell harvest, and some of the cell paste was frozen at –20°C overnight, thawed at room temperature, and alkaline lysed. Alkaline lysis was performed at 2 mL scale using the standard protocol, described in chapter 4. Each lysis condition was performed in duplicate, and the clarified alkaline lysates were assayed by HPLC.

Resuspension Concentration

As per the standard lysis protocol, described in the Materials and Methods section, *E. coli* cells were resuspended in 8 mL TE per gram wet cell weight prior to lysis experiments. A study was performed to determine the effect of resuspension concentration on the supercoiled plasmid yield. *E. coli* cell paste containing plasmid pSVβ was resuspended in TE at 2, 4, 8, 16 and 32 mL TE/g wcw. 0.5 mL of resuspended cells was lysed using an equal volume of standard lysis buffer and neutralised with an equal volume of neutralisation buffer. The clarified lysates were assays for supercoiled plasmid by Poros PI HPLC. All experiments were done in triplicate.

Effect of clarification conditions.

After alkaline lysis and neutralisation, the batch is clarified to remove flocculated cell debris. This can be performed using either centrifugation or filtration. A study was performed to determine the effect of varying the clarification conditions on plasmid yield and purity. *E. coli* DH5α pSVβ cells were alkaline lysed at 2 mL scale using the standard protocol. Neutralisation

buffer was added, and the samples mixed gently by inversion. Then the samples were clarified using the following conditions:

i) Chilled in ice-bath for 10 min followed by 13 krpm centrifugation for 30 min.

ii) Chilled in ice-bath for 10 min followed by 10 krpm centrifugation for 10 min.

ii) Not chilled, 13 krpm centrifugation for 30 min.

iv) Chilled in ice-bath for 10 min followed by DE filtration.

Following centrifugation or filtration, each sample was IPA precipitated, ethanol washed and resuspended in TE as described in chapter 4. Chilled neutralisation buffer (4°C) was used for all experiments, except condition (iii). The filtration using DE consisted of adding DE to alkaline lysate at a body feed of 40 g DE/L lysate. The sample was mixed gently by inversion for 2 minutes, and filtered through a 32 μm stainless steel mesh.

6.3.3 Standard lysis protocols

Lysis experiments were carried-out on 5 harvested cell pastes (Table 6.1), of which two were plasmid-containing cells and three were plasmid-deficient cells. The fermentation and harvest of the cell pastes is described in detail in chapter 4.

Cell Paste Name	Plasmid	Fermentation	Harvest Time
pSVβP1	pSVβ	5L reactor	36 hrs
pSVβP2	pSVβ	5L reactor	36 hrs
WtypeG1	No plasmid	2L shake flask	18 hrs
WtypeG2	No plasmid	2L shake flask	18 hrs
WtypeG3	No plasmid	2L shake flask	26 hrs

Table 6.1. Cell Pastes used in lysis studies.

Quantification of cellular chromosomal and plasmid DNA

Cell pastes shown in Table 6.1 were resuspended in 10 mL STET buffer (5% sucrose, 25 mM Tris, 10 mM EDTA, 5% Triton, pH 8.0). The resuspended cells were divided into 2 mL aliquots and Ready-Lyse lysozyme was added to 10 EU/mL. Each sample was incubated at 37°C for 1 hour with gentle mixing. Proteinase-K was added to a concentration of 1 mg/ml and the lysate incubated for 2 hours at 55°C. After digestion, the lysates were manually sheared in a 0.007" PEEK capillary at 3 to 6 ml/min (75,000 s^{-1} to 150,000 s^{-1} internal capillary wall strain rate). This level of capillary shear has been demonstrated to fragment chromosomal DNA without damaging the supercoiled plasmid DNA. Fragmentation of chromosomal DNA minimised chromosomal yield loss during clarification, maximising chromosomal DNA

recovery. The clarified lysates were IPA-precipitated, as described in chapter 4, resuspended in TE and assayed by Poros PI and Q-Sepharose HPLC.

Alkaline lysis and lysozyme-heat lysis

Some or all of the previously described cell pastes (Table 6.1) were resuspended, lysed and clarified at 2 mL scale using the standard alkaline lysis procedure or the standard lysozyme-heat lysis procedure described in Materials and Methods, chapter 4. Plasmid yield and chromosomal contamination was determined by Q-Sepharose and Poros PI HPLC assays.

6.3.4 Detergent concentration in lysis buffer

The two constituents of the alkaline lysis buffer are sodium dodecyl sulphate detergent (typically 1% w/v) and sodium hydroxide (typically 0.2 M NaOH). SDS plays a critical role during lysis by disrupting the *E. coli* cell wall. However, Kieser et al. (1984) reported that above a certain threshold concentration of SDS, the lysis performance was relatively insensitive to detergent concentration. To verify that result, pSVβ containing cell paste, pSVβP2, was alkaline lysed at 2 mL scale using 0.2 M NaOH and either 0.5%, 1% or 2% SDS. The lysate was neutralised and clarified as per the standard protocol and assayed by Poros PI HPLC. Each lysis condition was performed in duplicate.

6.3.5 NaOH concentration in lysis buffer: denaturation of plasmid and chDNA

Using NaOH concentration instead of pH to control DNA denaturation

Measurement of pH of TE buffers, lysis buffers and cell lysate was performed using Beckman pH/ISE meter (Beckman Instruments Inc., CA, USA). The pH probe was calibrated each day using pH 4, 7 and 10 standards from Fisher Scientific.

Effect of NaOH on pure DNA solutions.

The effect of NaOH concentration on pure supercoiled plasmids in TE was examined to determine the NaOH concentration range over which plasmids pSVβ (6 kb), pQR150 (13 kb), pQR186 (20 kb), and p5124 (116 kb) irreversibly denature. One volume (0.5 mL) of pure supercoiled plasmid, at 10 μg/mL to 50 μg/mL in TE, was mixed with one volume of NaOH (0 to 0.4 M NaOH) in a 2 mL tube. After 3 minutes the pH was reduced to pH 8 by the addition of one volume of 500 mM Tris, pH 7.5. The samples were assayed for intact supercoiled plasmid by Poros PI HPLC, Picogreen flourescence and agarose gel electrophoresis.

Effect of NaOH on cell lysate

In order to assess the effect of plasmid and chromosomal DNA denaturation on plasmid yield and purity over alkaline lysis, *E. coli* cells (both plasmid-containing and plasmid-deficient) were lysed with SDS over a range of NaOH concentrations and for a range of lysis times. To 0.5 mL of cell resuspension, one volume of 1% SDS, 0 to 0.4 M NaOH was added. Each sample was mixed gently by inversion. The lysates were neutralised, mixed gently, and clarified as per the standard protocol described in chapter 4, section 4.3.6. The clarified alkaline lysates were assayed for supercoiled plasmid, DNA impurities and RNA using Poros PI HPLC, Q-Sepharose, Picogreen fluorescence and agarose gel electrophoresis.

6.3.6 Denaturation time

In order to assess the effect of both NaOH concentration and lysis time on lysis performance, 0.5 mL resuspended pSVβ cells were lysed with one volume of 1% SDS, 0.1 to 0.3 M NaOH, and mixed gently by inversion. The samples were incubated for 2, 10 or 60 minutes, after which time one volume of chilled neutralisation buffer was added. The samples were mixed gently by inversion and clarified as per the standard protocol. All samples were prepared in duplicate.

6.3.7 Fluid mixing

Degradation rate of supercoiled plasmid in neat lysis buffers

Experiments were carried-out to estimate degradation times of supercoiled plasmid DNA in cells exposed to high NaOH concentrations. Resuspended cells (0.2 mL volume) were mixed rapidly with 30 volumes of 0.5% SDS lysis buffer with 0.1 M, 0.2 M or 0.4 M NaOH. Because the lysis reagent volume was so much greater than the cell suspension volume, the NaOH concentration remained essentially the same after addition of cells. After 5 s, 20 s or 90 s, the samples were rapidly diluted to 0.1 M NaOH using water while mixing vigourously. Each sample was then mixed gently for 5 minutes, after which they were neutralised and clarified as per the standard protocol. The clarified alkaline lysates were assayed by Poros PI HPLC. Each lysis condition was repeated in triplicate.

Supercoiled plasmid yield at worst-case mixing conditions

2 mL of 0.2 M NaOH was added drop-wise over 100 s to 2 mL volume of resuspended *E. coli* DH5α pSVβ cells in TE buffer in a test tube. The test-tube was not mixed until all the NaOH was added. Then the material was neutralised with 2 volumes of 500 mM Tris, pH 7.5 and assayed for supercoiled content by both Picogreen and HPLC assay. A control experiment was

run where the same volume of NaOH was added to pure plasmid in TE but mixed rapidly in less than 2 s.

Stirred Tank Mixing Studies

Several alkaline lysis experiments were carried out in a small mechanically agitated vessel to assess the impact of mixing on the yield and quality of plasmid DNA. The vessel had a diameter of 60 mm, was equipped with a standard 20 mm diameter, 6-bladed Rushton turbine impeller, and fitted with four vertical baffles, each 8mm wide, equally spaced around the vessel wall. The dimensions of the vessel were chosen to be geometrically similar to stirred tanks commonly used in mixing studies (Coulson et al., 1991). Figure 6.1 shows the dimensions of the stirred tank, baffles and impeller. The total volume of the vessel was 200 mL.

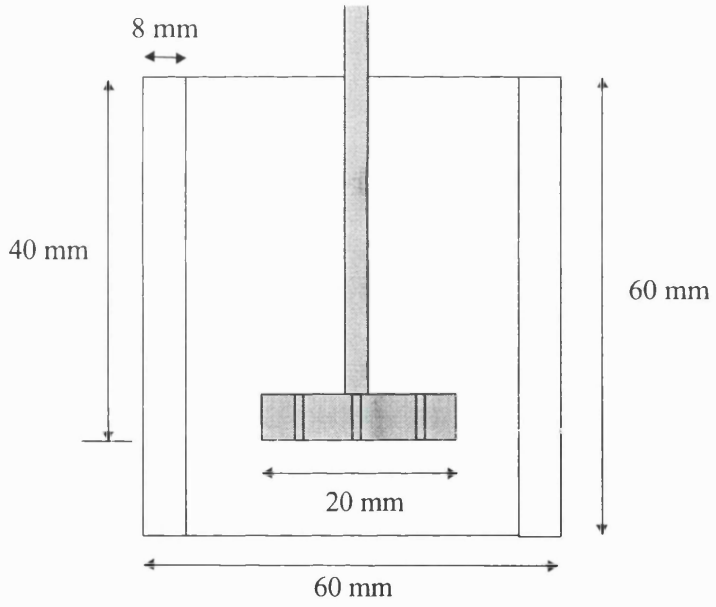

Figure 6.1. Scale-down stirred tank alkaline lysis reactor

Before lysing cells in the vessel, the macro-mixing time in the vessel was determined as a function of impeller speed by performing spiking studies with 5 M NaCl. The vessel was filled to 200 mL with resuspended cells and a conductivity probe was placed in the vessel. While mixing at a fixed impeller speed, 50 µl of 5 M NaCl was injected onto the liquid surface. The time taken for the conductivity to reach a steady-state, within 5% of its final value, was recorded. This was repeated for a selection of impeller speeds.

The effect of impeller speed during alkaline lysis on supercoiled plasmid yield was investigated. 100 mL of resuspended cells was placed in the vessel and lysis buffer was added over 2 minutes while stirring at set impeller speeds between 0 and 800 rpm. The lysis buffer was added

subsurface, directly into the outer edge of the impeller blades in all experiments. The first set of experiments was carried-out using 0.2 M NaOH, 1% SDS lysis buffer; the second set using 0.4 M NaOH lysis buffer, 1% SDS. Lysis buffer was added subsurface directly into the impeller blades, and was added to a final concentration of 0.1 M NaOH in all cases. After addition, the lysate was mixed at 800 rpm impeller speed for 10 minutes. The lysate was then neutralised by the addition of one volume of neutralisation buffer at 800 rpm impeller speed and clarified using the standard protocol. As a control, 0.5 mL of the same resuspended cells were lysed at 2 mL scale using the standard lysis protocol. All lysis experiments were done in duplicate.

6.3.8 Effect of fluid stress during lysis of plasmid-deficient cells.

Effect of fluid stress on chDNA contamination

Wild-type *E. coli* cell paste (plasmid-deficient) from three separate fermentations (WtypeG1, WtypeG2, WtypeG3) were resuspended in TE and lysed with one volume of lysis reagent (0.2 M NaOH, 1% SDS). The lysates were subjected to varying amounts of fluid stress. Samples were moderately stressed by straining 1 mL of sample in a cone-and-plate viscometer at 5 to 760 s^{-1}, for 10 to 20 minutes. Samples were subjected to high stress by forcing 5 mL of sample 10-times through a 0.010" ID PEEK capillary at flowrates up to 15 mL/min (internal wall strain rate of 130,000 s^{-1}). The samples were then neutralised and clarified using the standard protocol. The clarified lysate samples were assayed by Poros PI HPLC for chromosomal DNA.

Effect of shear on chromosomal DNA fragment size

Although the previous studies have shown that fluid shear during lysis does not cause a large increase in chromosomal DNA contamination in clarified lysates; it was of interest to determine if fluid shear was causing significant DNA fragmentation. Because single-stranded DNA is difficult to detect with ethidium bromide in agarose gels, it was advantageous to keep the chromosomal DNA in double-stranded form. Thus, for the purpose of assaying the samples by gel electrophoresis, the lysis operation was initially carried out in the absence of NaOH in the lysis solution, thus avoiding the denaturation step. Resuspended DH5α cells (plasmid-deficient) were gently mixed with 0.5 % SDS for 20 minutes to lyse the cells. The lysate was divided into 5 equal aliquots and each aliquot was subjected to a different level of fluid stress. Each aliquot was placed in a syringe and, using the Hamilton syringe-pump, pushed 10-times through a 5 cm long, 0.010" ID PEEK capillary at flowrates up to 20 mL/min. Samples of each lysate were taken for pulsed-field agarose gel electrophoresis. Samples for pulsed-field electrophoresis were pre-treated by digesting the cell debris with 0.1 mg/ml Proteinase-K at 55°C for 2 h. The remaining lysates were denatured with one volume of 0.2 M NaOH, mixed

gently by inversion, and neutralised and clarified as per the standard protocol. The clarified alkaline lysates were assayed for chromosomal DNA by Poros PI HPLC.

6.3.9 Effect of fluid stress on the lysis of plasmid-containing cells

E. coli DH5α pSVβ cell pastes were resuspended in TE and lysed with one volume of lysis reagent (0.2 M NaOH, 1% SDS). The lysates were subjected to varying amounts of fluid stress. Samples were moderately stressed by straining 1 mL of sample in a cone-and-plate viscometer at 5 to 760 s^{-1}, for 10 to 20 minutes. Samples were subjected to high stress by forcing 5 mL of sample 10-times through a 0.010" ID PEEK capillary at flowrates up to 15 mL/min (internal wall strain rate of 130,000 s^{-1}). The samples were then neutralised and clarified using the standard protocol. The clarified lysate samples were assayed for supercoiled plasmid DNA by agarose gel electrophoresis and Poros PI HPLC, and assayed for DNA impurities by Poros PI HPLC. Plasmid purity was defined as the percentage of the total DNA that is supercoiled. Non-supercoiled DNA impurities are chromosomal DNA and plasmid degradates (linear, open-circular and denatured plasmids).

6.3.10 Effect of fluid stress during neutralisation

E. coli DH5α pSVβ cell paste was resuspended in TE and lysed with one volume of lysis reagent (0.2 M NaOH, 1% SDS). The lysates were neutralised with one volume of neutralisation buffer. Neutralised cell lysate was moderately stressed by straining 1 mL of sample in a cone-and-plate viscometer at 5 to 760 s^{-1}, for 10 minutes. Neutralised cell lysate was subjected to high stress by forcing 5 mL of sample 10-times through a 0.010" ID PEEK capillary at a strain rate up to 30,000 s^{-1}. The samples were then clarified using the standard protocol. The clarified lysate samples were assayed for supercoiled plasmid DNA by agarose gel electrophoresis and Poros PI HPLC, and assayed for DNA impurities by Poros PI HPLC. Plasmid purity was defined as the percentage of the total DNA that is supercoiled. Non-supercoiled DNA impurities are chromosomal DNA and plasmid degradates (linear, open-circular and denatured plasmids).

6.4 Experimental results

6.4.1 Control experiments

Prior to investigating the effects of fluid mixing and fluid stress during alkaline lysis, several control experiments were performed to ensure that the storage, resuspension and clarification

procedures associated with alkaline lysis were robust, reliable and were not adversely affecting the performance of alkaline lysis.

Effect of freeze-thawing cell paste on clarified lysate purity

Figure 6.2 shows the yield of chromosomal DNA in clarified alkaline lysates, as measured by Poros PI HPLC, for two samples: i) cell paste lysed immediately after harvest, and ii) harvested cell paste frozen at –20°C overnight, thawed and then lysed. There was a small difference in the level of chromosomal DNA contamination between the clarified lysates; and the difference was within the standard deviation of the experiments. Results shown are the averages of 2 experiments on the same cell paste. It was concluded that the freezing cell paste for long-term storage, followed by thawing, should not detrimentally impact chromosomal DNA contamination.

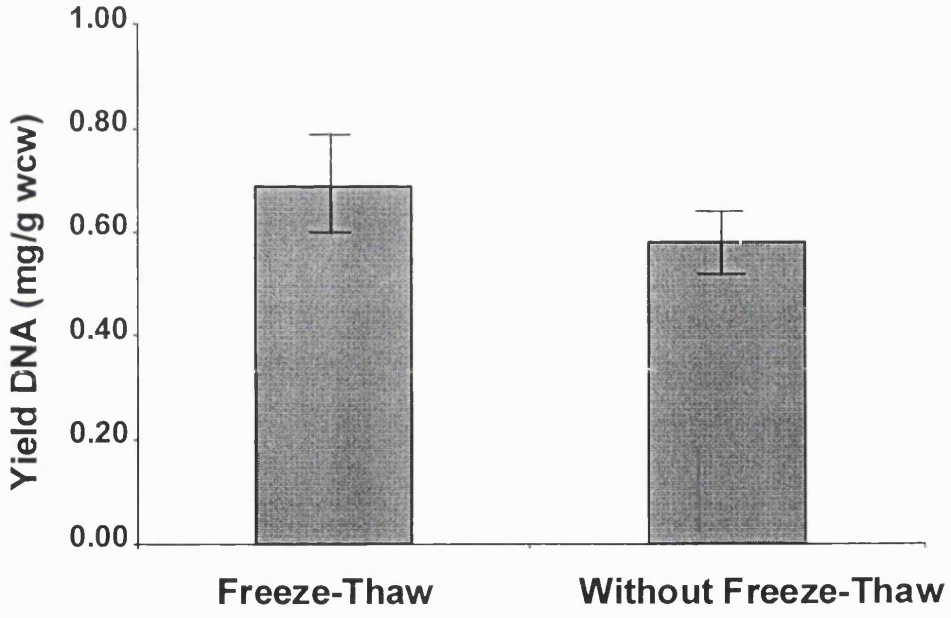

Figure 6.2. Bar chart showing the effect of freeze-thawing harvested *E. coli* cells on chDNA contamination post-alkaline lysis.

Resuspension Concentration

E. coli DH5α pSVβ cell paste was resuspended at different concentrations (L TE buffer/g wet cell weight). The supercoiled yield (mg SC plasmid/g wcw) in the clarified lysates is shown in Figure 6.3. The resuspension concentration significantly affects the supercoiled plasmid yield. At high cell paste concentrations, alkaline lysis was not efficient. This is probably due to the cells not being fully resuspended at high concentrations. The standard resuspension condition of 8 mL TE/g wcw was optimum for supercoiled plasmid yield, and was used throughout.

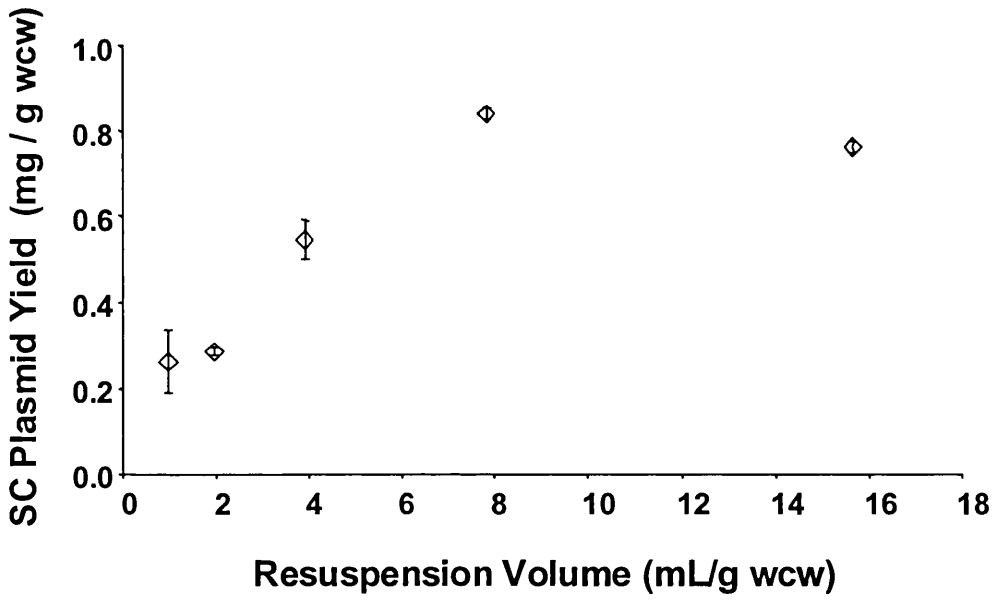

Figure 6.3. Plot showing the effect of cell resuspension volume on supercoiled plasmid yield. Error bars represent one standard deviation. Each data point represents the average of 3 separate experiments.

Effect of clarification conditions.

Figure 6.4 shows the plasmid yield and purity for the four different clarification conditions that were tested. Each data point is the average of 2 experiments. There was no significant variation in plasmid yield or purity between the clarification methods tested. However, for consistency the standard clarification procedure was used throughout.

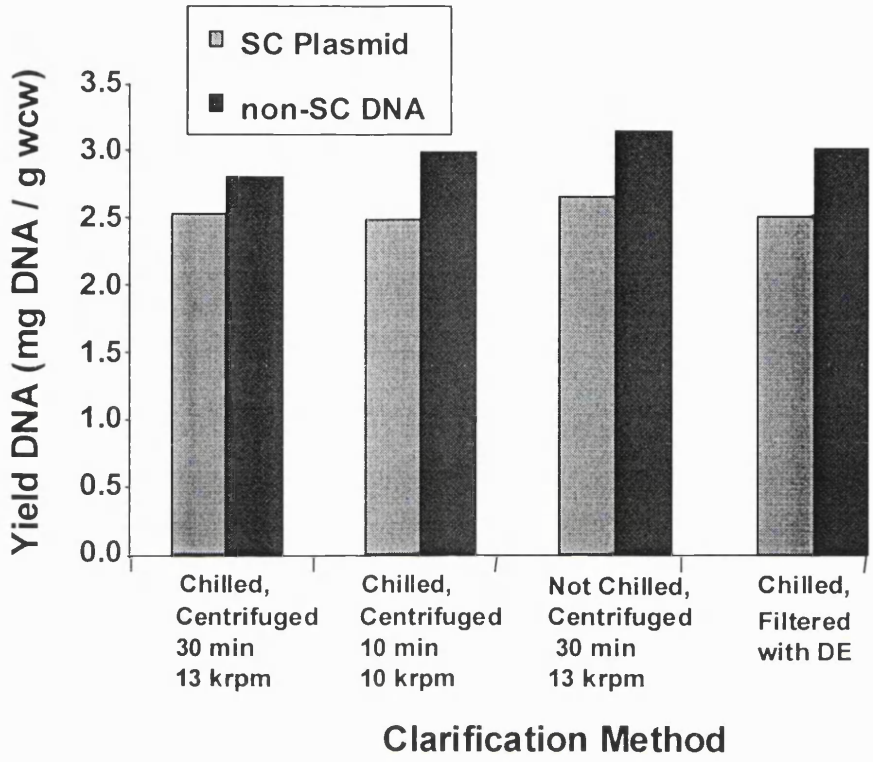

Figure 6.4. Bar chart showing the effect of clarification method on plasmid yield and chDNA contamination.

6.4.2 Standard lysis protocols

Before investigating the effects of fluid mixing and stress during alkaline lysis, it was essential to determine the total quantity of supercoiled plasmid and DNA impurities within *E. coli* cells. Following this, the standard lysis techniques were evaluated for extraction of plasmid product and clearance of DNA impurities.

Quantification of cellular chromosomal and plasmid DNA

Table 6.2 shows the supercoiled plasmid, open-circular plasmid, double-stranded chromosomal DNA, and single-stranded DNA extracted by completely digesting E coli DH5α cell pastes. For cell paste pSVβP1, the total amount of DNA in the plasmid containing cells was 4.0 mg/g wcw, of which 50% was chromosomal DNA and linear plasmid, 42.5% was supercoiled plasmid and 7.5% was open-circular plasmid. It was not possible to quantify linear plasmid fragments separately from chromosomal DNA using Q-Sepharose HPLC. However, a linear plasmid band was not visible on an agarose gel of the clarified lysate showing that linear plasmid was negligible in quantity. Thus, 85% of the total plasmid was in the supercoiled form and 15% of

the plasmid was in the open-circular form. Because some open-circular plasmid will be generated from the degradation of supercoiled plasmid during the lysis step, there was at most 15% open-circular plasmid present in the cells before digestion. The chromosomal DNA and supercoiled plasmid DNA yields were similar for cell paste pSVβP2; however, cell paste pSVβP2 contained twice as much open-circular plasmid. The amount of chromosomal DNA in the cell (about 2 mg/g wcw) corresponds to just under 2 copies of the genome per *E. coli* cell (Ingrahm et al, 1999).

The amount of chromosomal DNA in the plasmid-deficient cells harvested after 26 hours (WtypeG3) was 1.9 mg/g wcw, which was similar to the amount in the plasmid containing cells. Both the plasmid containing cells (pSVβP1 and psvβP2) and 26 hr plasmid-deficient cells were harvested while the cells were in stationary phase. In contrast, the plasmid-deficient cells harvested after 18 hrs (WtypeG1 or WtypeG2) were in late exponential phase and contained significantly more chromosomal DNA, 4.1 mg/g wcw. This amount of chromosomal DNA corresponds to about 4 copies of the genome per *E. coli* cell. Exponentially dividing cells are known to contain more copies of their genome than stationary phase cells (Ingrahm et al, 1999), which may explain the difference in chromosomal DNA observed between the cell pastes.

Although the supercoiled plasmid yields were similar for the batches of cell paste shown in Table 1.1, generally there was quite a variation in supercoiled plasmid yield depending on cell paste. Over the course of this work, 6 cell pastes containing plasmid pSVβ were assessed for supercoiled plasmid content, with total supercoiled plasmid yields in the range 1.5 to 3.5 mg/g wcw and chromosomal DNA yields in the range 2 to 5 mg/g wcw. Further details on the fermentation conditions and fermentation results for the pSVβ containing cell pastes are described in the thesis of Kay (2002).

Evaluation of standard alkaline lysis

E. coli cells, both plasmid-deficient and plasmid containing, were alkaline lysed, refer to Table 6.1. The plasmid and chromosomal DNA yields are shown in Table 6.3. The results shown are the averages of 2 experiments. The most significant result for the plasmid containing cells was that the supercoiled plasmid recovered from the cells using standard alkaline lysis was only 47% to 54% of the total supercoiled plasmid in the cells. Later studies (see section 6.4.4) showed that supercoiled plasmid degradation due to pH or fluid stress was low under the alkaline lysis conditions used; hence, the low yield was most likely due to either incomplete cell lysis or entrapment of supercoiled plasmid during neutralisation and flocculation.

Lysis Method	Cells	SC Plasmid mg / g wcw	OC Plasmid mg / g wcw	ds-chDNA mg / g wcw	ss-chDNA mg / g wcw	SC / Total DNA %
Proteinase-K Digestion	PsvbP1	1.7 ± 0.1	0.3 ± 0.05	1.9 ± 0.2	0.1 ± 0.03	42%
Proteinase-K Digestion	PsvbP2	1.7 ± 0.2	0.6 ± 0.1	2.2 ± 0.3	0.1 ± 0.05	37%
Proteinase-K Digestion	WtypeG1	N/A	N/A	4.0 ± 0.3	0.1 ±0.02	N/A
Proteinase-K Digestion	WtypeG2	N/A	N/A	3.9 ± 0.2	0.1 ± 0.03	N/A
Proteinase-K Digestion	WtypeG3	N/A	N/A	1.8 ± 0.1	0.1 ± 0.02	N/A

Table 6.2. Yields of plasmid and chromosomal DNA in 3 *E. coli* cell pastes.

HPLC analysis of clarified alkaline lysate from cell paste pSVβP1 showed 62% of the total DNA recovered was supercoiled plasmid, 15% open-circular plasmid, 8% double-stranded chromosomal DNA and 15% single-stranded DNA. Single-stranded DNA impurities consisted of denatured chromosomal DNA and denatured plasmid forms, both of which are linear, single-stranded fragments of DNA. As already discussed, determining the fraction of single-stranded DNA contaminants which are chromosomal in origin versus plasmid in origin can only be done using sequence analysis by PCR (Lahijani et al., 1998). If all of the single-stranded DNA impurities are chromosomal DNA, which is likely due to the relatively low initial levels of open-circular DNA in the cells, then 15% of the total initial chromosomal DNA in the cells was carried-over into the clarified lysate.

The yield of supercoiled plasmid from cell paste pSVβP2 was similar to that of pSVβP1. However, more single-stranded DNA impurity was present in the clarified lysate from cell paste pSVβP2, which reduced the lysate purity to 36%, compared to 62% purity from cell paste pSVβP1. Some of this decrease in purity was probably due to the increased open-circular plasmid content in cell paste pSVβP2; some of the open-circular plasmid will be denatured during alkaline lysis and carried-over into the clarified lysate. The denaturation of open-circular plasmid is discussed further in this chapter and in chapter 7.

The supercoiled plasmid purity after alkaline lysis (62% and 36%) reported here was lower than the value of 88% reported by Ciccolini et al (2002). This difference may be due using different

cell pastes, as well as differences in analytical techniques. Ciccolini et al used agarose gel electrophoresis to quantify DNA contamination, which tends to underestimate single-stranded chromosomal DNA contamination (the principal DNA contaminant) due to the poor binding of ethidium bromide to the single-stranded form of DNA. The supercoiled plasmid purity reported here is also significantly lower than the values reported by Chamsart et al. (2001) (< 2 % chromosomal DNA). The lysate samples assayed by Chamsart et al. were purified using Qiagen columns before assaying for chromosomal DNA, which could potentially have removed a significant amount of the DNA impurities.

For the plasmid-deficient cells, the amount of chromosomal DNA remaining after alkaline lysis, as a percentage of chromosomal DNA before lysis was 8%, 15% and 2%, for cell pastes WtypeG1, WtypeG2 and WtypeG3, respectively. Hence, there was a significant variation in the amount of chromosomal DNA contamination in the alkaline lysates from the three cell pastes. The amount of chromosomal DNA contamination in clarified alkaline lysates was a function of the amount released from the cells, as well as the amount that was removed from solution during the neutralisation/flocculation step. It was observed that the 26 hour harvested cells (WtypeG3) did not resuspend completely following addition of alkaline lysis reagent, so the low yield of chromosomal DNA for this cell paste was probably due to poor alkaline cell lysis. Alkaline lysis alone may not be a suitable lysis technique for this cell paste. For the more easily lysed cells, harvested after 18 hrs, 8% to 15% of the initial chromosomal DNA was found in the clarified lysate. By incubating the cells with SDS for 15 minutes before adding NaOH, to increase lysis efficiency, the amount of contaminating chromosomal DNA increased to 25% of the initial amount in the cells. Again, the amount of contaminating chromosomal DNA in the clarified alkaline lysates from the wild-type cell pastes was considerably higher than the values reported by Chamsart et al.

In summary, supercoiled plasmid yields using alkaline lysis were only about 50% of the total supercoiled plasmid within the cell, supercoiled plasmid purity was about 30% to 60%, and significant chromosomal DNA contamination occurred in all the clarified alkaline lysates tested.

Lysis Method	Cells	SC Plasmid mg / g wcw	OC Plasmid mg / g wcw	ds-chDNA mg / g wcw	ss-DNA mg / g wcw	Purity %
Alkaline Lysis	psvβP1	0.9 ±0.05 [1](53%)	0.2 ±0.02 [2](67%)	0.1 ±0.03	0.2 ±0.04 [3](15%)	64%
Alkaline Lysis	psvβP2	0.8 ±0.07 [1](47%)	0.3 ±0.01 [2](50%)	0.1 ±0.02	1.1 ±0.08 [3](52%)	34%
Alkaline Lysis	Wtype G1	N/A	N/A	0.02 ± 0.006	0.3 ±0.04 [3] (8%)	N/A
Alkaline Lysis	Wtype G2	N/A	N/A	0.02 ±0.005	0.6 ±0.08 [3] (15%)	N/A
Alkaline Lysis w/ pre-SDS	Wtype G2	N/A	N/A	0.02 ±0.006	0.8 ±0.05 [3] (25%)	N/A
Alkaline Lysis	Wtype G3	N/A	N/A	0.02 ±0.008	0.01 ±0.003 [3] (2%)	N/A

Table 6.3. Plasmid and chromosomal DNA yields after alkaline lysis for plasmid containing and non-plasmid containing *E. coli* cells. [1]Supercoiled plasmid post-alkaline lysis divided by initial amount in the cells. [2]Total open-circular plasmid DNA post-alkaline lysis divided by initial amount in the cells. [3]Total non-plasmid DNA divided by total initial chromosomal DNA in the cells before lysis.

Evaluation of lysozyme-heat lysis

Using lysozyme and heat to lyse E. coli cells for plasmid extraction is another common lysis method (Lee et al. 1994). The performance of lysozyme-heat lysis was evaluated for cell paste pSVβP2. The results shown in Table 6.4 are the averages of 2 experiments. The supercoiled plasmid yield using lysozyme-heat lysis was significantly better than alkaline lysis. The supercoiled plasmid yield using lysozyme followed by heat lysis at 20°C was 92% ± 6% of the total supercoiled plasmid in the cell. There was no significant difference between the supercoiled plasmid yield after heating at 20°, 70° or 75°C, but there was a decrease in

supercoiled plasmid yield at 80°C, and above. The purity after lysozyme-heat lysis ranged from 28% to 37%, compared to a purity of 35% after alkaline lysis. All of the DNA impurities after lysozyme-heat lysis were in the double-stranded form, as measured by Poros PI and Q-Sepharose HPLC assays. Therefore, purification steps to remove chromosomal DNA impurities after lysozyme-heat lysis (at 20°C to 85°C) must be capable of removing double-stranded linear DNA from supercoiled plasmid. In contrast, after alkaline lysis most of the contaminating chromosomal DNA was in single-stranded form.

Method	Cells	SC Plasmid mg / g wcw	Purity %
Lysozyme + 20 C	pSVβ, DH5α	1.6 ± 0.1	37%
Lysozyme + 70 C	pSVβ, DH5α	1.4 ± 0.1	35%
Lysozyme + 75 C	pSVβ, DH5α	1.5 ± 0.2	35%
Lysozyme + 80 C	pSVβ, DH5α	1.3 ± 0.1	33%
Lysozyme + 85 C	pSVβ, DH5α	1.2 ± 0.2	28%

Table 6.4. Yields of supercoiled plasmid DNA and sample purity for 3 lysis methods.

From these experiments it was concluded that the principal advantage of heating the cells after lysozyme treatment was not increased supercoiled plasmid yield or decreased chromosomal contamination, but instead was enhanced flocculation and clarification of the cell debris. The enhanced flocculation observed after heating was due to increased protein denaturation at high temperature.

6.4.3 Effect of detergent concentration in lysis buffer

E. coli cell paste, pSVβP2, was alkaline lysed at 2 mL scale using 0.2 M NaOH with various amounts of SDS detergent. The clarified alkaline lysates were assayed by Poros PI HPLC. There was no significant variation in supercoiled plasmid yield (0.8 ± 0.1 mg/g wcw) and purity (34% ± 3%) over the SDS concentration range investigated (0.5%, 1% or 2% w/v SDS).

6.4.4 Effect of NaOH in lysis buffer: denaturation of plasmid and chDNA

The purpose of the NaOH in lysis buffer is to increase the pH from pH 8 to about pH 12.7. This pH increase has two principal effects: i) increased cell lysis by denaturing cell wall and cell membrane constituents and ii) denaturation of DNA to single-stranded form. It has been reported by Birnboim et al. (1979) that double-stranded, linear DNA denatures to single-stranded form between pH 12 and pH 13 , and that supercoiled plasmid DNA typically denatures at a slightly higher pH than chromosomal DNA. If supercoiled plasmid DNA is denatured by high pH, the plasmid is converted to a compact, non-supercoiled form, which cannot be converted back to native, supercoiled plasmid. It has more recently been demonstrated by Thatcher et al. (1997), that there is a pH window of about ± 0.2 pH units below which no supercoiled plasmid denatures and above which all the supercoiled plasmid denatures irreversibly. They reported that this pH window lies between pH 12 to pH 13, and varied for different plasmids. It was suspected that the pH of the lysis buffer affected the mixing requirements during cell lysis; therefore, the effect of NaOH concentration and the time of exposure to NaOH on supercoiled plasmid yield and purity were studied in detail.

Using NaOH concentration instead of pH to control DNA denaturation

Due to the high concentration of cell debris which will foul a pH electrode, and the presence of Tris which can give erroneous pH values with some electrodes, accurately and reproducibly measuring the pH of alkaline lysate is generally not possible. Figure 6.5 shows the measured pH as a function of NaOH concentration in TE buffer and in *E. coli* cell resuspension. In the cell solution, there is a small decrease in pH, compared to TE buffer, due to the buffering effect of the cells. For both systems, at the pH where irreversible DNA denaturation occurs (pH 12 to 13), a large change in NaOH concentration produces only a small change in pH; hence, the pH can be accurately adjusted by the addition of NaOH. This is important since even a small error in pH measurement (± 0.2 pH units) can lead to significant levels of supecoiled plasmid degradation.

During alkaline lysis experiments, both the pH and the NaOH added were routinely monitored. It was determined over many experiments that lysing at a set NaOH concentration gave significantly more reproducible results than attempting to lyse cells at a set solution pH. This was most likely due to the difficulty in measuring pH in an alkaline lysate environment as already described.

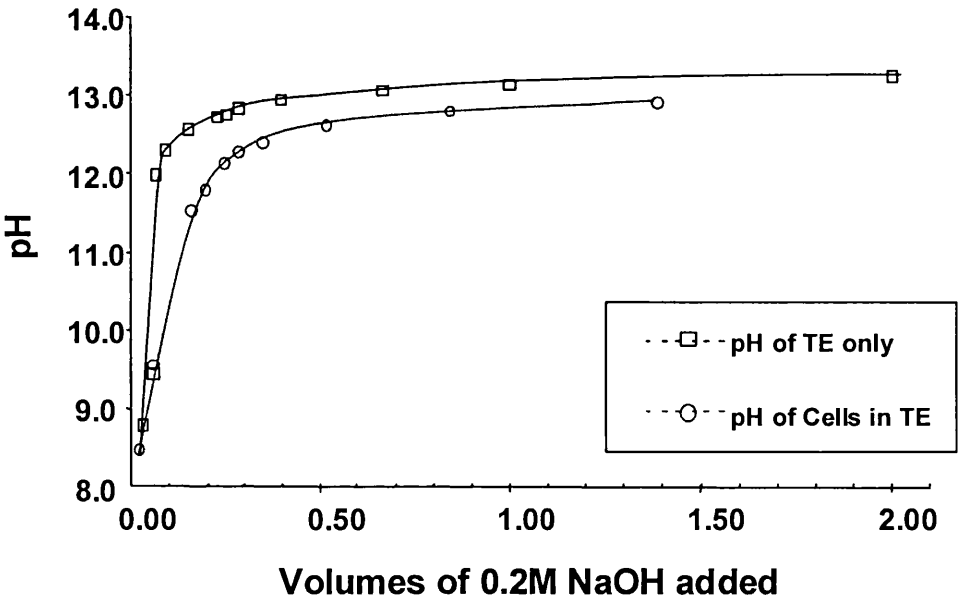

Figure 6.5 Plot showing the effect on pH of adding 0.2 M NaOH to TE buffer or cells in TE buffer.

Effect of NaOH on pure DNA solutions

Figure 6.6 shows the fraction of supercoiled plasmid pSVβ in pure plasmid solutions as a function of NaOH concentration, measured by Poros PI HPLC, agarose gel and Picogreen fluorescence. As shown in Figure 6.6, the three analytical techniques give consistent results. Each data point represents 2 replicate HPLC assays, 2 replicate flourescence assays or 4 replicate agarose gel electrophoresis assays. Supercoiled plasmid pSVβ remained in its native, intact form at low NaOH concentration from 0 to 0.1 M NaOH. Between 0.12 to 0.15 M NaOH, the supercoiled plasmid became irreversibly denatured, and was fully denatured above 0.15 M NaOH. Thus, there was a narrow window of NaOH concentration where supercoiled plasmid pSVβ goes from completely intact to completely denatured form.

The effect of NaOH concentration on all four plasmids pSVβ, pQR150, pQR186 and p5176 is shown in Figure 6.7. Data obtained from Picogreen assays were plotted as the change in concentration of supercoiled plasmid DNA (C) compared to initial supercoiled plasmid concentration (C_o). All 4 plasmids showed the same trend, a sharp decrease in supercoiled plasmid over a narrow range of NaOH concentration. The plasmids denatured at slightly different NaOH concentrations, but there was no trend between denaturation concentration and plasmid size. The C/C_o values were obtained directly from the Picogreen fluorescence intensities so that the final pseudo-steady value of 0.2 represents the background measurement

from irreversibly denatured plasmid. There was a slight decrease in fluorescence between 0 M and 0.1 M NaOH for all 4 plasmids. This is probably due to the small amount of chromosomal DNA impurity present in each sample, and not due to plasmid degradation. It has already been demonstrated in chapter 4 that chromosomal DNA and open-circular DNA denature to single-stranded form between 0.02 and 0.04 M NaOH (refer to Figure 4.3). Based on the denaturation characteristics of pure DNA, the optimum window of operation for alkaline lysis should be between about 0.04 and 0.12 M NaOH.

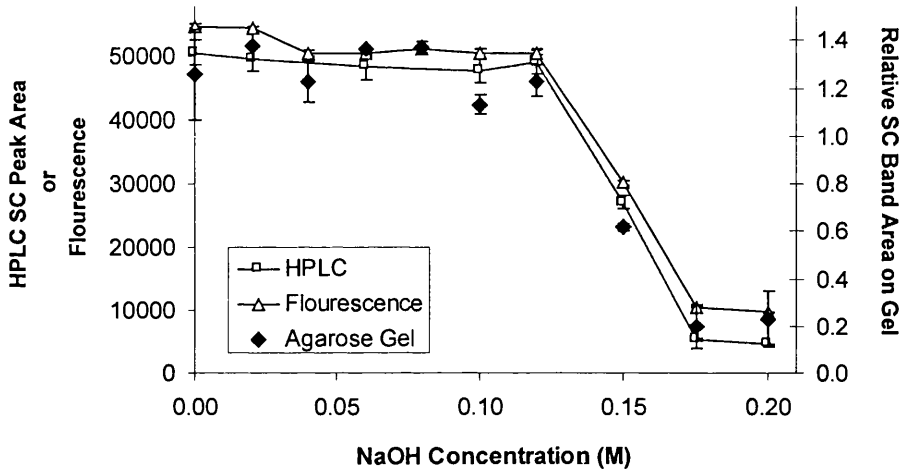

Figure 6.6 Plot showing the effect of sodium hydroxide concentration on supercoiled plasmid stability. Poros PI HPLC, Picogreen fluorescence and agarose gel electrophoresis were used to assay the samples for supercoiled plasmid. Error bars represent one standard deviation.

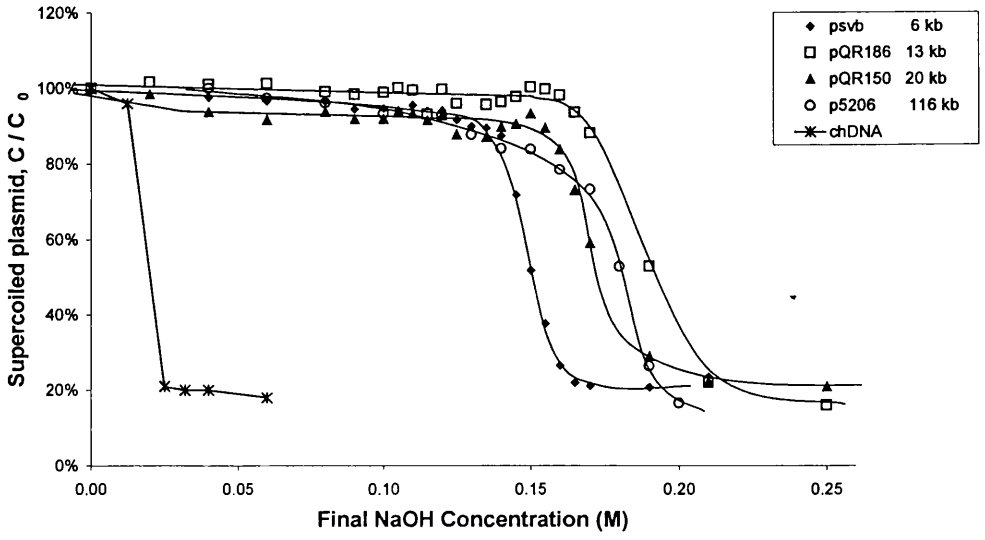

Figure 6.7.. Plot of relative supercoiled plasmid DNA concentration, C/C_0, (measured by Picogreen fluorescence) against sodium hydroxide concentration

Effect of NaOH on cell lysate

Figure 6.8 show the concentration of supercoiled plasmid in the clarified lysate as a function of the NaOH concentration during the lysis of *E. coli* DH5α pSVβ cell paste. Q-Sepharose HPLC, agarose gel electrophoresis and Picogreen assays were used to measure supercoiled plasmid content. The assays show the same trend, with an increase in supercoiled plasmid DNA yield as the NaOH concentration is increased from 0 M to 0.1 M NaOH probably due to improved cell lysis at higher pH. This was followed by a steady decrease in supercoiled yield at higher NaOH concentrations, due to supercoiled plasmid DNA denaturation. The drop in supercoiled plasmid beyond 0.1 M NaOH was not as dramatic as in pure solutions, possibly due to some buffering of the solution by the cellular debris.

In order to compare the effect of NaOH concentration on DNA denaturation in pure solution versus in cell lysates, it was necessary to know the solution pH during lysis for the two systems. Because the cells will effect the final pH of the lysis solution, it is important to consistently resuspend and lyse the cells at the same cell concentration, and to check supercoiled plasmid denaturation conditions when a new cell line is used. It should be noted that the pH over which plasmid degradation occurs is slightly lower for plasmids in cell lysate, as opposed to plasmids in pure TE buffer. It is unclear whether this measured difference is due to an error in pH measurement in the lysate solution or due to plasmid DNA being slightly more susceptible to degradation in a cell lysate environment. ..

Figure 6.9 shows the relative HLPC peak areas of all the nucleic acid species present in the clarified lysate, as measured by Q-Sepharose assay. The RNA concentration increased as the lysis concentration increased from 0 M to 0.06 M NaOH, after which the RNA concentration remained constant. This indicated that cell lysis was slightly less effective at low NaOH concentrations. Double-stranded chromosomal DNA and open-circular DNA were only present at very low concentrations below 0.06 M NaOH. This was in agreement with previous studies (see chapter 4) that chromosomal and open-circular plasmids are fully denatured to single-stranded DNA above 0.04 M NaOH. There was a sharp increase in single-stranded DNA at NaOH concentrations above 0.15 M, probably due to the supercoiled plasmid being degraded to single-stranded, denatured form.

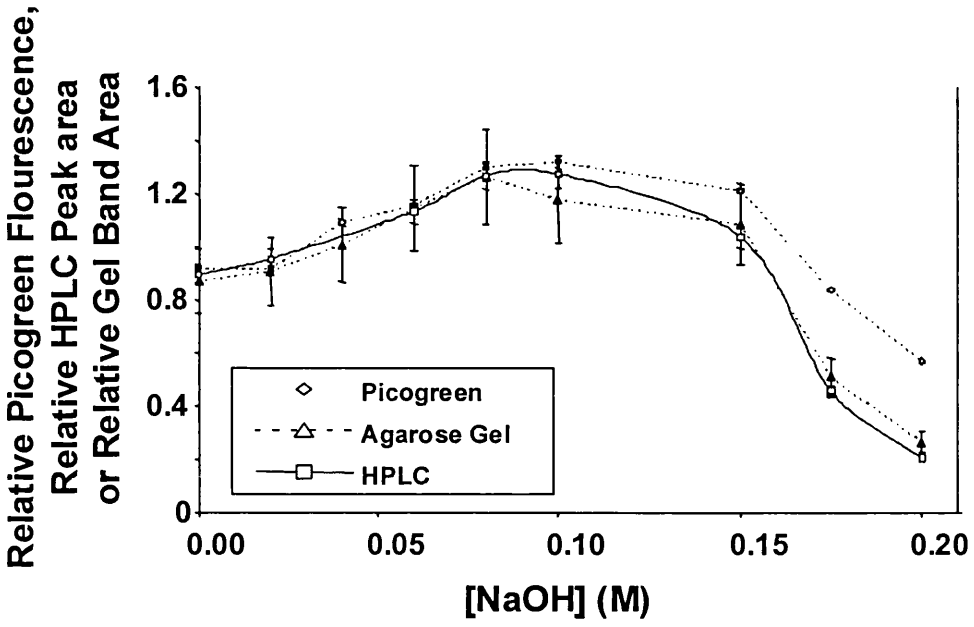

Figure 6.8. Effect of NaOH concentration on supercoiled plasmid DNA recovery in alkaline lysates.

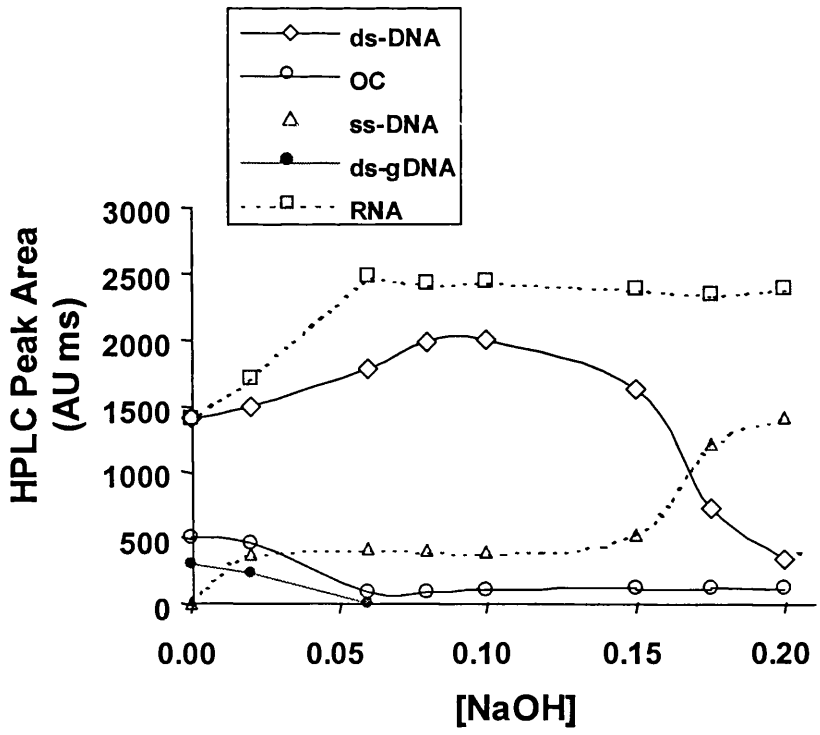

Figure 6.9. Effect of NaOH concentration during alkaline lysis on SC plasmid, OC plasmid, ss-DNA, ds-chDNA and RNA contamination in clarified lysates. Note: the RNA peak area was divided by 15 to fit on the y-axis.

Lysis of plasmid-deficient cells enabled accurate quantification of chromosomal DNA separately from plasmid degradates. Figure 6.10 shows the concentration of both double- and single-stranded DNA in the clarified lysate as a function of NaOH concentration during lysis of plasmid-deficient cells. Total chromosomal DNA contamination increased in the clarified lysate as the NaOH concentration increased, probably due to increased cell lysis at higher pH. Figure 6.10 shows, although an increased concentration of NaOH did not decrease chromosomal DNA contamination, that a high NaOH concentration close to 0.1 M NaOH was necessary to convert the entire chromosomal DNA to single-stranded form. To maximise plasmid yield and minimise double-stranded chromosomal DNA contamination, it was concluded that a target lysis concentration close to 0.1 M NaOH was optimum for the *E. coli* DH5α pSVβ system. This optimum NaOH concentration may be lower or higher depending on supercoiled plasmid or cell strain.

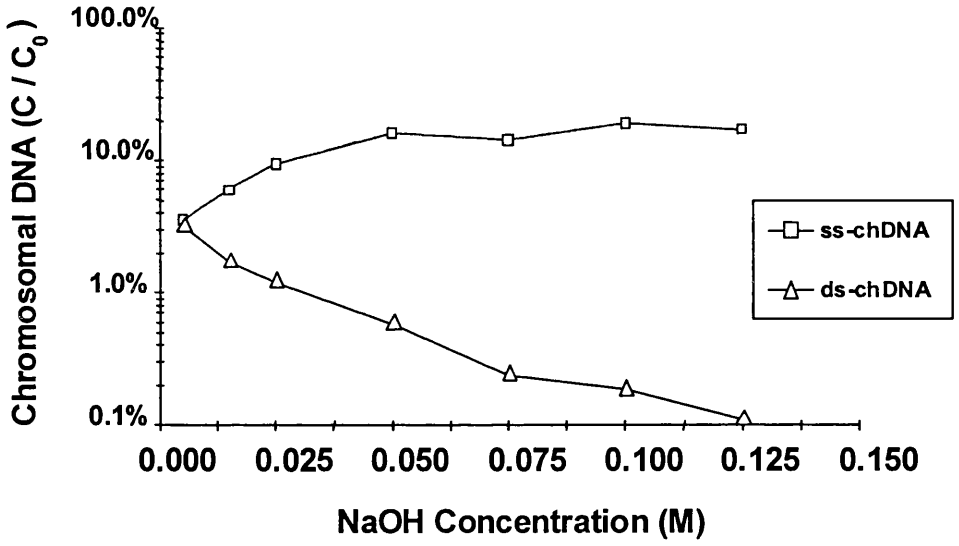

Figure 6.10 Plot showing the effect of sodium hydroxide concentration during alkaline lysis on chromosomal DNA concentration in clarified lysate.

6.4.5 Denaturation time

Figure 6.11 shows a contour plot of the supercoiled plasmid yield as a function of the NaOH concentration during lysis of DH5α pSVβ cells and as a function of the lysis time (the time between the end of lysis buffer addition and the start of neutralisation). Lysis time did not strongly affect the supercoiled plasmid yield; only lysate that was maintained at high pH (pH $\gtrsim$ 12.3) for 60 minutes showed a moderate decrease in supercoiled plasmid DNA. The amount of chromosomal DNA contamination was not significantly affected by lysis time either, as shown

in Figure 6.12. The decrease in sample purity at high NaOH concentration was due to the decreased supercoiled plasmid yield not an increase in chromosomal DNA contaminant. The optimum conditions were about 0.09 M NaOH and 10 minutes lysis time.

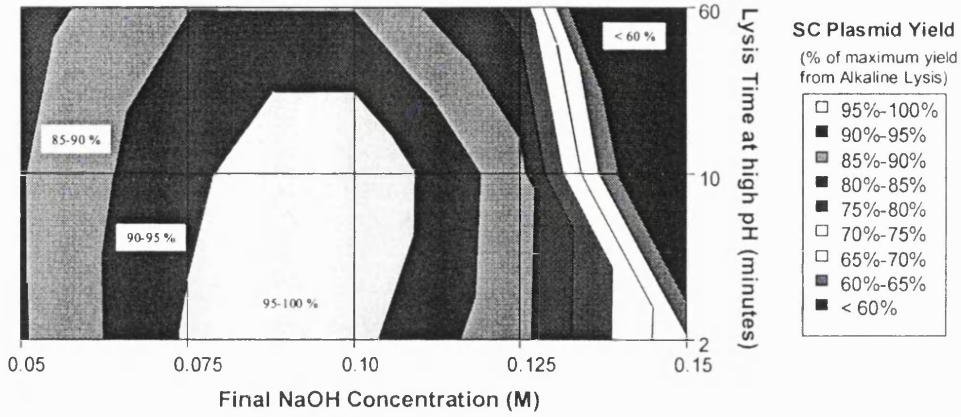

Figure 6.11 Two-dimensional contour plot showing the combined effects of lysis time and sodium hydroxide concentration on plasmid yield over alkaline lysis.

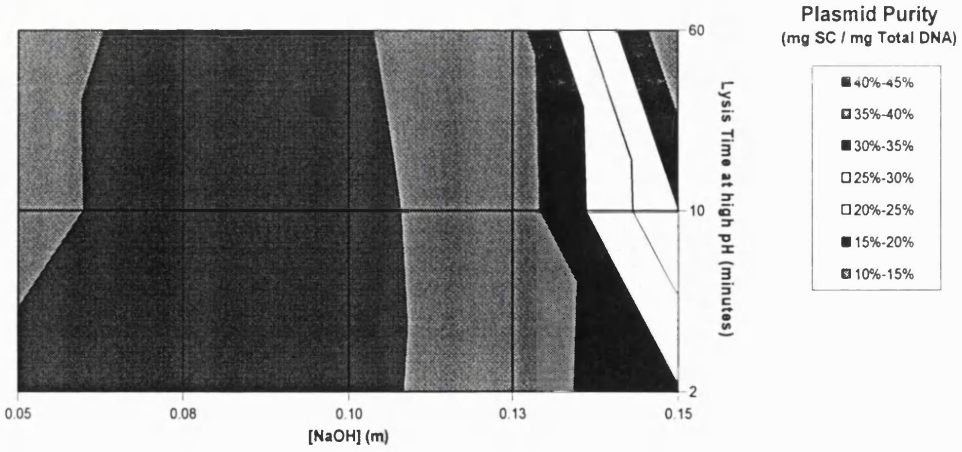

Figure 6.12 Two-dimensional contour plot showing the combined effects of lysis time and sodium hydroxide concentration on plasmid purity over alkaline lysis.

6.4.6 Fluid mixing

Prolonged exposure of supercoiled plasmid DNA to NaOH greater than 0.15 M concentration was demonstrated to cause irreversible plasmid degradation. Because lysis buffer is typically 0.2 M NaOH concentration, plasmid DNA can potentially be degraded if mixing of cells and

lysis regent is slow, where some of the cell solution can be exposed to high NaOH concentrations. Therefore, the required mixing time for an alkaline lysis reaction vessel will depend on the rate of supercoiled plasmid denaturation when exposed to concentrated lysis buffer. The vessel mixing time should be significantly less than the plasmid degradation time. This degradation time consists of the time taken for the cells to lyse, releasing plasmid DNA, and the time taken for the plasmid to denature when exposed to inhomogeneous regions of high NaOH concentration.

Degradation rate of supercoiled plasmid in neat lysis buffers

Figure 6.13 shows the supercoiled plasmid DNA yield as a function of *E. coli* cell exposure time to neat lysis buffers (0.2 M NaOH, 1% SDS or 0.4 M NaOH, 1% SDS). The plasmid yield is shown relative to the plasmid yield in the control at 0.1 M NaOH, 1% SDS. Compared to the control, there was significant plasmid yield loss even at an exposure time of only a few seconds, for the 0.2 and 0.4 M NaOH lysis buffer experiments. Based on this data, the mixing time in an alkaline lysis reactor should be significantly less than 5 s, using 0.2 M NaOH or 0.4 M NaOH lysis buffers.

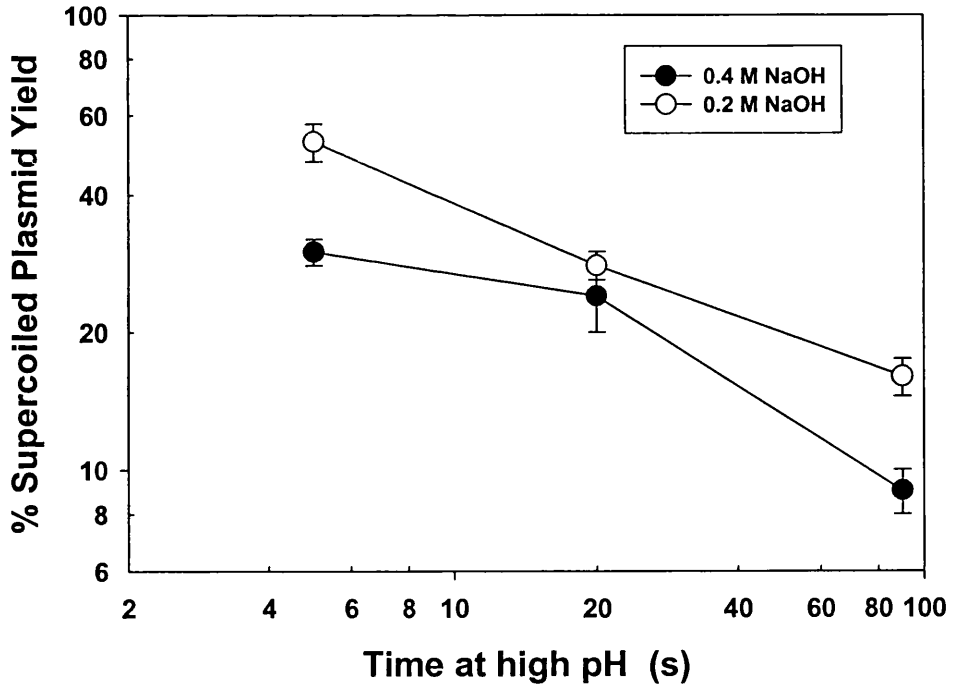

Figure 6.13. Supercoiled plasmid DNA yields (C/C_0) as a function of time of exposure of plasmid containing cells to denaturing NaOH concentrations. Each data point represents the average of 3 experiments.

Supercoiled plasmid yield at worst-case mixing conditions

Having established that high concentrations of NaOH in lysis buffer caused supercoiled plasmid DNA degradation, and that plasmid DNA degradation occured in less than a few seconds, it was obvious that the rate of mixing of lysis buffer and resuspended cells could affect the supercoiled plasmid yield. It was advantageous to first establish the effect on plasmid yield of lysis at "worst-case" mixing conditions. In order to estimate, a priori, worst case plasmid degradation, a concentration of 0.125 M NaOH was assume to be the cut-off in NaOH concentration above which plasmid would be irreversibly denatured. In practice, one volume of 0.2 M NaOH would be added to one volume of resuspended cells. Under worst case conditions there would be no mixing, and the cells and lysis buffer would be left to mix by diffusion (top box in Figure 6.14). Because the diffusion rate of NaOH is significantly higher than that of *E. coli* cells, the NaOH would rapidly diffuse into the cells. If, after expanding by 60%, the NaOH concentration is uniform (middle box in Figure 6.14), then 60% of the cells will be exposed to 0.125M NaOH, and 60% of the supercoiled plasmid would be denatured irreversibly. However, because of concentration profiles between the plasmid and NaOH phases, a significantly smaller percentage of cells would be exposed to a high NaOH concentration, maybe 20% (bottom box in Figure 6.14).

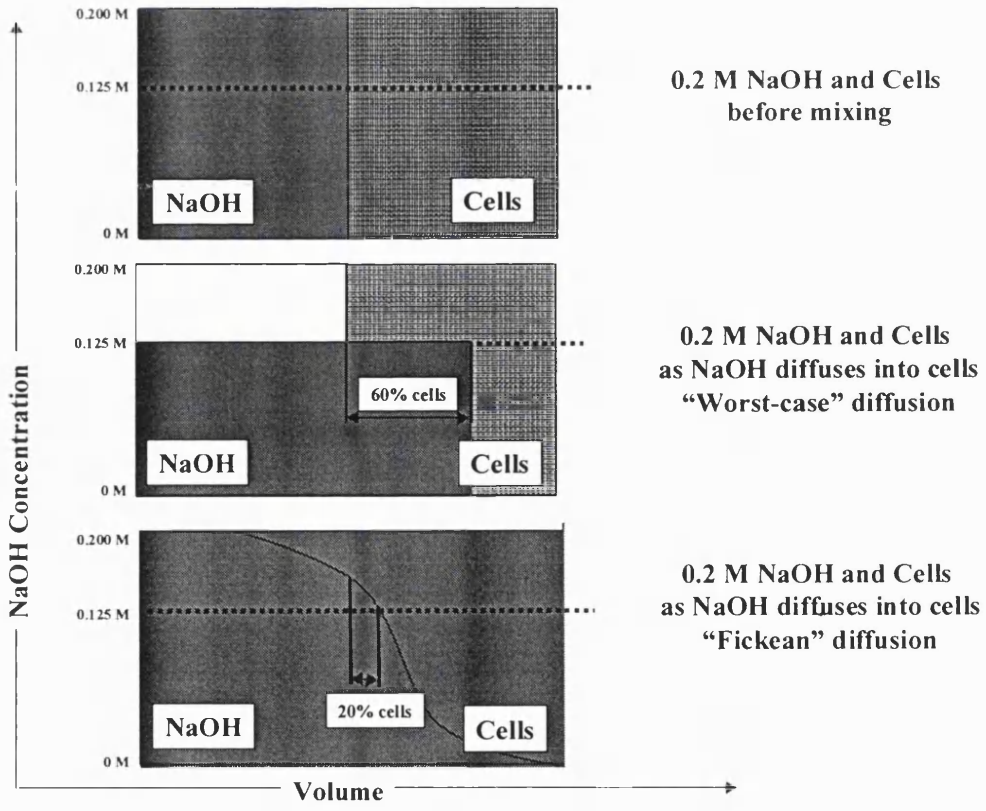

Figure 6.14. Schematic showing diffusion of NaOH into resuspended cells.

A small-scale experiment was run to determine the actual amount of plasmid degradation under worst case mixing conditions, as described in Materials and Methods. Figure 6.15 shows the supercoiled yield for the worst case mixing conditions and for the case of rapid mixing. There was a 16 - 18% loss of supercoiled plasmid DNA for the worst case mixing condition. Hence, under conditions of worst possible mixing, supercoiled plasmid degradation should be less than about 20% of total supercoiled plasmid, using 0.2 M NaOH lysis buffer. Lysis experiments were performed in a scaled-down stirred tank and a scaled-down opposed jet device to determine actual plasmid degradation levels, as a function of NaOH concentration and mixing times. The results of mixing experiments in stirred tanks are discussed in the following section; mixing in opposed jets is discussed in chapter 8.

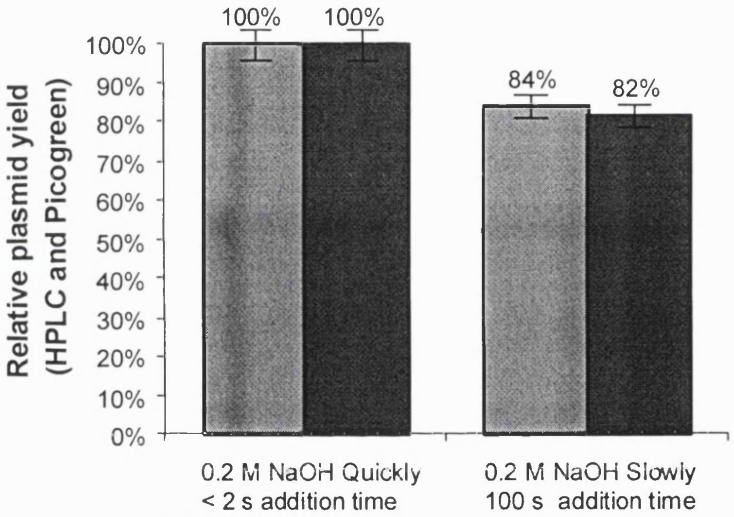

Figure 6.15 Bar chart showing the effect of addition rate of 0.2 M NaOH to pure supercoiled plasmid DNA.

Stirred Tank Mixing Studies

Lysis mixing experiments were performed with a scale-down stirred tank, as described in Materials and Methods. Figure 6.1 shows a schematic of the scale-down stirred tank and 6-bladed Rushton impeller. The measured macro-mixing time in the vessel was 10 s to 80 s, depending on impeller speed, as shown in Figure 6.16. Also shown is the theoretical vessel macro-mixing time that is based on Equation 2.3 to Equation 2.5, in section 37. The calculated macro-mixing time is in reasonable agreement with the observed macro-mixing time.

For this set of experiments, the lysis buffer was added subsurface directly into the impeller. In order to prevent supercoiled plasmid degradation, the lysis buffer needs to rapidly reach a uniform concentration at the microscopic level. Therefore, the micro-mixing time in the region close to the impeller is probably a more important criterion of plasmid degradation than the overall tank macro-mixing time. The micro-mixing time at the impeller could not be easily

measured, but the theoretically calculated micro-mixing time at the impeller is shown in Figure 6.16. The theoretically calculated micro-mixing time was calculated using Equation 2.1, Equation 2.2 and Equation 2.8 that are based on Kolmogoroff turbulence theory, as described in chapter 2. This assumes that the energy dissipation in the region near the impeller $\varepsilon_{impeller}$ is significantly higher than the average energy dissipation ε_{av} throughout the vessel (Harnby et al., 1992). A value for $\varepsilon_{impeller} / \varepsilon_{av}$ of 40, and a solution viscosity of 0.005 Pa s, were used in these calculations (Ciccolini et al. 1998). The predicted micro-mixing time varied from a few seconds up to tens of seconds depending on impeller speed.

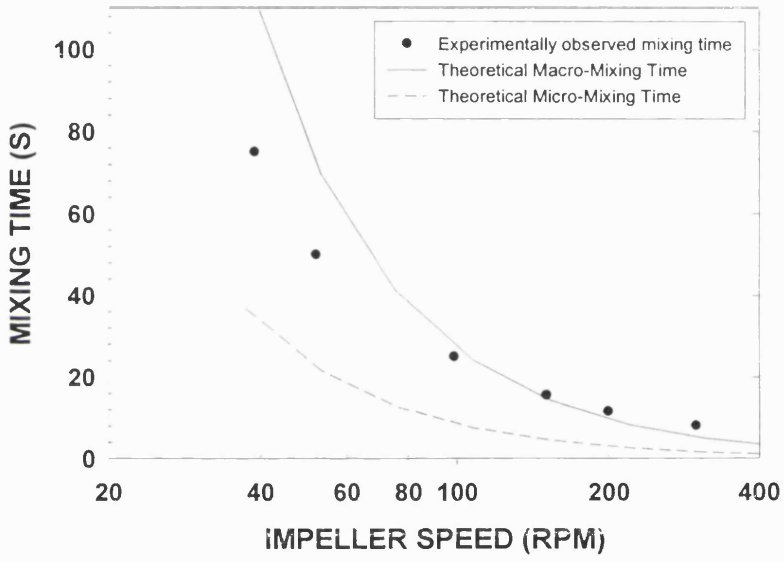

Figure 6.16. Plot showing relationship between stirred tank macro-mixing time and impeller speed.

The effect of impeller speed and NaOH concentration on supercoiled plasmid yield, during lysis in the stirred tank, was investigated. Figure 6.17 shows the effect of lysis reagent concentration and impeller speed on supercoiled plasmid yield. Each data point is the average of two experiments. Addition of 0.2 M NaOH lysis reagent to resuspended cells without mixing gave supercoiled plasmid yield of 84 %, compared to the control lysis done at 2 mL scale. Lysis while mixing at 50 rpm and 200 rpm gave 95% and 100% supercoiled plasmid yield, respectively. Thus, even gentle mixing at 50 rpm is sufficient to reduce supercoiled plasmid yield loss to only 5%. The vessel mixing time at 50 rpm was measured at 50 seconds; this is significantly longer than the 5 seconds it takes supercoiled plasmid to degrade in 0.2 M NaOH lysis buffer. At 50 rpm, the micro-mixing time in the region next to the impeller was estimated to be about 20 seconds. Excessive plasmid denaturation is probably avoided by the rapid diffusion rate of H^+ ions, some neutralisation of the NaOH by the cell debris, and because the

lysis reagent concentration of 0.2 M NaOH was not far above the supercoiled plasmid degradation concentration (0.12 to 0.15 M).

Currently, the alkaline lysis and neutralisation operation involves a 3-fold increase in batch volume from the resuspended cell volume. This creates a significant expense in terms of capital equipment at the lysis stage, and downstream, to process this increased batch volume. Instead of adding 1 volume of 0.2 M NaOH to the cells, to end up at 0.1 M NaOH, one could add 0.33 volumes of 0.4 M NaOH, significantly reducing the volume increase. However, there is potential for significantly greater plasmid degradation using more concentrated NaOH in the lysis buffer. Figure 6.17 also shows the plasmid yields using more concentrated 0.4 M NaOH lysis buffer. Moderate mixing at 200 rpm was not sufficient to prevent significant supercoiled plasmid degradation (60% SC plasmid yield loss) using 0.4 M NaOH. At a very high impeller speed of 800 rpm, the yield of plasmid DNA was 100% compared to the small-scale control. The calculated micro-mixing times at 200 rpm and 800 rpm were 2.3 s and 0.3 s, respectively. As the NaOH concentration increases in the lysis buffer, mixing time must decrease significantly to avoid product yield loss.

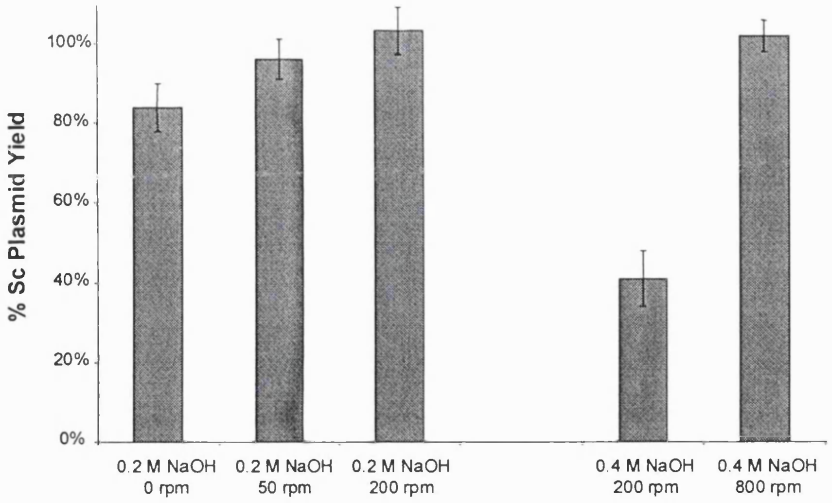

Figure 6.17. Plot showing effect of impeller speed and NaOH concentration on SC yield

6.4.7 Effect of fluid stress on the lysis of plasmid-deficient cells

It was demonstrated in the previous section that moderate to high impeller speeds in stirred tanks are required during alkaline lysis to prevent plasmid degradation from exposure to poorly mixed regions of NaOH. The effect of fluid shear on plasmid and chromosomal DNA in an alkaline lysis environment was studied. It has already been demonstrated by Levy et al. (1999) that shear rates of the order to 10^6 s^{-1} are required to break small plasmids (6 – 20 kb). In contrast, chromosomal DNA can easily be degraded at shear rates of 10^2 s^{-1}. Degradation of

chromosomal DNA into short, difficult to remove fragments is generally considered to a disadvantage in any alkaline lysis mixing operation. Because quantification of chromosomal fragments separately from plasmid fragments is difficult, wild-type DH5α *E. coli* cells that did not contain plasmids were used in the following lysis studies.

Effect of fluid stress on chDNA contamination

Figure 6.18, Figure 6.19 and Figure 6.20 show the total chromosomal DNA in the clarified lysates as a function of shear rate during alkaline lysis, for cell pastes WtypeG2, WtypeG1 and WtypeG3, respectively. The first figure shows data after shearing the lysates in a cone-and-plate viscometer, the latter figures after shearing through PEEK capillaries. Each data point represents the average of 3 separate experiments. The chromosomal DNA yields for the three cell pastes were 9% to 12%, 6% to 8% and 1% to 9% of the initial chromosomal DNA in the cell pastes WtypeG2, WtypeG1, and WtypeG3, respectively. There was significant scatter in the chromosomal contamination results shown in Figure 6.18. The chromosomal DNA contamination after 10 min strain in the cone-and-plate viscometer are significantly different than the results after 20 min mixing. This set of experiments were the initial set of experiments using the cone-and-plate viscometer; based on the variation in the results there may have been errors introduced into the experiment.

Figure 6.19 and Figure 6.20 showed that chromosomal DNA only increased moderately with increasing fluid strain rate in the PEEK capillary, up to 10,000 s^{-1}, for cell pastes WtypeG1 and WtypeG3. Cell paste WtypeG3 showed a very low level of chromosomal DNA contamination (1%) at shear rates below 10,000 1/s. This low level of chromosomal contamination was probably due to poor cell lysis, as this cell paste had previously been observed not to lyse effectively by alkaline lysis. The significant increase in chromosomal contamination between 10,000 1/s and 100,000 1/s, for this cell paste, may have been due to improved cell lysis caused by the high fluid shear stress. It is unlikely that fluid shear rates in stirred tanks, static mixers or opposed jet mixers would exceed 10,000 1/s. Hence, fluid stress during the lysis stage should not significantly increase the amount of chromosomal DNA contamination in clarified lysates.

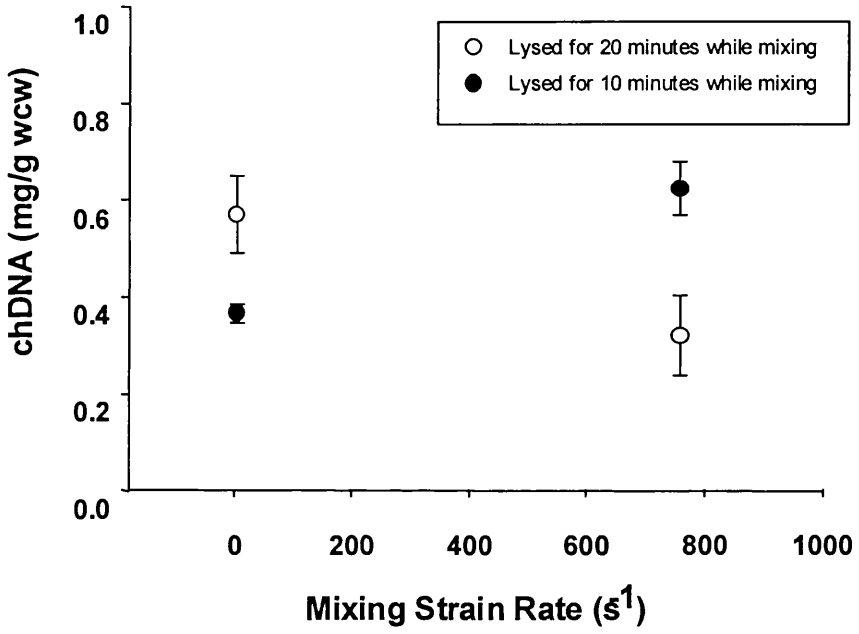

Figure 6.18. Effect of fluid strain rate on chromosomal DNA contamination in clarified alkaline lysate, for alkaline lysis in a cone-and-plate rheometer. Using cell paste WtypeG2. Each data point represents 3 separate lysis experiments. Error bars represent one standard deviation.

Effect of fluid stress on chDNA fragmentation

Figure 6.21 shows an agarose gel after pulsed-field electrophoresis of stressed lysate samples. The gel demonstrates the impact of fluid stress on the size of double-stranded chromosomal DNA fragments. The gels were scanned and the results plotted in Figure 6.22 as molecular size range (kb) of fragments against shear rate. The gel shows that the breakage of double-stranded chromosomal DNA occurs effectively at all shear levels tested, and the chromosomal size decreased with increasing shear rate. The results shown in Figure 6.22, indicate the concentration of the chromosomal DNA in the clarified alkaline lysates was not significantly affected by shear rate and remained about 20% of the total chromosomal DNA in the cells before lysis. Hence, chromosomal DNA size does not significantly affect the amount of it that flocculates during alkaline lysis-neutralisation.

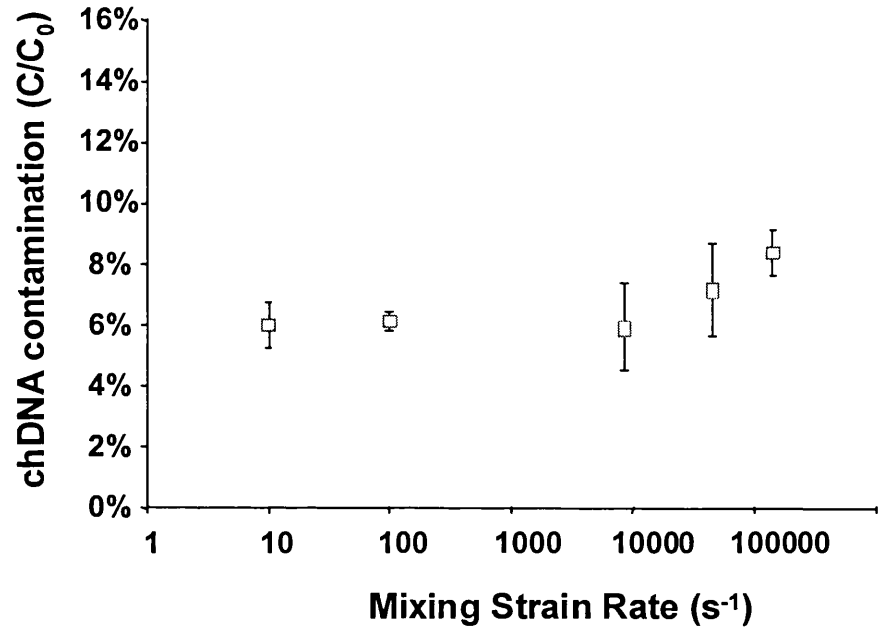

Figure 6.19. Effect of shear during alkaline lysis on chromosomal DNA contamination for wild-type *E. coli* cells. Each data point represents 3 separate lysis experiments. Error bars represent one standard deviation

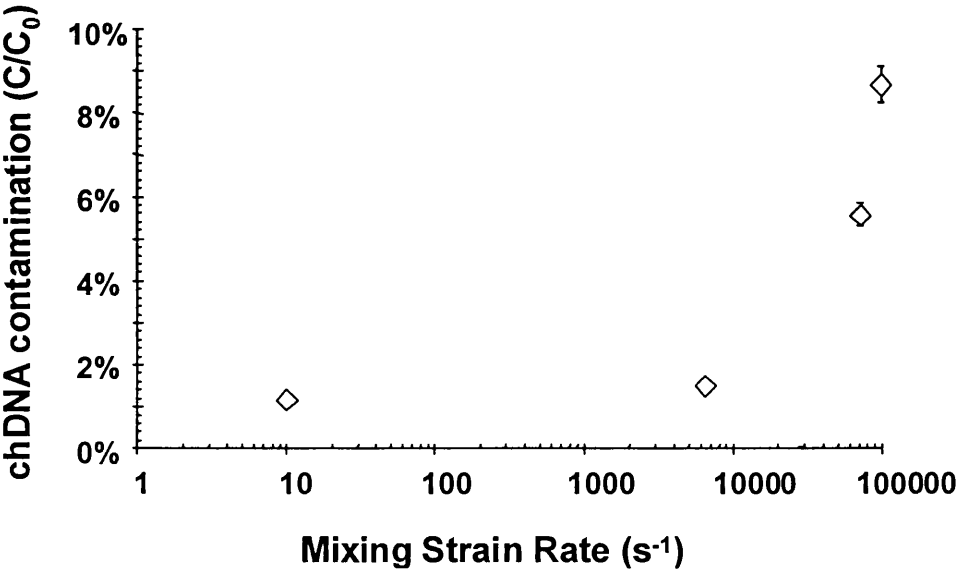

Figure 6.20. Effect of shear during alkaline lysis on chromosomal DNA contamination for wild-type *E. coli* cells. Each data point represents 3 separate lysis experiments. Error bars represent one standard deviation.

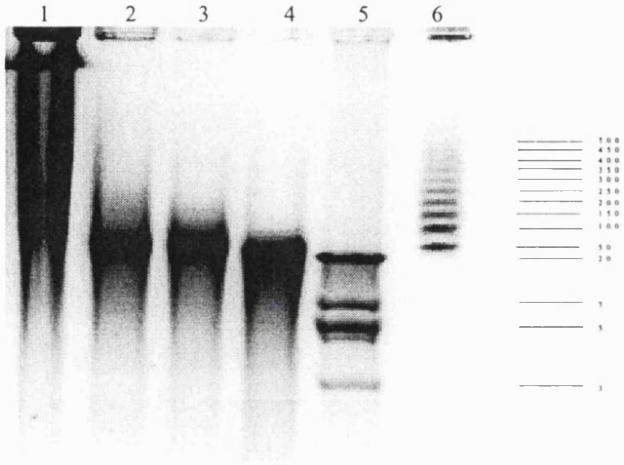

Figure 6.21 Agarose gel of sheared cell lysates. 1) 300 1/s, 2) 2500 1/s, 3) 20,000 1/s, 4) 60,000 1/s, 5) λ-DNA digest, 6) λ-DNA ladder

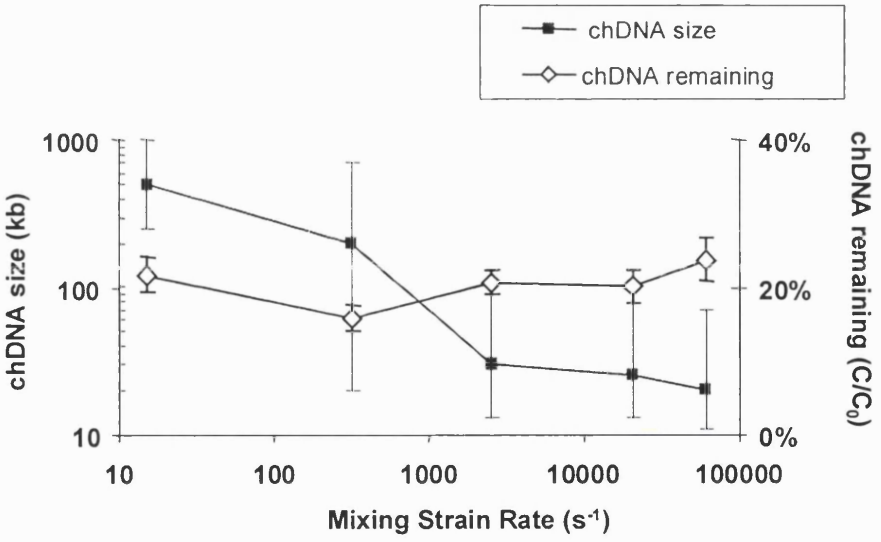

Figure 6.22 Effect of shear rate during SDS lysis on subsequent chromosomal DNA size and contamination after alkaline lysis.

6.4.8 Effect of fluid stress on the lysis of plasmid-containing cells.

Figure 6.23 shows the plasmid yield and purity as a function of strain rate in the cone-and-plate viscometer; while Figure 6.24 and Figure 6.25 show the plasmid yield and purity as a function of strain rate in PEEK capillaries. Each data point represents the average of 3 experiments. Although there was significant DNA contamination in all the samples, the purity was not affected by fluid stresses during alkaline lysis, below strain rates of 10,000 s^{-1}. The shear rates

used during lysis would have reduced the chromosomal DNA fragment size considerably. Fluid strain rates below 100,000 s-1 did not detrimentally impact supercoiled plasmid yield, in fact some increase in supercoiled plasmid yield over alkaline lysis was observed, probably due to improved cell lysis. Above 100,000 s^{-1} appeared to have caused some reduction in supercoiled plasmid yield.

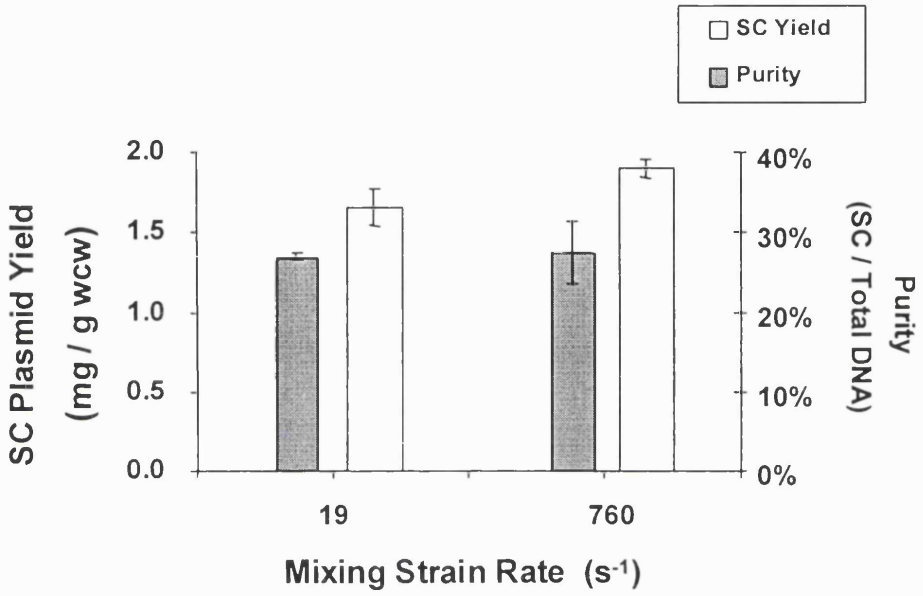

Figure 6.23. Bar chart showing the effect of fluid stress on plasmid yield and plasmid purity, after 15 minutes mixing in a cone-and-plate viscometer

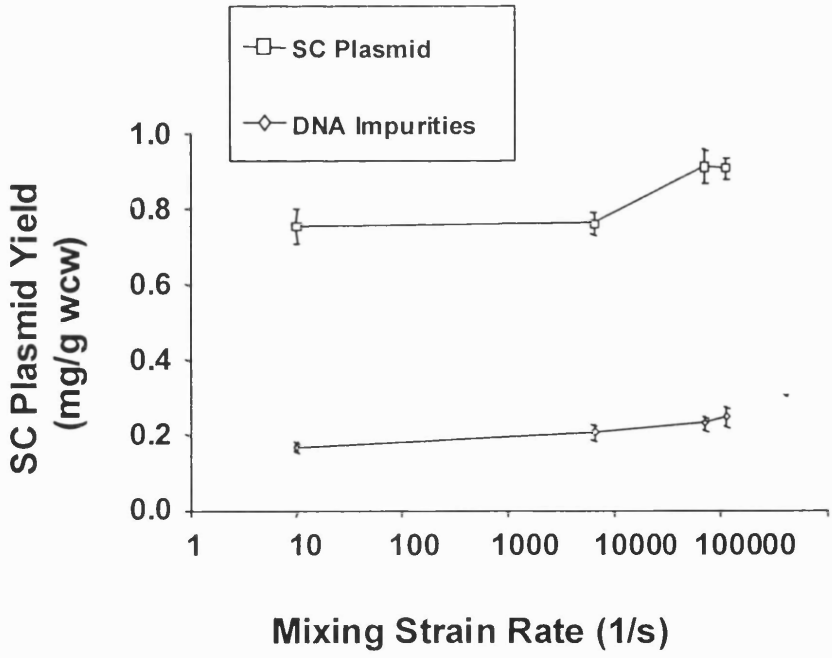

Figure 6.24. Effect of fluid strain rate in PEEK capillaries on chromosomal DNA contamination. Each data point represents duplicate experiments.

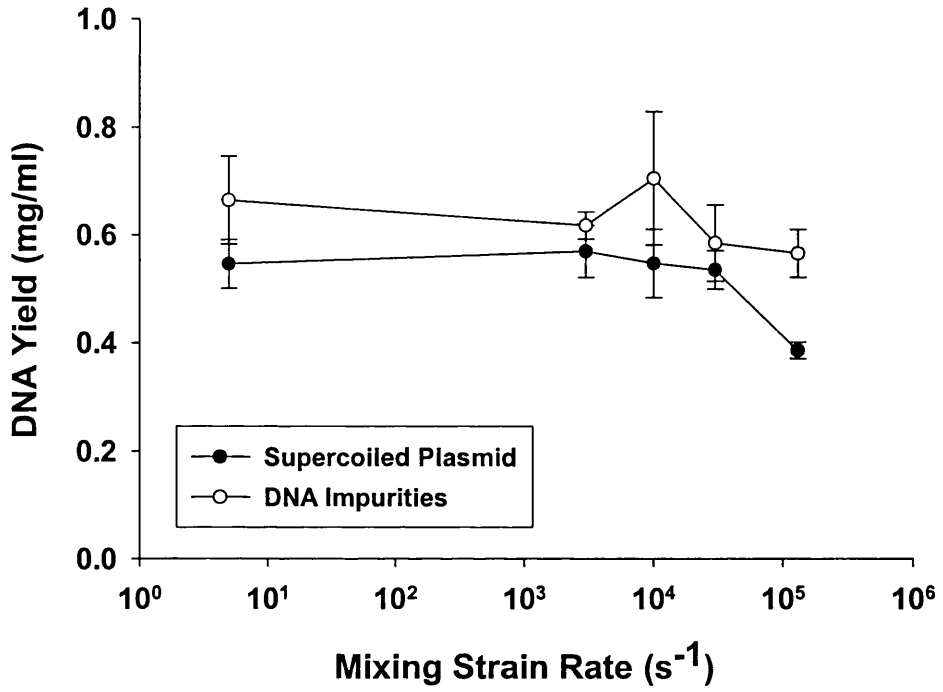

Figure 6.25. Effect of fluid strain rate in PEEK capillaries on chromosomal DNA contamination. Each data point represents triplicate experiments.

6.4.9 Effect of fluid stress during neutralisation

After alkaline lysis, neutralisation buffer is added to the cell lysate. This causes the precipitation of SDS-protein complexes that form a gelatinous flocculate with the chromosomal DNA and cell debris. It has been reported by Ciccolini et al. (2002) that shearing this gelatinous flocculate leads to significantly higher levels of chromosomal contamination in clarified lysates. Two separate studies were carried-out to determine the effect of shear during neutralisation on chromosomal DNA contamination. Neutralised alkaline lysates were subjected to fluid shear rates ranging from 5 to 60,000 1/s in cone-and-plate viscometers and PEEK capillaries. They were then clarified by centrifugation, IPA precipitated, resuspended in TE buffer and assayed by HPLC.

Figure 6.26 and Figure 6.27 show that fluid stress after neutralisation did not affect plasmid purity. Presumably, once chromosomal DNA has precipitated with proteins and SDS, high fluid stress will not return the DNA to the solution phase. Each data point represents the average of 3 and 2 experiments for

Figure 6.26 and Figure 6.27 respectively.

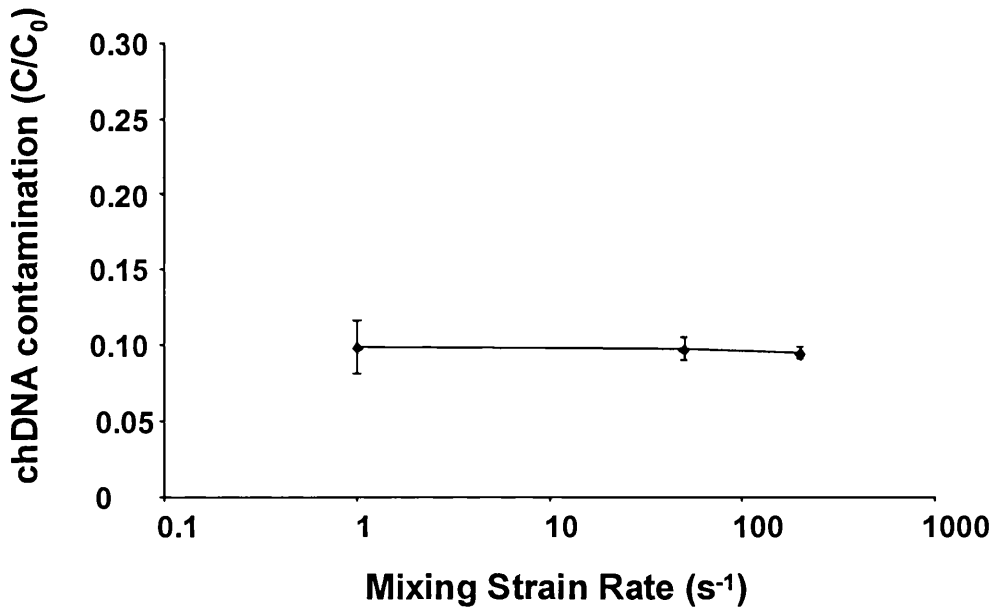

Figure 6.26. Plot showing the effect of fluid stress during neutralisation on chromosomal DNA yield, after 15 minutes shear in a cone-and-plate viscometer.

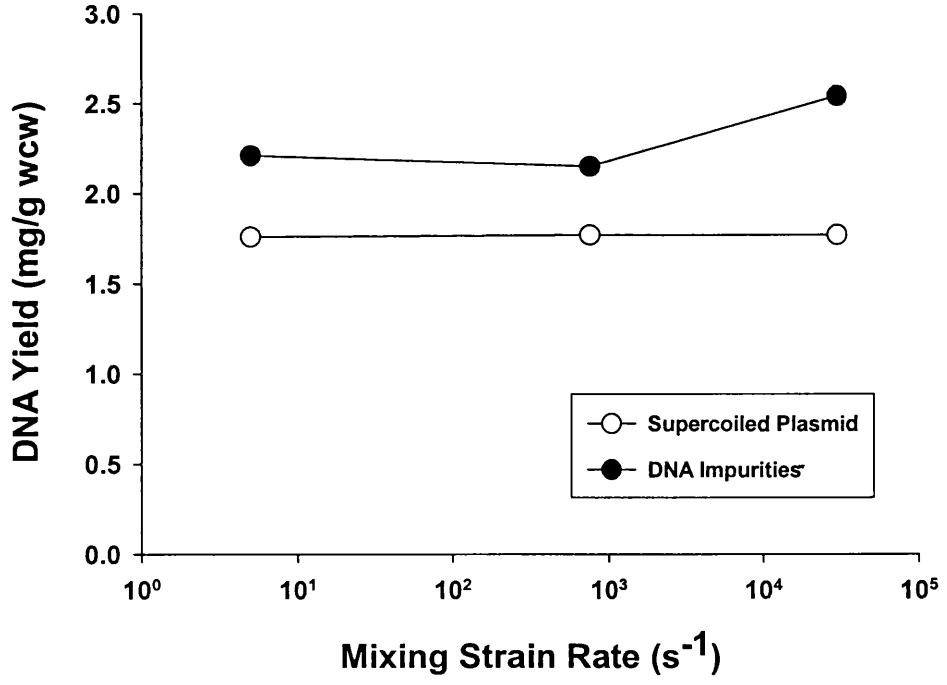

Figure 6.27. Plot showing the effect of fluid stress during neutralisation on plasmid yield and plasmid purity, after 10 passes through PEEK capillaries.

6.5 Discussion

6.5.1 DNA denaturation and mixing requirements

Measurement of pH during alkali addition is complicated by the highly viscous nature of the cell lysate, which together with the high concentration of proteins in the lysate, quickly leads to fouling of the pH probe making accurate pH measurement unfeasible. Instead of monitoring solution pH, it was determined in this thesis that monitoring the NaOH concentration in the alkaline lysate provided a more robust, reliable method for controlling cell lysis. Data was presented in this chapter which showed that addition of NaOH to TE-buffered plasmid solutions caused native supercoiled plasmid to irreversibly denature over a narrow window of NaOH concentration. This window was about 0.02 M wide, and typically occurred between 0.12 to 0.18 M NaOH. It was determined that this denaturation phenomenon was not a function of plasmid size, over the range of plasmid sizes from 6 kb to 116 kb.

It was demonstrated using plasmid-containing cells, that both supercoiled plasmid yield and chromosomal DNA contamination were only moderately affected by the NaOH concentration during alkaline lysis, at NaOH concentrations below the plasmid denaturation point. Therefore, based solely on the criteria of maximising supercoiled plasmid yield and minimising DNA impurities, alkaline lysis should be performed at a low NaOH concentration, significantly less than 0.1 M, to prevent any possibility of supercoiled plasmid denaturation. It should be noted that Thatcher et al (1997) reported that high pH increased chDNA removal, which was contrary to the observations made in this thesis. In was shown in this thesis that denaturation of chromosomal DNA to single-stranded form occurred between 0.02 to 0.04 M NaOH in TE buffered solutions. It was also shown that a higher concentration of NaOH, typically 0.08 M NaOH, was required to denature the entire chromosomal DNA in an alkaline lysate environment. The removal of chromosomal DNA at high NaOH concentrations observed by Thatcher et al. may in fact have been the conversion of double-stranded chromosomal DNA to single-stranded form. Single-stranded DNA does not show-up well on ethidium bromide stained agarose gels, such as those used by Thatcher et al.

The optimal NaOH concentration during lysis, for conversion of DNA impurities to single-stranded form while maximising supercoiled plasmid yields, was between 0.08 M and 0.12 M NaOH. Unfortunately, cell lysis in this NaOH concentration range was significantly more difficult. The NaOH concentration of the lysis buffer added to the cells was now greater than the concentration that caused irreversible supercoiled denaturation. Therefore, to prevent product degradation, the lysis buffer must be rapidly mixed with the cells. However, to date there had not been a detailed study published on the relationship between lysis buffer

concentration, lysis buffer mixing and plasmid denaturation rate. It was demonstrated in this chapter that plasmid irreversibly denatures in less than a few seconds when exposed to denaturing NaOH concentrations.

One of the disadvantages of the alkaline lysis step is the significant volume increase over lysis and neutralisation, typically a 3-fold increase in batch volume. While not a significant problem at laboratory scale, this volume increase at manufacturing scale would add significantly to both the capital and operating costs of a DNA purification facility. Instead of adding a large volume of a moderately concentrated NaOH lysis solution, a small volume of a highly concentrated NaOH lysis buffer can be added to the cells. Using highly concentrated lysis buffer has the advantage that the batch volume increase is significantly smaller, however, it was also demonstrated in this chapter that irreversible denaturation is faster as the concentration of NaOH in the lysis buffer increases. It was demonstrated that scale-down stirred tanks at moderate impeller speeds provided sufficiently fast mixing when 0.2 M NaOH lysis buffer was utilised, however, very high impeller speeds were required when 0.4 M NaOH lysis buffer was utilised.

6.5.2 Fluid stress-induced DNA degradation

It was shown in chapter 5 that the onset of supercoiled plasmid degradation starts at about $1x10^5$ s^{-1} for pure plasmid pSVb solutions in a capillary shear device. Levy et al. (1999) has reported that plasmids in a clarified lysate environment are less prone to shear degradation than in TE buffer. Minimal degradation of pSVb was observed by Levy et al. in clarified lysates up to a shear rate of $5x10^5$ s^{-1} in a capillary rheometer and up to a shear rate of $5x10^6$ s^{-1} in a rotating disk rheometer. However, all of these studies have been done at a neutral pH, and Adam et al. (1977) has showed that DNA s more susceptible to fluid stress-induced degradation at higher pH. It was demonstrated in this chapter that plasmid pSVβ yield was insensitive to fluid shear during alkaline lysis, up to fluid strain rates of $1x10^5$ s^{-1} in a capillary flow device, despite being at high pH. Above fluid strain rates of $1x10^5$ s^{-1} some decrease in supercoiled plasmid yield was observed.

There have been conflicting reports that fluid stress during cell lysis may or may not lead to increased chromosomal contamination in the clarified alkaline lysate. Ciccolini et al. (2002) stated that increased fluid stress led to moderate increases in chromosomal DNA contamination, up to 25% chDNA contamination at a fluid strain rates of 760 s^{-1}. In contrast, a study by Chamsart et al. (2001) showed that fluid strain rates up to 760 s^{-1} did not lead to chromosomal DNA contamination greater than 2% after further downstream purification using Qiagen columns. It was observed in this thesis, that chromosomal DNA contamination in clarified

alkaline lysate was typically high (about 20% to 60% compared to supercoiled plasmid), but varied considerably depending the on the batch of cell paste lysed. Chromosomal DNA contamination levels as low as 1% were observed from one batch of cell paste. In most cases, chromosomal contamination levels observed were usually similar or higher than the levels observed by Ciccolini et al. The cell strains were used here were the same as used by Ciccolini et al, but the novel HPLC assays used here were more sensitive at detecting single-stranded chromosomal DNA that agarose gel electrophoresis. It was observed in this chapter that the amount of chromosomal DNA impurity in the clarified alkaline lysate was only moderately sensitive to fluid stress up to strain rates of $1x10^4$ s^{-1}. Ciccolini et al. observed the same moderate increase in chromosomal DNA contamination with strain rate, but over a much narrow range, 0 to 760 s^{-1}. The low chromosomal DNA impurity levels observed by Chamsart may possibly be due to chromosomal DNA removal over Qiagen purification or possibly differences in *E. coli* cell strain.

In was demonstrated that chromosomal DNA size was very sensitive to fluid stress, and was degraded to smaller and smaller chromosomal fragments as the shear rate increased from 10^1 to 10^5 s^{-1} in a capillary shear device. At a shear rate of 10^3 s^{-1} the size of chromosomal DNA fragments was about 30 kb and decreased to about 20 kb at 10^5 s^{-1}. The actual shear rate that chromosomal DNA will experience during alkaline lysis will depend on the required mixing time and on the method of mixing. Comparing the chromosomal DNA fragment size as a function of strain rate in pure solution (chapter 5) versus during alkaline lysis, it is apparent that chromosomal DNA is more susceptible to fragmentation in an alkaline lysis environment than in pure TE buffer, pH 8.0. This is expected, as chromosomal DNA will be in single-stranded form during alkaline lysis, and a single-stranded DNA chain should be weaker than a double-stranded DNA chain.

Figure 6.28 shows the predicted fluid mixing time and fluid strain rates, as a function of impeller speed in a 1000 L stirred tank, based on Equation 2.8, Equation 2.15 and Equation 2.16. A density of 1000 kg/m^{-3} and viscosity of 0.005 Pa s was used for the liquid. The micro-mixing time was calculated based on the energy dissipation rate close to the impeller, while the macro-mixing time was based on the time to achieve a macroscopic, homogeneous concentration throughout the tank. There is a significant variation in strain rate depending on location within the tank. Shown in Figure 6.28 are the strain rates based on the average turbulent energy dissipation in the tank and on the maximum turbulent energy dissipation at the impeller. Also shown is the strain rate within the boundary layer of the impeller. Strain rates in the impeller boundary layer are significantly higher than the strain rate due to turbulent eddies. Although only a small percentage of the tank volume passes through the impeller boundary

layer, if mixing proceeds for an hour, often an entire tank volume may pass through the impeller boundary layer. Hence, careful scale-up and impeller design can be important to reduce fluid shear.

In order to achieve short mixing times in stirred tanks, high fluid strain rates will occur. The actual level of fluid strain that will occur will depend on the micro-mixing time required, which will depend on the concentration of lysis buffer being added to the cells (refer to section 6.4.6). Utilisation of lysis buffers above 0.2 M NaOH concentration will require micro-mixing times no longer than 1s, which (referring to Figure 6.28) will lead to strain rates on the order of 1000 s^{-1} in the case of the 1000 L stirred tank. Therefore, chromosomal fragments will be generated within the size range of 20 to 40 kb. The appropriate selection of downstream unit operations must be made to ensure that these chromosomal DNA fragments can be removed (refer to chapter 8). The critical strain rate for 116 kb and 20 kb plasmid degradation was shown in chapter 5 to be 10^4 and 10^5 s^{-1}, respectively. It is unlikely that shear rates in a stirred vessel would reach levels of 10^4 to 10^5 s^{-1}, therefore, shear-induced degradation of most plasmids, should not be a concern in stirred tanks.

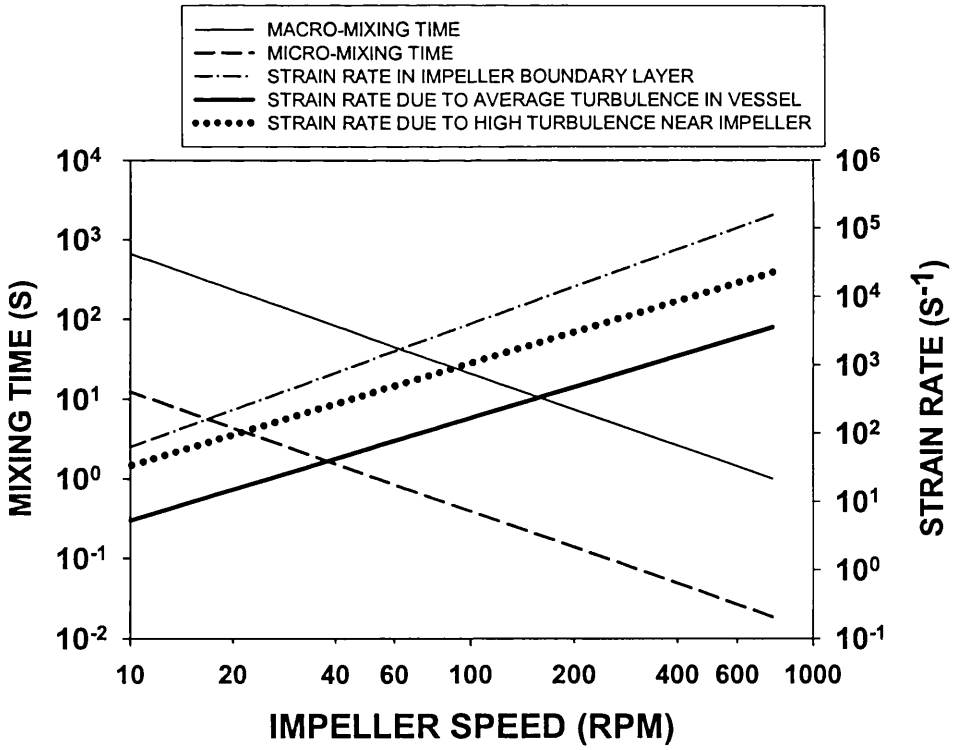

Figure 6.28. Plot showing the effect of impeller speed on mixing performance and fluid stress in a 1000 L stirred tank. All lines are calculated from mixing and fluid stress theory as described in chapter 2.

6.6 Conclusions

It was shown that monitoring NaOH concentration during alkaline lysis is a robust method of controlling plasmid and chromosomal DNA denaturation, in contrast to monitoring pH which is difficult to measure accurately in an alkaline lysis environment. It was demonstrated for a range of plasmid sizes (from 6 to 116 kb) that supercoiled plasmids irreversibly denature over a narrow window of sodium hydroxide concentration. The plasmids examined all denatured between 0.13 ± 0.03 M NaOH. At NaOH concentrations below the plasmid denaturation concentration, the rate of degradation of supercoiled plasmid to denatured form was slow (~ 10% degradation/hour). Above the critical NaOH concentration, the rate of plasmid degradation is very fast, on the order of seconds. It was shown that using the appropriate NaOH concentration, chromosomal DNA can be completely converted to single-stranded form, leaving plasmid DNA in its native supercoiled form. The form of chromosomal DNA (single- vs. double-stranded) and the size of the chromosomal DNA were shown not to significantly affect its removal over alkaline lysis and neutralisation.

It was shown that the mixing requirements during alkaline lysis were dependent on the NaOH concentration at which lysis is performed. This in turn is dependent both on the level of chromosomal DNA denaturation that that is required and the increase in batch volume that is considered acceptable over lysis and neutralisation. It was shown that significant plasmid yield loss can occur during alkaline lysis buffer addition in stirred tanks, and that the micro-mixing time in such vessels must be less than the supercoiled plasmid degradation time at high NaOH concentration (micro-mixing must be complete within seconds).

While the level of chromosomal DNA denaturation does not significantly affect the quantity of chromosomal DNA in the clarified lysate, the quantity of double- versus single-stranded chromosomal DNA may be a critical factor in its downstream removal. Similarly, while the level of fluid stress only moderately affects the quantity of chromosomal DNA in the clarified lysate, the size of that chromosomal DNA may also be a critical factor in its downstream removal. Therefore, we conclude that the alkaline lysis step can only be properly optimised by taking into account its effect on the subsequent downstream purification steps. Chapter 7, which follows, examines the effect of chromosomal DNA denaturation and chromosomal DNA size on chromosomal DNA downstream removal from the supercoiled plasmid product. Chapter 8 then describes the design of an improved alkaline lysis reactor based on the fundamentals studies of DNA stress-induced degradation (chapter 5), the requirements that downstream purification puts on alkaline lysis (chapter 7), and the understanding of the lysis step (chapter 6).

7 Effect of DNA denaturation and fragmentation on downstream processing

It was demonstrated in the previous chapter, where the effect of fluid mixing and fluid shear on alkaline cell lysis was studied, that optimisation of the alkaline lysis operation must be performed in conjunction with an understanding of how DNA denaturation and fragmentation influence subsequent downstream purification steps. This chapter studies the effects of DNA denaturation and fragmentation on a small selection of typical DNA purification operations. The unit operations investigated were:

- Filtration: Various pore sizes
- Precipitation: Calcium Chloride and CTAB
- Size Exclusion Chromatography: Sephacryl S1000 SF
- Anion Exchange Chromatography: Q-Sepharose and Poros PI
- Adsorption: Silica Gel

This chapter starts with a summary of results, followed by a brief introduction into the motive for these investigations. The materials and methods used in these experiments are then described. The experimental results are then presented, and finally this chapter concludes with a discussion of the results obtained.

7.1 Brief summary of results

Table 7.1 summarised the experimental results presented in this chapter. It was determined that several of the separation techniques investigated were very effective at removing single-stranded chromosomal DNA from supercoiled plasmid based on the differences in chemistry between single-stranded chromosomal DNA and the double-stranded supercoiled plasmid. Some of the experimental techniques investigated were marginally effective at removing chromosomal DNA (both double- and single-stranded forms), based on the size difference between chromosomal DNA and supercoiled plasmid. There was no technique that was good at removing double-stranded chromosomal DNA. Therefore, maximising the conversion of chromosomal DNA to single-stranded form during alkaline lysis is essential.

Technique	Removal of ss-Chromosomal DNA		Removal of ds-Chromosomal DNA	
	Effectiveness	Based -on	Effectiveness	Based -on
Filtration	Poor	Size	Poor	Size
Calcium Chloride	Good	ss vs ds.	Moderate	NA
CTAB	Moderate	Size	Moderate	Size
Sephacryl S1000	Poor	Size	Poor	Size
Q-Sepharose	Good	ss vs ds.	Moderate	Size
Poros PI	Good	ss vs ds.	Moderate	Size
Silica Gel	Good	ss vs ds.	No Separation	NA

Table 7.1. Methods of separating single and double-stranded chromosomal DNA from supercoiled plasmid, and effectiveness of each technique.

7.2 Introduction

It was demonstrated in the previous chapter that good fluid mixing during alkaline lysis is necessary to prevent supercoiled plasmid degradation, and that fluid mixing can lead to extensive chromosomal DNA fragmentation. Reduction of the lysis pH reduces the need for rapid mixing, and decreases chromosomal DNA degradation, but can lead to increased levels of double-stranded chromosomal DNA relative to single-stranded DNA, post alkaline lysis. Therefore, optimisation of alkaline lysis requires an understanding of how DNA size and form affect its removal downstream of the alkaline lysis and clarification steps.

Several DNA purification unit operations that are reported in the literature as being used for chromosomal DNA removal are investigated.

7.3 Materials and methods

7.3.1 Filtration

Dead-end filtration is commonly used during DNA purification processes, upstream to clarify cell lysate, mid-process to remove precipitates, or at the end of the process for sterile filtration (Levy et al., 2000). There is the possibility that large chromosomal DNA fragments may be separated from the smaller supercoiled plasmids during these filtration steps. However, fragmentation of chromosomal DNA may significantly decrease this separation. In order to test if chromosomal DNA can be separated from supercoiled plasmid using dead-end filtration, E.

coli DH5α cell pastes, from plasmid deficient cells, was alkaline lysed. The cells were lysed and clarified under conditions of low fluid stress, using the standard lysis and clarification protocol. 2 mL of clarified alkaline lysate was placed in a syringe and pushed through five different filters:

1. Whatman 1 filter paper
2. Whatman 42 filter paper
3. 1.2 micron PVDF Millipore filter
4. 0.45 micron PVDF Millipore filter
5. 0.20 micron PVDF Millipore filter

A small plastic filter-holder was used to hold the Whatman filter paper, and connect it to the syringe. Each filtration experiment was repeated in duplicate, and assayed by Poros PI HPLC.

7.3.2 Precipitation using CTAB

Effect of chromosomal denaturation

Using pure double- and single-stranded chromosomal DNA, a solution of 100 μg/ml double-stranded chromosomal DNA and 100 μg/ml ss-DNA was prepared in TE buffer. A stock solution of 0.03% CTAB in 20 mM NaCl was prepared. Using the CTAB stock solution, and a 20 mM NaCl solution, a series of CTAB solution from 0 to 0.03% CTAB w/v, 20 mM NaCl, were prepared. An equal volume of each CTAB solution was added to 0.5 mL of chromosomal DNA solution. Each sample was mixed gently for 10 minutes and centrifuged at 13 krpm for 20 minutes. To each supernatant, two volumes of 100% ethanol were added to precipitate DNA. Each sample was centrifuged, as above, to pellet the DNA precipitate. Each pellet was washed with 70% ethanol, and resuspended in 0.2 mL TE buffer. Each resuspended sample was assayed by Poros PI HPLC for single- and double-stranded chromosomal DNA.

Effect of chromosomal DNA fragment size on post-CTAB resuspension

In chapter 5, pure double-stranded chromosomal was shear degraded to smaller fragment size by forcing it through PEEK capillaries at different flowrates. Three of these pure solutions of chromosomal DNA fragments, at 15, 40 and 90 kb average size as determined by pulsed-field gel electrophoresis, were used for CTAB experiments. Each of the three chromosomal solutions, at approximately 10 μg/ml, was divided into 12 separate 0.5 mL aliquots. Each solution was precipitated with one volume of CTAB solution, 0.3% CTAB, 20 mM NaCl. A solution of pure supercoiled plasmid pSVb, at 10 μg/ml was divided into 12 separate aliquots and each precipitated using CTAB. Each sample was centrifuged at 13 krpm for 20 minutes to pellet the DNA. The supernatants were discarded. Each set of samples was then resuspended in 0.5 mL of 0 M to 1.2 M NaCl. Each sample was mixed gently for 10 minutes and then

centrifuged for 20 minutes at 13 krpm. Each supernatant was transferred to a new tube and 5 M NaCl was added to each sample to a concentration of 2 M NaCl and mixed for 5 minutes. Each sample was then diluted 1:5,000 with 2M NaCl and assayed using Picogreen fluorescence assay.

7.3.3 Calcium chloride precipitation

Effect of denaturation conditions

The effect of NaOH concentration during alkaline lysis on calcium chloride precipitation of the clarified lysate was investigated. Clarified alkaline lysates, from a plasmid-containing (pSVβ) and a plasmid-deficient cell paste, were prepared on the 2 mL scale using the standard lysis and clarification protocol, except that the concentration of NaOH during lysis was 0, 0.05, 0.075 or 0.10 M NaOH. A 5 M $CaCl_2$ solution was added to 0.5 mL of each clarified lysate to a concentration of 0.5 M $CaCl_2$. Each sample was mixed on a shaker for 30 min and then centrifuged at 13 krpm for 30 minutes. The pellets were discarded and each supernatant was precipitated with 2 volumes of ethanol and centrifuged at 13 krpm for 30 minutes. The pellets were washed with 70% ethanol and resuspended in 0.3 mL TE. Each sample was assayed by Poros PI HPLC for supercoiled plasmid, and DNA impurities.

Effect of DNA Shear

Clarified alkaline lysate was prepared from a plasmid-containing, and a plasmid-deficient cell paste, using the standard lysis protocol. These lysates were stressed by forcing them through a 0.010" PEEK capillary at a one of five different flowrates, 10-times, using a Hamilton syringe pump. After stressing each sample, they were neutralised and clarified as per the standard protocol. Each of the five clarified alkaline lysates was precipitated with 0.5 M $CaCl_2$. The samples were centrifuged, ethanol precipitated, resuspended and assayed as described in the previous section.

7.3.4 Size exclusion chromatography using Sephacryl S1000

A 10 cm long, Pharmacia-XK column was packed with Sephacryl –S1000 SF chromatography resin, and equilibrated in TE buffer. 100 µl of pure chromosomal DNA at 40 µg/mL or pure supercoiled plasmid DNA pSVβ at 30 µg/mL was injected onto the Sephacryl column at flowrates from 0.05 to 1.0 mL/min. The elution of DNA was monitored by absorbance at 260 nm.

7.3.5 Anion exchange chromatography: Poros PI and Q-Sepharose

Pure chromosomal DNA, at approximately 150 μg/mL was fragmented under conditions of varying fluid stress. Aliquots of DNA, 2 mL, were placed in a plastic syringe and manually pushed through a 0.01" ID, 0.007" ID or 0.005" ID, 5 cm long PEEK capillary, as described in Materials and Methods, chapter 5. The size of the chromosomal DNA fragments was determined by pulsed-field gel electrophoresis.

7.3.6 Adsorption using silica gel

Binding capacity

0.5 mL aliquots of pure single-stranded chromosomal DNA at 10 μg/ml, 1 M NaCl, 10 mM Tris, pH 7.0, were placed in 1 mL test-tubes. 0.5 mL of silica gel at solution at 0, 40, 80, 120, 160 and 200 mg/mL in 1.0 M NaCl, 10 mM Tris, pH 7 was added to the tubes. The samples were moderately mixed for 2 hours on a shaker at room temperature. The samples were centrifuged at 13 krpm for 5 minutes and the supernatants assayed by Poros PI HPLC for single-stranded DNA content. The supernatants were diluted 1:2 before HPLC assay to reduce the NaCl concentration in the samples.

Purification of supercoiled plasmid DNA

The ability of silica gel to remove chromosomal DNA from supercoiled plasmid was tested on CTAB-purified lysate. Clarified alkaline lysate was prepared from E. coli DH5α pSVβ cells at 2 mL scale using the standard protocol. The clarified lysate was further purified by CTAB precipitation (ref). 1 mL of clarified lysate was mixed with 0.1 mL of 0.3% w/v CTAB in 20 mM NaCl. The sample was centrifuged at 13 krpm, 30 minutes. The pellet was resuspended in 0.5 mL of 1 M NaCl, 10 mM Tris, pH 7.0. The resuspension was precipitates with 1 mL 100% ethanol and centrifuged at 13 krpm, 30 minutes. The pellet was washed with 70% ethanol and resuspended in 2 mL Tris, pH 7.0 to make the CTAB-purified lysate. 5 M NaCl was added to 0.5 mL of the CTAB-purified lysate to a concentration of 1 M NaCl, followed by 1 mL of 100 mg/mL silica gel, 1 M NaCl, 10 mM Tris, pH 7.0. The sample was mixed for 2 h on a vortexer-shaker and then centrifuged at 13 krpm for 5 minutes to pellet the silica. The supernatant was assayed by Poros PI HPLC for supercoiled plasmid DNA and DNA impurities. The CTAB-purified lysate, before silica treatment, was also assayed by Poros PI HPLC.

Removal of open-circular plasmid DNA

0.5 mL of pure heat-degraded plasmid (refer to section 4.3.7) was denatured-renatured using the standard protocol and adjusted to 1 M NaCl. The sample was incubated with silica gel at 200 mg silica/ μg total DNA for 2 h at room temperature with moderate mixing. The sample was

centrifuged at 13 krpm, 5 min to remove the silica. The supernatant was assayed by agarose gel electrophoresis to determine supercoiled and open-circular plasmid concentration. The original heat-degraded plasmid was also run on the same gel.

7.4 Experimental results

7.4.1 Filtration of clarified alkaline lysates

Figure 7.1 shows the yield of chromosomal DNA across the filtration steps, as a function of filter-type used. Despite the clarified lysate being prepared under conditions of low shear, to maximise chromosomal DNA size, the removal of chromosomal DNA across the filters was low. Hence, separation of supercoiled plasmid DNA and chromosomal DNA across filtration operations will in general be poor, and therefore fragmentation of chromosomal DNA will not significantly affect removal of chromosomal DNA.

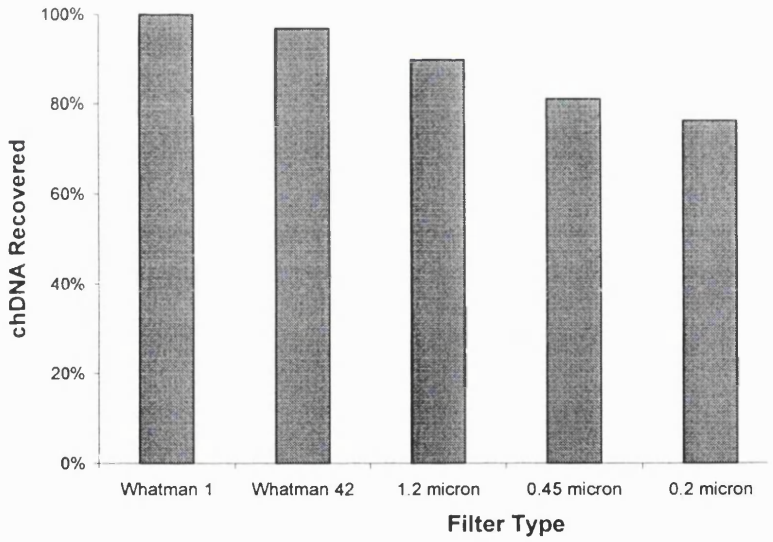

Figure 7.1. Effect of dead-end filtration on chromosomal DNA transmission in alkaline lysates.

7.4.2 Precipitation using CTAB

Lander et al. (2002) has reported the use of CTAB to precipitate DNA in cell lysates. This precipitation technique is an excellent way of separating DNA from RNA, cell debris, protein and endotoxin. Although separation of chromosomal DNA was minimal during the precipitation step, they reported some separation of chromosomal DNA through careful resuspension of the CTAB pellet using an optimum NaCl concentration. The effect of

chromosomal DNA denaturation and fragmentation on its resuspension using CTAB was investigated.

Effect of chromosomal denaturation

Figure 7.2 shows the concentration of both double- and single-stranded chromosomal DNA in a pure DNA solution as a function of CTAB concentration. The precipitation of DNA was not significantly affected by whether it was in double-stranded or single-stranded form. Therefore CTAB cannot be used to separate DNA based on whether it is in double- or single-stranded form, and the degree of chromosomal DNA denaturation during alkaline lysis should not impact CTAB performance.

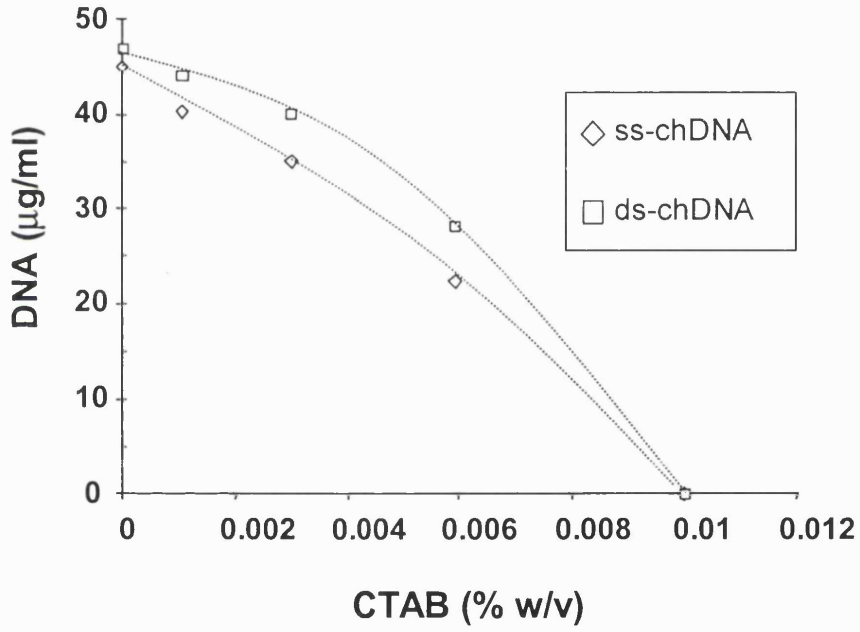

Figure 7.2. Effect of CTAB concentration on double- and single-stranded chromosomal DNA in solution.

Effect of chromosomal DNA fragment size on post-CTAB resuspension

Lander et al. reported that careful resuspension of CTAB-DNA precipitate at a specific NaCl concentration provided some separation of supercoiled plasmid DNA from chromosomal DNA impurities, as the supercoiled plasmid resuspended at a slightly lower NaCl concentration than the bulk of the chromosomal DNA. Three solutions of chromosomal DNA fragments and one solution of supercoiled plasmid were precipitated using CTAB, as described in Materials and Methods. Figure 7.3 shows the concentration of chromosomal DNA and supercoiled plasmid in solution as a function of the NaCl concentration used to resuspend the DNA-CTAB pellets. The small and medium chromosomal DNA fragments resuspended at the same NaCl concentration

as the supercoiled plasmid, however the large chromosomal DNA fragments (90 kb) did not go back into solution as easily as the other samples. Therefore, some separation of chromosomal DNA and supercoiled plasmid DNA can be achieved using CTAB precipitation and NaCl resuspension provided that the chromosomal DNA is of a sufficient size. The chromosomal DNA in alkaline lysates can potentially be very large (500 kb), therefore potentially much better separation of chromosomal DNA and supercoiled plasmid could potentially be achieved than was observed in these experiments.

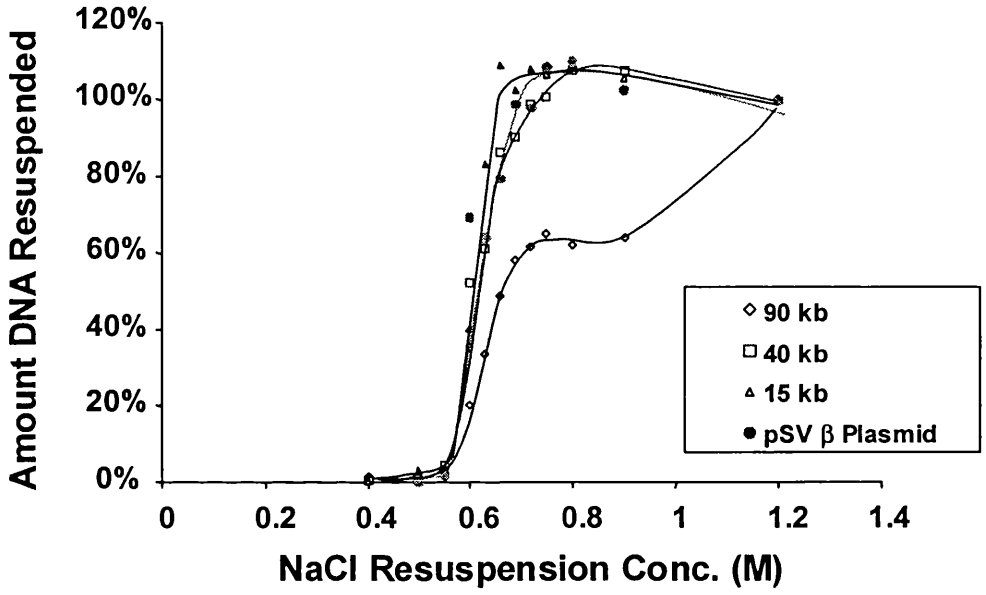

Figure 7.3. Effect of fluid stress on chromosomal resuspension

7.4.3 Calcium chloride precipitation

Effect of denaturation conditions

Figure 7.4 shows the concentration of chromosomal DNA after calcium chloride precipitation of clarified alkaline lysates made from plasmid-deficient *E. coli* cell paste. The alkaline lysates were lysed at 0, 0.05, 0.075 or 0.10 M NaOH. There was a significant reduction in chromosomal DNA contamination when the NaOH concentration during alkaline lysis was increased from 0 to 0.05 M NaOH and a further decrease in chromosomal DNA contamination when the NaOH concentration was increased to 0.075 M NaOH. Therefore, when calcium chloride precipitation is used, it is essential that the DNA is exposed to a sufficiently high concentration of NaOH during alkaline lysis.

Figure 7.5 shows the concentration of supercoiled plasmid DNA and DNA impurities after calcium chloride precipitation of clarified alkaline lysates made from plasmid-containing *E. coli* cell paste. The alkaline lysates were lysed at 0, 0.05, 0.075 or 0.10 M NaOH. There was a

steady increase in supercoiled plasmid yield with increasing concentrations of NaOH during lysis, probably due to better lysis efficiency. There was a drop in the amount of DNA impurities when the NaOH concentration during lysis was increased from 0 to 0.05 M NaOH. However, the reduction in the amount of impurities was not as significant as seen with the chromosomal DNA in the plasmid-deficient cells. Possibly, removal of plasmid degrades is not as effective with calcium chloride as the removal of larger chromosomal DNA impurities.

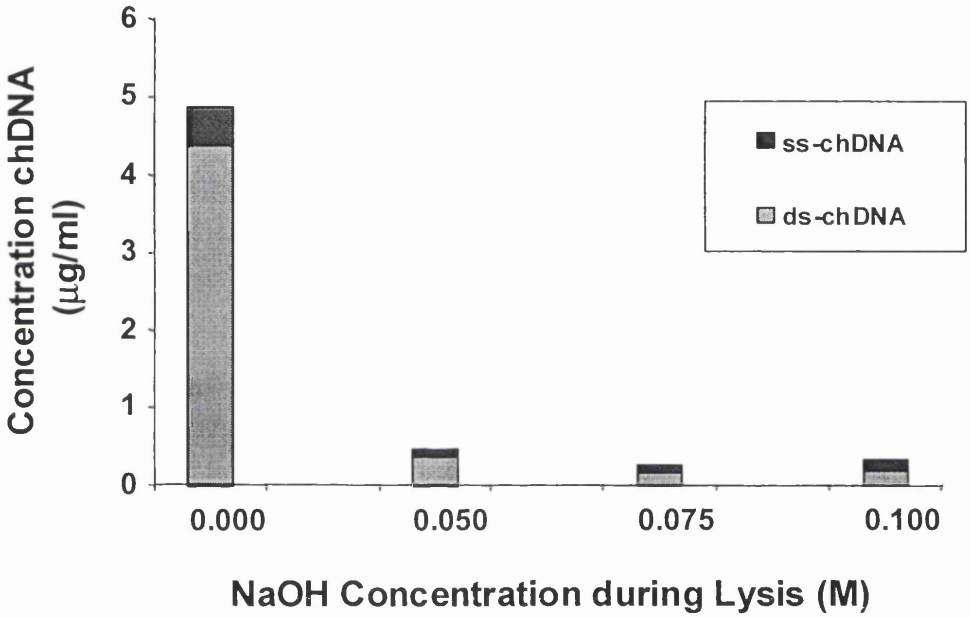

Figure 7.4. The effect of NaOH concentration during alkaline lysis on chromosomal DNA precipitation during subsequent calcium chloride precipitation

Effect of DNA Shear

Figure 7.6 shows the concentration of double- and single-stranded chromosomal DNA after calcium chloride precipitation of stressed alkaline lysate samples, from plasmid-deficient cell paste. There was no significant effect of fluid stress during alkaline lysis on chromosomal DNA contamination, except possibly at the lowest strain rate during lysis. At the lowest strain rate, there was some increase in chromosomal DNA contamination, possibly due to poor mixing of the lysis buffers. Figure 7.7 shows the supercoiled plasmid concentration and the DNA impurity concentration in clarified lysate samples post-calcium chloride precipitation. There was some variation in supercoiled plasmid yield between the different samples, there was no significant trend in plasmid yield or purity as a function of fluid strain rate during lysis.

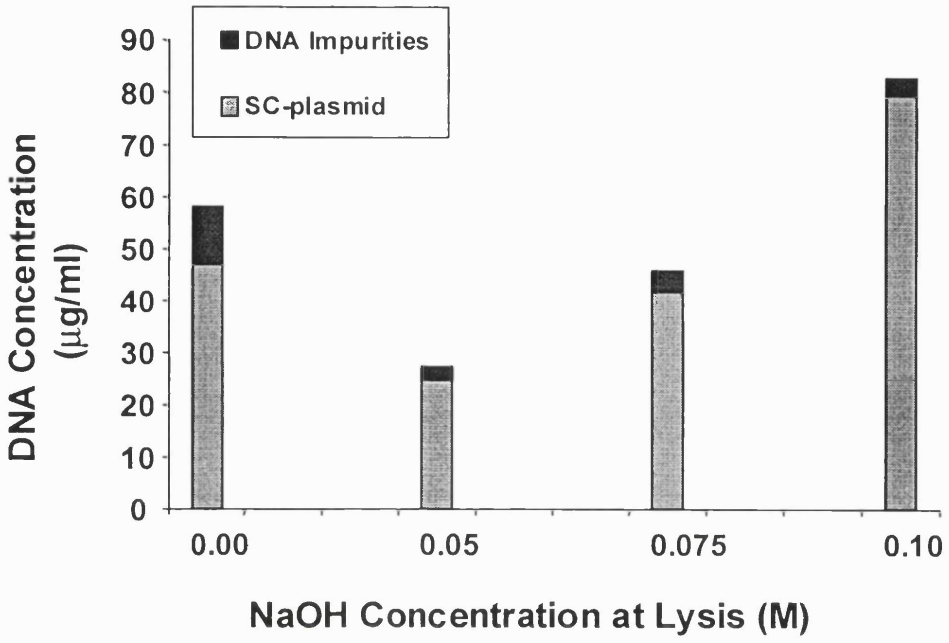

Figure 7.5. Effect of NaOH concentration on plasmid and impurity concentration in calcium chloride precipitated alkaline lysates.

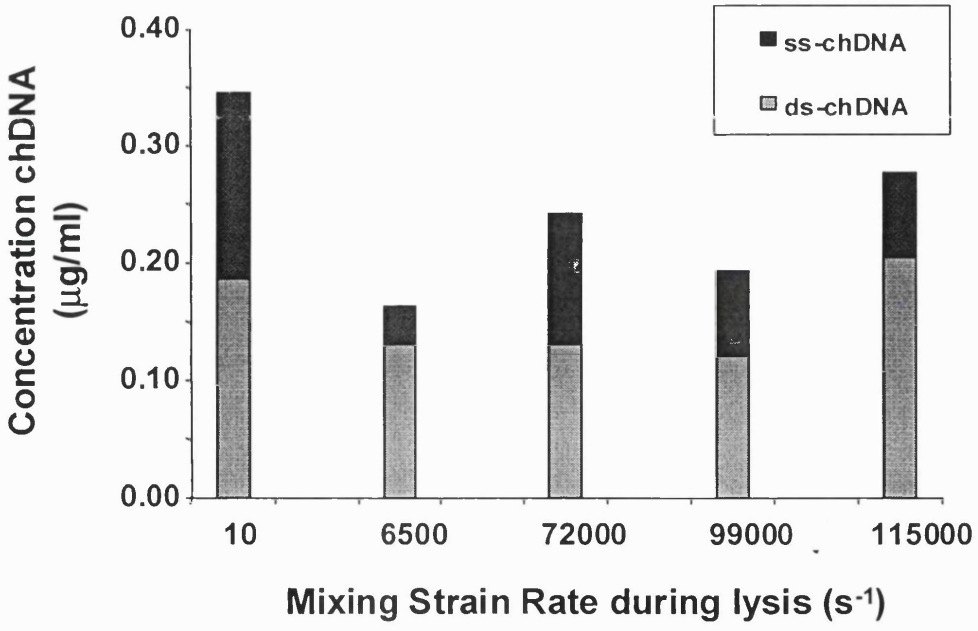

Figure 7.6. Concentrations of double-stranded and single-stranded chromosomal DNA in calcium chloride precipitated alkaline lysates.

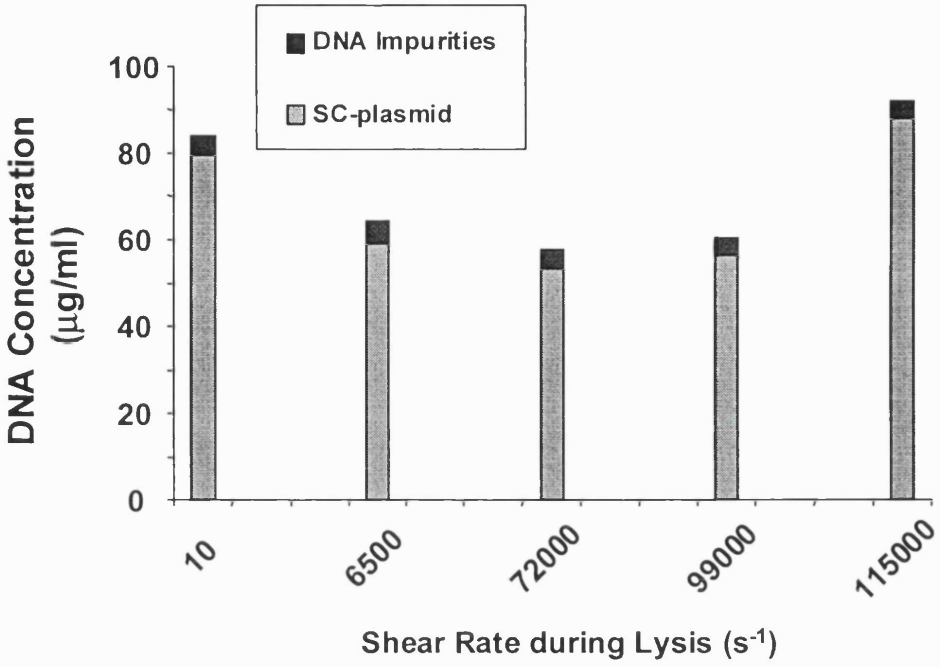

Figure 7.7. Supercoiled plasmid DNA concentration and DNA impurity concentration in clarified alkaline lysates.

7.4.4 Size exclusion chromatography using Sephacryl S1000 SF

Ferreira et al. (1997 and 1998) reported separation of a small 4 kb plasmid and chromosomal DNA using Sephacryl S1000 SF chromatography resin. The small plasmid eluted slightly later than most of the chromosomal DNA. To test the separation of plasmid pSVb and chromosomal DNA using this resin, supercoiled plasmid and chromosomal DNA were injected into the column and eluted at 0.1 mL/min flowrate. Figure 7.8 shows chromatograms from injection of supercoiled plasmid pSVb, chromosomal DNA and TE buffer onto the Sephacryl column. The TE buffer eluted as a single peak at 8.5 minutes. The plasmid and chromosomal DNA eluted as a separate peak at 5.5 minutes, with some RNA impurities and possibly small DNA fragments eluting at 8.5 minutes. It was apparent that the supercoiled plasmid was barely entering the pores of the resin, and that most chromosomal DNA was also too large to enter the resin. Hence, there was only very minimal separation of the supercoiled plasmid and chromosomal DNA using the resin, with the supercoiled plasmid at about the same time as the chromosomal DNA. This marginal separation was despite using chromosomal DNA prepared under gentle shear conditions, maximising the size of the chromosomal DNA fragments. Therefore size exclusion chromatography is probably not a viable unit operation for DNA purification of most

sizes of plasmids, particularly when the poor scaleability of size exclusion chromatography is considered.

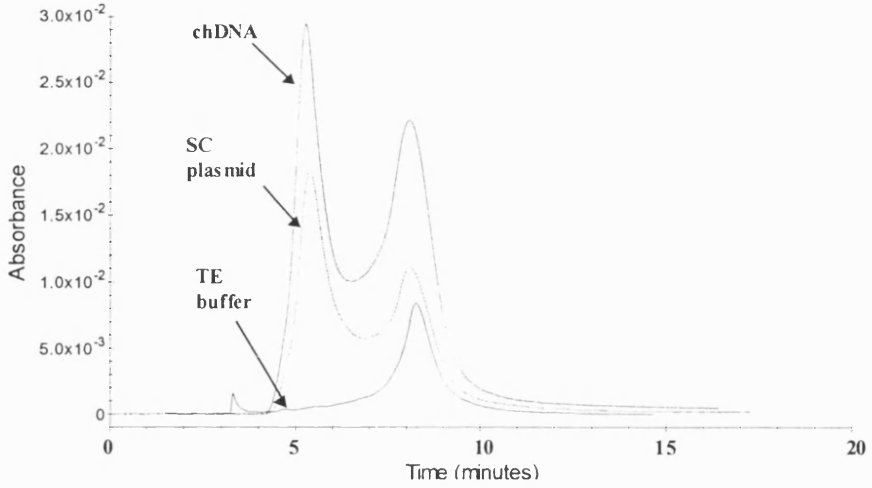

Figure 7.8. Chromatogram of pure supercoiled plasmid injection and pure chromosomal DNA injection on Sephacryl column

7.4.5 Anion exchange chromatography: Poros PI and Q-Sepharose

Effect of DNA denaturation

It has already been demonstrated in chapter 4, that the anion exchange resins Poros PI and Q-Sepharose separate single-stranded chromosomal DNA from supercoiled plasmid DNA. Therefore, the effect of chromosomal DNA denaturation on chromosomal DNA removal over Poros PI or Q-Sepharose is critical. It has already been shown in chapter 5 that the NaOH concentration during alkaline lysis needs to be at least 0.08 to 0.1 M NaOH to ensure conversion of chromosomal DNA to single-stranded form that can be separated from supercoiled plasmid production a Q-Sepharose or Poros PI column.

Effect of DNA size

It has already been demonstrated in chapter 4, that the yield of chromosomal DNA eluted from Poros PI columns is less than 100% when the chromosomal DNA has not been fragmented by fluid stress. It is apparent that the amount of chromosomal DNA that elutes from the column is dependent on the chromosomal DNA fragment size. Figure 7.9 shows the amount of chromosomal DNA eluted from Q-Sepharose columns as a function of double-stranded DNA fragment size. Considerable chromosomal DNA becomes trapped on the Q-Sepharose column, when the chromosomal DNA is sufficiently large. Although Q-Sepharose resin has the same binding affinity for supercoiled plasmid and double-stranded chromosomal DNA, this results demonstrates that considerable double-stranded DNA can be separated from supercoiled

plasmid based on the larger size of chromosomal DNA. To maximise double-stranded chromosomal DNA removal using Q-Sepharose resin, reduction on fluid stress during lysis is important.

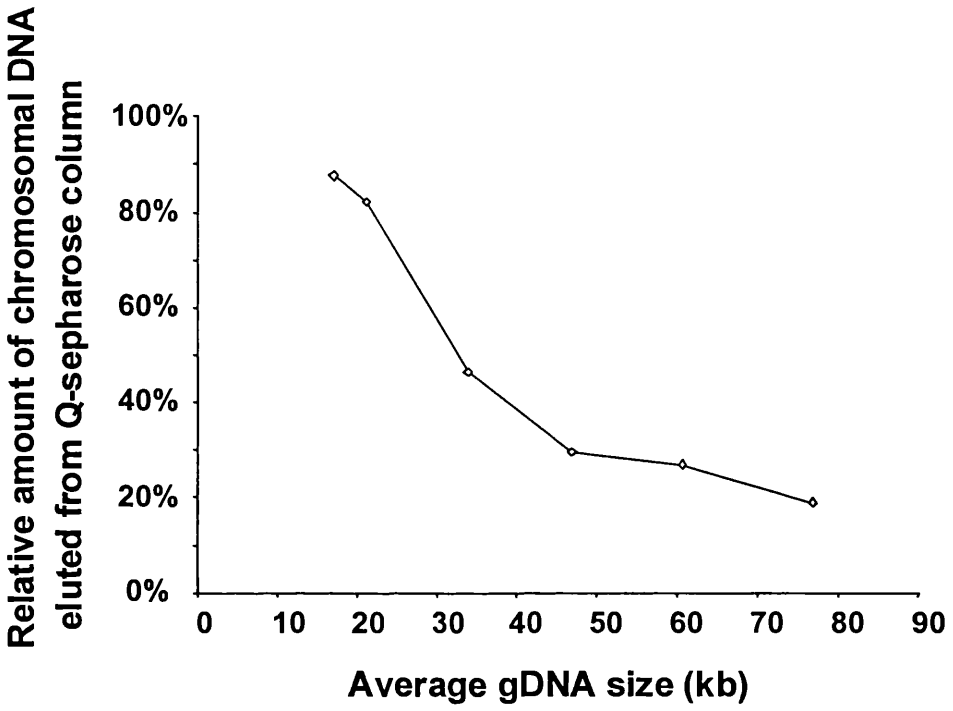

Figure 7.9. Plot showing effect of chromosomal DNA size on amount of DNA eluted from Q-Sepharose Hi-trap column.

7.4.6 Adsorption using silica gel

Binding capacity

Silica was demonstrated in chapter 4 to be a suitable resin for separation of chromosomal DNA and supercoiled plasmid due to the higher affinity of silica for single-stranded DNA compared to double-stranded DNA. Following suitable pH treatment to denature chromosomal DNA to single-stranded form, leaving supercoiled plasmid double-stranded, the chromosomal DNA and supercoiled plasmid can be separated. Due to the very low cost of silica gel, it was investigated as a means of purifying plasmid DNA at manufacturing scale by adsorbing the chromosomal DNA. It was determined in chapter 4, that at NaCl concentrations less than 1 M NaCl, supercoiled plasmid did not bind to silica at pH 7.0, while single-stranded DNA did bind. Experiments were performed to determine the binding capacity of single-stranded chromosomal DNA to silica gel at 1 M NaCl, as described in Materials and Methods. The binding capacity of silica gel for DNA was determined to be about 100 μg ss-DNA/g silica gel, at pH 7.0, 1 M

NaCl. This is about half the binding capacity of Q-Sepharose resin for DNA, reported by Prazeres et al. (1998). Thus, 2 kg of silica gel would purify 5g of supercoiled plasmid containing 4% chromosomal DNA impurity (10 L solution of 200g/L silica gel, 0.5 mg/mL supercoiled plasmid).

Purification of supercoiled plasmid DNA

Figure 7.10 is a bar graph showing the concentration of chromosomal DNA in a supercoiled plasmid sample before and after treatment with silica gel, as described in Materials and Methods. The chromosomal DNA was reduced from about 35% to about 1% impurity as measured by HPLC assay. The plasmid DNA yield loss was negligible. Due to the low cost of silica gel, silica gel adsorption would be suitable method for laboratory scale and pilot scale plasmid DNA purification. However, because of its relatively low binding capacity, silica gel adsorption would probably not be ideal at manufacturing scale.

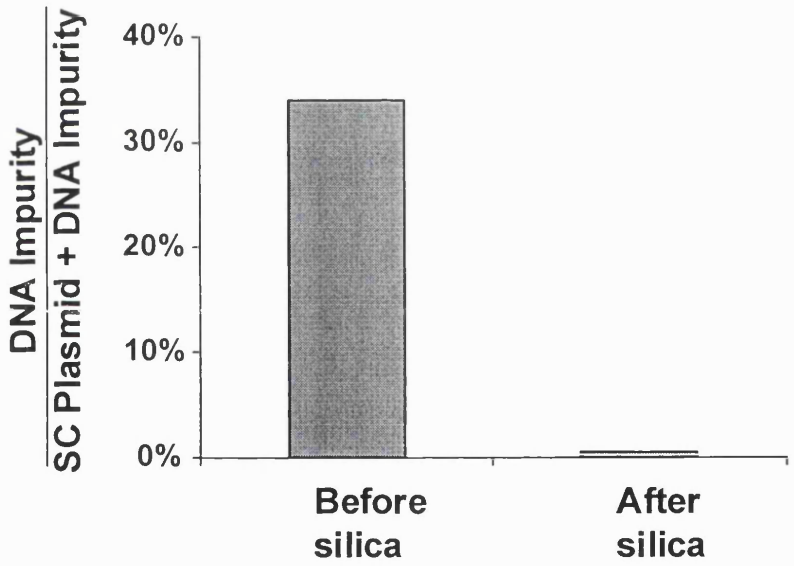

Figure 7.10 Plot showing the % chromosomal DNA before and after silica gel treatment.

Removal of open-circular plasmid DNA

Separation of open-circular plasmid DNA can also be achieved using silica gel adsorption. As already shown in chapter 4, open-circular plasmid can be converted to single-stranded form at a lower pH than supercoiled plasmid. After pH denaturation, single-stranded plasmid forms can be separated from supercoiled plasmid forms using silica gel adsorption. Figure 7.11 shows a heat-degraded plasmid sample containing predominantly open-circular plasmid, with some supercoiled plasmid, before and after denaturation and silica gel adsorption. As shown in the

figure, after denaturation and adsorption virtually all of the open-circular plasmid was removed with negligible supercoiled plasmid yield loss.

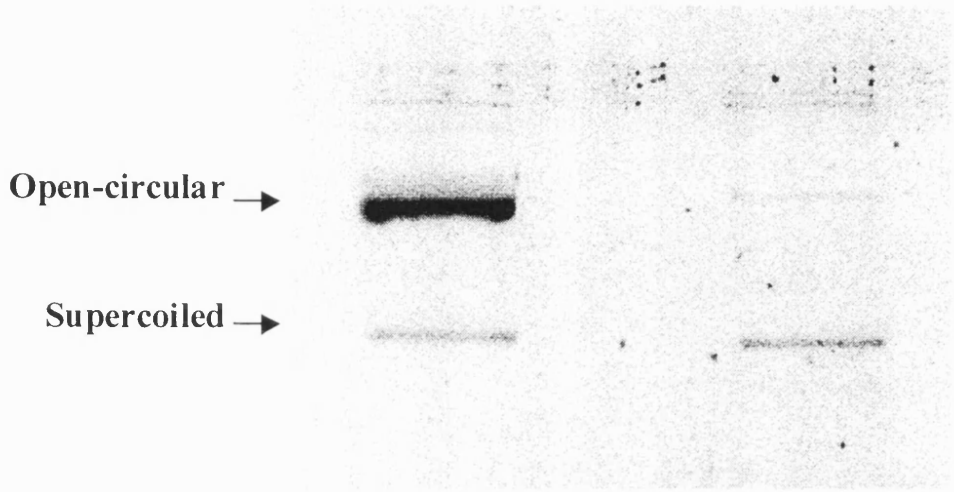

Figure 7.11. Agarose gel showing removal of degraded plasmid forms using pH denaturation and silica gel. Left lane: Initial heat-degraded pure plasmid sample. Right lane: after pH denaturation, and 2 hours incubation with silica gel.

7.5 Conclusion

It was demonstrated in this chapter that single-stranded chromosomal DNA can be efficiently separated from supercoiled plasmids DNA using inexpensive precipitation, chromatographic or adsorption techniques such as calcium chloride precipitation, Q-Sepharose chromatography or silica gel adsorption. In contrast, separation of double-stranded DNA from supercoiled plasmid could only be achieved based on size-based separation (such as CTAB precipitation or filtration) and the efficiency of the size-based separations was generally poor. Therefore, it has been demonstrated that maximising conversion of chromosomal DNA to single-stranded form is a critical design criterion for the alkaline lysis operation. If denaturation of chromosomal DNA is not complete, a second denaturation step, post-alkaline lysis, should be considered.

Although, none of the size-based separation techniques was efficient at clearing the entire chromosomal DNA, some techniques did clear a significant fraction of the chromosomal DNA impurity (refer to Table 7.1). Therefore, a second design criterion for the alkaline lysis step should be prevention of chromosomal DNA fragmentation. The relative importance of these two design criteria will depend on the downstream purification operations that are being used in a particular DNA purification process. In general, conversion of chromosomal DNA to single-

stranded form should be significantly more important than prevention of chromosomal fragmentation, due to the ease of clearing single-stranded chromosomal DNA compared to clearing double-stranded chromosomal DNA.

The next chapter will discuss the design of an improved alkaline lysis reactor, based on the improved understanding of DNA degradation and alkaline lysis performance and its effect on downstream purification operations.

8 Design of an opposed jet mixer for alkaline lysis

Previously, chapter 4 presented results into assay development to measure DNA shear-induced degradation, and chapters 5 and 6 presented results into the effects of fluid mixing and fluid shear on DNA degradation in a model flow system and during alkaline lysis. The effect of DNA denaturation and DNA fragmentation on overall downstream process performance was examined in chapter 7. This chapter seeks to apply the knowledge gained from these previous chapters into designing an improved alkaline lysis step for DNA purification processes. It was demonstrated in chapter 6 on alkaline lysis, that moderate to high impeller speeds are required for adequate mixing during alkaline lysis, and that the likely shear rates produced will lead to significant chromosomal DNA fragmentation. With this in mind, an alternative mixing strategy consisting of an opposed jet mixer was examined. Computational Fluid Dynamics simulation, and laboratory experiment, was performed to understand and predict the performance of the jet mixer.

This chapter starts with a brief summary of results, which is followed by an introduction into the motivation for designing an opposed jet lysis reactor. This is followed by a description of the materials and methods used for the CFD simulation of the jet mixer and of the materials and methods used for the experimental studies of the jet mixer. The CFD simulation results are then presented, followed by the experimental results. Finally, the chapter concludes with a discussion of the CFD and experimental results.

8.1 Brief summary of results

CFD analysis of an alkaline lysis operation in an opposed jet mixer predicted that the rates of fluid mixing would be very fast and that the levels of fluid stress would be very low. Dimensional analysis of CFD simulation predictions showed the relationship between fluid stress and mixing times and jet geometry, jet flowrate and solution density and viscosity. Understanding these relationships should allow confident scale-up of jet mixing devices from bench-top to manufacturing scale. Experimental studies using the jet mixer verified the rapid mixing time obtainable and demonstrated it to be an efficient technique for mixing cells and lysis buffer during alkaline lysis. Comparison of CFD predictions to experimental observations demonstrated the validity of the CFD results.

8.2 Introduction

From the studies of chapter 6 and 7, it was concluded that moderate to high levels of fluid mixing, together with low levels of fluid shear, are required during alkaline lysis to optimize overall process performance. This chapter describes in detail the Computational Fluid Dynamics analysis, and the experimental verification, of an improved alkaline lysis reactor which gave improved performance over more commonly used impeller-driven mixing tanks. The improved alkaline lysis reactor was an opposed jet mixer consisting of two jets of liquid, one containing cell resuspension, and the other containing lysis buffer. The jets were positioned directly facing each other such that the jets impacted and mixing of cells and lysis buffer took place in the region between the jets.

An inelastic collision between two jets at very high relative velocity causes rapid energy dissipation in the impingement zone which controls the smallest eddy size within which molecular diffusion is needed for further micro-mixing. Due to the very short mixing times attainable in opposed jets (Harnby et al., 1992), and the short exposure time of the fluids to regions of high shear (Ciccolini et al., 2002), it was anticipated that an opposed jet device would provide superior performance to conventional stirred tanks. Opposed jets are widely used in reaction injection molding (RIM) processing equipment to provide good micro-mixing for viscous fluids. There is a number of qualitative and quantitative impingement mixing studies reported in the RIM literature; however, the geometry of such mixers differs significantly from that employed here. Several groups have reported on the performance of two opposed Tees for fluid mixing (Tosun et al., 1987; Forney et al., 1990; Cozewith et al., 1989; O'Leary et al., 1985). Again, however, the mixer geometry was not the same as required here for alkaline lysis. Mahajan et al. (1996) reported on the performance of opposed jets, similar in design to the opposed jets used in this work. Using the Bourne reaction to experimentally measure mixing rates (Harnby et al., 1992) they correlated the performance of three small scale jets against jet flow rate and jet diameter. Their study was limited to small-scale jets.

In order to predict the mixing characteristics of opposed jet mixers across a range of jet flowrates and jet diameters, Computational Fluid Dynamics (CFD) analysis was performed. As described in detail in Chapter 3, a computer model of the opposed jet mixer was created and flow streamlines, fluid pressures, shear rates and energy dissipation rates within the model were calculated using CFD simulation. The simulation results were analyzed to determine the characteristic mixing time within the opposed jet mixer, and to determine the levels of fluid stress between the jets. In addition, the fluid dynamics in jets of varying diameters was simulated, in order to determine the effects of scaling the unit from bench-top to pilot to

manufacturing scale. After CFD analysis, a small number of experiments were run using an opposed jet mixing device to lyse *E. coli* cells containing plasmid pSVβ.

8.3 Experimental materials and methods

8.3.1 Jet mixing equipment

Two separate Hamilton syringe pumps were used to force lysis solution and resuspended cell solution into opposed jets; the solutions impinged and were collected below the impingement region in a plastic container. Figure 8.1 shows a schematic of the opposed jets and the plastic assembly for aligning the jets. The jets were made of PEEK tubing, and could be varied from 0.0025" to 0.08" internal diameter (0.06 to 2.0 mm ID). The two jets could be either the same diameter, or different diameters.

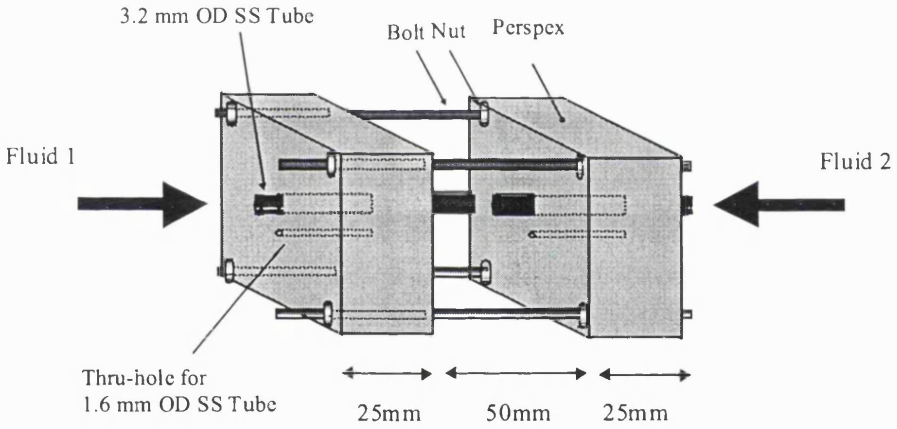

Figure 8.1. Diagram of opposed jet mixing device

8.3.2 Pure plasmid DNA and NaOH mixing studies

Pure supercoiled plasmid pSVb at 1 µg/ml in TE was mixed with NaOH (0.2 M, 0.4 M o 1.0 M NaOH) using the opposed jet mixer. Both the plasmid and NaOH jets were 0.010" ID PEEK capillaries (0.254 mm ID). The flowrate of the pSVβ solution was set to give a jet velocity of 1 m/s. The flowrate the NaOH solution was set relative to the plasmid flowrate such that the NaOH concentration after mixing was always 0.1 M NaOH. After mixing 5 mL of plasmid solution, the solution was neutralised with 2 volumes of 500 mM Tris, pH 7.5. The samples were assayed for supercoiled plasmid content by Picogreen assay.b

8.3.3 Alkaline lysis mixing studies

To determine the performance of opposed jets at mixing resuspended cells and alkaline lysis buffer, E. coli DH5a pSVb cells were lysed using 1% SDS, 0.2 M NaOH or 2% SDS, 0.4 M NaOH in the opposed jet mixer, at various flowrates. In all cases, the relative flowrate of the

cell solution to the lysis solution was set to give a final mixed concentration of 0.1 M NaOH. The diameters of the cell resuspension and lysis buffer jets were 0.02" and 0.007" ID for the 0.4 M NaOH study or 0.04" and 0.04" ID for the 0.2 M NaOH study, respectively. After mixing, each lysate was neutralised with a volume of neutralisation buffer equal to the cell resuspension volume. The samples were clarified as per the standard protocol and assayed by Poros PI HPLC for supercoiled plasmid and DNA impurities. In parallel with the jet mixing studies, resuspended cells were lysed and clarified at 2 mL scale using the standard protocol, using one volume of 1% SDS, 0.2 M NaOH. This control lysis samples was also assayed by Poros PI HPLC.

8.4 Computational fluid dynamics results

8.4.1 Materials and methods

The Materials and Methods used for opposed jet model development are described in detail in chapter 3 on Computational Fluid Dynamics, section 3.4. Three different jet models were created and simulated. The jet models were:

Model 1) Equal jets, impinging subsurface (submerged), 1-phase system

Model 2) Equal jets, impinging in air (non-submerged), 2- or 3-phase system

Model 3) Non-equal jets, impinging in air (non-submerged), 2- or 3-phase system

For each CFD model, the flow equations were solved iteratively; if the iterative process converged then a solution to the flow problem was obtained. In general, it required 1000 to 100,000 iterations for convergence to be reached depending mostly on the number of grids used to sub-divide the model geometry. In addition to solving the flow equations, an important criterion for a valid CFD solution was grid-size independence. The solution to the CFD equations must become independent of the grid-size used to sub-divide the model geometry for a sufficiently fine grid size. For all opposed jet models, the flow equations were solved using different size grids to check that the final results were grid-size independent when sufficiently fine grids were used. This procedure is described in detail in chapter 3. After obtaining a grid-size independent CFD model, the CFD predictions were compared to analytical or empirical predictions as a check to ensure that the simulations were converging to realistic solutions. Analytical expressions for the pressure drop within the jet nozzles, and the entrance length before the flow becomes fully developed, was available. An empirical expression for the energy dissipation between the jets was also available. The CFD predictions were compared to these analytical and empirical predictions. Where analytical or empirical expressions were not

available to describe the behaviour of the jets, dimensionless analysis was performed on the simulation data.

8.4.2 Model 1: Equal diameter, sub-surface jets

Although, alkaline lysis mixing would most likely be performed using non-submerged jets, the submerged case was simulated first because it involved one fluid phase and therefore should be less prone to potential errors associated with multi-phase modelling. It represented a useful starting point to check that the simulations were giving realistic results. Following successful simulation of 1-phase opposed jets; 2- and 3- phase models were simulated.

Model convergence

Using the model geometry shown in Figure 3.2 (top), the submerged opposed jet flow (Model 1) was simulated using the Low Re κ–ε model, at 5 m/s inlet velocity (Re = 20,000), for 4 cm long, 4 mm ID opposed jets of water. For a particular mesh, the simulation was run until there was no significant change in the fluid velocity, pressure, turbulent energy and turbulent energy dissipation between subsequent iterations. Solutions typically required 1,000 to 100,000 iterations before convergence. After a solution was obtained, the geometry was re-meshed and the simulation re-run. Figure 8.2 shows the effect of the number of girds on the predicted energy dissipation in the region directly between the jets. As the number of grids in the model was increased, the energy dissipation decreased rapidly and then levelled-off. The convergence of the energy dissipation was most closely monitored because the energy dissipation was the parameter that determines the quality of fluid mixing between the jets (see Equation 2.2). The fluid velocity and pressure converged more rapidly than the energy dissipation. In order to minimise computation time, the model consisting of 11,000 grids was used for all subsequent simulations of equal, submerged jets.

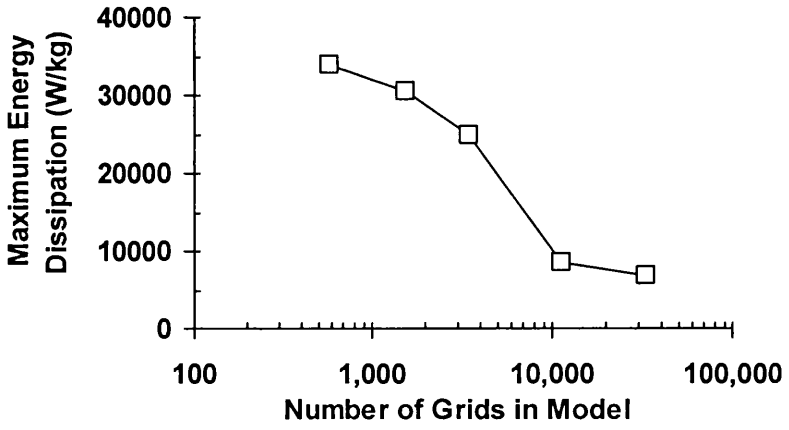

Figure 8.2 Plot showing the decrease in CFD predicted maximum energy dissipation as the number of grids increased. Convergence is seen above 10,000 grids.

Jet nozzle pressure drop

CFD simulations were run for 4 mm ID submerged jets (Model 1) at 0.2 m/s (Re = 800) using the laminar flow models. An analytical expression was available for the pressure drop along the jet nozzle entrance pipe, Equation 2.21. The CFD simulation predicted a pressure drop per unit length within the jet nozzle of 400 Pa/m, once fully developed parabolic flow was established. This CFD predicted result exactly matched the analytically calculated result of 400 Pa/s. The CFD simulation predicted that the entrance region of the nozzle would be 17 cm, which was close to a value of 19 cm using the analytical approximation of Equation 2.23.

Jet energy dissipation rate

An analytical expression for the energy dissipation in opposed jets was not available, but empirical expressions for the energy dissipation of a single jet flowing into large body of fluid (a submerged, unbounded jet) was available, refer to Equation 2.9 in chapter 2. A value for κ of 0.1 was used, which is the value generally used for submerged, unbounded jets at high velocity. Using Equation 2.9, the empirically calculated energy dissipation rate for 4 mm ID opposed jets impinging at 5 m/s is 3100 W/kg. In order to compare the CFD results to this analytical expression, a CFD simulation was run using Model 1 for 4 mm ID water jets impinging at 5 m/s (high velocity jets, Reynolds number is 20,000). The low Re κ–ε model was used for the simulation.

Figure 8.3 shows the CFD calculated energy dissipation contours for the submerged jet. The maximum energy dissipation between the jets was taken as the region of maximum energy dissipation rate through which 90% of the jet flows through. The region of maximum energy dissipation rate coincides with the stagnation region between the jets. Also shown in Figure 8.3 is the 90% flow streamline. The CFD predicted maximum energy dissipation rate was 3000 W/kg. Hence, the CFD prediction of energy dissipation rate, in submerged jets at high Reynolds number, closely matches the empirical prediction of 3100 W/kg. Thus, CFD Model 1 gave realistic predictions for the flow behaviour within the jet nozzles, and the CFD predicted jet pressure drop and turbulent energy dissipations rate were within the expected range. After using CFD to successfully predict the behaviour of submerged impinging jets, non-submerged impinging jets were simulated using CFD (Model 2, 2-phase).

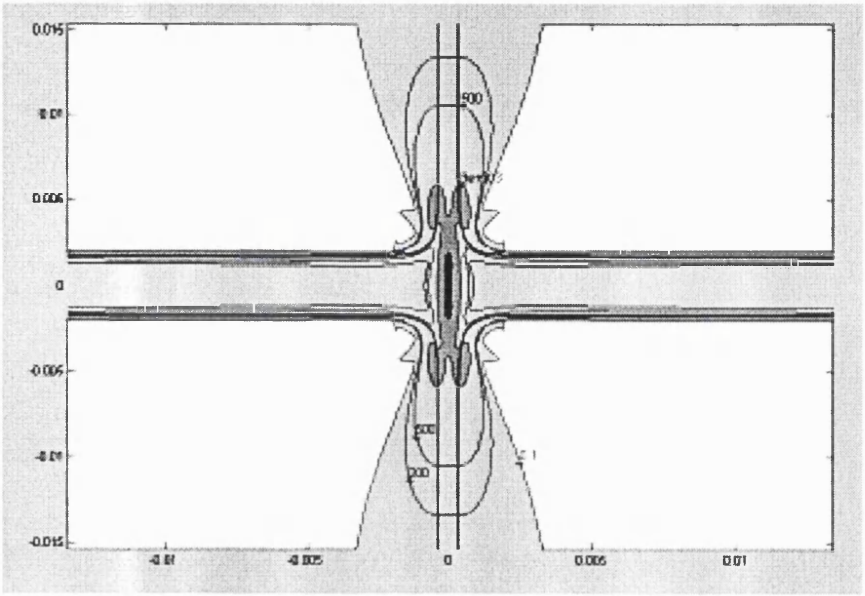

Figure 8.3. Filled contour plots for the CFD predicted energy dissipation rates between submerged jets. Jet velocity was 5 m/s, 4 mm ID jets. Also shown are the fluid streamlines that encompass 90% of the fluid flow.

8.4.3 Model 2: Equal diameter, non-submerged impinging jets

The dimensions of Model 2 geometry were the same as Model 1 (refer to Figure 3.2, top). Model 2 consisted of liquid jets impinging in air, compared to liquid jets impinging in liquid for Model 1.

Model Convergence

A set of simulations was run with Model 2 using jets of water at 1 m/s (Re = 4000) to check for grid-size independence. The Low Re κ–ε model was the turbulence model used. Figure 8.4 shows the effect of the number of grids used to sub-divide the flow domain on the energy dissipation in the region directly between the jets. The CFD predicted maximum energy dissipation between the jets decreased rapidly as the number of grids increased and converged above 1500 grids. In order to minimise computation time, the model consisting of 1570 grids was used for all subsequent simulations of equal, non-submerged jets.

Comparing the grid convergence study for Model 1 with Model 2, the submerged jet model required significantly more grids for convergence. It was observed in Model 1 that there were localised regions at the exit of the jet nozzles where significant energy dissipation occurred. This was caused by high velocity liquid leaving the jet nozzle and entraining stationery liquid. When a low number of grids were used, the CFD simulation gave an inordinately high energy dissipation rate in this region. It required long simulation times and a large number of grids to

achieve convergence of energy dissipation rate in this region. In contrast, for Model 2 the high velocity liquid exiting the jet nozzle was entraining stationary air, which did not lead to high levels of energy dissipation. This may explain why Model 1 required a larger number of grids before model convergence was achieved.

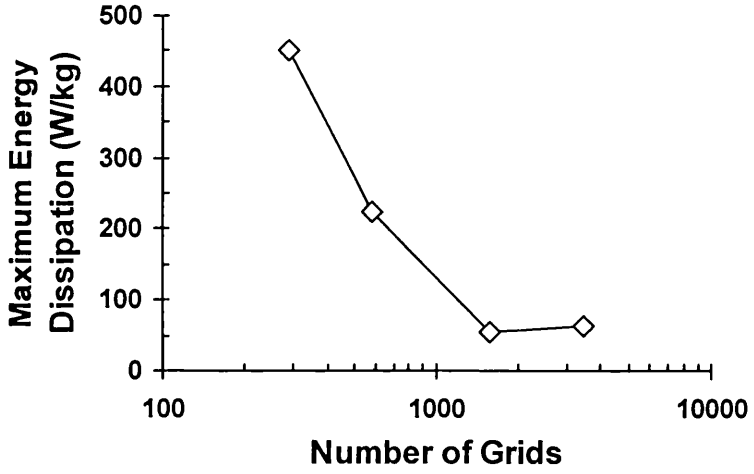

Figure 8.4 Plot shows the convergence in CFD predicted maximum energy dissipation as the number of grids increases. Convergence is seen above 1000 grids.

Effect of turbulence model

In order to examine the effect of turbulence model on CFD computed jet energy dissipation rate, jets were simulated using the both the κ–ε and the Low Re κ–ε models, at 1 m/s jet velocities using Model 2.

Figure **8.5** shows contour plots of the energy dissipation rate calculated using the two turbulence models. Also shown in the plots are the 90% flow streamlines (90% of the fluid flows between these streamlines). The maximum energy dissipation rate was taken as the region of maximum energy dissipation through which 90% of the fluid flows, which coincided with the stagnation region between the jets. The maximum energy dissipation between the jets was 17 and 23 W/kg for the κ–ε and Low-Re κ–ε models, respectively. Hence, there was only a moderate difference between the computed energy dissipation rates using the different eddy viscosity models. As already described, the mixing time is only a weak function of energy dissipation; therefore, the different turbulence models will predict similar mixing times. All subsequent calculations were done using the Low Re κ–ε model, which is more appropriate for the low Reynolds numbers that apply to the jet simulations.

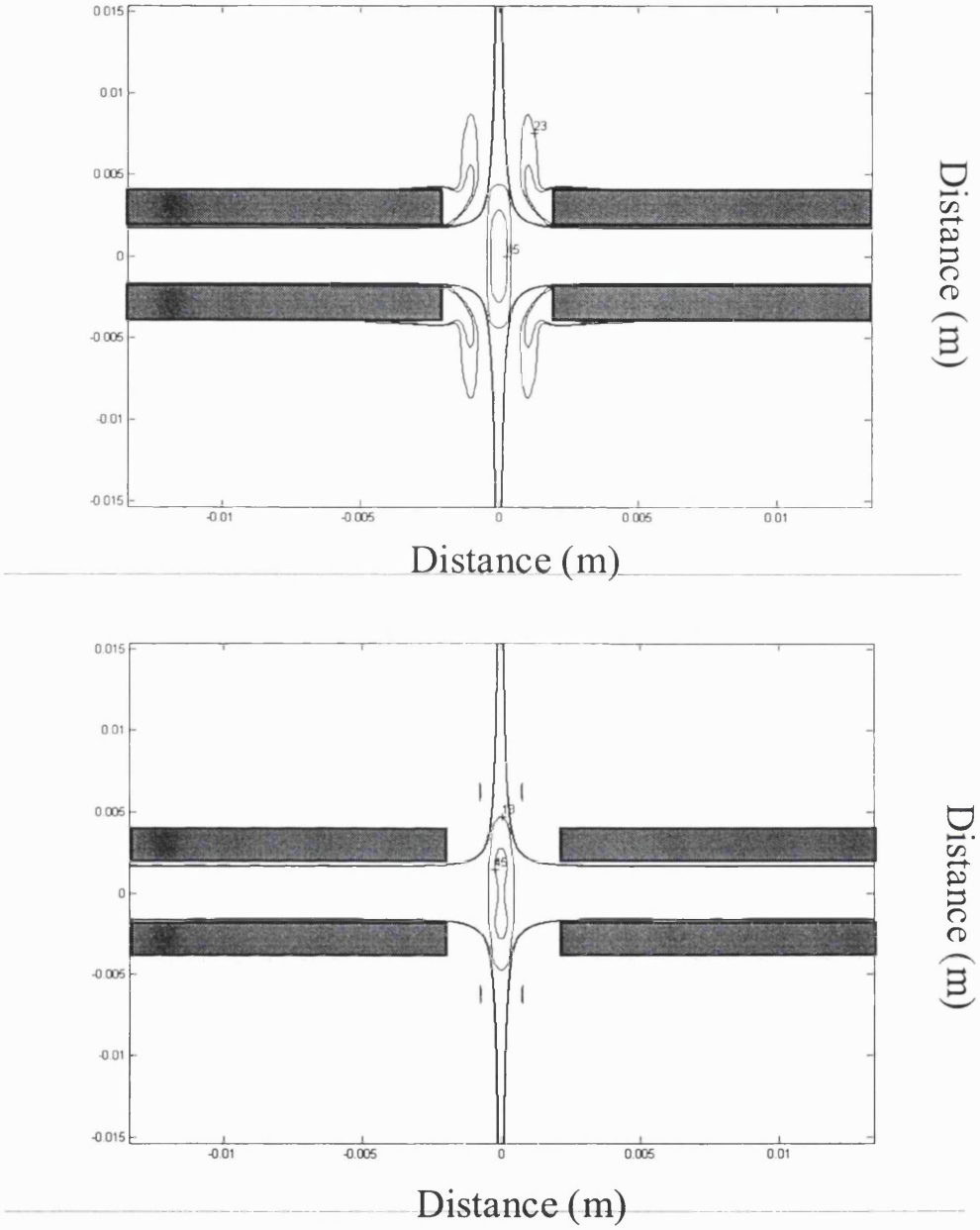

Figure 8.5. Contour plots of CFD predicted maximum energy dissipation between opposed water jets at 1 m/s velocity. Top: K–ε model. Bottom: Low Re κ–ε model. Also shown in the plots are the 90% flow streamlines. The predicted energy dissipation in the elliptical region between the jets was 17 and 23 W/kg for the K–ε model and Low Re κ–ε model, respectively. The K–ε model predicts a small amount of energy dissipation in the gas-phase close to the jet impingement region; this should not affect the jet mixing performance.

Jet energy dissipation rate

Typical CFD results using Model 2 are shown in Figure 8.7; the fluid speed, shear rate and energy dissipation rate between 4 mm ID opposed jets are shown as contour plots. In this example, the jet velocity was 1 m/s. The fluid speed and energy dissipation contours were calculated directly by the CFX software. The shear rates were calculated from the velocity gradient data, as explained in section 3.6.1. As shown in the contour plots, the maximum shear rate and maximum energy dissipation rate between the jets were 200 s^{-1} and 10 W/kg, respectively. From Equation 2.1 and Equation 2.2, an energy dissipation rate of 10 W/kg corresponds to a micro-mixing time of less than 100 ms. Hence, very short micro-mixing times can be achieved at relatively low levels of fluid stress.

Figure 8.6 shows the CFD calculated energy dissipation over a range of jet velocities for three different diameter opposed jets (0.5, 4 and 12 mm ID). Refer to Table 3.5 for a complete list of simulations. As shown in the Figure 8.6, the energy dissipation rate (ε) varied over 4 orders-of-magnitude, depending on jet diameter (d) and jet velocity (u). Due to this significant variation in energy dissipation rate, it is essential to understand the effects of jet diameter and jet velocity on energy dissipation to successfully scale-up an opposed jet mixer.

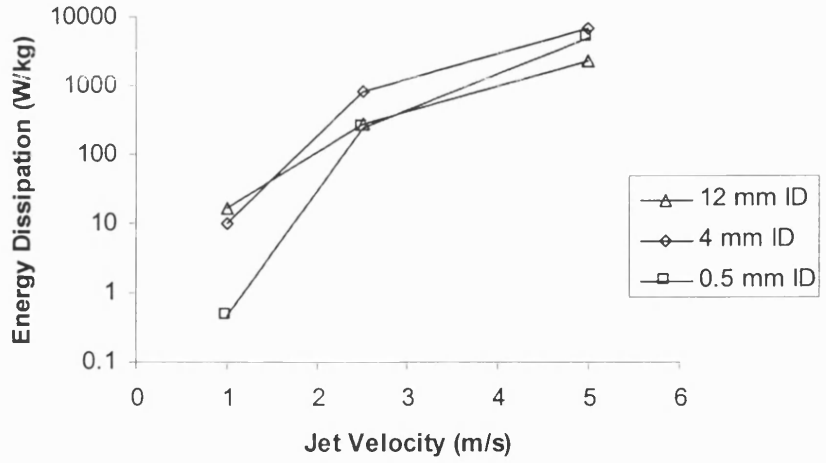

Figure 8.6 Plot showing the energy dissipation for 3 different ID jets as a fucntion of jet velocity. The opposed jet system should be scaled by jet velocity.

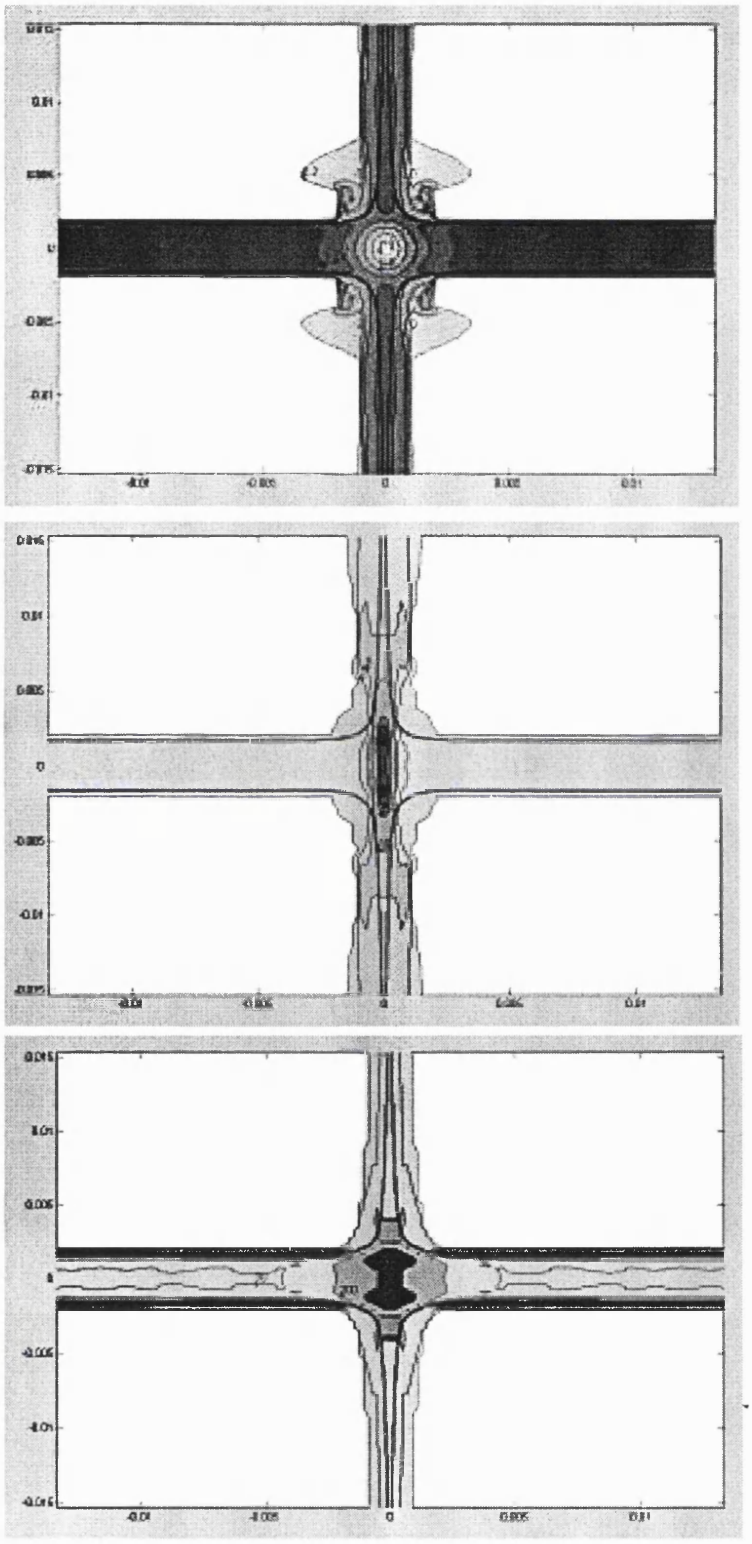

Figure 8.7 Contour plots of speed (top), energy dissipation (middle) and strain rate (bottom) between 4 mm ID opposed jets, at 1 m/s average jet velocity, Model 2. The jets enter from the left and right, impinge, and exit radially.

Dimensional analysis was performed on the CFD predictions of turbulent energy dissipation rate and fluid strain rate for CFD Model 2. Based on the relationship between energy dissipation rate, jet diameter and jet velocity (refer to section 2.3.3) the appropriate combination of variables to represent dimensionless energy dissipation is $\varepsilon d/u^3$. The data from Figure 8.6 was re-plotted as dimensionless energy dissipation versus jet Reynolds number (Equation 2.11) and is shown in Figure 8.8. After this transformation, all the data now falls onto a single curve. As shown in Figure 8.8, at low jet Reynolds numbers the dimensionless energy dissipation rate is very low. The dimensionless energy dissipation increases with increasing Reynolds number up to about 8000. At high Reynolds numbers, > 8000, the dimensionless energy dissipation becomes independent of Reynolds number. This relationship between energy dissipation and Reynolds number is similar to the relationship between Power number and Reynolds number in stirred tanks, where the Power number becomes independent of Reynolds number at high Reynolds numbers.

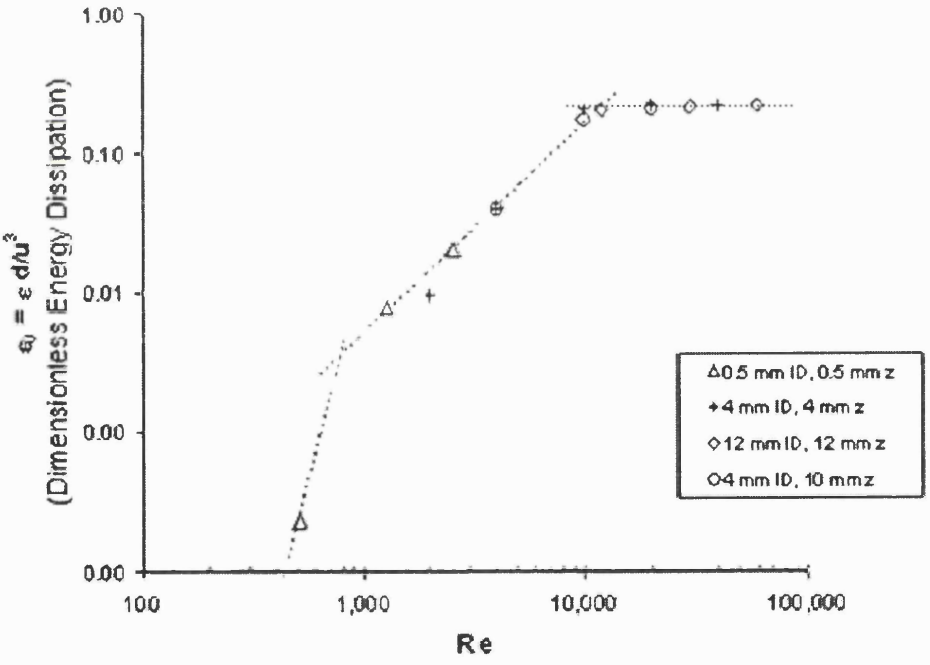

Figure 8.8. Plot of CFD calculated dimensionless energy dissipation rate versus jet Reynolds number for opposed jets impinging in air (Model 2).

Fluid strain rate between jets

As well as the energy dissipation rate, the strain rate between the jets is an important operating parameter. High strain rates were shown to degrade plasmid and chromosomal DNA in chapter 5, leading to chromosomal DNA fragmentation and decreased supercoiled plasmid DNA yield, as shown in chapters 5, 6 and 7. As shown in Figure 8.7, CFD simulation predicts that the region of highest strain rate occurs at the stagnation point between the jets, as expected. Figure

8.9 shows a plot of the CFD calculated dimensionless maximum strain rate between opposed jets as a function of jet Reynolds number, for three different jet diameters (0.508, 4 and 12 mm ID). The dimensionless strain rate was taken to be ε'd/u, where ε' is the CFD calculated maximum strain rate, d is the jet internal diameter and u is the jet velocity. The maximum strain rate was taken as highest strain rate that occurred in the opposed jet flow for a given jet geometry and flow rate. The dimensionless strain rate is relatively independent of Reynolds number, particularly at higher Reynolds numbers.

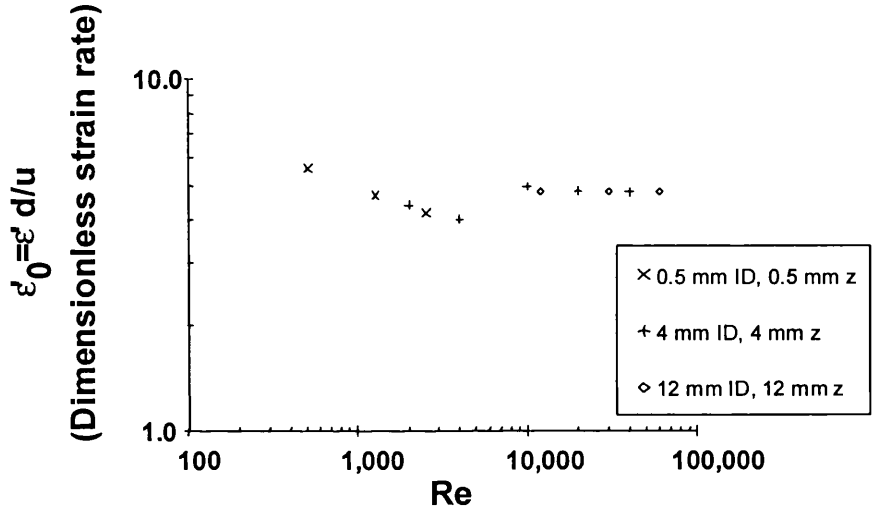

Figure 8.9. Plot of dimensionless maximum strain rate versus Reynolds number for opposed jets of water impinging in air for 3 different diameter jets.

8.4.4 Effect of Jet Separation Distance

From the analytical expression derived for turbulent energy dissipation between opposed jets (Equation 2.5), varying the separation between the jets should not affect the overall energy dissipation between the jets. Figure 8.10 shows the energy dissipation for 4mm ID jets of water, impinging in air, over a range of jet velocities, for jets at two different separation distances. The separation between the jets did not affect the energy dissipation for these simulations.

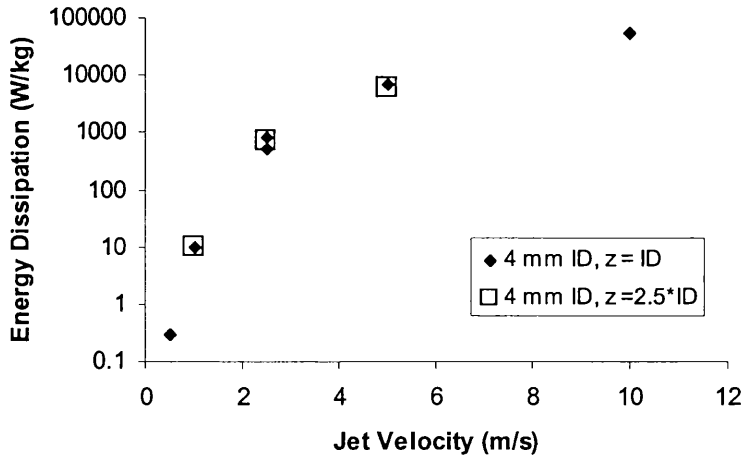

Figure 8.10 Plot showing the effect of separation distance between the jets on energy dissipation rate.

8.4.5 Model 3: Different diameter, non-submerged impinging jets

The dimensions of Model 3 geometry were different from Model 1 and Model 2 geometry in that the diameters of the opposed jets were not taken to be equal (refer to Figure 3.2, bottom). In addition, Model 3 consisted of 3 fluid phases: 2 liquid phases (0.4 M NaOH and water) impinging in a gas phase (air).

Model Convergence

Using the geometry for different diameter jets, shown in Figure 3.2 (bottom), the flow was simulated using the Low Re κ–ε model using a range of grid sizes. As about 1000 grids were required for Model 2 convergence, a large number of grids (close to 1000) were used as the starting point for Model 3 convergence studies. The larger jet had an internal diameter of 1.574 mm and had a velocity of 8 m/s. The smaller jet had an internal diameter of 0.508 mm and had an inlet velocity of 25.37 m/s; the velocity of the smaller jet was chosen so that the jets would have the same momentum. Both jets were given the properties of water, and the gas was given the properties of air (see Table 3.1 for the properties of the fluids). The jets were spaced at twice the jet diameter of the larger jet.

Figure 8.11 shows the effect of the number of grids on the maximum energy dissipation in the region directly between the jets. The maximum energy dissipation rate was taken to be the maximum energy dissipation rate in a region through which 90% of the larger jet flowed through. As shown in the figure, the energy dissipation between the jets had converged even at the smallest number of grids used. The mesh of 4000 grids was used for subsequent calculations. Note: at first glance the energy dissipation rates shown in Figure 8.11 may appear

to be inordinately high (300,000 W/kg), leading one to presume that the CFD simulation was not converged. However, this particular set of CFD simulations was performed at very high jet impingement velocities. The water jet was given a high velocity of 8 m/s compared to 5 m/s for Model 2. However, to ensure momentum balanced jets, the NaOH jet had to have a very high velocity of 25.37 m/s. As energy dissipation in opposed jets will be expected to roughly scale as the jet velocity cubed, an energy dissipation rate of 300,000 W/kg is in fact entirely in-line with a u^3 dependence. This will be discussed further in the next section on energy dissipation.

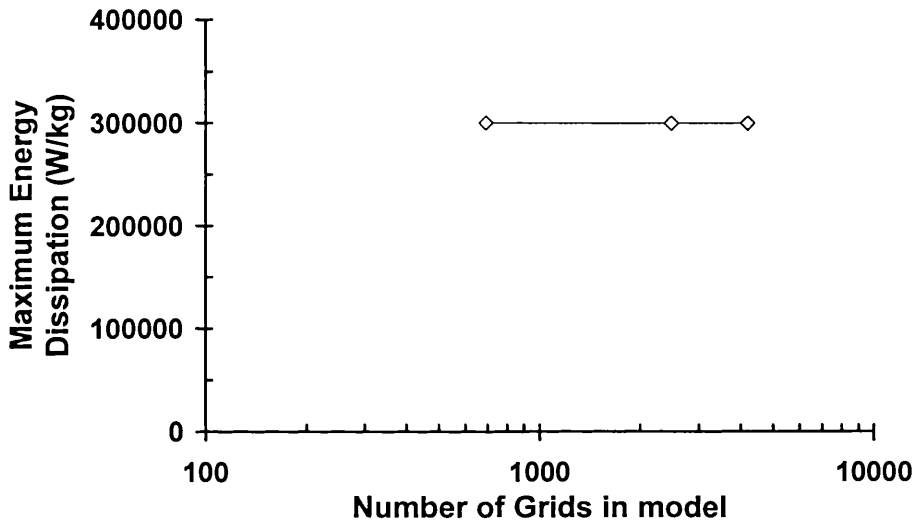

Figure 8.11. Plot of the CFD predicted maximum energy dissipation rate versus number of grids for Model 3, at 8 m/s and 25.37 m/s jet impingement velocities. The energy dissipation rate is converged to a constant value at 700 grids and above.

Energy dissipation in non-equal opposed jets

Opposed jets will only have equal flowrates if mixing requires equal volumes of two fluids to be combined together. This is typically the case in alkaline lysis, when one volume of 0.2 M NaOH is added to one volume of resuspended cells to end-up with a 0.1 M NaOH solution. However, to reduce process volumes it would be advantageous to use more concentrated NaOH. Take for example the case where 1/3rd volume of 0.4 M NaOH is added to 1 volume of cells to end-up with a 0.1 M NaOH solution. The flowrate of the lysis reagent would be 1/3rd the flowrate of the cell resuspension in an opposed jet device. If equal diameter jets were used the velocity of the lysis reagent jet would be 1/3rd the velocity cell resuspension jet. Because the energy dissipation is a very strong function of the jet velocity, $\varepsilon \propto u^3$, the low velocity of the lysis reagent could significantly reduce the quality of the mixing in the opposed jet mixer.

Alternatively, the diameter of the lysis reagent jet could be reduced. This would increase the velocity and momentum of the lysis reagent jet. For example, if the diameter of the lysis jet was reduced to 1/3rd the diameter of the cell resuspension jet, then the velocity of the lysis jet would increase 9-fold, and the momentum 3-fold. Thus, by using a jet diameter ratio of 1/3rd, the jets would impact with equal momentum and with a lot more energy. A contour plot showing the energy dissipation rate from a typical CFD simulation of non-equal diameter jets is shown in Figure 8.12.

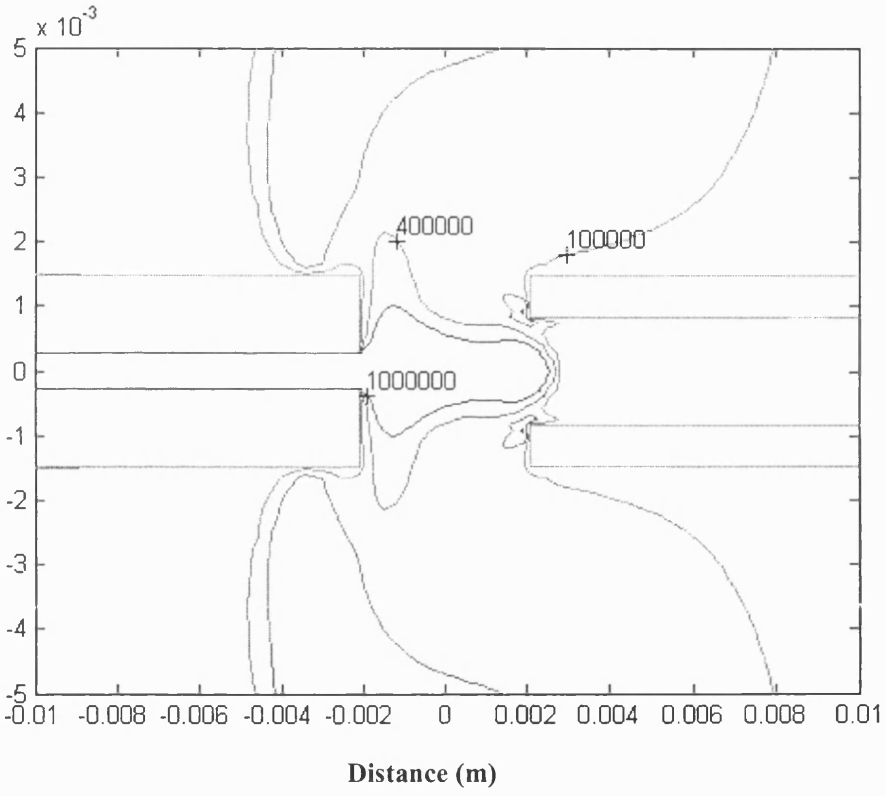

Figure 8.12. Contour plot of turbulent energy dissipation rate (W/kg) for non-equal diameter opposed jets of water. The system consists of a 0.508 mm ID jet at 25.37 m/s jet velocity (left) impacting a 1.574 mm ID jet at 8 m/s jet velocity (right).

In order to examine the effect of jet diameter and jet velocity on the mixing characteristics of non-equal diameter opposed jets, a set of simulations was run using 0.5 mm, 1.58 mm and 12 mm ID opposed jets impinging against smaller diameter jets. The ratio of the smaller jet diameter to large jet diameter was varied from 0.16:1 to 1:1. Refer to Table 3.6 in chapter 3 for a complete list of simulations performed. Figure 8.13 shows a plot of the CFD predicted dimensionless maximum energy dissipation versus the Reynolds number for non-equal opposed

jets, of 0.5, 1.58 and 12 mm internal diameters. In order to calculate the dimensionless maximum energy dissipation rate, the geometric average of the jet velocities was used as the appropriate jet velocity, and the geometric average of the jet diameters was used as the appropriate jet diameter. The Reynolds number was the Reynolds number of the larger jet. Similarly to the case of equal opposed jets, the energy dissipation is a strong function of Reynolds number at low Reynolds number, but becomes independent of Reynolds number at high Reynolds number. The dimensionless maximum energy dissipation rate is about 0.10 which is about half the value predicted by CFD for equal diameter jets, Model 2. The slightly lower value of 0.10 for non-equal diameter opposed jets is expected as most of the energy is supplied by only one of the jets.

The fact that the CFD predicted dimensionless energy dissipation converged to a value close to empirically observed values (Yim et al., 2000), and that all three model simulations (Model 1, Model 2 and Model 3) all give similar predictions of dimensionless energy dissipation, provides reassurance that all three CFD models have converged to meaningful results. The CFD results in Figure 8.13 were obtained over a range of jet velocities, giving a wide range of jet energy dissipation rates (from < 1 W/kg to >300,000 W/kg). It should be noted that although very high energy dissipation rates were obtained (for example 300,000 W/kg in Figure 8.11) when very high jet velocities were used, the CFD predicted dimensionless energy dissipation of 0.1 shows that these high energy dissipation rates were entirely as expected based on the velocity-cubed dependence of energy dissipation rate.

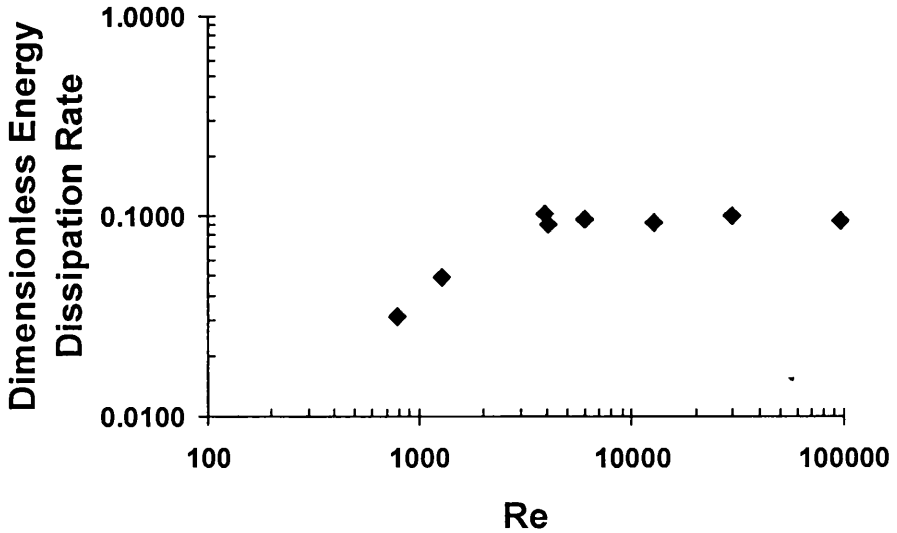

Figure 8.13 shows a plot of the CFD predicted dimensionless energy dissipation versus Reynolds number for non-equal diameter opposed jets. At high Reynolds number, the dimensionless maximum energy dissipation is about 0.10, which is similar to the results for equal diameter opposed jets.

Energy dissipation: Comparison of equal and non-equal diameter opposed jets

In order the assess the effect of jet diameter ratio on energy dissipation, a set of simulations were run comparing equal diameter opposed jets (Model 2) and non-equal diameter opposed jets (Model 3). Model 2 consisted of two equal diameter 12 mm ID opposed jets (Jet A and Jet B); Model 3 consisted of a 12 mm ID jet (Jet A) and a 3.87 mm ID jet (Jet B). For both Model 2 and Model 3, the volumetric flowrate of Jet B was chosen to be one third of the flowrate of the opposing jet, Jet A. The diameter of Jet B in Model 3 was chosen so that the jets are momentum balanced. Refer to Table 3.6 in chapter 3 for a complete list of the simulations. Figure 8.14 shows the CFD predicted maximum energy dissipation rate achieved in both jet systems as a function of Jet A velocity. By reducing the diameter of the Jet B, in order make Jet A and Jet B momentum balanced, there is about a 10-fold increase in energy dissipation rate between the jets. However, by reducing the diameter of Jet B, increasing its momentum, there is an increase in fluid stress between the opposed jets. Figure 8.15 shows the CFD predicted strain rate for the equal diameter jets and for the momentum balanced jets. There was about a 2-fold increase in strain rate due to the reduction in Jet B diameter, along with the 10-fold increase in energy dissipation rate.

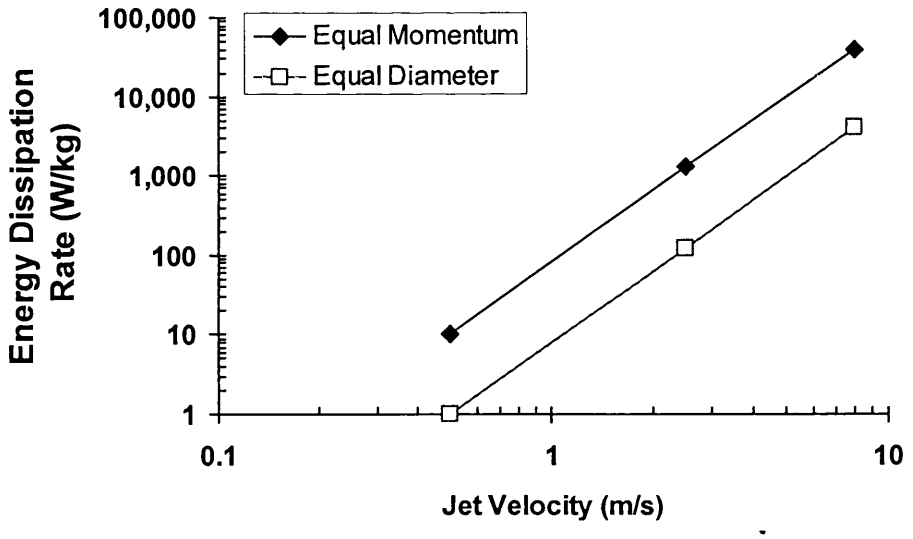

Figure 8.14. Energy Dissipation Rate between two sets of opposed jets, as function of jet velocity, where the flowrate of one jet was required to be 3-times the flowrate of the other jet. In the first system, the diameters of the jets were equal, in the second system the diameters of the jets were not equal but instead they were momentum balanced. Note the significant variation in energy dissipation rate between the jets as a function of jet velocity.

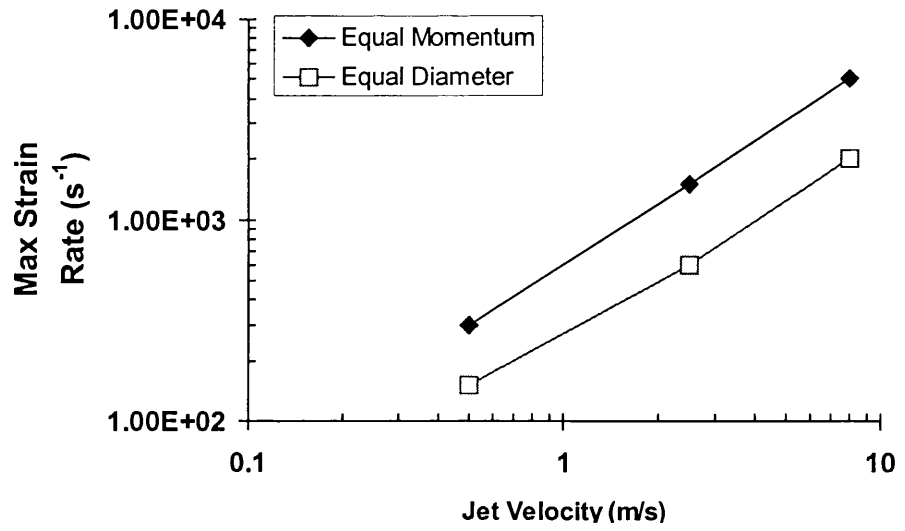

Figure 8.15. Plot showing the maximum strain rate between opposed jets for equal diameter jets and different diameter, but momentum balanced, jets.

8.5 Experimental studies

From the CFD simulation results discussed in the previous section, it was anticipated that an opposed jet mixing device could be used to mix cells and lysis buffer during alkaline lysis, providing short mixing times and minimising supercoiled plasmid DNA yield loss due to irreversible denaturation. A small-scale opposed jet device was investigated to determine its overall performance as a lysis reactor. The jet mixer is described in detail in the Experimental Materials and Methods section in this chapter.

8.5.1 Jet mixing studies using pure supercoiled plasmid DNA

Figure 8.16 shows the supercoiled plasmid yield achieved after mixing pure plasmid pSVβ with NaOH in an opposed jet mixer at 1 m/s, to end-up at a final concentration of 0.1 M NaOH. The NaOH that was mixed with the plasmid solution was 0.2 M, 0.4 M or 1.0 M NaOH. After mixing, the solutions were neutralised as described in Materials and Methods. The yield of supercoiled plasmid DNA was close to 100% in all cases. The mixing time in the opposed jet mixer was sufficiently short to prevent supercoiled plasmid degradation. This also shows that concentrated NaOH can be used to denature-renature supercoiled plasmid solutions, thus avoiding a large increase in batch volume.

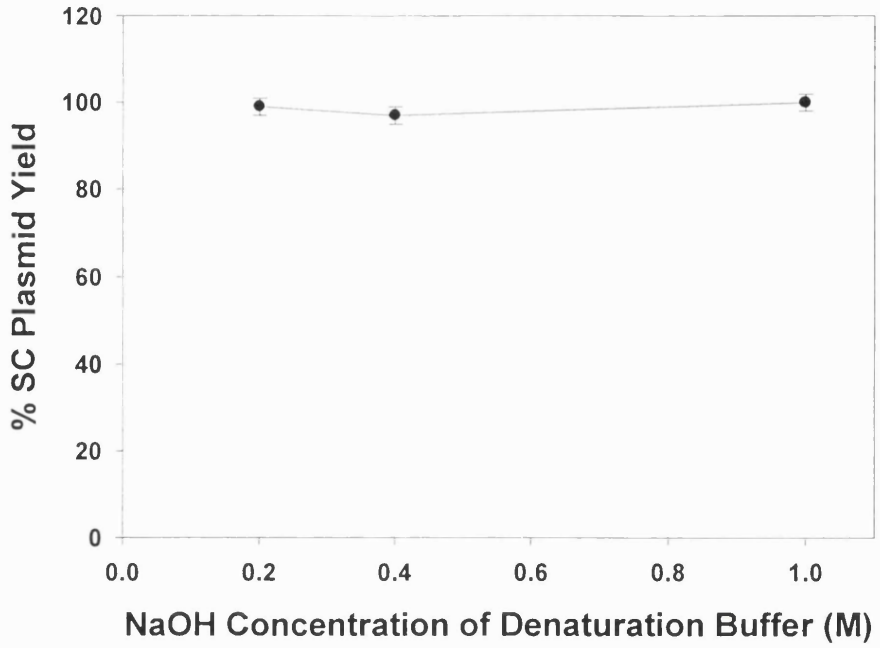

Figure 8.16. Effect of Jet velocity on supercoiled plasmid yield using 0.4 M NaOH lysis buffer.

8.5.2 Jet mixing studies using resuspended E. coli cells

Figure 8.17 shows the yield and purity of supercoiled plasmid DNA, after lysis of E. coli DH5α pSVβ cells using opposed jets, as a function of jet flowrate. The yield is shown relative to a small-scale lysis control. The supercoiled plasmid yield was comparable to the small-scale lysis result across all jet velocities. These results show that even at very low flowrates, the mixing between the opposed jets was fast enough to prevent supercoiled plasmid degradation. This is in contrast to the results observed using concentrated lysis buffer to lyse cells in stirred tanks, where high impeller speeds were required to prevent plasmid yield loss.

The purity of the small-scale lysis control sample was comparable to the jet lysis results, at about 35 % purity. It is interesting to note that at the lowest jet flowrate investigated, there was a significant increase in sample purity. It is not certain whether this high purity was due to lysing at very low levels of fluid stress, or was an experimental error.

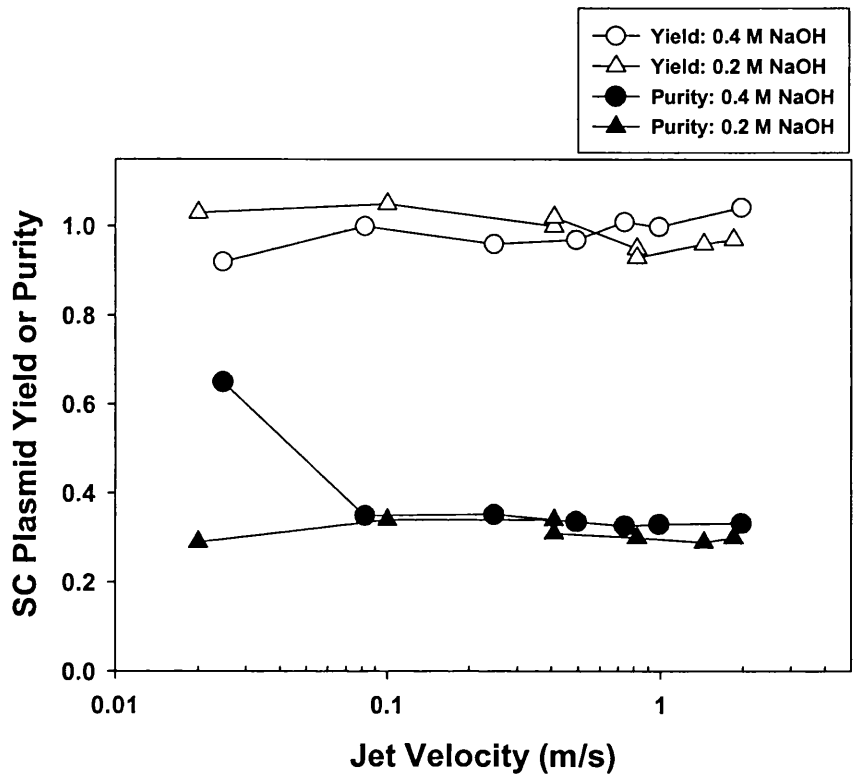

Figure 8.17. Effect of Jet velocity on supercoiled plasmid yield and purity using 0.2 M or 0.4 M NaOH lysis buffer.

8.6 Discussion

8.6.1 Convergence of CFD models

Although CFD simulation is no longer considered in its infancy, a sufficient number of assumptions usually have to be made regarding the governing fluid flow equations that CFD calculations cannot be unequivocally relied upon. Therefore it is essential to carefully examine each CFD model to show that it is both internally consistent and giving physically realistic results. To be internally consistent, a CFD model must be grid size independent; for a given geometry and flow conditions the CFD results (pressure, velocity and energy dissipation distributions) must be independent of the number of grids used to subdivide the model geometry. Grid size convergence studies for opposed jet Model 2 and Model 3 showed that the CFD results for both models had converged at 1000 grids and above, corresponding to a length of 40 microns for each individual grid.

It is appropriate to ask why the CFD simulations are converging at this grid size. The Low Re κ–ε model was used to model the opposed jet flow. This model does not use wall functions to model the behaviour of flows near solid boundaries, but instead integrates the flow equations through the boundary layer to the wall (refer to sections 3.2.33.2.4). This model should be valid over all Reynolds numbers provided that the CFD grid is fine enough to resolve the boundary layers. In a bulk turbulent flow in a jet nozzle, there will be a laminar sublayer and buffer layer between the turbulent core and the wall of the jet nozzle. An estimate for the thickness of the laminar and buffer layers in a pipe is provided by Coulson et al. (1991):

$$0 < y+ < 5 \qquad \text{laminar sublayer}$$

$$5 < y+ < 30 \qquad \text{buffer layer}$$

$$y+ = (y/d).(f/2)^{0.5}.Re$$

Equation 8.1

In this equation, y is the thickness of the boundary layer, d is the pipe thickness, f is the friction factor and Re is the pipe Reynolds number. Using this equation for a 4 mm ID jet of water at 5 m/s gives a laminar sublayer thickness of 50 microns and a buffer layer of 300 microns. Therefore the CFD models converge when the size of the grids is small enough to resolve the jet nozzle boundary layer for Models 2 and 3.

CFD Model 1 consisted of opposed jets impinging subsurface in liquid. As explained previously in this chapter, entrainment of stagnant fluid by the exiting jets gave very high localised energy dissipation rates in this system, and these high energy dissipation rates did not converge to realistic valves until 10,000 grids was used subdivide the model geometry. This model was the only one of the three models that had not fully converged to constant energy dissipation rates at the highest number of grids tested; there was still about a 20% difference in CFD predicted energy dissipation rate between the highest numbers of grids tested. However, based on the second derivative of energy dissipation rate versus grid number shown in Figure 8.2 is appeared that the CFD model was converging rapidly and that any error in CFD predicted mixing performance would be small. This is supported by the agreement of CFD Model 1 results with CFD Models 2 and 3 results, by agreement with analytical calculations, by agreement with empirical calculations and by agreement with other published jet mixing data, as described in the following sections.

8.6.2 Comparison of CFD mixing with analytical and empirical equations

In order to validate a CFD model it is important to compare the CFD predictions to available analytical or empirical results. The pressure drop and energy dissipation rate predicted by CFD was compared to available equations. The analytically calculated pressure drop in the jet

nozzles matched the CFD predictions exactly. The CFD simulations predicted that the energy dissipation rate at high Reynolds number, for all three jets models, should be 0.1 to 0.2 times u^3/d. An empirical or analytical correlation for the energy dissipation in opposed jets could not be found in the published scientific literature, however the energy dissipation in unbounded submerged jets can be estimated from the empirical correlation, $\varepsilon = 0.1\ u^3/d$ (Yim et al., 2000). Thus, the CFD results compares very favourably to the empirical correlation for energy dissipation given by Yim. Therefore it is clear that jet Model 1, 2 and 3 are giving realistic predictions of the fluid flow behaviour.

8.6.3 Comparison of CFD Model 1 and Model 2 mixing results with experimental data

The CFD predicted energy dissipation, ε, is given in Figure 8.8, as a function of jet diameter and velocity, for equal jets impinging in air, and can be summarised as:

$$\varepsilon = (u^3/d)\ (3\text{x}10^{-5}.\ \text{Re})^{1.5}\ ,\ \text{Re} < 800$$

$$\varepsilon = (u^3/d)\ (5\text{x}10^{-4}.\ \text{Re})^{0.6},\ 800<\text{Re}<10{,}000$$

$$\varepsilon = 0.2\ u^3/d,\ \text{Re}>10{,}000$$

Equation 8.2

The CFD prediction for energy dissipation can be compared to the results of Tosun et al. (1987) where a time-dependent, competitive reaction was used to measure mixing quality in opposed Tees. Figure 8.18 shows the relationship between mixing quality and Reynolds number in the opposed Tee system. This figure is reproduced directly from the work of Tosun et al. (1987). The mixing quality is defined such that a mixing index of 1.0 indicates instantaneously fast mixing and a mixing index of 0 indicates slow, poor mixing. At Reynolds numbers above 10000 the mixing quality is independent of Reynolds number, which parallels the CFD prediction in this thesis (compare to Figure 8.8). Moreover, at Reynolds number below 10,000 there is a rapid decline in mixing performance.

Baldyga et al. (1995) correlated the energy dissipation rate (10^3 to 10^4 W/kg) in a turbulent free jet discharging into a tank against the jet mixing performance, using a u^3/d dependence of energy dissipation rate. While they obtained a good match between theory and experiment at high jet Reynolds numbers greater than 10000, at a lower jet Reynolds numbers of 5200 they saw a significant deviation between jet mixing performance and theoretical predictions. Although their system consisted of a free jet discharging into a tank, compared to opposed jets used in this work, the rapid decrease in jet energy dissipation rate predicted by CFD for opposed jets may explain some of the results observed by Baldyga for a jet discharging into a tank.

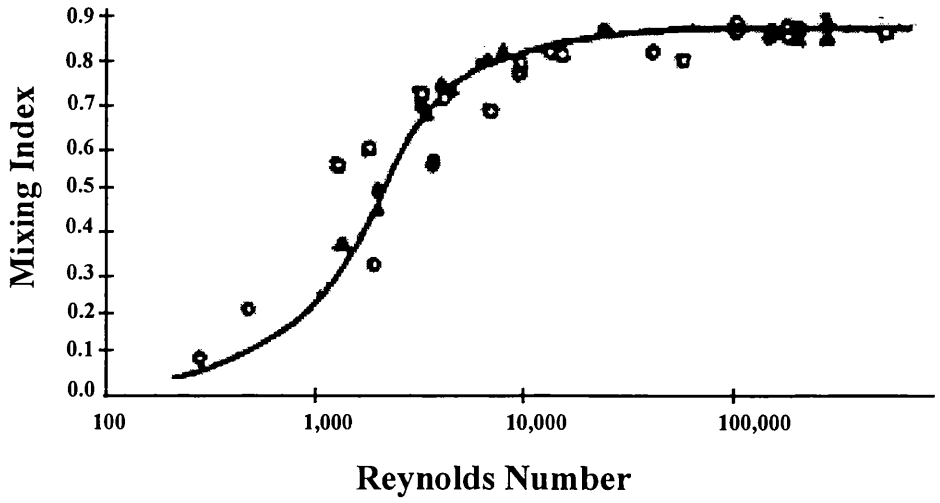

Figure 8.18. Effect of Reynolds number on Mixing performance for Opposed Mixing Tees. Graph reproduced from Tosun et al. (1987). The triangles, circles and squares represent opposed tees with left : right diameters of 0.9 : 10.3 mm, 1.8 : 7.1 mm and 0.9 : 7.1 mm, respectively.

Mahajan et al. (1996) performed a similar study to Tosun, except their jet geometry was similar to the geometry used in this thesis. Using a competitive chemical reaction, they measured the mixing quality as a function of jet operation flowrate for three different diameter jets. They performed their mixing study for the case where the opposed jets impinged subsurface (a flooded impingement chamber) and for the case where the jets impinged in air (an empty impingement chamber). The relationship between mixing quality and jet Reynolds number that Mahajan et al. measured is shown in Figure 8.19 and Figure 8.20, for non-submerged and submerged jets, respectively. It should be noted that Mahajan's definition of the mixing index is such that a mixing index of 0 represents good, fast mixing and a mixing index of 1 represents poor, slow mixing. As shown in the figures, there was a significant variation in mixing performance depending on jet diameter and jet Reynolds number.

In theory the observed mixing index should be a unique function of the jet mixing time. Therefore, in order to correlate the mixing performance across different jet diameters, Mahajan et al. plotted the mixing index for each jet against the theoretically calculated jet micro-mixing time. If the theoretically calculated jet micro-mixing time is correct, the mixing data for all of the jets should fall on a single-curve. Mahajan et al calculated the micro-mixing time based on jet energy dissipation rate (Equation 2.2). Their jet energy dissipation rate was calculated based on the total kinetic energy in the jets being dissipated in a volume, V, between the jets. They

determined that they could achieve a moderate correlation between measured mixing performance and calculated jet micro-mixing time across all three jets, if they assumed that the dissipation volume was proportional to the square of the jet diameter. There were two principal disadvantages to their correlation. First, the dimensions of the correlation were not consistent, as the dissipation volume must be correlated against the cube of a length scale. Second, the model still failed to correlate all of the data obtained from the opposed jets mixing experiments.

Because Mahajan et al. (1996) have correlated the mixing performance of opposed jets, similar in design to the jets that were modelled in this thesis, their data offers an ideal opportunity to test the validity of the CFD model developed in this thesis. The energy dissipation as a function of jet velocity, jet Reynolds number and jet diameter was calculated based on the CFD model predictions, Equation 8.2. Then, in the same manner as Mahajan et al., the micro-mixing time at each jet condition was calculated using Equation 2.2 and plotted against the mixing index, as shown in Figure 8.21 and Figure 8.22. The CFD model correlates the performance of the three opposed jets extremely well across all flowrates tested, for both the non-submerged and submerged jet cases. This goes a long way to validating the CFD model developed in this thesis.

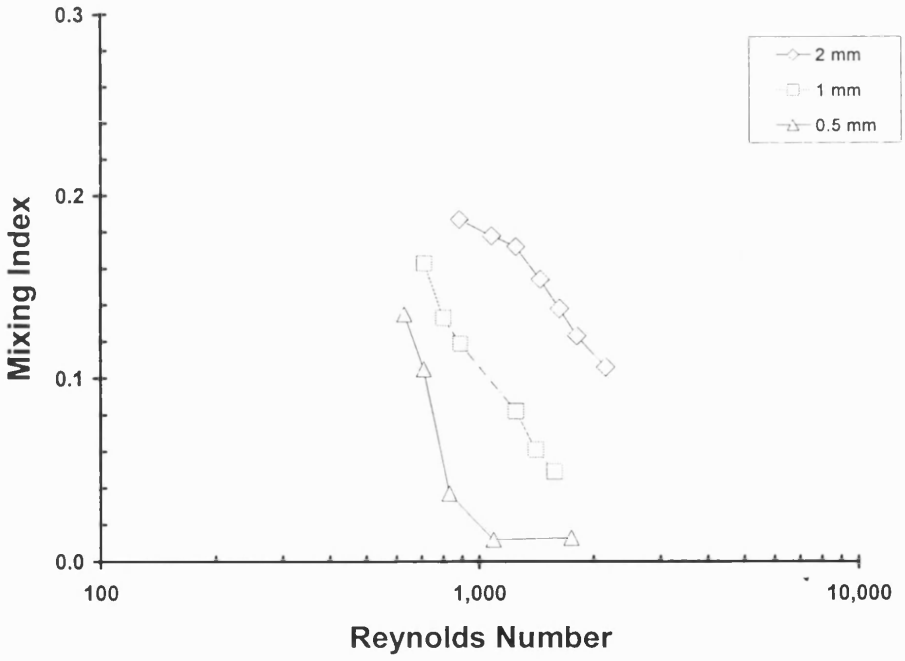

Figure 8.19. Plot showing the quality of mixing as a function of Reynolds number in three different diameter opposed jets, non-submerged case. This plot is reproduced from the data of Mahajan et al. (1996).

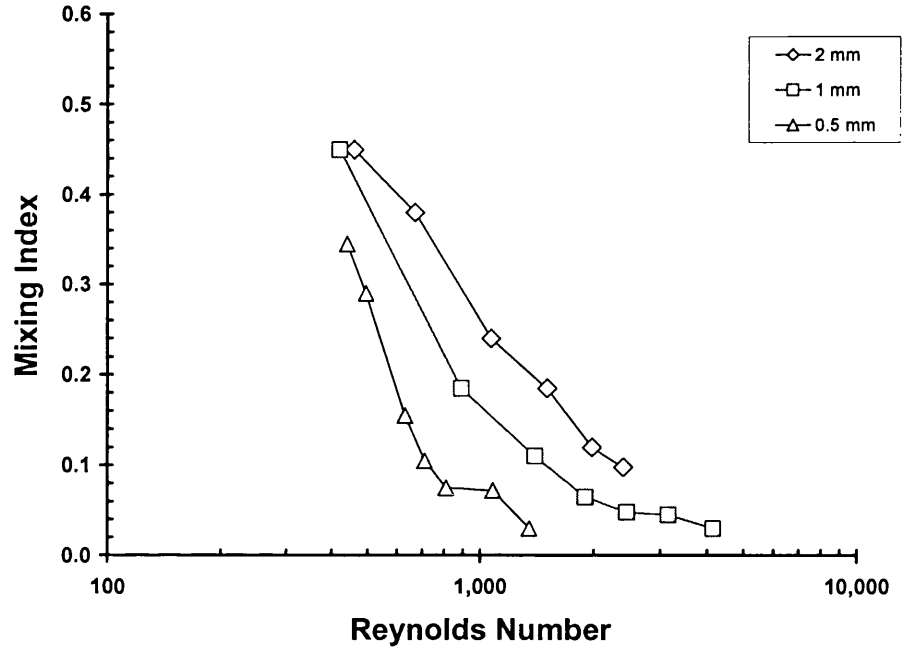

Figure 8.20. Plot showing the quality of mixing as a function of Reynolds number in three different diameter opposed jets, submerged case. This plot is reproduced from the data of Mahajan et al. (1996).

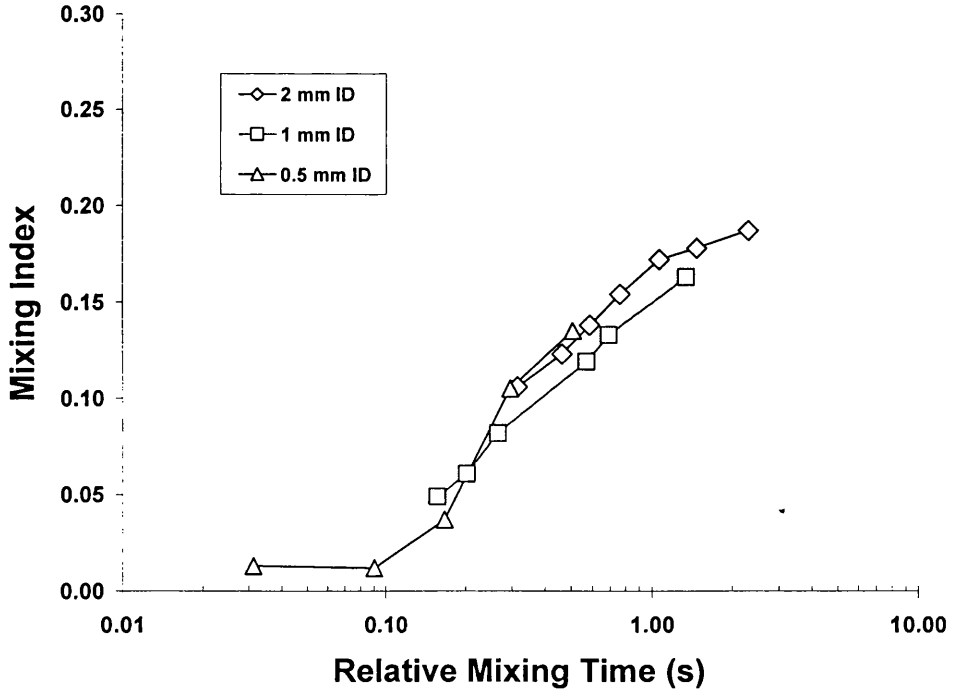

Figure 8.21. Plot showing the correlation between relative mixing time and the quality of micro-mixing in opposed jets.

The relative mixing time for both the non-submerged and the submerged jet cases was calculated based on Equation 8.2. Although Equation 8.2 was derived from the CFD results for non-submerged opposed jets, the same equation correlates the data for submerged opposed jets very well, as shown in Figure 8.22. It was demonstrated for one jet diameter and flowrate (refer to 8.4.2), that the energy dissipation in submerged jets was half that in non-submerged jets. Therefore, in calculating the energy dissipation for submerged jets, Equation 8.2 was used and the resulting energy dissipation was multiplied by a factor of 0.5.

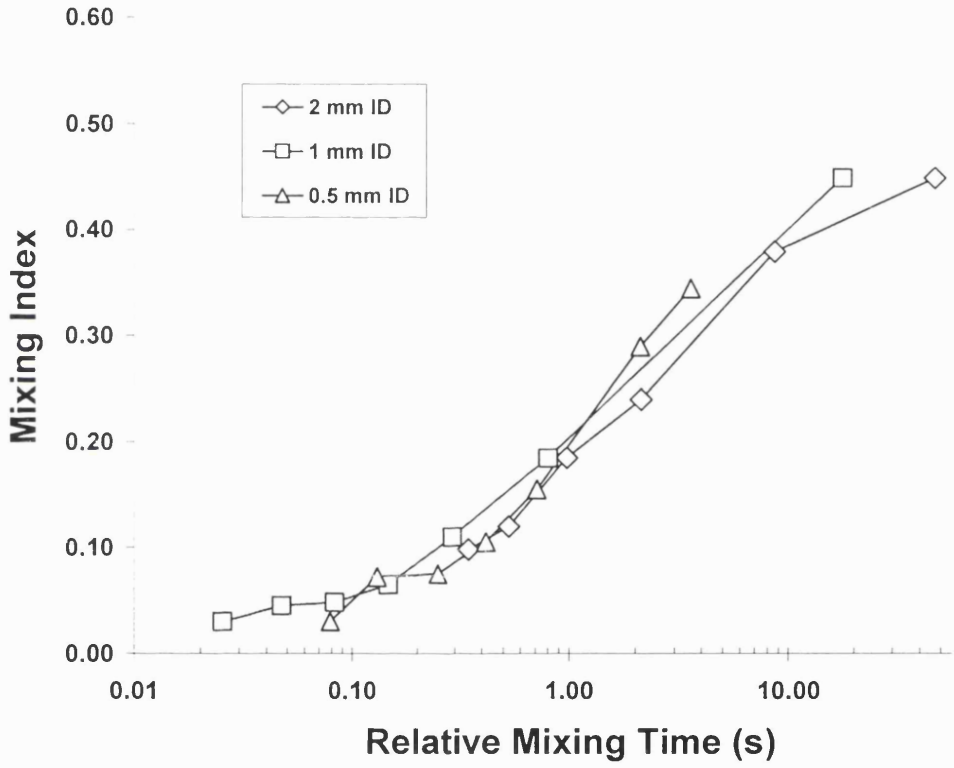

Figure 8.22. Plot showing the correlation between relative mixing time and the quality of micro-mixing in opposed jets: submerged case.

The results of Figure 8.21 and Figure 8.22, for the submerged and non-submerged jet cases, are combined in Figure 8.23. Using Equation 8.2, and accounting for the 2-fold lower energy dissipation in submerged jets compared to non-submerged jets, the mixing in both jet systems is correlated reasonably well.

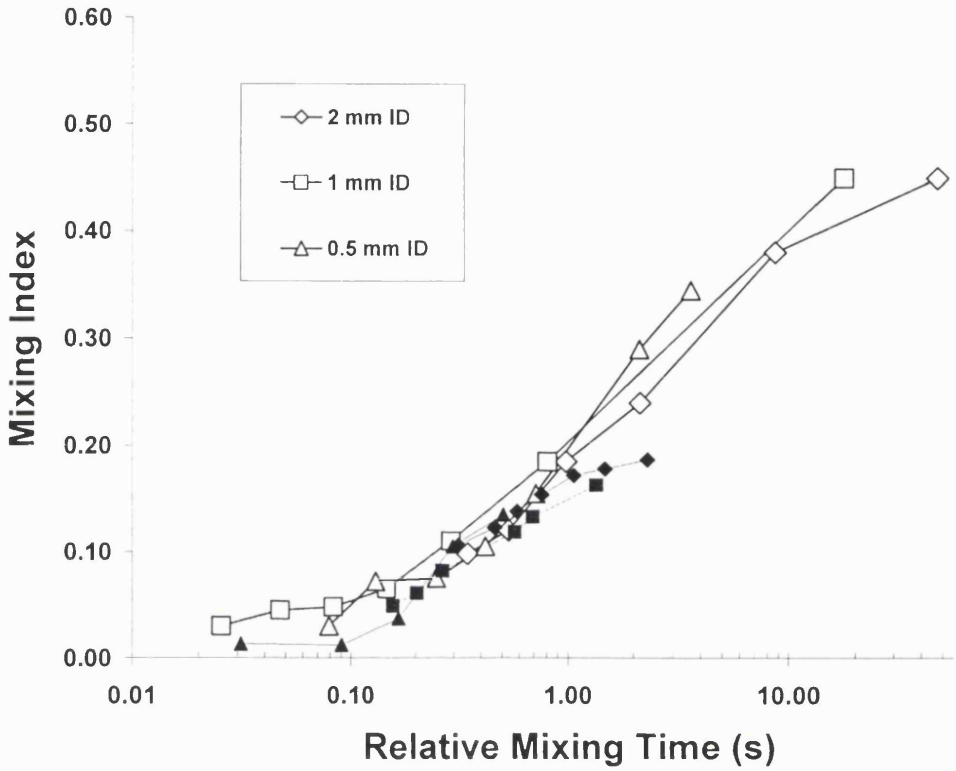

Figure 8.23. Plot showing the correlation between relative mixing time and the quality of micro-mixing in opposed jets. Open symbols represent submerged jets, filled symbols represent non-submerged jets.

In the jet experiment, where *E. coli* cells were lysed with NaOH in the opposed jet mixer, it was surprising that the yield of supercoiled plasmid remained high after jet mixing at the lower range of jet velocities tested. At the low range of jet velocities tested, the fluid flow in the jets would have been laminar and the CFD predicted energy dissipation rate would have been very low. Hence, the turbulent eddies would have been large, leading to long micro-mixing times. Possibly, the small length scales at which these jet mixing experiments were run (0.007" ID lysis buffer jet equals 178 micron ID) would have reduced the length scale over which diffusion took place, negating somewhat the requirement for turbulent mixing. The radius of the 0.007" ID jet was 89 microns, which using Equation 2.2, a viscosity of 5 mPa s and the diffusion rate of NaOH, corresponds to a micro-mixing time of 0.6 s. Therefore, even without turbulent mixing, diffusion of NaOH across the radius of the jets will occur in less than a second. Further experiments are required to verify the CFD predictions for energy dissipation rate and fluid stresses at scales larger than the scales investigated here, or investigated by Mahajan et al. (1996).

Comparison of CFD fluid stress predictions with empirical results

Approximating opposed jets as two facing point sink flows (Metzner et al. 1970), the following approximation for the fluid strain rate can be derived: $\varepsilon' = 0.5\ u/d$. The CFD model for opposed jets predicted the same dependence on the jet velocity and jet diameter, however the maximum strain rate between the jets was substantially higher: $\varepsilon' \sim 4.7\ u/d$. The CFD predicted maximum strain rate is about 9-fold higher than the analytical prediction. The CFD predicted average strain rate between the opposed jets was typically 4- to 8-fold lower than the maximum strain rate, which more closely matches the analytical prediction. It is important to take into account the maximum strain rate between opposed jets when stress-induced degradation must be avoided.

Operation and scale-up of opposed jets based on CFD predictions

The relationship between the dimensionless energy dissipation ($\varepsilon\ d/u^3$) and Reynolds number, shown in Figure 8.8, dictates how opposed jet mixing devices should be routinely operated. In order to operate under robust conditions, the jets should always impinge under turbulent flow conditions, at Reynolds numbers greater than 10000. For example, a 4 mm ID jet of water at 2.5 m/s will have a Reynolds number of 20000. A two-fold decrease in jet velocity will reduce the Reynolds number to 10000, and will reduce the energy dissipation rate 8-fold. However, a further 2-fold decrease in jet velocity, will reduce the Reynolds number below 10000, and lead to an further 27-fold reduction in energy dissipation rate. Fluctuations in jet velocity have a much more significant effect on energy dissipation rate at Reynolds numbers below 10000.

The relationship between the dimensionless energy dissipation ($\varepsilon\ d/u^3$) and Reynolds number, shown in Figure 8.8, also dictates how opposed jet mixing devices should be scaled-up from laboratory to manufacturing scale. For scale-up of an opposed jet mixer, to maintain constant mixing conditions between jets of different sizes the energy dissipation rate (ε) should be kept constant. Because $\varepsilon\ d/u^3$ is a constant at all Reynolds numbers greater than 10000, maintaining ε constant involves keeping u^3/d constant across all scales of operation. Therefore, as the jet diameter, d, increases at larger scales of operation, the jet velocity should be increased slightly at larger scales. For example, an 8-fold increase in jet diameter necessitates a 2-fold increase in jet velocity to maintain the same jet mixing time.

Because the dimensionless strain rate is relatively constant across all Reynolds numbers, the actual strain rate will be approximately equal to u/d across all scales of operation. At larger scales, the fluid velocity, u, does not need to increase as rapidly as the diameter, d, in order to maintain constant mixing time, as previously explained. Therefore, at larger scales of operation,

u/d will decrease, meaning that the elongational strain rate will decrease. For example, an 8-fold increase in jet diameter will decrease the elongational strain 4-fold, keeping the jet mixing time constant. The decrease in fluid stress at increased jet scale is demonstrated in Figure 8.24 which shows a plot of the maximum strain rate between the jets versus the Kolmogoroff length scale of eddies between the jets. The Kolmogoroff length squared should be directly proportional to the micro-mixing time (Equation 2.2) and hence, should be a measure of the mixing quality. One can see that as the jet diameters become larger, the strain rate at a given Kolmogoroff length decreases.

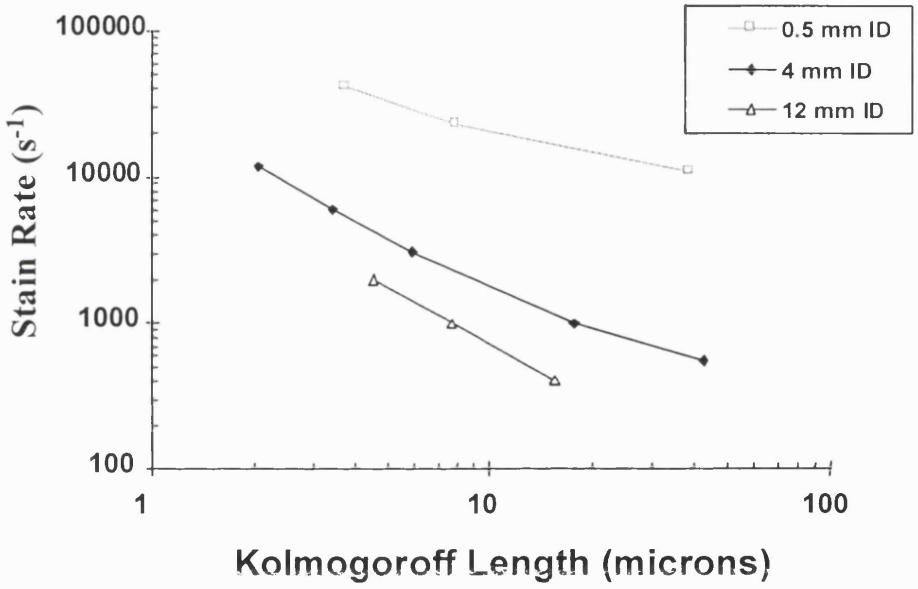

Figure 8.24. Plot showing the Kolmogoroff length versus strain rate for opposed jets at three different jet diameters.

8.7 Conclusion

CFD simulations of opposed liquid jets (impinging in liquid or in air) were shown to converge to realistic solutions using a sufficiently high number of grids to subdivide the model geometries. The maximum energy dissipation between equal diameter opposed jets, impinging in air, was shown to be proportional to the velocity cubed at jet Reynolds numbers above 8000. The dimensionless maximum energy dissipation ($\varepsilon d/u^3$) was a constant at Re > 8000 and equal to 0.2. Below a Reynolds number of 8000, there was a sharp decline in the dimensionless maximum energy dissipation. Therefore, for robust jet mixing the CFD results predict that opposed jets should be scaled-up and operated at Reynolds numbers above 8000. The dimensionless maximum energy dissipation for opposed jets impinging in liquid was calculated by CFD to be 0.1 which is the same value as unbounded subsurface jets. The value of 0.1 for

the dimensionless energy dissipation rate in jets impinging in liquid, as opposed to 0.2 for jets impinging in air, is probably due to the increased frictional losses to the surrounding liquid for jets impinging in liquid. Opposed jets of different diameter were shown to obey the same qualitative behaviour as equal diameter opposed jets. Based on using a geometric mean velocity and diameter, the dimensionless maximum energy dissipation at high Reynolds number was calculated to be 0.1.

The CFD calculated energy dissipation rate in submerged and non-submerged jets was used to correlate opposed jet mixing performance data against jet diameter and jet velocity. The CFD simulations were shown not only to correlate jet mixing data across different diameter jets over the jet velocities tested, but also to correlate mixing performance in subsurface and non-subsurface jets.

CFD simulations of opposed jets were predicted excellent performance as an alkaline lysis mixer. Firstly, CFD predicted rapid mixing to achieve high levels of chromosomal DNA denaturation without denaturing supercoiled plasmid DNA, and secondly, CFD predicted low fluid strain rates during mixing to maximise chromosomal DNA fragment size. The excellent mixing characteristics of an opposed jet mixer was verified by mixing supercoiled plasmid DNA with concentrated NaOH while avoiding supercoiled denaturation and by lysing *E coli* plasmid-containing cells with concentrated NaOH and achieving higher plasmid yields than using conventional stirred tank mixers.

9 Discussion

The objective of this thesis was to study the influence of fluid mixing and fluid shear during DNA downstream purification on final product quality. This chapter pulls together the thesis results, presented in Chapters 4 to 8, to discuss their significance with respect to designing DNA purification processes.

The relevance of this work is due to the exponentially increasing demand of gene therapy trials for large quantities of pure DNA. The manufacture of pure DNA typically involves the expression of the genes of interest in a suitable host micro-organism followed by purification of the required DNA from the aqueous cell suspension. The production of intact DNA molecules for gene therapy presents some unique challenges for the biochemical engineer. Principally, the large size of typical DNA molecules cause them to be highly susceptible to chain scission when exposed to the fluid mechanical stresses that occur in typical purification equipment such as mixing devices or chromatography columns. This chain scission can significantly decrease product yield and purity. Unfortunately, reduction of fluid stresses in purification equipment is not a trivial problem; certain levels of fluid mixing/mass transfer are required to separate product molecules from impurities, and this fluid mixing generates fluid stress. Therefore, significant research is required into the combined effects of fluid mixing and fluid stress on the performance of DNA purification processes.

This chapter, which discusses the results of the thesis, is divided into two sections.

- Firstly, this chapter discusses the advantages and disadvantages of the methodologies used or developed in this thesis for researching or designing novel production processes.
- Secondly, this chapter amalgamates the experimental and Computational Fluid Dynamics results presented in Chapters 4 to 8 to discuss their significance with respect to DNA purification processes.

9.1 Process research and design methodology

This section discusses the methodologies used in this thesis for researching and developing a novel production process. In general, the research and development of bio-separation processes requires, firstly, a detailed understanding of the fundamental chemical and physical properties of bio-molecules and, secondly, knowledge of the chemical and physical environments the bio-molecules will experience. For the biochemical engineer, detailed knowledge of fundamental chemical and physical properties is typically acquired from the scientific literature, along with additional information provided from the Basic Research department. The engineer will usually be required to perform targeted experiments to understand some additional properties of the bio-molecules that are relevant to the purification environment that the molecules will experience. Process development will then proceed to understand the behaviour of the bio-molecules in scale-down purification equipment in order to gain sufficient understanding of the purification unit operations with which to confidently design and implement a large-scale purification process. The experimental methodology used in this thesis was designed with the goal of understanding the effects of fluid stress on DNA purification from fundamental chemical and physical properties, through scale-down experimentation, through to manufacturing-scale.

The organisation of the thesis is represented in Figure 9.1. In designing a DNA purification process to minimise the detrimental effects of fluid stress, it is essential to know how fluid stress changes as the process is scaled-up (going from left to right in Figure 9.1), which will be referred to as Scale-up knowledge. It is also important to know how detrimental effects of fluid stress at each process step affect the performance of subsequent downstream operations (going from top to bottom in Figure 9.1). This will be referred to as Windows of Operation knowledge. In order to gain Scale-up knowledge and Windows of Operation knowledge relating to the effects of fluid stress, certain experimental and design methodologies were employed in this thesis:

1. Developing the analytical tools to determine DNA quantity, size and conformation throughout the downstream purification process, from cellular lysis through to the final product.
2. Using Computational Fluid Dynamics (CFD) to characterise fluid mixing and shear within fundamental model flow systems and scale-down devices and using those CFD models to design manufacturing scale devices.
3. Experimentally determining the effects of fluid mixing and fluid shear on DNA degradation in model systems and in specific unit operations, and then determining the effect of DNA structure on the performance of subsequent downstream purification steps.

4. Developing an experimental method of measuring plasmid DNA degradation under highly dilute concentrations using a novel fluorescence-based assay technique. This method enables plasmids to be potentially used as probes for fluid mixing and fluid stress in manufacturing scale equipment.

The advantages and disadvantages of each of these methodologies will now be discussed.

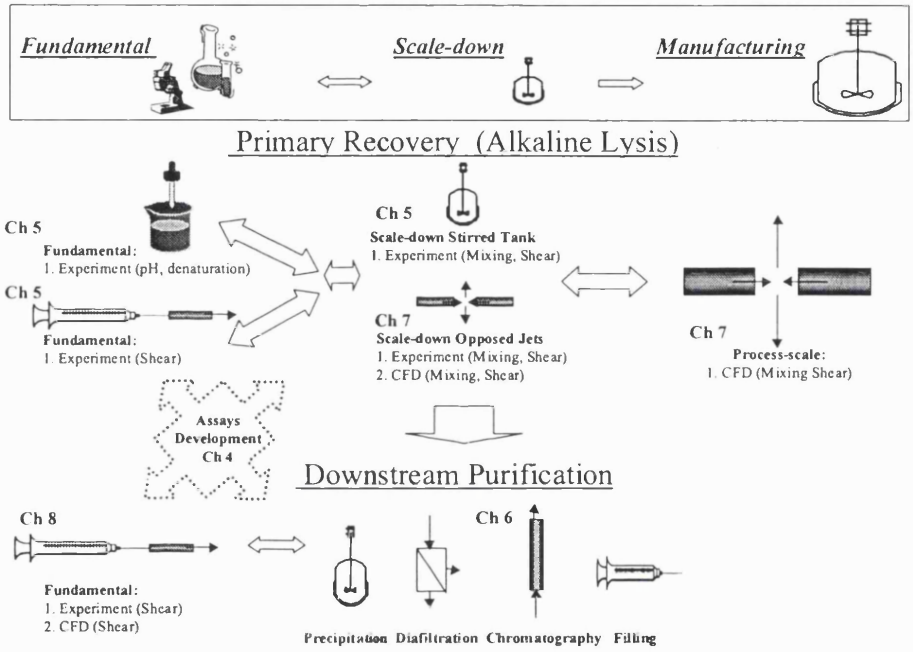

Figure 9.1. Organisation of thesis with respect to DNA purification process development.

9.1.1 Analytical development

This investigation into the effects of fluid stress on DNA process streams required the analytical tools to determine the structure, quantity and purity of the DNA present. It was essential for this investigation that the assays used were able to resolve the differences between samples to the required level of accuracy, and that the assays were robust and could be performed within a feasible time. It was apparent early on that the available analytical techniques were inadequate for resolving the effects of fluid mixing and fluid shear on DNA containing samples. Therefore a conscious decision had to be made to allocate time towards assay development. The advantages and disadvantages of developing novel HPLC and fluorescent analytical techniques shall be discussed separately with respect to assaying alkaline lysate samples and pure plasmid samples.

Alkaline Lysate samples

The goal of alkaline lysis is to maximise SC plasmid yield and minimise DNA impurity yield; therefore, it was essential to be able to quantify the SC plasmid product and all of the DNA impurities. Table 9.1 shows the DNA species present during alkaline lysis and the assays that can be used. The standard analytical technique for quantifying DNA species is agarose gel electrophoresis. This technique can be used quantify double-stranded plasmid species (SC, OC and linearised plasmid), however, the technique is labour intensive and slow to run and requires many replicates to achieve low standard deviations between replicate samples. Utilisation of low melting point agarose, presented in chapter 4, reduced sample diffusion and improved sample accuracy. Picogreen is another standard technique for measuring DNA. This technique can be modified to measure supercoiled plasmid DNA (Levy et al. 2000). However, because single-stranded chromosomal DNA fluoresces up to 30% that of supercoiled plasmid, samples that contain high levels of DNA impurities, such as alkaline lysates, can give erroneous results when assayed using this technique.

The principal failing of agarose gel electrophoresis and Picogreen assays is their inability to accurately quantify the majority of the DNA impurities. This is partly due to the low binding of ethidium bromide or Picogreen to single-stranded DNA, and partly due to the diffuse banding of double- and single-stranded chromosomal DNA on agarose gels. Therefore, it is difficult to optimise alkaline lysis with respect to chromosomal DNA removal using these analytical techniques. Development of HPLC assays, using Q-Sepharose and Poros PI anion exchange resins, allowed more accurate and faster assaying for both plasmid product and DNA impurities. As the alkaline lysis results presented in chapter 6 showed, both supercoiled plasmid yield and chromosomal DNA yield were relatively insensitive to fluid stresses during lysis. Therefore the use of more accurate assays dispelled the idea that high fluid stresses during lysis produced significantly more chromosomal DNA.

The new HPLC assays also showed that a high NaOH concentration did not dramatically affect either supercoiled plasmid or chromosomal DNA yield, but instead was essential for conversion of double-stranded chromosomal DNA to single-stranded form. Agarose gel electrophoresis did not provide accurate information on chromosomal DNA contamination and provided no information as to whether the chromosomal DNA was in single- or double-stranded form; therefore, it was not possible to optimise alkaline lysis using the standard agarose gel assay. Therefore, although considerable time was invested in HPLC assay development, proper process optimisation of the alkaline lysis step would not have been feasible, otherwise.

Pure plasmid samples

The relevant DNA species during fluid shear experiments were principally the SC plasmid product, OC and linear plasmid; for these experiments solutions of pure plasmid DNA were used. Again, agarose gel electrophoresis was used to quantify plasmid species, however the same shortcomings of agarose gel electrophoresis applied, namely low accuracy, labour intensive procedures and slow turn-around time. Development of HPLC assays, using Q-Sepharose and Poros PI anion exchange resins, and modified fluorescence assays using Picogreen, allowed more accurate and faster assaying of both plasmid product and DNA impurities.

Unlike the case for alkaline lysis, the development of novel assays to monitor pure supercoiled plasmid shear degradation did not provide additional information over using old assay techniques. Instead the novel assays vastly increased the number of experiments that could be assayed. However, the development of development of the modified Picogreen assay will allow the monitoring of plasmid degradation under dilute conditions in manufacturing-scale equipment; this is discussed separately in this chapter.

Process Parameter	Initial Species to assay	Assay	Degradates to assay	Assay
Poor Mixing during Lysis	SC Plasmid	HPLC PG Gel	denatured-SC Plasmid	Gel
	OC Plasmid	HPLC Gel	ss-Plasmid and ss-linearised Plasmid	Gel?
	linearised-Plasmid	Gel, HPLC	ss-linearised Plasmid	Gel?
	ds-chDNA	Gel?, HPLC	ss-chDNA	Gel?
				HPLC
High Fluid Stress	SC Plasmid	HPLC PG Gel	OC or linearised Plasmid fragments	Gel HPLC
	OC Plasmid	HPLC Gel	linearised Plasmid fragments	Gel HPLC
	linearised-Plasmid	Gel	linearised Plasmid fragments	Gel
	ds- or ss-chDNA	Gel	ds- or ss-chDNA fragments	Gel

Table 9.1. Chemical Species to be assayed

9.1.2 Computational fluid dynamics

Introduction

The objective of this thesis was to improve the understanding of DNA purification processes, specifically with respect to unit operations involving fluid mixing and fluid shear. Along with laboratory experiments, Computational Fluid Dynamics (CFD) was used to achieve this goal. This section discusses the advantages and disadvantages that were encountered using Computational Fluid Dynamics (CFD) as a tool for researching, developing and designing bio-separation processes.

Figure 9.1 shows the process design methodology that was employed in this thesis for the alkaline lysis step, the initial downstream recovery step during plasmid DNA purification. Fundamental experiments were performed to understand the effects of pH, mixing and shear on DNA degradation. This was followed by experiments using scale-down stirred tanks and opposed jets to quantify fluid dynamical properties of these devices. Finally a manufacturing-scale Opposed Jets Mixer was designed for alkaline lysis based on the fundamentals of DNA denaturation and shear degradation within the scale-down devices. In this thesis, CFD was employed at all three stages of process development (fundamental research, scale-down experimentation and large scale-development). The advantages and limitations of CFD that were encountered in this thesis will now be discussed within the framework of using CFD as a process research and design tool.

CFD as a Research and Design Tool

The principal advantage of CFD is that it allows the engineer to gain insight into the fundamental fluid dynamical behaviour of a fluid flow system. Frequently, detailed information from CFD simulation, such as shear rate, pressure drop, and energy dissipation rate, is not possible or not feasible to acquire experimentally. This was certainly the case for the shear rate and energy dissipation rate distributions within the Capillary Shear Device (Chapter 5) or the Opposed Jet Mixer (Chapter 8). Verification of the local shear rate distribution and the local energy dissipation rate distribution within the devices was not experimentally feasible within the timelines of this thesis. Thus, the CFD simulation results were an invaluable resource in understanding the DNA shear degradation phenomena at the entrance to the capillaries and the mixing and shear properties of opposed jets.

The second advantage of CFD is its ability to be used as a design tool. Once the model geometry has been built, gridded, and verified to be converging appropriately, it is usually straightforward to modify the model geometry and re-run the CFD simulation to try and optimise the performance of the flow device. For a bioprocess engineer, the ability to perform "what-if" calculations using CFD is particularly advantageous when it comes to process scale-up. It is frequently trivial to increase the size of the model geometry and re-run the CFD simulations to determine the effect of scale-up on the fluid dynamics within a flow device. By performing CFD simulations on the Opposed Jet Mixer over a range of flowrates and jet sizes it was possible to predict the shear rate and mixing rates across a range of scales of operation. Using CFD simulations, the relationships developed between Reynolds number and energy dissipation rates within Opposed Jet Mixers should enable design and operation of mixers under robust, scaleable conditions.

Reliability of CFD Simulation Predictions with Respect to Bio-Process Design

The principal disadvantage of CFD modelling arises due to the limitations of current-day computers to solve the Navier-Stokes equations for fluid flow. These equations can currently only be solved exactly for laminar flows. Although nearly all relevant engineer fluid flows are turbulent in nature, current computers are too slow to solve the Navier-Stokes equations for turbulent fluid flows. Instead, various turbulent models are used to model the fluid flow behaviour. All of the current turbulent models are partly empirical in nature, and the shortcomings of CFD modelling is directly related to the shortcomings of the turbulent model used. The shortcomings of the different turbulence models require that the CFD user has extensive knowledge of the limitations of each model, and knows which turbulence models are most appropriate for specific problems. Even when the most appropriate turbulence models are applied to solve a fluid dynamics problem, for all but the most basic of flow problems the user can not be entirely confident that the CFD results will be completely predictive of real-world flow behaviour.

With the prohibitive capital cost of manufacturing-scale equipment and the necessity of rapid-time-to-market for biopharmaceutical products, troubleshooting equipment in the manufacturing plant must be avoided at all costs. Thus, design of large-scale purification processes requires a very high degree of confidence in the performance of each piece of manufacturing equipment long before the equipment is used to purify product. The fluid dynamics within purification equipment critically affects the separation of the bio-molecules by affecting mass transfer, heat transfer and fluid stresses. To confidently design a manufacturing-scale process, scale-down experiments must be run to determine the effects of the fluid dynamics on the bio-separation. Because CFD modelling alone is not sufficient to predict, with absolute assurance, the fluid dynamical behaviour of bio-separation equipment, a bioprocess should never be designed and built based solely on CFD simulation.

Using CFD to Complement Experimental Research

If CFD modelling must be verified using experiment, what is the advantage of CFD modelling? Although CFD simulation results cannot be completely depended upon, assuming the user has reduced the model geometry to a feasible size and chosen an appropriate turbulence model, in the majority of cases the CFD results will be a close approximation to the real flow behaviour. Therefore, CFD can be an invaluable tool to target which fundamental, scale-down, or manufacturing-scale experiments need to be performed. For example, in the majority of cases the bioprocess design engineer must decide between different designs of equipment for each unit operation in a process stream. CFD simulations on a range of process equipment could be used to determine which pieces of process equipment are least likely to cause stress-induced to a

biomolecule. After choosing the most appropriate piece of equipment based on CFD simulation, the performance of the equipment can be verified experimentally using scale-down equipment.

Not only does the CFD simulation help reduce the amount of scale-down experiments required, but the detailed fluid dynamics information obtained from CFD is invaluable when it comes to understanding how the equipment will behave at large-scale. Moreover, if a CFD model for a piece of pilot-scale equipment has been developed, it is usually a trivial exercise to increase the geometry of the model to simulate the equipment at manufacturing scale. While CFD simulation can not definitively predict the fluid dynamics performance at manufacturing scale, any CFD predictions of errant fluid dynamical behaviour act as invaluable warnings that potential problems may arise and should be addressed.

In this thesis, experimental verification of the CFD model results was not performed the capillary device but was performed for the opposed jets mixer. Where approximate analytical expressions for shear rates or energy dissipation rates were available, the CFD results were close to the analytical calculations. The CFD predictions for the capillary device and opposed jet mixers were highly valuable in understanding the behaviour in the devices. The high level of extensional shear at capillary entrances predicted by CFD led to experiments that verified that DNA degradation was occurring at the capillary entrance. Similarly, the CFD prediction that the mixing rate in the Opposed Jet Mixer decreases rapidly with Reynolds numbers below 8000, irrespective of operating scale, indicates that the performance of the Opposed Jet Mixer at low Reynolds numbers should be checked experimentally to avoid potential problems with poor mixing. In the end, the CFD predictions for the opposed jets mixer accurately matched the experimental data of Mahajan et al. (1996).

Allocation of Resources to CFD

The second major disadvantage of CFD simulation is the user time it requires developing a CFD model. CFD model development involves creation of a model geometry using a suitable computer graphics program, followed by several stages of gridding the geometry, running the simulation, and refining the grid, until a convergent solution is obtained. This process can take from weeks to months depending on the complexity of the flow geometry and the experience of the CFD user. Although having a CFD model of a piece of process equipment is a valuable tool, the question arises as to whether the bioprocess engineers time would be better spent running scale-down experiments in the laboratory? There is probably no easy answer to this question.

Currently CFD simulation cannot generally be used to model entire pieces of process equipment (instead CFD models are usually based on engineering "hot-spots" within equipment). In addition, there is currently a lack of absolute confidence in CFD results; thus, important CFD predictions need to be verified experimentally. Therefore, based on the time taken to develop the CFD models used in this thesis, it is the opinion of the author that the process engineer's time is not maximised performing CFD simulation. Instead, the engineer's time is better spent approximating the fluid dynamical behaviour within the "hot-spots" of process equipment using analytical expressions, instead of using CFD, and then verifying the important analytical predictions experimentally. The high elongational shear rate at entrance of the capillary device discovered through CFD simulations can be analytically approximated from point-sink flow calculations. Similarly, the decrease in energy dissipation in the opposed jet mixer at low Reynolds number can be assumed from turbulence theory. Therefore, analytical calculations can be used to roughly approximate the important CFD results for both the capillary device and opposed jet mixer, and these calculations can be done in minutes to hours. A competent bioprocess engineer would then experimentally verify these analytical predictions. In contrast, the CFD models developed in this required several months of work (some of which was training of the author with the CFD software package) and the CFD results still required experimental verification.

If CFD models of complicated process equipment were more accurate or faster to develop, then CFD modelling would be a significantly enhanced tool for the bioprocess engineer. For complicated equipment, analytically approximating the fluid dynamics throughout the flow domain and pin-pointing all the engineering "hot-spots" is significantly more difficult. Therefore, a CFD model of the entire piece of equipment would give significantly more information than analytical calculations alone. Unfortunately, CFD modelling of an entire piece of complicated process equipment is still in its infancy and is both time-consuming and inaccurate. In an academic environment, where fundamental fluid dynamics investigations into process equipment are being performed, not having the time constraints of supplying a valuable biopharmaceutical product to market, CFD provides a valuable insight into the underlying fluid dynamical behaviour of bio-separation operations and is probably worth pursuing.

9.1.3 Windows of operation

A typical purification process consists of a series of several purification steps. The goal of the development engineer is optimisation of the process to maximise the final product yield and purity at the end the entire purification stream. In practice, however, a process is optimised to maximise product yield and purity over each individual process step, rather than the entire

process. This is because optimisation of all of the process variables at once is simply too large an optimisation problem, so instead the problem is broken down into smaller units, each unit typically being one process step. Sometimes, the set of process parameters which will maximise the final product yield and purity, over the entire process, can differ significantly from the set of process parameters which optimise each individual process step.

As a hypothetical example, consider the series of process steps starting with alkaline lysis and clarification and followed by chromatography. Optimisation of alkaline lysis and clarification may involve gentle mixing conditions during lysis to prevent chromosomal DNA chain scission due to fluid stress, maximising chromosomal DNA removal during clarification. However, these gentle mixing conditions may limit the denaturation of chromosomal DNA during lysis leading to poor removal of the chromosomal DNA over the proceeding chromatography step. Therefore, the overall-process optimal conditions may involve better mixing over lysis, somewhat poorer chromosomal removal over clarification, but significantly better chromosomal DNA removal over chromatography. In this thesis, an effort was made to follow the effects of process changes several steps downstream to observe the overall process effects of changing upstream process variables.

It was demonstrated in chapter 6 that low to moderate levels of NaOH concentration or fluid stress did not have a significant effect on the plasmid purity. However, the size and form of the chromosomal DNA impurities was significantly affects by the NaOH concentration and fluid stress. Although chromosomal DNA size and form did not have a significant effect on its removal over alkaline lysis, it was demonstrated in chapter 7 that this can appreciably affects its removal in downstream purification steps. It was concluded that alkaline lysis should be primarily optimised with respect to maximising chromosomal denaturation, and alkaline lysis should be proceeded by unit operations such as Poros PI chromatography, calcium chloride precipitation or silica adsorption that are very effective at removing single-stranded chromosomal DNA.

In contrast, it was demonstrated that chromosomal DNA impurities were predominantly double-stranded after lysozyme and heat lysis below 85°C. At temperatures higher than 85°C the supercoiled plasmid begins to degrade during heat lysis. Therefore, heat lysis should be optimised with respect to minimising chromosomal DNA fragmentation, and the heat lysis step should be proceeded by unit operations such as Q-Sepharose, CTAB that remove chromosomal DNA based on its size relative to plasmid DNA.

9.1.4 Probes for fluid stress

When designing a plasmid DNA production process to minimise the detrimental effect of fluid stress on final product quality, it is essential to be have detailed knowledge of the fluid dynamic environment DNA molecules will experience within each piece of equipment in the purification stream. Therefore, an equally important objective of this thesis was to investigate and develop methodologies for determining fluid stress fields in scale-down and industrial equipment. One method already discussed, knowing the detailed geometry of the equipment, is to calculate using CFD simulation the internal strain rates within a piece of equipment. An alternative and probably more reliable method of determining fluid stress levels with equipment is to measure the degradation rate of known compounds within the equipment.

It has been demonstrated in this thesis that supercoiled plasmids have several unique features that make them good candidates as probes for fluid stress. Firstly, supercoiled plasmids unlike linear DNA can only exist as a completely intact double-stranded chain. Just one nick in the backbone of a supercoiled molecule will cause it to loose its supercoiling. Therefore, supercoiled plasmids will respond more homogeneously to a fluid stress field compared to double-stranded chromosomal DNA molecules that may have many single-stranded nicks randomly positioned along their backbone. Secondly, supercoiled plasmids are relatively small, so that from very dilute concentrations to higher concentrations seen in purification processes, the plasmids should behave as isolated molecules. Therefore the stress-induced degradation behaviour of supercoiled plasmid under dilute conditions should be similar to its behaviour at higher concentrations during plasmid purification. Thirdly, different supercoiled plasmids are available that have widely different susceptibilities to stress-induced degradation. Fourthly, the kinetics of supercoiled plasmid degradation is a simple first-order reaction that appears to follow the TABS theory for stress-induced molecular bond scission. Finally, it has been demonstrated that the degradation of supercoiled plasmid to open-circular plasmid can be monitored at extremely dilute plasmid concentrations. Therefore, very little supercoiled plasmid is required for large-scale studies. Although, the analytical techniques developed in this thesis made supercoiled plasmid an excellent candidate as a probe for fluid stress, the use of supercoiled plasmids as a probe has to be demonstrated. This will be highlighted in chapter 10 on future work.

9.2 DNA purification at manufacturing scale

The previous section discussed the methodologies applied to researching and designing a DNA purification process to minimise the detrimental effects associated with fluid mixing and fluid stress. After applying these methodologies, a more detailed knowledge was acquired of:

- The effect of the fluid dynamic environment on plasmid and chromosomal DNA molecules.
- The fluid dynamic environment DNA molecules will experience within equipment in the purification stream, at different scales of operation.
- How degradation of plasmid and chromosomal DNA affects final downstream product yield and purity.

This section amalgamates, and discusses, the experimental and CFD results with respect to the design of a DNA purification process.

9.2.1 Scale-up of alkaline lysis.

It was demonstrated in chapter 6 that mixing during alkaline cell lysis can be critical, particularly when using concentrated lysis buffer. As the cellular contents are released during alkaline lysis, the rheology of the lysis solution alters from an initially Newtonian state with a viscosity close to water to a non-Newtonian viscoelastic state (Ciccolini et al. 2000). Under steady fluid stress, the apparent viscosity is dominated by the higher molecular weight of chromosomal DNA, with a maximum viscosity value 25 to 30 times that of water. The impact of viscoelasticity on mixing is unknown but the literature evidence suggests that for otherwise similar conditions, the elastic properties of the solution will reduce flow leading to poorer mixing. With the high lysate viscosity, the effects of viscoelasticity and the requirements for rapid mixing, the choice of a mixing device is not a trivial problem, particularly if chromosomal fragmentation is to be avoided.

Two principle mixing strategies have been employed for alkaline lysis: stirred tanks and static mixers, both of which are discussed in greater detail in chapter 2. Alkaline lysis in stirred tanks at scales up to 50 L, has already been demonstrated Chamsart et al. (2000). They showed that, following further purification by Qiagen purification and alcohol precipitation, alkaline lysate contained a satisfactorily low concentration of chromosomal DNA (< 2% contamination), together with a satisfactory supercoiled plasmid yield (1 mg / g wcw). Of the static mixers used for alkaline lysis, two principal types of have been used for alkaline lysis: conventional in-line static mixers (Wan et al., 1998), and jet mixers (Ciccolini et al., 2002). To date, little has been published on the performance of either of these static mixers for alkaline lysis.

If alkaline lysis is done in a stirred tank, then moderate to high impeller speeds will be required to ensure that micro-mixing times are short, avoiding supercoiled plasmid denaturation. Using 0.2 M NaOH lysis buffer, an impeller speed between 50 rpm to 200 rpm was required in the 200 mL stirred vessel. For 0.4 M NaOH lysis buffer, an impeller speed between 200 rpm and 800 rpm was required to prevent supercoiled plasmid denaturation. The calculated macro-mixing

time in the 200 mL stirred vessel at 200 rpm and 800 rpm was 9.5 s and 1.2 s, respectively. The calculated micro-mixing time in the stirred vessel at 200 rpm and 800 rpm was 2.9 s and 0.4 s. In order to scale-up the 200 mL stirred tank to pilot-scale and manufacturing-scale it is important to maintain a constant mixing time in the stirred vessel.

In order to scale-up the tank based on constant macro-mixing time the impeller speed, N, must be maintained constant. However, maintaining the impeller speed constant on scale-up requires significant power input to drive the impeller. Figure 9.2 shows the power requirements as a function of scale to achieve macro-mixing times of 10 s or 1 s. Based on a maximum feasible impeller motor power of 100 kW, the maximum tank sizes that can be used to achieve a macro-mixing time of 1 s is about 700 L. The maximum tank size that can be used to achieve a macro-mixing time of 10 s is about 10,000 L. Therefore, 0.2 M NaOH can be used as a lysis buffer up to large-scales of 10,000 L, while 0.4 M NaOH lysis buffer can only be used up to about 700 L. Alternatively, the micro-mixing time at the tank impeller could be maintained constant. Maintaining a constant micro-mixing time close to the impeller requires that the power input to the tank increases in proportion to the volume of the tank. This leads to a significant power input to the tank in large-scale tank, however it requires lower power input on scale-up than maintaining a constant macro-mixing time. However, maintaining a constant micro-mixing time at the impeller may not ensure adequate mixing characteristics if lysis buffer is swept rapidly from the near-impeller region. At large scales, utilisation of more concentrated lysis buffers like 0.4 M NaOH would be extremely advantageous, as doubling and tripling the volumes of already large batches should be avoided. Unfortunately this requires short mixing times that are not feasible using stirred tanks at large scale due to power requirements.

As well as problems associated with fluid mixing, there will be an increase in fluid stress within stirred tanks upon scale-up. It was demonstrated in chapter 5, that elongational stresses degrade supercoiled and plasmid DNA. In a stirred tank environment elongation stresses will predominantly occur between fluctuating turbulent eddies. These turbulent eddies can either occur in the boundary layer of the impeller or due to turbulence in the bulk fluid. Figure 9.3 shows the turbulent stresses and impeller boundary stress in a stirred tank as a function of tank volume, at a constant micro-mixing time in the near-impeller region of 0.3 s. The turbulent stresses within the tank remain constant if the tank is scaled-up to maintain a constant micro-mixing time, but there is a considerable increase in impeller boundary stress. If the tank is scaled-up based on constant macro-mixing time, rather than micro-mixing time, then the increase in fluid stress will be even greater.

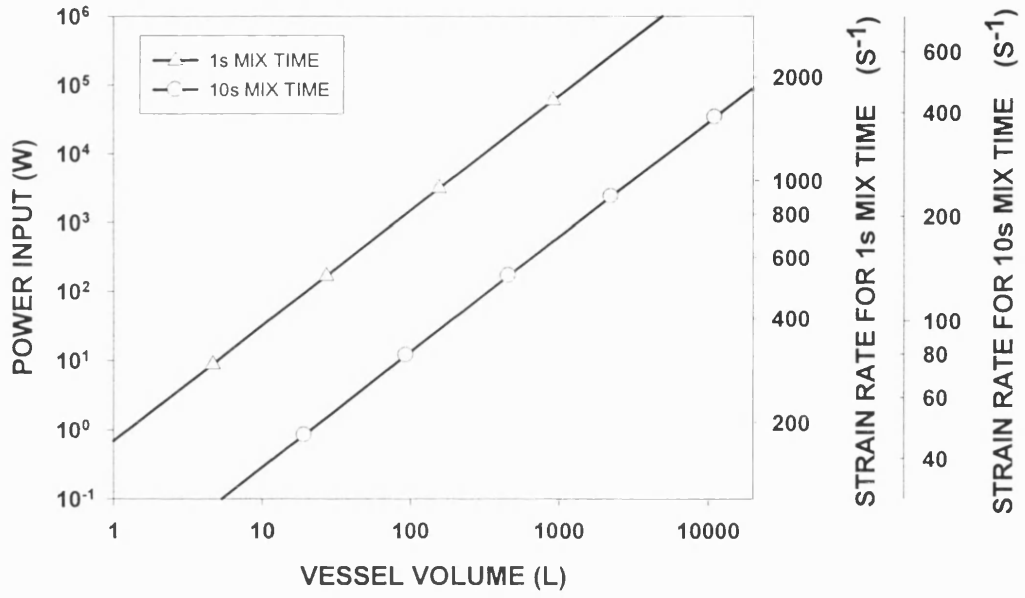

Figure 9.2. Plot showing the effect of vessel volume on power requirements for mixing. The power input and fluid stresses increase rapidly with increasing vessel size and with decreasing mixing time.

It was demonstrated in chapters 6 and 7 that increased fluid stress during alkaline lysis leads to increased chromosomal DNA fragmentation and decreased chromosomal DNA removal during downstream purification. Therefore, utilisation of stirred tanks for alkaline lysis at large-scale will lead to significantly increased chromosomal DNA fragmentation, which should be avoided.

It is useful here to estimate the scale of operation required to make 1 million doses of plasmid in one batch, for a plasmid dose of 1 mg. Estimating fermentation yields of 5 mg plasmid/g wcw (Varley et al., 1999), and estimating 50% and 70% plasmid yields over purification and filling respectively, then the resuspended cell volume immediately prior to alkaline lysis would be 5,000 L. This would increase to 10,000 L after lysis reagent addition and 15,000 L after neutralisation. Hence, it is not unreasonable to envisage 10,000 L lysis reactors for future manufacturing scale production of gene therapy plasmid vectors. Due to the difficulty in achieving rapid mixing at these scales, and the increase in fluid stress, static mixers may be a better mixing solution than stirred tank mixing for large scales of operation.

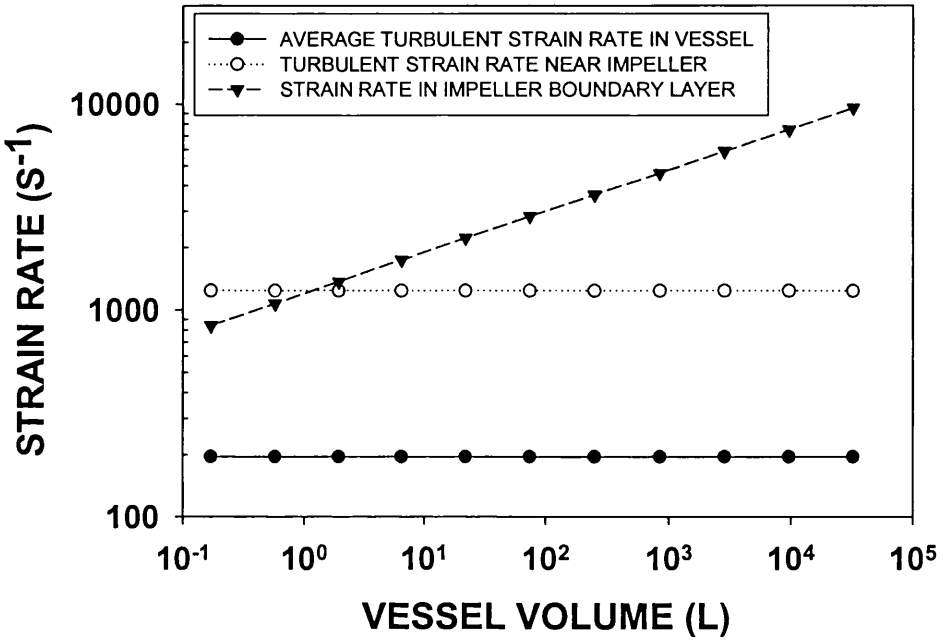

Figure 9.3. Plot showing the fluid stress in a stirred tank as a function of tank volume, at a constant tank micro-mixing time of 0.3 s.

CFD predictions of opposed jet mixing at different scales of operation showed that mixing times in opposed jets can be maintained constant across different scales of operation by mixing at appropriate jet velocities. The jet velocities required to achieve excellent mixing characteristics are well within the range of practical jet velocities, and increases in scale require only moderate increases in jet velocity to maintain the same mixing time. In addition, the magnitude of fluid stress should actually decrease with increasing jet velocity. Therefore, opposed jets are an excellent strategy for alkaline lysis mixing with respect to process scale-up.

9.2.2 Downstream purification strategies

Apply second denaturation-renaturation step.

Opposed jet mixing was demonstrated as a means of denaturing residual chromosomal DNA during downstream plasmid purification. It was demonstrated in chapter 6 that alkaline lysates typically contained a small amount of residual double-stranded chromosomal DNA. There are several effective purification techniques for removing single-stranded chromosomal DNA from supercoiled plasmid DNA, while in contrast removal of double-stranded chromosomal DNA is very difficult and expensive. By denaturing residual chromosomal DNA prior to a single-stranded DNA purification step, residual chromosomal DNA can be virtually eliminated. Use of highly concentrated denaturation buffer avoided an excessive increase in batch volume, but

required very rapid mixing to avoid plasmid degradation, which were easily achievable using opposed jets. If the entire DNA impurities are not converted to single-stranded form after alkaline lysis, a second denaturation-renaturation step should be considered prior to purification steps where chromosomal DNA is being removed. This second denaturation-renaturation step is feasible if opposed jets are employed to mix in concentrated NaOH, avoiding an excessive increase in batch volume. . The additional denaturation step is a highly effective method of removing residual open-circular plasmid DNA, as shown in chapter 7

Reduction of fluid stress during purification

It was demonstrated in chapter 5, that elongational fluid stresses are more effective at degrading supercoiled plasmid DNA than shear stresses. Therefore, equipment and flow paths should be designed to minimise elongational stresses at stages in the purification process where chromosomal contamination is still high. Due to the susceptibility of chromosomal DNA to fluid stress-induced degradation, unit operations that rely on chromosomal DNA size for its removal should be implemented as early on in the purification sequence as possible. Therefore, unit operations such as CTAB should be implemented as soon as possible after alkaline lysis. It may be more effective to alkaline lyse at low concentrations of NaOH, and reduce fluid mixing to very low levels. A unit operation such as CTAB can then be used to remove large chromosomal DNA fragments. This can be followed by a second denaturation-renaturation step to convert the remaining chromosomal DNA to single-stranded form, prior to single-stranded chromosomal DNA removal using Q-Sepharose or Poros PI chromatography.

It was demonstrated in chapter 5 that the stress-induced degradation of plasmid DNA was consistent with elongational stress causing plasmid strain and subsequent chain scission in fluid flows that were elongational or between the eddies of turbulent flows. It was demonstrated that large plasmids were significantly more susceptible to stress-induced degradation than small plasmids. Although chromatographic techniques are highly effective at removing single-stranded chromosomal DNA, these techniques generate appreciable levels of elongational stress between the chromatography resin. Therefore, if there is a movement towards using larger plasmids for gene therapy unit operations such as precipitation should be utilised to prevent plasmid degradation.

10 Conclusions

Plasmid and linear DNA degradation in a model flow field was determined to be consistent with elongational stress causing DNA stretching and subsequent scission. It appeared that DNA was susceptible to degradation in fluid flows that are highly elongational or between eddies in turbulent flows when eddies are small enough to impart significant fluid stress onto the DNA coils. Supercoiled plasmid degradation was well modelled by the TABS theory of bond scission. The conformation of DNA prior to degradation affected its rate of degradation, which in turn was affected by DNA size and solution properties such as ionic strength.

New HPLC- and fluorescence-based assays for plasmid and chromosomal DNA impurities were developed. These assays proved essential in determining DNA stress-induced degradation rates and in understanding and optimising a specific DNA purification step, cell lysis. This highlighted the importance of having robust and accurate analytical techniques available to the bioprocess engineer.

To predict fluid mixing rates and fluid stress levels within equipment, Computational Fluid Dynamics (CFD) was utilised. The CFD predictions were validated against experimental observations and proved extremely useful in understanding the fluid dynamical behaviour in a model fluid stress device and in an opposed jet mixer. This demonstrates how CFD is now becoming a valuable engineering tool for designing and optimising bioseparation processes.

For the primary DNA purification unit operation, alkaline cell lysis, it was determined that fluid stress leads to significant chromosomal DNA fragmentation. Although this did not significantly affect chromosomal DNA removal over alkaline lysis and clarification, it was demonstrated that chromosomal DNA fragmentation was detrimental depending on the choice of subsequent downstream operations. Reduction of fluid stresses could be achieved at the expense of poorer mixing; however it was determined that poor fluid mixing can lead to supercoiled plasmid yield loss particularly at high lysis buffer concentrations, and that high lysis buffer concentrations were required for effective chromosomal DNA denaturation. Therefore optimisation of the lysis step involved understanding the combined effects of chromosomal DNA fragmentation and denaturation on chromosomal DNA removal during subsequent downstream purification. The lysis step could only be effectively optimised by considering the effects of lysis on the entire process stream, a Windows of Operation approach. Opposed jets were used to improve mixing and significantly decrease fluid stress during lysis.

11 Future work

11.1.1 DNA as a probe for fluid stress

It was demonstrated that the degradation of supercoiled plasmids can be measured at extremely dilute conditions, using a modified fluorescence-based assay, and that plasmids have many properties that make them suitable molecules to be used as probes for fluid stress in large-scale equipment. The degradation rates of different size plasmids should be measured in different types of equipment, and in different scales of equipment, to determine if plasmid degradation correlates against fluid stress in equipment; and hence can be used as a generic probe for fluid stress.

Similarly, chromosomal DNA has several properties that makes it useful for monitoring fluid stress in equipment, particularly the sensitivity of chromosomal DNA to fluid stress. Comparisons of chromosomal DNA fragment size in different equipment, such as stirred vessels, chromatography columns and filters should be made to determine if the underlying mechanism of chromosomal DNA degradation is fluid elongation stress, and if chromosomal DNA can then be used as a probe for fluid stress.

11.1.2 Effects of solution properties on DNA degradation

A consistent picture of DNA degradation in the model flow fields within the capillary flow device is emerging. The effects of solution properties such as ionic strength and pH should be investigated to determine if DNA degradation rates are consistent with current polymer stretching and scission theories.

11.1.3 Stress-induced degradation of large plasmids

The purification of large plasmids is complicated enormously due to the susceptibility of the large molecules to stress-induced degradation. The effects of fluid stress in a range of relevant engineering equipment require further study.

11.1.4 Investigation of opposed jets at larger scale

CFD predictions of opposed jets were validated against published experimental DNA for jet flowrates from about 0.05 to 1.0 L/min, in 0.5 mm to 2 mm ID jets. This was a sufficient flowrate to use opposed jets for pilot-scale alkaline lysis operations. It would be interesting to determine if the CFD predictions of opposed jet performance were valid at larger scales of

operation. Having developed a CFD model for opposed jets it would be easy to perform more simulations over a wider range of jet Reynolds numbers and solution properties to determine if the CFD predictions of chapter 8 still apply.

11.1.5 Understanding chromosomal DNA flocculation

It was demonstrated that the majority of the chromosomal DNA is typically removed during cell lysis, neutralisation and clarification. However, residual chromosomal DNA always remains post-lysis and clarification. The removal of the chromosomal DNA is only moderately affected by the size of the DNA. A better understanding of the mechanism of chromosomal DNA flocculation during lysis and neutralisation is required to better optimise the alkaline lysis step.

11.1.6 Improving downstream purification

Currently, there are only a very limited number of methods to remove chromosomal DNA impurities from supercoiled plasmid cheaply and effectively at large-scale. It would be interesting to determine if utilisation of a second denaturation step, post-alkaline lysis, to denature all residual DNA impurities, followed by Q-Sepharose chromatography, could be used to remove all the denatured DNA impurities cheaply and effectively. Alternatively, calcium chloride precipitation, silica absorption or cellulose acetate could be used instead of Q-Sepharose, to remove single-stranded DNA.

12 References

Abeles, R., Frey, P., Jencks, W. Biochemistry. Jones and Bartlett . 1992.

Adam, R., Zimm, B. Shear degradation of DNA. Nucleic Acids Research. 4, 5, 1513-1536. 1977.

Atkins, E., Taylor, M. Elongational flow studies on DNA in aqueous solution and stress-induced scission of the double-helix. Biopolymers. 32, 911-923. 1992.

Baldyga, J., Bourne, J., Gholap, R. The influence of viscosity on mixing in jet reactors. 50, 1877-1880. 1995

Barton, M., Harding, P., Zuccarelli, A. General method for detecting and size large plasmid. Analytical biochemistry. 226, 235-240. 1995.

Baumann, C., Smith, S., Bloomfield, V., Bustamante, C. Ionic effects on the elasticity of single DNA molecules. Proceedings of the National Academy of Sciences. 94, 6185-6190. 1997.

Bensimon, D., Simon, A. Croquette, V., Bensimon, A. Stretching DNA with a receding meniscus. Physical Review Letters. 74, 4754-4757. 1995.

Bird, R. Dynamics of polymers liquids. John Wiley, New York. 1977.

Birnboim, H., Doly, J. A rapid alkaline lysis procedure for screening recombinant plasmid DNA. Nucleic Acids Research. 7, 1513-1522. 1979.

Boom, R., Sol, C., Salimans M., Jansen, C., Wertheim-van Dillen, P., van der Noordaa, J. Rapid and simple method for purification of nucleic acids. Journal of clinical microbiology. 28, 3, 495-503. 1990.

Bowman, R., Davidson, N. Hydrodynamic shear breakage of DNA. Biopolymers. 11, 2601-2624. 1972.

Burgi, E., Hershey, A. Specificity and concentration limit in self-protection against mechanical breakage of DNA. Journal of Molecular Biology. 4, 313-315. 1962.

Carlson, A., Signs, M., Lierman, L., Boor, R., Jim Jem, K. Mechanical disruption of *Escherichia coli* for plasmid recovery. Biotechnology and bioengineering. 48, 303-315. 1995.

Carrington, S., Odell, J. How do polymers stretch in stagnation point extensional flow-fields? Journal of Non-Newtonian Fluid Mechanics. 67, 269-283. 1996.

Carrington, S., Tatham, J., Odell, J. Macromolecular dynamics in extensional flows: 1. Birefringence and viscometry. Polymer. 38, 16, 4151-4164. 1997.

Carter, M., Milton, I. An inexpensive and simple method for DNA purification on silica particles. Nucleic Acids Research. 21, 4, 1044-1045.

Champion, J., North, P. Determination of hydrodynamic degradation of DNA using flow birefringence techniques. Journal of Physical Chemistry. 212, 1585-1592. 1972.

Chamsart, S.; Patel, H.; Hanak, J.A.J.; Hitchcock, A.G.; Nienow, A.W. Biotechnology and Bioengineering. The impact of fluid-dynamic-generated stresses on chDNA and pDNA stability during alkaline cell lysis for gene therapy products. 75, 4, 387-392. 2001.

Chandra, A., Pankaj, P., Kost, T., Gray, J. Large-scale purification of plasmid DNA by fast protein liquid chromatography using a Hi-Load Q-Sepharose column. Analytical Biochemistry. 203, 169-172. 1992.

Cherry, R., kwon, K., Transient Shear Stresses on a Suspension Cell in turbulence. Biotechnology and Bioengineering. 36, 563-571 1990.

Ciccolini, L., An engineering study of the alkaline lysis operation for the recovery of supercoiled plasmid DNA for gene therapy. Thesis. Department of Biochemical Engineering. University College London. 2000.

Ciccolini, L., Ayazi Shamlou, P., Titchener-Hooker, N. A mass balance study to assess the extent of contaminant removal achieved in the operations for the primary recovery of plasmid DNA from *Escherichia coli* cells. Biotechnology and Bioengineer. 77, 7, 796-805. 2002.

Ciccolini, L., Ayazi Shamlou, P., Titchener-Hooker, N., Ward, J. Time course of SDS-alkaline lysis of recombinant bacterial cells for plasmid release. Biotechnology and Bioengineering. 60, 6, 768-771. 1998.

Coulson, J., Richardson, J. F., Backhurst, J., Harker, J. Chemical Engineering. Volume 1. Pergamon Press. Oxford. 1991.

Cozewith, C., Busko, M. Design correlations for mixing tees. Industrial and Engineering Chemistry Research. 28, 1521-1530. 1989.

Craft, T., Graham, L., Launder, B. Impinging jet studies for turbulent model assessment –II. An examination of the performance of four turbulent models. Journal of Heat and Mass Transfer. 36, 10, 2685-2697. 1993.

Creighton, T. Proteins-structure and molecular properties. W.H. Freeman and Company, New York. 1993.

Dancis, B. Shear breakage of DNA. Biophysical Journal. 24, 489-503. 1978.

Davison, P. The effect of hydrodynamic shear on the deoxyribonucleic acid from T2 and T4 bacteriophages. Biochemistry. 45, 1560-1568. 1959.

De Gennes, P. Coil-stretch transition of dilute flexible polymers under ultrahigh velocity gradients. The Journal of Chemical Physics. 60, 12, 5030-5042. 1974.

Evans, R., Xu, Z., Bohannon, K., Wang, B., Bruner, M., Volkin, D. Evaluation of degradation pathways for plasmid DNA in pharmaceutical formulations via accelerated stability studies. Journal of Pharmaceutical Sciences. 89, 1, 76-87. 2000.

Feliciello, I., Gianni, C. A modified alkaline lysis method for the preparation of highly purified plasmid DNA from *Escherichia coli*. Analytical Biochemistry. 212, 394-401. 1993

Ferreira, G., Cabral, J., Prazeres, D. A Comparison of gel filtration chromatographic supports for plasmid purification. Biotechnology Techniques. 11, 6, 417-420. 1997.

Ferreira, G., Cabral, J., Prazeres, D. Monitoring of process streams in the large-scale production and purification of plasmid DNA for gene therapy applications. Pharmaceutical Pharmacology Communications. 5, 57-59. 1999.

Ferreira, G., Cabral, J., Prazeres, D. Purification of supercoiled plasmid DNA using chromatographic processes. Journal of Molecular Recognition. 11, 250-251. 1998.

Ferreira, G., Monteiro, G., Prazeres, D., Cabral, J. Downstream processing of plasmid DNA for gene therapy and DNA vaccine applications. Tibtech. 20, 18, 380-387. 2000.

Fishman, D., Patterson, G. Light scattering studies of supercoiled and nicked DNA. Biopolymers. 38, 535-552. 1996.

Forney, L., Gray, G. Optimum design of a tee mixer for fast reactions. AIChE Journal. 36, 11, 1773-1776. 1990.

Frenkel, J. Orientation and rupture of linear macromolecules in a dilute solutions under the influence of viscous flow. Acta Physocichimica U.R.S.S. 19, 1, 51-76. 1944.

Friedman, T. The road toward human gene therapy – a 25-year perspective. Annals of Medicine. 29, 575-577. 1997.

Fuciarelli, A, Sisk, E., Thomas, R., Miler, D. Induction of base damage in DNA solutions by ultrasonic cavitation. Free Radical Biology and Medicine. 18, 2, 231-238. 1995.

Ghoniem, S., Chauveteau, G., Moan, M., Wolff, C. Mechanical degradation of semi-dilute polymer solutions in laminar flows. The Canadian Journal of Chemical Engineering. 59, 450-454. 1981.

Grenville, R., A new theory improves the correlaton of blend time for turbulent jet mixed vessels. Transcripts IChemE, 74, 391-396. 1996.

Hagerman, P. Flexibility of DNA. Annual Review of Biophysics and Biophysical Chemistry. 17, 265-286. 1988.

Harnby, N., Edwards, M., Nienow, A. Mixing in the process industries. Butterworth Heinemann. 1992.

Harrington, R., Zimm, B. Degradation of polymers by controlled hydrodynamic shear. 69, 1, 161-175. 1965.

Henzler, H. Particle Stress in Bioreactors. Advances in Biochemical Engineering/Biotechnology. 67, 35-82. 2000.

Hershey, A., Burgi, E. Molecular homogeneity of the deoxyribonucleic acid of phage T2. Journal of Molecular Biology. 2, 143-152. 1960.

Hoare, M., Narendranathan, T., Flint, J., Heywood-Waddington, D., Bell, D., Dunnill, P. Disruption of protein precipitates during shear in couette flow and in pumps. Industrial and Engineering Chemistry Fundamentals. 21, 402-406. 1982.

Hunkler, D., Nguyen, T., Kausch, H. Polymer solutions under elongational flow: 2. An evaluation of models of polymer dynamics for transient and stagnation point flows. Polymer. 37, 4271-4282. 1996.

Igou, D., Lo, J., Clark, D., Mattice, W., Younathan, E. On the nature of interaction of dodecyl sulfate with proteins. Evidence from uncharged polypeptides. Biochemical and Biophysical Research Communications. 60, 1, 140-145. 1974.

Ingrahm, Maaløe, Neidhardt. Growth of the Bacterial Cell. Sinauer. 1983

Johnson, D., Wood, P., Hrymak, A. The effect of geometrical parameters on the flow field of an opposed jet RIM mix head: equal flow and matched fluids. The Canadian Journal of Chemical Engineering. 74, 40-48. 1996.

Kieser, T. Factors affecting the isolation of CCC DNA from *Streptomyces lividans* and *Escherichia coli*. Plasmid. 12, 19-36. 1984.

Lahijani, R., Duhon, M., Lusby, E., Betita, H., Marquet, M. Quantitation of host cell DNA contaminate in pharmaceutical-grade plasmid DNA using competitive polymerase chain reaction and enzyme-linked immunosorbent assay. Human gene therapy. 9, 1173-1180. 1998.

Lander, L., Winters, M., Meacle, F. Process for the scaleable purification of plasmid DNA.. United States Patent. Number 09/745,217. 2000.

Lander, R., Manger, W., Scouloudis, M., Ku, A., Davis, C., Lee, A. Gaulin homogenisation: A mechanistic study. Biotechnology Progress. 16, 80-85. 2000.

Lander, R., Winters, M., Meacle, F. , Buckland, B., Lee, A. Fractional precipitation of plasmid DNA from lysate by CTAB. Biotechnology and Bioengineering. 79, 7, 776-784. 2002.

Langowski, J., Giesen, U. Configurational and dynamic properties of different length superhelical DNAs measured by dynamic light scattering. Biophysical Chemistry. 34, 9-18. 1989.

Larson, R., Perkins, T., Smith, D., Chu, S. Hydrodynamics of a DNA molecule in a flow field. Physical Review E. 55, 2, 1794-1797. 1997

Lee, A., Sagar, S. A method for large scale plasmid purification. International Patent. WO 96/36706. 1996.

Lee, G., Chrisey, L., Colton, R., Direct measurement of the forces between complementary strands of DNA. Science. 266, 771-773. 1994.

Levich, V. Physico-Chemical Hydrodynamics. Prentice-Hall, New Jersey. 1962.

Levinthal, C., Davison, P. Degradation of deoxyribonucleic acid under hydrodynamic shearing forces. Journal of Molecular Biology. 3, 674-683. 1961

Levy, M., Ciccolini, L., Yim, S., Tsai, J., Titchener-Hooker, N., Ayazi Shamlou, P., Dunnill, P. The effects of material properties and fluid flow intensity on plasmid DNA recovery during cell lysis. Chemical Engineering Science. 54, 3171-3178. 1999.

Levy, M., Collins, I., Yim, S., Ward, J., Titchener-Hooker, N., Ayazi Shamlou, P., Dunnill, P. Effect of shear on plasmid DNA in solution. Bioprocess Engineering. 20, 7-13. 1999.

Levy, M., Lotfian, P., O'Kennedy, R., Lo-Yim, M., Ayazi Shamlou, P. Quantitation of supercoiled circular content in plasmid DNA solutions using a fluorescence-based method. Nucleic Acids Research. 28, 12, 1-7. 2000.

Levy, M., O'Kennedy, R., Ayazi Shamlou, P., Dunnill, P. Biochemical engineering approaches to the challenges of producing pure plasmid DNA. Tibtech. 18, 296-305. 2000.

Lindahl, T., Anderson, A., Rate of chain breakage at apurinic sites in double-stranded deoxyribonucleic acid. Biochemistry. 54, 503-512. 1997.

Luo, Y., Han, Z., Chin, S., Linn, S. Three chemically distinct types of oxidants formed by iron-mediated Fenton reactions in the presence of DNA. Proceedings of the National Academy of Sciences. 91, 12438-12442. 1994.

Lyubchenko, Y., Shlyakhtenko, S. Visualisation of supercoiled DNA with atomic force microscopy *in situ*. Biophysics. 94, 496-501. 1997.

Macosko, C. Rheology principles, measurements, and applications. Wiley-VCH.1994.

Mahajan, A., Kirwan, D. Micromixing Effects in a Two-Impinging-Jets Precipitator", AIChE Journal, 42, 1801-1890. 1996.

Marko, J. Stretching DNA. Macromolecules. 28, 8759-8770. 1995.

Marquet, M., Horr, N.A., Meek, J.A. Process development for the manufacture of plasmid DNA vectors for use in gene therapy. Biopharm. 26-37 1995.

McHugh, P., Meacle, F., Hoare, M. A HPLC Assay for Different Nucleic Acid Forms. (in progress)

McHugh, P. Purification of DNA using Calcium Chloride. Thesis. (in progress)

Melzak, K., Sherwood, C., turner, R., Haynes, C. Driving forces for DNA adsorption to silica in perchlorate solutions. Journal of Colloid and Interface Science. 181, 635-644. 1996.

Metzner, A. B., Metzner, A.P. Stress levels in rapid extensional flows of polymeric fluids. Rheolgica Acta. Band 9. 174-181. 1970.

Mhashilkar, A., Chada, S., Roth, J., Ramesh, R. Gene therapy therapeutic approaches and implications. Biotechnology Advances. 19, 279-297. 2001.

Middaugh, C., Evans, R., Montgomery, D., Casimiro, D. Analysis of plasmid DNA from a pharmaceutical perspective. Journal of Pharmaceutical Sciences. 87, 131-146. 1998.

Moan, M., Chauveteau, G., Ghoniem, S. Entrance effect in capillary flow of dilute and semi-dilute polymer solutions. Journal of Non-Newtonian Fluid Mechanics. 5, 463-474. 1979.

Moreau, N., Tabary, X., Le Goffic, F. Purification and separation of various plasmid forms by exclusion chromatography. Analytical Biochemistry. 166, 188-193. 1987.

Mountain, A. Gene therapy: the first decade. Trends in Biotechnology. 18, 119-128. 2000.

Murphy, J., Wibbenmeyer, J., Fox, G., Willson, R. Purification of plasmid DNA using selective precipitation by compaction agents. Nature Biotechnology. 17, 822-823. 1999.

Muthumani, K., Kudchodkar, S., Pavlakis, G., Weiner, D. Issues for improving multi-plasmid DNA vaccines for HIV-1. Vaccine. 20, 19999-2003. 2002.

Nabel, G. Direct gene transfer with DNA-liposome complexes in melanoma: expression, biological activity, and lack of toxicity in humans. Proceedings of the National Academy of Sciences. 90, 11307-11311. 1993.

Nandakumar, M., Norderg, E., Mattiasson, B. Integrated flow-injection processing for on-line quantification of plasmid DNA during cultivation of E. coli. Biotechnology and Bioengineering. 73, 5, 406-411. 2001.

Nguyen, T., Kausch, H. Chain scission in transient extensional flow kinetics and molecular weight dependence. Journal of Non-Newtonian Fluid Mechanics. 30, 125-140. 1988.

Nguyen, T., Kausch, H. Mechanochemical degradation in transient elongational flow. Advances in Polymer Sciences. 100, 74-182. 1992.

Nguyen, T., Kausch, H. Mechano-chemical degradation of polymer solution in capillary flow: laminar and turbulent regime. Chima. 40, 129-135. 1986.

North, P., Champion, J. Hydrodynamic Degradation of DNA. Journal De Chimie Physique. 71, 10, 1282-1284. 1974.

Noy, A., Vezenov, D., Kayyem, J., Meade, T., Lieber, C. Stretching and breaking duplex DNA by chemical force microscopy. Chemical Biology. **4**, 519-527. 1997.

O'Leary. C., Forney, L., Optimisation of in-line mixing at 90° Tee. Industrial and Engineering Chemistry Process Design and Development. 24, 332-340. 1985.

Odell, J., Keller, A. Rabin, Y. XXXX get Reference

Odell, J., Keller, A., Muller, A. Thermomechanical degradation of macromolecules. Colloid Polymer Science. 324, 270-307. 1992.

Odell, J., Keller, H. Flow-induced chain fracture of isolated linear macromolecules in solution. Journal of Polymer Science. 24, 1889-1916. 1986.

Odell, J., Taylor, M. Dynamics and thermomechanical stability of DNA in solution. Biopolymers. 34, 1483-1493. 1994.

Oefner, P., Mulligan, J., Davis, R. Efficient random subcloning of DNA sheared in a recirculating point-sink flow system. Nucleic Acids Research. 24, 20, 3879-3886. 1996.

Perkins, T., Smith, D., Chu, S. Single polymer dynamics in an elongational flow. Science. 276, 2016-2021. 1997.

Perkins, T., Smith, D., Larson, R., Chu, S. Stretching of a single tethered polymer in a uniform flow. Science. 268, 83-87. 1995.

Peterlin, A. Hydrodynamics of linear macromolecules. Pure and Applied Chemistry. 12, 563-586. 1966.

Prazeres, D., Ferreira, G., Monteiro, G., Cooney, C., Cabral, J. Large-scale production of pharmaceutical-grade plasmid DNA for gene therapy: problems and bottlenecks. Tibtech. 17, 169-174. 1999.

Prazeres, D., Schluep, T., Cooney, C. Preparative purification of supercoiled plasmid DNA using anion-exchange chromatography. Journal of chromatography A. 806, 31-45. 1998.

Qiagen giga-prep handbook. Need reference.

Ram, N., Cope, K., Durham, D. Scaleable method for the production of plasmid DNA using hydrophobic interaction chromatography. Hydrophobic Interaction Chromatography Conference, Phoenix, Azirona. 1999.

Raucci, G., Maggi, C., Parente, D. Capillary electrophoresis of supercoiled DNA molecules: parameters governing the resolution of topoisomers and their separation from open forms. Analytical Chemistry. 72, 821-826. 2000.

Reese, H., Zimm, B. Fracture of polymer chains in extensional flow: experiments with DNA and an molecular dynamics simulation. Journal of Chemical Physics. 92, 4, 2650-2662. 1990.

Romanowski, G., Lorenz, M., Wachernagel, W. Adsorption of plasmid DNA to mineral surfaces and protection against DNAase I. Applied and Environmental Microbiology. 57, 4, 1057-1061. 1991.

Rouse, P. A theory of the linear viscoelastic properties of dilute solutions of coiling polymers. The Journal of Chemical Physics. 21, 7, 1272-1280. 1953.

Ryskin, G. Calculation of the effect of polymer additive in a converging flow. Journal of Fluid Mechanics. 178, 423-440. 1987.

Sambrook, J., Fritsch, E., Maniatis, T. Molecular cloning: A laboratory manual, 2nd edition, Cold Spring Harbor Laboratory Press, New York. 1989.

Sayers, J., Evans, D., Thomson, J. Identification and eradication of a denatured DNA isolated during alkaline lysis-based plasmid purification procedures. Analytical Biochemistry. 241, 186-189. 1996

Schaer, E., Guichardon, P., Falk, L., Plasari, E. Determination of local energy dissipation rate in impinging jets by a chemical reaction method. Chemical Engineering Journal. 72, 125-138. 1999.

Scopes, R. Protein purification: Principles and practice. Springer-Verlag, New York. 1994.

Singer, V., Jones, L., Yue, S., Haugland, R. Characterisation of Picogreen reagent and development of a fluorescence-based solution assay for double-stranded DNA. Analytical Biochemistry. 249. 228-238. 1997.

Smith, D., Babcock, H., Chu, S. Single-polymer dynamics in steady shear flow. Science. 283, 1724-1730. 1999.

Smith, D., Chu, S. Response of flexible polymers to a sudden elongational flow. Science. 281, 1335-1339. 1998.

Smith, S., Cui, Y., Bustamante, C. Over-stretching b-DNA: The elastic response of individual double-stranded and single-stranded DNA molecules. Science. 271, 795-799. 1996

Smith, S., Finzi, L., Bustamente, C. Direct mechanical measurements of the elasticity of single DNA molecules by using magnetic beads. Science. 258, 1122-1126. 1992.

Solc, K., Stockmayer, W. Shape of a random-flight chain. The Journal of Chemical Physics. 54, 6, 2756-2757. 1971

Strick, T., Allemand, J., Bensimon, D., Croquette, V. Behaviour of Supercoiled DNA. Biophysical Journal. 74, 2016-2028. 1998.

Talboys, B., Dunnill, P. Effect of shear on membrane-associated enzymes: studies of isolated progesterone 11α-hydroxylase complex from Rhizopus nigricans. Biotechnology and Bioengineering. 27, 1726-1729. 1985.

Thatcher, D., Hitchcock, A., Hanak, J., Varley, D. Method of plasmid DNA production and purification. International Patent. WO 97/29190. 1997

Theodossiou, I., Dunnill, P. Methods of enhancing the recovery of plasmid genes from neutralised cell lysate. Bioprocessing Engineering. 20, 147-156. 1999.

Thorstenson, Y., Oefner, P., Davis, R. An automated hydrodynamic process for controlled, unbiased DNA shearing. Genome methods. 8, 848-855. 1998.

Tosun, G. A study of micromixing in tee mixers. Industrial and Engineering Chemistry Research. 26, 1184-1193. 1987.

Unger, D, Muzzio, F. Laser-induced fluorescence technique for the quantification of mixing in impinging jets. AIChE Journal. 45, 12, 2477-2486. 1999

Unger, D., Muzzio, F., Brodkey, R. Experimental and numerical characterisation of viscous flow and mixing in an impinging jet contractor. The Canadian Journal of Chemical Engineering. 76, 546-555. 1998.

Varley, D.L., Hitchcock, A.G., Weiss, A.M.E., Horler, W.A., Cowell, R., Peddie, L., Sharpe, G., Thatcher, D., Hanak, J. Production of plasmid DNA for human gene therapy using modified alkaline lysis and expanded bed anion exchange chromatography. Bioseparation. 8, 209-217. 1999.

Versteeg, H., Malalasekera, W. An introduction to computational fluid dynamics. Longman Group. 1995

Wan, N., McNeilly, D., Christopher, C. Method for lysing cells. United States Patent. Number 5,837,529. 1998.

Wang, M., Lai, E. Pulsed field separation of large supercoiled and open-circular DNAs and its application to bacterial artificial chromosome cloning. Electrophoresis. 16, 1-7. 1995.

Wang, M., Yin, H., Landick, R., Gelles, J., Block, S. Stretching DNA with optical tweezers. Biophysical Journal. 72, 1335-1346. 1997.

Yim, S., Shamlou, P. The engineering effects of fluids flow on freely suspended biological macro-materials and macromolecules. Advances in Biochemical Engineering/Biotechnology. 67, 83-122. 2000.

Zimm, B. Journal of Chemical Physics. 24, 269, 1956.

Zimm, B., Reese, H. The degradation of T7 DNA in converging flow. Nucleic Acids Research. 18, 15, 4469- 4470. 1990.